

MATERIALS PHYSICS AND MECHANICS

Vol. 51, No. 7, 2023

125

MATERIALS PHYSICS AND MECHANICS

Principal Editors:

Alexander Belvaev

Andrei Rudskoi

Institute for Problems in Mechanical Engineering of the Russian Academy of Science (RAS), Russia

Peter the Great St. Petersburg Polytechnic University, Russia

Founder and Honorary Editor: Ilya Ovid'ko (1961-2017)

Institute for Problems in Mechanical Engineering of the Russian Academy of Sciences (RAS), Russia

Associate Editor:

Anna Kolesnikova

Artem Semenov

Institute for Problems in Mechanical Engineering of the Russian Academy of Sciences (RAS), Russia Peter the Great St. Petersburg Polytechnic University, Russia

Editorial Board:

E.C. Aifantis

Aristotle University of Thessaloniki, Greece

K.E. Aifantis

University of Florida, USA

U. Balachandran

Argonne National Laboratory, USA

A. Bellosi

Research Institute for Ceramics Technology, Italy

S.V. Bobylev

Institute for Problems in Mechanical Engineering (RAS), Russia

A.I. Borovkov

Peter the Great St. Petersburg Polytechnic University, Russia

G.-M. Chow

National University of Singapore, Singapore

Yu. Estrin

Monash University, Australia

A.B. Freidin

Institute for Problems in Mechanical Engineering (RAS), Russia

Y. Gogotsi

Drexel University, USA

I.G. Goryacheva

Institute of Problems of Mechanics (RAS), Russia

D. Hui

University of New Orleans, USA

G. Kiriakidis

IESL/FORTH, Greece

D.M. Klimov

Institute of Problems of Mechanics (RAS), Russia

G.E. Kodzhaspirov

Peter the Great St.Petersburg Polytechnic University, Russia

S.A. Kukushkin

Institute for Problems in Mechanical Engineering (RAS), Russia

T.G. Langdon

University of Southampton, U.K.

V.P. Matveenko

Institute of Continuous Media Mechanics (RAS), Russia

A.I. Melker

Peter the Great St. Petersburg Polytechnic University, Russia

Yu.I. Meshcheryakov

Institute for Problems in Mechanical Engineering (RAS), Russia

N.F. Morozov

St.Petersburg State University, Russia

R.R. Mulyukov

Institute for Metals Superplasticity Problems (RAS), Russia

Yu.V. Petrov

St.Petersburg State University, Russia

N.M. Pugno

Politecnico di Torino, Italy

B.B. Rath

Naval Research Laboratory, USA

A.E. Romanov

Ioffe Institute (RAS), Russia

A.M. Sastry

University of Michigan, Ann Arbor, USA

B.A. Schrefler

University of Padua, Italy

N.V. Skiba

Institute for Problems in Mechanical Engineering (RAS), Russia

A.G. Sheinerman

Institute for Problems in Mechanical Engineering (RAS), Russia

R.Z. Valiev

Ufa State Aviation Technical University, Russia

K. Zhou

Nanyang Technological University, Singapore

"Materials Physics and Mechanics" Editorial Office:

Phone: +7(812)552 77 78, ext. 224 E-mail: mpmjournal@spbstu.ru Web-site: http://www.mpm.spbstu.ru

International scientific journal "Materials Physics and Mechanics" is published by Peter the Great St. Petersburg Polytechnic University in collaboration with Institute for Problems in Mechanical Engineering of the Russian Academy of Sciences in both hard copy and electronic versions.

The journal provides an international medium for the publication of reviews and original research papers written in English and focused on the following topics:

- Mechanics of composite and nanostructured materials.
- Physics of strength and plasticity of composite and nanostructured materials.
- Mechanics of deformation and fracture processes in conventional materials (solids).
- Physics of strength and plasticity of conventional materials (solids).
- Physics and mechanics of defects in composite, nanostructured, and conventional materials.
- Mechanics and physics of materials in coupled fields.

Owner organizations: Peter the Great St. Petersburg Polytechnic University; Institute of Problems of Mechanical Engineering RAS.

Materials Physics and Mechanics is indexed in Chemical Abstracts, Cambridge Scientific Abstracts, Web of Science Emerging Sources Citation Index (ESCI) and Elsevier Bibliographic Databases (in particular, SCOPUS).

© 2023, Peter the Great St. Petersburg Polytechnic University © 2023, Institute for Problems in Mechanical Engineering RAS



МЕХАНИКА И ФИЗИКА МАТЕРИАЛОВ

Materials Physics and Mechanics

Том 51, номер 7, 2023 год

Учредители:

Редакционная коллегия журнала Главные редакторы:

д.ф.-м.н., чл.-корр. РАН **А.К. Беляев** Институт проблем машиноведения Российской академии наук (РАН)

д.т.н., академик РАН **А.И. Рудской** *Санкт-Петербургский политехнический университет Петра Великого*

Основатель и почетный редактор: д.ф.-м.н. И.А. Овидько (1961-2017)

Институт проблем машиноведения Российской академии наук (РАН)

Ответственный редактор

д.ф.-м.н. А.Л. Колесникова

Институт проблем машиноведения Российской академии наук (РАН) д.ф.-м.н. **А.С. Семенов** Санкт-Петербургский политехнический университет

Петра Великого

Международная редакционная коллегия:

д.ф.-м.н. С.В. Бобылев

Институт проблем машиноведения РАН, Россия

к.т.н., проф. А.И. Боровков

Санкт-Петербургский политехнический ун-т Петра Великого, Россия

д.ф.-м.н., проф. Р.З. Валиев

Уфимский государственный технический университет, Россия

д.ф.-м.н., академик РАН И.Г. Горячева

Институт проблем механики РАЙ, Россия

д.ф.-м.н., академик РАН Д.М. Климов

Институт проблем механики РАН, Россия

д.т.н., проф. Г.Е. Коджаспиров

Санкт-Петербургский политехнический ун-т Петра Великого, Россия

д.ф.-м.н., проф. С.А. Кукушкин

Институт проблем машиноведения РАН, Россия

д.ф.-м.н., академик РАН В.П. Матвеенко

Институт механики сплошных сред РАН, Россия

д.ф.-м.н., проф. А.И. Мелькер

Санкт-Петербургский политехнический ун-т Петра Великого, Россия

д.ф.-м.н., проф. Ю.И. Мещеряков

д.ф.-м.н., проф. **Ю.н. мещеряков** Институт проблем машиноведения РАН, Россия

д.ф.-м.н., академик РАН Н.Ф. Морозов

Санкт-Петербургский государственный университет, Россия

д.ф.-м.н., чл.-корр. РАН Р.Р. Мулюков

Институт проблем сверхпластичности металлов РАН, Россия

д.ф.-м.н., чл.-корр. РАН **Ю.В. Петров** Санкт-Петербургский государственный университет, Россия

д.ф.-м.н., проф. А.Е. Романов

Физико-технический институт им. А.Ф. Иоффе РАН, Россия

д.ф.-м.н. Н.В. Скиба

Институт проблем машиноведения РАН, Россия

д.ф.-м.н., проф. А.Б. Фрейдин

Институт проблем машиноведения РАН, Россия

д.ф.-м.н. А.Г. Шейнерман

Институт проблем машиноведения РАН, Россия

Prof., Dr. E.C. Aifantis

Aristotle University of Thessaloniki, Greece

Dr. K.E. Aifantis

University of Florida, USA

Dr. U. Balachandran

Argonne National Laboratory, USA

Dr. A. Bellosi

Research Institute for Ceramics Technology, Italy

Prof., Dr. G.-M. Chow

National University of Singapore, Singapore

Prof., Dr. Yu. Estrin

Monash University, Australia

Prof., Dr. Y. Gogotsi

Drexel University, USA

Prof., Dr. **D. Hui**

University of New Orleans, USA

Prof., Dr. G. Kiriakidis

IESL/FORTH, Greece

Prof., Dr. T.G. Langdon

University of Southampton, UK

Prof., Dr. N.M. Pugno

Politecnico di Torino, Italy

Dr. B.B. Rath

Naval Research Laboratory, USA

Prof., Dr. A.M. Sastry

University of Michigan, Ann Arbor, USA

Prof., Dr. B.A. Schrefler

University of Padua, Italy Prof. Dr. **K. Zhou**

Nanyang Technological University, Singapore

Тел.: +7(812)552 77 78, доб. 224 E-mail: mpmjournal@spbstu.ru Web-site: http://www.mpm.spbstu.ru

Тематика журнала

Международный научный журнал "Materials Physics and Mechanics" издается Санкт-Петербургским политехническим университетом Петра Великого в сотрудничестве с Институтом проблем машиноведения Российской академии наук в печатном виде и электронной форме. Журнал публикует обзорные и оригинальные научные статьи на английском языке по следующим тематикам:

- Механика композиционных и наноструктурированных материалов.
- Физика прочности и пластичности композиционных и наноструктурированных материалов.
- Механика процессов деформации и разрушения в традиционных материалах (твердых телах).
- Физика прочности и пластичности традиционных материалов (твердых тел).
- Физика и механика дефектов в композиционных, наноструктурированных и традиционных материалах.
- Механика и физика материалов в связанных полях.

Редколлегия принимает статъи, которые нигде ранее не опубликованы и не направлены для опубликования в другие научные издания. Все представляемые в редакцию журнала "Механика и физика материалов" статъи рецензируются. Статъи могут отправляться авторам на доработку. Не принятые к опубликованию статъи авторам не возвращаются.

Журнал "Механика и физика материалов" ("Materials Physics and Mechanics") включен в систему цитирования Web of Science Emerging Sources Citation Index (ESCI), SCOPUS и РИНЦ.

© 2023, Санкт-Петербургский политехнический университет Петра Великого © 2023, Институт проблем машиноведения Российской академии наук

Contents

Silicon nanomagnetism N.T. Bagraev, N.A. Dovator, L.E. Klyachkin	1-6
Destruction threshold of ZrO ₂ under microsecond magnetic-pulse action S.I. Krivosheev, G.A. Shneerson, S.G. Magazinov, D.V. Zhukov, K.V. Voloshin	7-14
Synthesis and characterization of iron-doped TiO ₂ nanotubes for dye-sensitized solar cells B. Samran, E.N. Timah, P. Thongpanit, S. Chaiwichian	15-21
A kinetic model of the stress-induced void evolution in pentagonal whiskers and rods A.S. Khramov, S.A. Krasnitckii, A.M. Smirnov, M.Yu. Gutkin	22-33
Toughening of nanocrystalline alloys due to grain boundary segregations: Finite element modeling A.G. Sheinerman, R.E. Shevchuk	34-41
Elastic properties of additively produced metamaterials based on lattice structures A.I. Borovkov, L.B. Maslov, M.A. Zhmaylo, F.D. Tarasenko, L.S. Nezhinskaya	42-62
Modal and harmonic analysis of the rotor system involving four different materials by finite element code: Ansys workbench N. Afane, S. Zahaf, M. Dahmane, A. Belaziz, N. Rachid	63-98
Evaluation of mechanical properties of ABS-based fiber composite with infill using 3D printing technology P. Venkataramana, S.P. Jani, U. Sudhakar, M. Adam Khan, K. Sravanthi	9-106
Assessment of physical and vibration damping characteristics of sisal/PLA biodegradable composite Y. Munde, A.S. Shinde, I. Siva, P. Anearo	7-116
Stiffness characteristics of implanted steel plates after exposure to corrosion R.R. Giniyatullin, N.M. Yakupov, V.G. Kuznetsov	7-123
Physical and mechanical properties of modified chrome coatings S. Vodopyanova, G. Mingazova, R. Fomina, R. Sayfullin	24-136
Increasing of the resistance against contact corrosion of LAIDP with steel tool joints V.N. Malyshev, M.Ya. Gelfgat, A.I. Shcherbakov, A.A. Alkhimenko	37-142
Assessment of industrial safety at oil refining facilities based on stochastic modeling G.Kh. Samigullin, S.A. Nefedyev, L.G. Samigullina, A.Yu. Bruslinovskiy	3-147

Silicon nanomagnetism

Submitted: August 1, 2023

Approved: August 14, 2023

Accepted: September 15, 2023

N.T. Bagraev, N.A. Dovator, L.E. Klyachkin [™]

Ioffe Institute, St. Petersburg, Russia

☑ leonid.klyachkin@gmail.com

Abstract. The paper studied the dependence of the magnitude of the magnetic field induced in the contour formed by the edge channels of the silicon nanosandwich structure on the magnitude of the external magnetic field used for pre-magnetization. The measurements were carried out using a fluxgate magnetometer inside a magnetic screen, which ensures the value of the variation in the magnetic field induction no more than 0.1 nT. The experimental results obtained are in good agreement with preliminary estimates that take into account the energy of negative-U dipoles, and thus confirm the defining role of the spin—orbit interaction in quantum transport in the edge channels of the silicon nanosandwich structure. The presence of nanomagnetism in the contour of the edge channels of nanosandwich structures based on the classical semiconductor silicon, which were created using planar technology methods widely used to create processors and various integrated circuits, is demonstrated for the first time.

Keywords: silicon nanosandwich; edge channel; magnetic flux quantum; negative-U centers; nanomagnetism

Acknowledgements. The work was financed within the framework of the State assignment on topic 0040-2019-0017 "Interatomic and atomic-molecular interactions in gases and condensed matter; quantum magnetometry and multiphoton laser spectroscopy".

Citation: Bagraev NT, Dovator NA, Klyachkin LE. Silicon nanomagnetism. *Materials Physics and Mechanics*. 2023;51(7): 1-6. DOI: 10.18149/MPM.5172023 1.

Introduction

The development and improvement of planar technology in the first decades of the 21st century has led to the creation of high-performance processors with feature sizes of just a few nanometers. Only a few companies in the world have technologies with element sizes below 14 nm: their competition has led to a race to reduce the size of elements and, accordingly, to increase their number per unit area. However, the situation is currently close to saturation for several reasons. First, there are fundamental physical limitations to creating equipment to implement technology with feature sizes smaller than approximately 1 nm. Secondly, high density of elements in the processor chip, with any variant of its classical architecture (stabilized DC power supply), leads to the flow of a large operating current through a unit area, which requires solving the complex problem of Joule heat removal. The fact that this problem will arise sooner or later became obvious several decades ago. Today it is clear that a further increase in the concentration of elements with a decrease in their size becomes practically impossible.

The search for a solution to this problem has led to the development of a number of alternative directions. One of them is the creation of nanomagnetic chips that perform logical switching under the influence of a magnetic field, which can significantly reduce the energy load compared to a classical processor [1–6]. One such nanomagnetic chip is a multilayer structure consisting of thousands of layers of nanomagnets that can act as individual logic

elements [7]. Scientists working in this direction believe that the use of such chips creates opportunities for parallelization of calculations, and, in addition, makes it possible to offer functions for dynamically changing the processor architecture, which can be optimized each time to perform a specific task.

In addition, in recent decades, special attention has been paid to the development of such a direction of nanophysics as spintronics, which uses the dynamics of the magnetic moment for the transfer and storage of information, as well as the magnetic properties of materials in computational operations [8–12]. Thus, research in this area led to the development of spin magnetic memory devices with a cell size of less than 10 nm, in which information is encoded and stored not in electron charges, as in conventional electronics, but in their spins [13].

It should be noted that from the point of view of the interaction of the electrical and magnetic properties of materials, it is especially tempting to consider the possibility of obtaining magnetic nanostructures without paramagnetic impurities based on classical semiconductors, for example, silicon, to which methods of planar technology widely used to create processors and integrated circuits for various purposes are applicable.

Therefore, another direction, alternative to those described above, is the creation of low-dimensional silicon nanosandwich structures (SNS), in the edge channels (ECs) of which quantum transport of charge carriers is realized at high, up to room, temperatures. Developments in this direction are based on the achievements of nanophysics and nanotechnology of quantum-sized structures, which display size quantization effects, quantum interference, and enable ballistic transport and single-electron tunneling of charge carriers [14,15]. One of the most important experimental results obtained when studying the effects of quantum spin-dependent transport in the above-mentioned SNS structures is the demonstration of the spin field transistor effect [16], which became possible due to the spin—orbit interaction in the ECs, and, accordingly, the resulting quantum spin interference.

This paper presents the results of experiments to study the behavior of the magnetic moment arising in the EC contour in a SNS structure under the influence of an external magnetic field. These experiments are a continuation of studies of spin-dependent transport in SNS structures with the aim of creating SNS-based memory cells that can be switched by a magnetic field.

Method

An experimental SNS built in Hall geometry, which is an ultra-narrow p-type silicon quantum well (QW) limited by δ -barriers heavily doped with boron (5×10^{21} cm⁻³) on the surface of n-silicon (100), is shown in Fig. 1(a). It was previously established that edge channels (ECs) are formed in the SNS quantum well during technological processes, and boron atoms in the δ -barriers limiting the ECs form trigonal dipole negative-U centers (Fig. 1(b)). This circumstance significantly suppresses electron–electron interaction in such an EC, thus resulting in a long relaxation time of the carriers [15].

It was shown that the EC of the studied SNS consists of pixels: areas of interference of single carriers, and, taking into account the value of their two-dimensional density (3×10^{13} m⁻²), the pixel length is approximately 16.1 m (Fig. 1(c)), and the resistance of a single carrier per pixel is quantized and amounts to " h/e^2 ". In this case, each pixel consists of layers containing boron dipoles with an area $S_{\text{pixel}} = 16.1 \, \mu\text{m} \times 2 \, \text{nm}$, through which the carrier tunnels, since the QW is limited by these two layers with a width and height of approximately 2 nm [17]. In addition, the spin polarization of single carriers was experimentally discovered in the ECs of the SNS under study, and it was concluded that the ECs are coupled and the carriers in them have opposite spin orientations (Fig. 1(d)) [18].

Silicon nanomagnetism 3

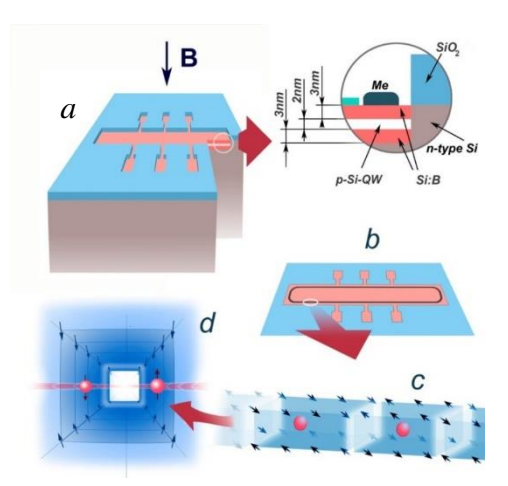


Fig. 1. Experimental SNS built in Hall geometry (a); topological edge channel of SNS (b), in which single charge carriers occupy its individual areas, pixels (c); polarized carriers are transported along opposite walls of the edge channel pixels (d)

It was discovered [17] that when varying the magnitude of the magnetic field B applied perpendicular to the SNS surface, due to Faraday electromagnetic induction, sequential capture of single magnetic flux quanta occurs on single carriers in pixels, and an induction current I_{ind} appears in the EC:

$$I_{ind} = n \frac{\Delta E}{\Delta \Phi}, \tag{1}$$

where ΔE is the change in energy when varying the magnitude of the magnetic flux in the quantum interference region; $\Delta \Phi = \Delta BS$; ΔB is the change in the external magnetic field inside the quantum interference region of area S; n is the number of pixels. Previously conducted studies of the de Haasvan Alphen and quantum Hall effects [15] showed that with the above two-dimensional carrier concentration and pixel size, the capture of a magnetic flux quantum by a single pixel occurs at a value of $\Delta B = 120$ mT. Wherein $\Delta \Phi = \Delta BS = \Phi_0 = h/e$. An important factor for further research is that the EC in the SNS is a contour with a length of 4.7 mm and a width of 0.2 mm (Fig. 1(b)).

If the SNS is not connected to any external power source, then, accordingly, no current can flow in its EC other than I_{ind} induced in the EC pixels by an external magnetic field directed perpendicular to the SNS surface. Moreover, in the case of a high relaxation time in the EC, such an induced current turns out to be persistent [19].

Considering the above, it becomes clear that nanomagnetism can be realized in ECs of SNS structures. Therefore, the purpose of this work was to conduct experiments demonstrating this possibility, namely, to study the induced magnetic field arising in the ECs of a SNS under the influence of an external magnetic field.

The experiments were carried out according to the following procedure. First, the experimental sample at room temperature was placed for 300 seconds in the gap of an electromagnet, which, when turned on, created a homogeneous magnetic field directed perpendicular to the surface of the sample. After this, the sample was removed from the electromagnet gap and placed in a laboratory setup to measure the magnetic moment, at room temperature as well. Then this cycle was repeated multiple times at other values of the external magnetic field.

The laboratory shielded installation used in the experiments is made in the form of a five-layer cylindrical magnetic shield. Moreover, all the internal cylinders are made of M-79 grade permalloy, and the outer cylinder (50 cm in diameter and 70 cm in length) is made of ARMCO steel. The cylinders have lids made of the same material. The innermost cylinder houses a Helmholtz coil powered by a constant (regulated) current supply, which is used both to create an internal uniform magnetic field and to compensate for the residual magnetic field caused by

the penetration (inside the screen) of the external laboratory field and the residual magnetization of permalloys shells. The resulting shielding coefficients (in the frequency range 0–1 Hz) had values of 700 for the longitudinal (along the screen axis) and 5000 for the transverse (perpendicular to the screen axis) components of the magnetic field. During the experiments, the magnitude of variations in the magnetic field induction inside the installation was monitored using a cesium vapor quantum magnetometer and practically did not exceed \pm 0.1 nT.

To measure magnetization (magnetic moment), we used a single-component fluxgate magnetometer with a resolution of ~0.5 nT in the frequency band 0–1 Hz. Measurements of the magnetization arising in the sample were carried out as follows. The fluxgate magnetometer placed in the center of the Helmholtz coil was continuously measuring the longitudinal component of the magnetic field of a given value of +30 nT. Then, we moved the (pre-magnetized) sample close to it and measured the shift in the magnitude of the longitudinal component of the magnetic field. The results obtained were used to determine the dependence of the shift in the magnitude of the magnetic field at the location of the fluxgate on the magnitude of the magnetic field of the electromagnet pre-magnetizing the sample.

Results and Discussion

Figure 2 shows the experimental dependence of magnetization M arising in the contour formed by the SNS ECs on the external magnetic field of the magnetization performed.

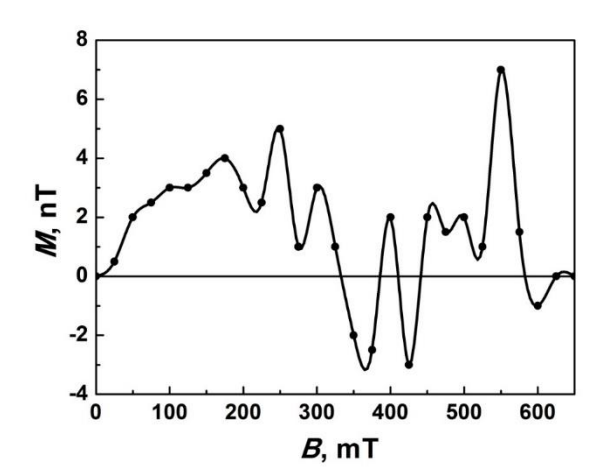


Fig. 2. Dependence of the magnetization arising in the contour formed by the SNS ECs on the external magnetic field of the magnetization performed

It was experimentally discovered that the obtained values of M are maintained for a long time (at least a day), since the current induced by an external magnetic field in the EC contour does not decay in time, due to the fact that transport in the ECs is ballistic in nature. Local maxima in the dependence M = f(B) correspond to those values of the magnetizing field at which a magnetic flux quantum per pixel is captured (120 mT), i.e. when:

$$\Delta \Phi = \Delta BS = \Phi_0 = h/e \tag{2}$$

However, the experimentally obtained $B_{\rm ind}$ values slightly exceed the expected result. Since the magnitude of the energy change when capturing a magnetic flux quantum per pixel $\Delta E = 2\mu_B \Delta B$ (where μ_B is the Bohr magneton), then, taking into account the number of pixels in the EC contour (in the geometry of the experimental sample, the EC length is 9.8 mm; with the above two-dimensional density of single carriers in the EC, the pixel length is 16.1 μ m; number of pixels is 609) and Eq. (2), the expected value of the induced current according to Eq. (1) turns out to be $I_{\rm ind} \sim 10^{-10}$ A, which (with the area of the EC contour $\Delta S = 10^{-6}$ m²) is too small to correspond to the obtained experimental results.

Silicon nanomagnetism 5

This discrepancy between the experimental results and the expected results is explained by the peculiarity of the ECs in the SNS, which is formed between the chains of negative-U boron dipoles. Quantum transport in an EC is carried out along its boundaries by decoupling/coupling of dipoles [20–22]. This means that in the absence of external energy sources and at B=0, there are no free carriers in the EC pixels, since they are localized on negative-U dipoles. In this case, since, as was shown in [18], the spin–orbit interaction plays the main role in quantum transport in ECs in SNSs, energy E=44 meV is required for carrier release. With this value of $E=410^{-15}$ Wb, E=400, an induced current E=401. In accordance with Faraday's law of electromagnetic induction, such a current in the EC limiting the SNS creates a magnetic moment E=401, the values of which correspond to the observed value of the measured magnetization E=401.

$$M = I_{ind}S, (3)$$

where $S \approx 10^{-6} \text{ m}^2$ – the area of the EC contour in the model of the frame with the current formed by the SNS limited by the ECs. In this case, the induced current flows through the ECs.

Thus, the obtained experimental values of M are in good agreement with preliminary estimates that take into account the energy of negative-U dipoles, and, thereby, confirm the decisive role of the spin-orbit interaction in quantum transport in ECs in the SNS. In this case, carriers with both spin up and spin down are induced in the ECs, which make a total contribution to the induced current in the EC contour.

When the external magnetizing field increases to a value corresponding to the capture of a magnetic flux quantum (B = 120 mT), an increase in the value of M is observed (Fig. 2). The external magnetic field the SNS is placed in of such a magnitude generates a stable induced magnetic field that does not decay for a long time (at least a day). Therefore, the subsequent introduction of a SNS into an external magnetic field of greater magnitude leads to the appearance of an induced current, which, in turn, induces a magnetic field of the opposite direction in it. This effect, similar to the Meissner effect, manifests itself in the oscillating nature of the dependence M = f(B) with a further increase in the external magnetizing field.

It should be noted that a significant increase in the oscillation amplitude (Fig. 2) with an increase in the external magnetic field may be associated with the possible capture of several magnetic flux quanta at once by a single pixel [15].

Conclusions

The obtained experimental results for the first time indicate the presence of nanomagnetism in the contour of the edge channels of nanosandwich structures based on the classical semiconductor, silicon, which were created by means of planar technology methods widely used to create processors and various integrated circuits. The demonstrated effect of changing $\partial E/\partial \Phi$ value is similar to changing entropy $\partial E/\partial T$, since the presence of negative-U centers is a regulator of entropy [20,23,24].

References

- 1. Kasatkin SI, Murav'ev AM, Amelichev VV, Kostyuk DV. Spin-logic nanoelements. *Bulletin of the Russian Academy of Sciences: Physics*. 2017;81(8): 1023–1026.
- 2. Arava H, Derlet PM, Vijayakumar J, Cui J, Bingham NS, Kleibert A, Heyderman LJ. Computational logic with square rings of nanomagnets. *Nanotechnology*. 2018;29(26): 265205.
- 3. Zhao Y, Jiang K, Li C, Liu Y, Zhu G, Pizzochero M, Kaxiras E, Guan D, Li Y, Zheng H, Liu C, Jia J, Qin M, Zhuang X, Wang S. Quantum nanomagnets in on-surface metal-free porphyrin chains. *Nat. Chem.* 2023;15: 53–60.
- 4. Blachowicz T, Ehrmann A. New Materials and Effects in Molecular Nanomagnets. *Appl. Sci.* 2021;11(16): 7510.

- 5. Rana B, Mondal AK, Bandyopadhyay S, Barman A. Applications of nanomagnets as dynamical systems: I. *Nanotechnology*. 2022;33(6): 062007.
- 6. Rana B, Mondal AK, Bandyopadhyay S, Barman A. Applications of nanomagnets as dynamical systems: II. *Nanotechnology*. 2022;33(8): 082002.
- 7. Becherer M, Breitkreutz-v. Gamm S, Eichwald I, Ziemys G, Kiermaier J, Csaba G, Schmitt-Landsiedel D. A monolithic 3D integrated nanomagnetic co-processing unit. *Solid-State Electronics*. 2016;115(B): 74–80.
- 8. Bader SD, Parkin SSP. Spintronics. Ann. Rev. Condens. Matter. Phys. 2010;1: 71–88.
- 9. Csaba G, Imre A, Bernstein GH, Porod W, Metlushko V. Nanocomputing by field-coupled nanomagnets. *IEEE Transactions on Nanotechnology*. 2002;1(4): 209–213.
- 10. Luo Z, Dao TP, Hrabec A, Vijayakumar J, Kleibert A, Baumgartner M, Kirk E, Cui J, Savchenko T, Krishnaswamy G, Heyderman LJ, Gambardella P. Chirally coupled nanomagnets. *Science*. 2019;363(6434): 1435–1439.
- 11. Moreno LE, Baldoví JJ, Gaita-Ariño A, Coronado E. Spin states, vibrations and spin relaxation in molecular nanomagnets and spin qubits: a critical perspective. *Chem. Sci.* 2018;9(13): 3265–3275.
- 12. Chiesa A, Macaluso E, Petiziol F, Wimberger S, Santini P, Carretta S. Molecular Nanomagnets as Qubits with Embedded Quantum-Error Correction. *J. Phys. Chem. Lett.* 2020;11(20): 8610–8615.
- 13. Hong J, Dong K, Bokor J, You L. Self-assembled single-digit nanometer memory cells. *Applied Physics Letters*. 2018;113(6): 062404.
- 14. Bagraev NT, Galkin NG, Gehlhoff W, Klyachkin LE, Malyarenko AM. Phase and amplitude response of the '0.7 feature' caused by holes in silicon one-dimensional wires and rings. *J. Phys.: Condens. Matter.* 2008;20(16): 164202.
- 15. Bagraev NT, Grigoryev VY, Klyachkin LE, Malyarenko AM, Mashkov VA, Rul NI. High-temperature quantum kinetic effect in silicon nanosandwiches. *Low Temperature Physics*. 2017;43(1): 110–119.
- 16. Klyachkin LE, Bagraev NT, Malyarenko AM. Spin transistor effect in edge channels of silicon nanosandwiches. *Materials Physics and Mechanics*. 2023;51(4): 85-95.
- 17. Klyachkin LE, Bagraev NT, Malyarenko AM. Macroscopic quantum effects of electromagnetic induction in silicon nanostructures. *Mater. Phys. Mech.* 2022;50(2): 252–265.
- 18. Bagraev NT, Danilovskii EY, Klyachkin LE, Malyarenko AM, Mashkov VA. Spin Interference of Holes in Silicon Nanosandwiches. *Semiconductors*. 2012;46(1): 75–86.
- 19. Imri Y. Introduction to Mesoscopic Physics. 2002.
- 20. Bagraev NT, Gusarov AI, Mashkov VA. Spin-correlated transfer of electrons through dangling bonds in semiconductors. *Sov. Phys. JETP*. 1989;68(4): 816–825.
- 21. Šimánek E. Superconductivity at disordered interfaces. *Solid State Commun.* 1979;32(9): 731–734.
- 22. Ting CS, Talwar DN, Ngai KL. Possible mechanism of superconductivity in metal-semiconductor eutectic alloys. *Phys. Rev. Lett.* 1980;45(14): 1213–1217.
- 23. Landauer R. Spatial Variation of Currents and Fields Due to Localized Scatterers in Metallic Conduction. *IBM Journal of Research and Development*. 1957;1(3): 223–231.
- 24. Landauer R. Electrical resistance of disordered one-dimensional lattices. *The Philosophical Magazine: A Journal of Theoretical Experimental and Applied Physics*. 1970;21(172): 863–867.

THE AUTHORS

Bagraev N.T.

e-mail: bagraev@mail.ioffe.ru

Dovator N.A.

e-mail: Nicolai.Dovator@mail.ioffe.ru

Klyachkin L.E. 🗓

e-mail: leonid.klyachkin@gmail.com

Destruction threshold of ZrO₂ under microsecond magnetic-pulse action

Submitted: March 30, 2023

Accepted: November 22, 2023

Approved: April 18, 2023

S.I. Krivosheev, G.A. Shneerson ⁽¹⁾, S.G. Magazinov ⁽²⁾, D.V. Zhukov, K.V. Voloshin ⁽¹⁾

Peter the Great St. Petersburg Polytechnic University, St. Petersburg, Russia ⊠ magazinov_sg@mail.ru

Abstract. The paper describes the magnetic pulse method for the formation of controlled pressure pulses in a microsecond range of duration for testing the dynamic mechanical strength of brittle materials. The scheme of the experimental setup includes a pulse current generator (PCG), the magnetic pulse loading system, the pulse current measuring system and the sample. The main parameters of the developed experimental setup are given - charging voltage, capacitance, inductance, active resistance of the PCG. Zirconium dioxide samples were tested according to this method. Numerical simulation of pulsed magnetic and dynamic mechanical fields during testing of materials is performed. Experimental pulses of the generated pressure are calculated. Based on the results of experiments and numerical modeling, the dynamic mechanical strength of zirconium dioxide under loading mode I was determined based on the described method.

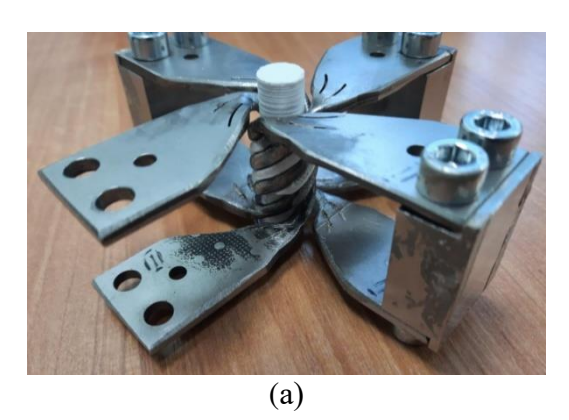
Keywords: pulsed magnetic fields; magnetic pulse loading; high strain rate deformation; testing of materials

Acknowledgements. This work was supported by the Russian Science Foundation (grant no. 18-19-00230). The results of the work were obtained using the computing resources of the supercomputer center of Peter the Great St. Petersburg Polytechnic University.

Citation: Krivosheev SI, Shneerson GA, Magazinov SG, Zhukov DV, Voloshin KV. Destruction threshold of ZrO₂ under microsecond magnetic-pulse action. *Materials Physics and Mechanics*. 2023;51(7): 7-14. DOI: 10.18149/MPM.5172023_2.

Introduction

Large current and power loads, typical for the operation of high-powered electrophysical installations, require consideration of the strength properties of all elements that make up the equipment and operate under conditions of combined effects. So, when generating strong pulsed magnetic fields, current-carrying elements (coils of the solenoid) experience the action of Lorentz forces and Joule heating, and the insulation that separates them experiences mechanical and thermal loads and the effect of applied impulse voltage. The stress state in these systems is quite complex, and the performance of the solenoid is determined by limiting current loads, which determine the choice of material of the coils, and by the properties of the insulation, which ensures the electrical strength of the structure. In this case, the insulation can perform the function of containing deformations of current-carrying elements. Examples are the designs of solenoids with quasi-forceless windings described in [1,2], the mechanical stresses in which are significantly reduced with an increase in the elastic modulus of the material filling the inter-turn gaps. Therefore, it is of interest to study the strength characteristics of media having a high modulus of elasticity (ceramic dielectrics) under loading conditions close to those realized in magnets with a pulsed field. An example would be a magnet with inertial confinement of the screen, which balances its front-end part, described in [3]. The magnet (Fig. 1) is designed to obtain a magnetic field in a small volume in the form of a pulse with a duration of $10~\mu s$ and an induction amplitude of up to 50~T. Numerical simulation showed that in the insulation between the winding coils, the mechanical stress calculated by the von Mises criterion, can reach 1~GPa.



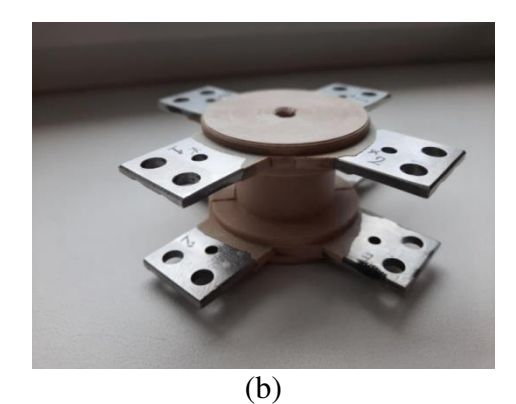


Fig. 1. Solenoid with quasi-forceless windings: (a) coils; (b) insulation of coils

This article describes an installation designed to generate controlled pressure pulses and an experimental-calculation method for determining the threshold breaking load of a dielectric in the microsecond range of exposure durations.

Testing of the installation was carried out during testing of zirconium dioxide. In the experiments described, the pressure wave front propagation time to the edge of the sample is commensurate with the pulse duration; therefore, a necessary part of the work was the use of computer simulation to calculate the mechanical stress, taking into account the process of formation and propagation of the pressure wave.

It is known that the mechanical properties of materials, such as the elastic limit, hardening factor [4–10] and tensile strength depend on the deformation rate of materials. There are various methods for testing the dynamic properties of materials [11-14], but the loading schemes used in these methods are very conservative and cannot be used in sample configurations that are not traditional for these methods. A magnetic-pulse method [15–22] for the formation of shock loads is used in this work. The material under study in this work (zirconium dioxide) does not have pronounced plastic properties and its deformation characteristic can be represented as a linear dependence of mechanical stresses on relative deformations, therefore, the main interest in determining the mechanical properties of zirconium dioxide is its dynamic strength limit, in the time range, close to operating conditions of the solenoid.

Methods

Formation of controlled pressure pulses. To study the dynamic tensile strength, this work uses a magnetic-pulse technique for generating controlled pressure pulses [19–21], adapted to testing materials with a high tensile strength, a simplified diagram of which is shown in Fig. 2.

In the above test scheme, there are three blocks: a pulsed currents generator (PCG) I, a Rogowski coil II, a magnetic-mechanical loading system III, and a test sample 2.

The geometric dimensions of the tested zirconium dioxide specimens are: length 23 mm, width 23 mm, thickness 8 mm, groove length 15 mm, groove height 3 mm, groove top rounding radius 1.5 mm. Sample elasticity modulus E = 210 GPa, density $\rho = 6200$ kg/m³.

The pulsed currents generator (PCG) I consists of impulse capacitors with a total capacity of TPCG = 30 μ F, a charging voltage of up to 25 kV, a low-inductance busbar L_{PCG} = 75 nH and a controlled spark gap S_{PCG} , made of two parallel thyratrons of the TDI4-250k / 20PE type with a control unit PB-3DV/2E.

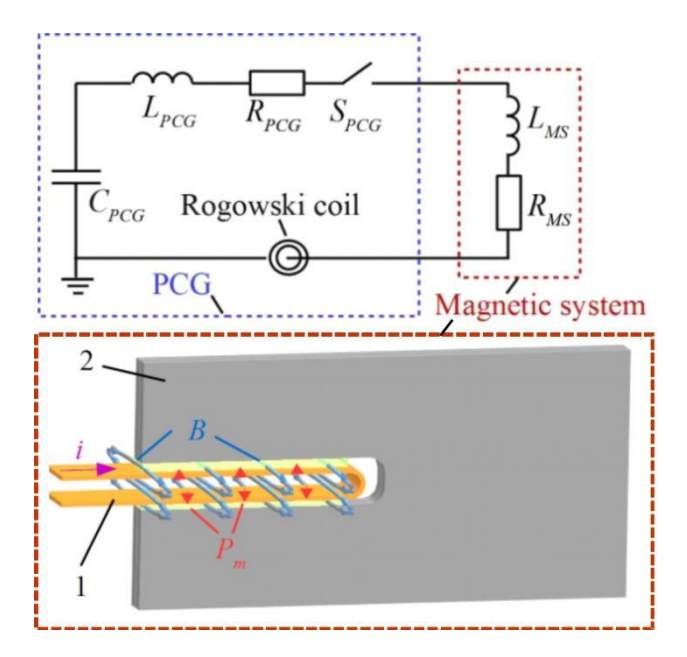


Fig. 2. Scheme of magnetic-pulse testing of the dynamic tensile strength of materials: 1 - copper flat busbars, 2 - test sample

The Rogowski coil II is connected through an integrating RC-circuit with an integration constant much longer than the measured signal to the input of oscilloscope to record the PCG discharge current.

Loading system III is made of flat closely spaced copper bifilar busbars, 0.3 mm thickness, 10 mm width. There is a groove in the sample with flat copper busbars placed.

After the PCG capacitors are charged to a predetermined voltage level, using a controlled spark gap, the PCG is discharged onto copper bars, where pulsed magnetic field is formed. The magnetic field interacts with the flat busbar current and generates a pulsed magnetic pressure, which is transferred to the edges of the sample's groove. Under the influence of this pressure, the sample's groove opens, which leads to the formation of a region of maximum mechanical stresses at the top of the groove.

By adjusting the charging voltage of capacitors and/or the width of the copper busbars of the magnetic-mechanical loading device, it is possible to vary the amplitude of magnetic pressure acting on the sample. The charging voltage and busbars width corresponding to the sample destruction threshold are experimentally determined. The charging voltage corresponding to the threshold voltage is the voltage, below which the destruction of sample is not observed, and with an increase in voltage, the destruction of sample occurs. During the discharge, pulsed current is measured. With the help of numerical simulation, the mechanical stress at the top of the sample is determined, which corresponds to dynamic tensile strength for a given form of loading.

A typical experimental oscillogram of the current of test setup in the short circuit mode is shown in Fig. 3.

The current pulse is approximated by the following expression: $i(t) = I_m \cdot \sin(2\pi/T \cdot t) \cdot \exp(-t/\tau), \tag{1}$ where $I_m = I_m / c_m$ maximum current value without attenuation, $c_m = \sqrt{I/C} = 50$ MO is the

where $I_m = U_0/\rho$ - maximum current value without attenuation, $\rho = \sqrt{L/C} = 50 \text{ M}\Omega$ is the wave resistance, $T = 2\pi\sqrt{LC} = 9.5 \text{ ms}$ is the period of oscillation, $\tau = 21 \text{ ms}$ is the attenuation constant.

The charging voltage of the test set can be changed in the range $U_0 = 5...25$ kV which corresponds to $I_m = 100...500$ kA.

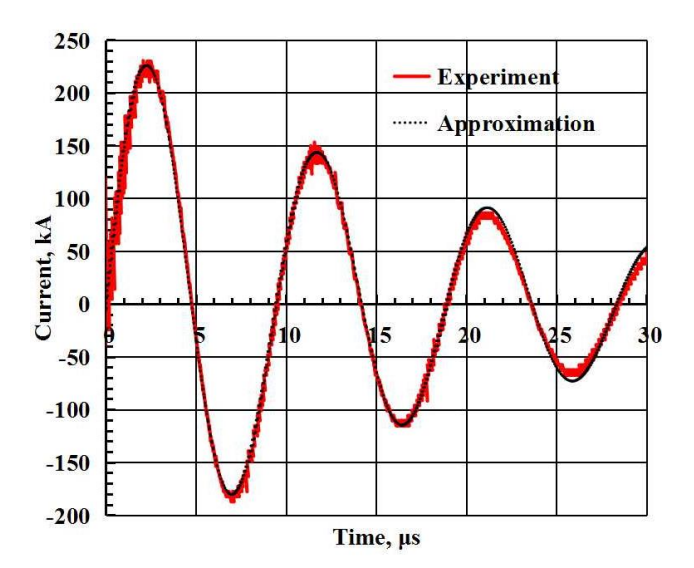


Fig. 3. Typical oscillogram of the experimental current

Flowing through the flat bifilar busbars, the pulsed current forms a pulsed magnetic field between them, which creates pressure on the busbars, determined by the expression:

$$P_m(t) = k_m \cdot \mu/2 \cdot (i(t)/c)^2, \tag{2}$$

where c is the width of the flat busbars, k_m is a rate that is equal to 1 with a uniform distribution of current density in the busbars, which occurs if the width of the busbars is much larger than the gap between them. Under experimental conditions, the values of this coefficient lie in the range $k_m = 0.4...0.8$ and are determined by the results of numerical simulation of the magnetic field for given dimensions of flat busbars and pulsed current parameters.

Computer modelling. To determine the magnetic pressure coefficient k_m under experimental conditions, a numerical simulation of a pulsed magnetic field in the Comsol Multiphysics environment was performed with respect to the vector magnetic potential A, defined by the expression:

$$\Delta \overline{A} - \sigma \mu \frac{\partial \overline{A}}{\partial t} = \mu \overline{J},\tag{3}$$

where σ , μ are the electrical conductivity and magnetic permeability respectively.

According to the known distribution of the vector magnetic potential, it is possible to determine all the parameters of the magnetic field, such as the magnetic field induction $\overline{B} = \overline{V} \times \overline{A}$, magnetic field strength $\overline{H} = \overline{B}/\mu$, current density $\overline{J} = \overline{V} \times \overline{H}$. The vector product of the magnetic field induction and the current density gives the vector of the volumetric Lorentz force $\overline{f}_L = \overline{J} \times \overline{B}$ acting on the copper bars. By integrating the vertical component of this force over the cross section of the conductor, the magnetic pressure of the magnetic-mechanical loading system is determined, which is transmitted to the edges of the sample's groove [23].

To determine the mechanical stresses at the top of the sample groove (the zone of maximum mechanical stresses), a numerical simulation of the dynamic mechanical field in the Comsol Multiphysics environment was performed based on Newton's second law in differential form with a linear deformation dependence determined by Hooke's law:

$$m\frac{\partial^2 \overline{u}}{\partial t^2} = \overline{f}_L - \nabla \cdot \ddot{\sigma},\tag{4}$$

$$\sigma = E \cdot \varepsilon, \tag{5}$$

where u is the vector of displacements, σ is the mechanical stress tensor, m is mass, ε is strain tensor, E is elastic moduli tensor.

Results

A series of experiments was carried out on samples of zirconium dioxide, the tire width in all experiments was kept constant and equal to 10 mm. The charging voltage of the test setup was empirically determined, corresponding to the sample destruction threshold $U_S = 6 \text{ kV}$.

When the charging voltage decreased below U_S , the destruction of the samples was not observed, and the excess of the charging voltage above the U_S value led to the destruction of the samples (see Fig. 4).

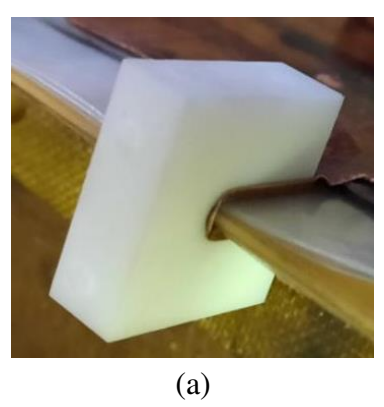




Fig. 4. Samples after testing: (a) the charging voltage is less than the threshold; (b) the charging voltage is above the threshold

Based on the numerical simulation of the magnetic field, the magnetic pressure coefficient $k_m = 0.55$ was determined and the time dependences of the magnetic pressure acting on the sides of the samples' grooves were found. They are shown in Fig. 5(a).

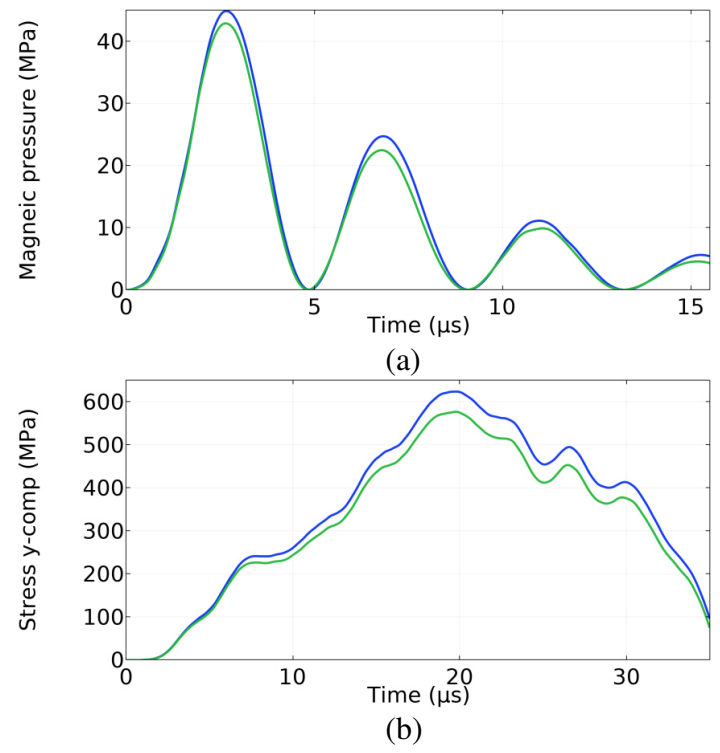


Fig. 5. Graphs of the dependences of the magnetic pressure (a) applied to the edges of the sample's groove and the calculated value of the y-component (tensile) of the mechanical stress (b) at the top of the sample's groove on time, close to the fracture threshold: blue curve - corresponds to the experiment with the destruction of the sample; green curve - without destruction of the sample

On the basis of numerical simulation of dynamic mechanical deformation of samples under the influence of pulsed pressure corresponding to the experimental conditions, the time dependence of tensile mechanical stress at the top of the groove, where it takes on a maximum value, was constructed (Fig. 5(b)).

The given data in Fig. 5(b) show that the amplitude of the threshold value of the y-component of mechanical stress of the tested samples is between the green curve corresponding to the experiment without sample destruction and the blue curve corresponding to the experiment with sample destruction. Thus, it can be argued that the threshold value under conditions of described experiments (for a pulse duration of $36 \mu s$) is $600 \pm 50 MPa$.

3D modeling of the process has been completed. A spatial distribution of the y-component of stress tensor is shown Fig. 6(a) for one fourth of the sample. For the point at the top of the sample's groove in Fig. 6(b) shows the time dependences of x, y, z - the components of the stress tensor and the von Mises equivalent stress.

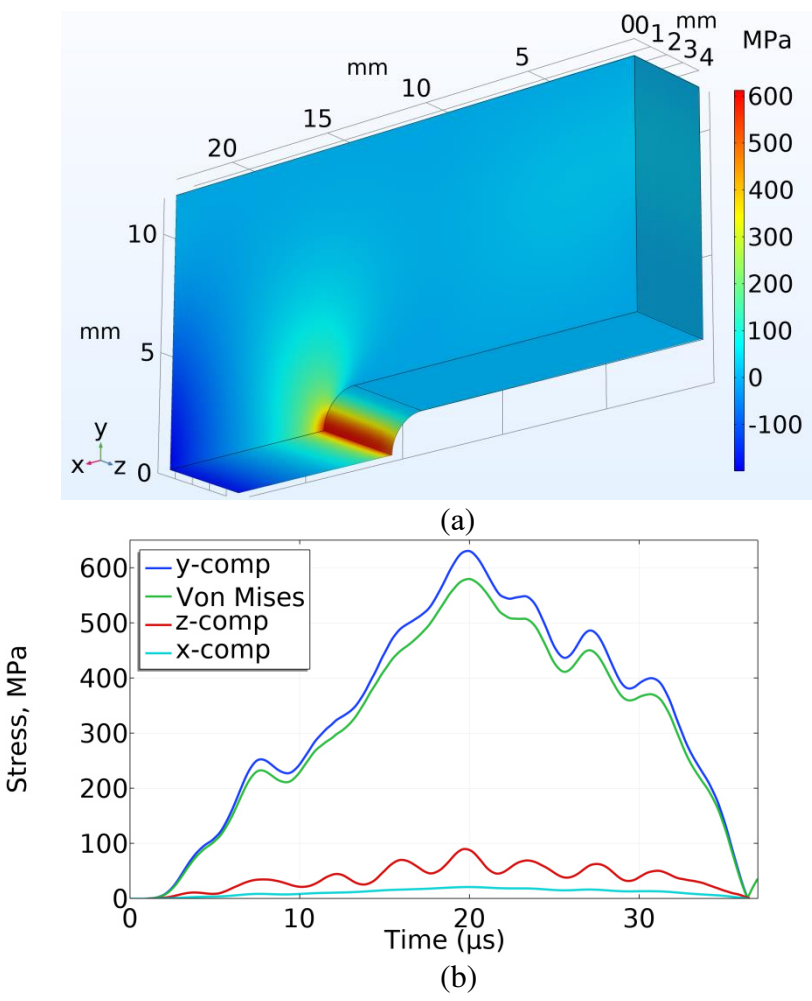


Fig. 6. Results of numerical simulation of dynamic deformation of samples under loading close to the fracture threshold: (a) distribution of the y-component of mechanical stresses (one fourth of the symmetry sample) at the time of maximum $t = 20 \, \mu s$; (b) time dependences x, y, z - components of the stress tensor and the equivalent stress at the top of the sample's groove

According to the results presented in Fig. 6, it can be seen that the mechanical wave length $\lambda = T \cdot (E/\rho)^{1/2} = 55$ mm is comparable to the characteristic dimensions of the samples $(23 \times 23 \times 8 \text{ mm})$. The shape of the mechanical stress curves at the top of the groove does not repeat the shape of the applied magnetic pressure due to the dynamic nature of loading the edges of the groove with a uniformly distributed magnetic pressure. In this mode, at the top of the

slot, there is a superposition of stress waves formed under the influence of magnetic pressure on the entire slot boundary. The observed behavior of the dependences of stresses at the top of the groove observed in the calculations is related to the finite rate of stress propagation caused by the action on the sides of the groove, and corresponds to the description of similar processes under dynamic and shock-wave loading [24,25]. An analysis of the simulation results demonstrates the absence of a shock-wave nature of loading; therefore, we can assume that in our case, the loading mode of the samples is intermediate between wave and quasistatic.

From Fig. 6(b) it can be seen that the tensile y-component of the mechanical stress tensor dominates at the top of the sample's groove, the x and z components make up 3 and 14 % of the y-component, respectively. The von Mises stress at the top of the groove is 92 % of the y-component of the tensor.

Conclusion

Based on the testing of samples of zirconium dioxide, the possibility of testing the dynamic mechanical strength of materials in mode I by the magnetic pulse method was shown.

The dynamic tensile strength according to von Mises of the tested samples of zirconium dioxide when loaded by the magnetic-pulse method in mode I was 550 ± 50 MPa with a mechanical stress duration of $36~\mu s$.

References

- 1. Nemov AS, Lagutkina AD, Shneerson GA. A Conceptual 3-D Design of a Non-Destructive Two-Layer Quasi-Force-Free Magnet for Megagauss Field Generation. *IEEE Transactions on Magnetics*. 2022;3(58): 8000609.
- 2. Shneerson GA, Nemov AS, Lagutkina AD. Designing quasi-force-free configurations of non-destructive megagauss magnets. In: *Proc. 8th Euro-Asian Pulsed Power Conference (EAPPC 2020)*. 2020. p.1–26
- 3. Shneerson GA, Parfentyev AA, Titkov VV, Krivosheyev SI, Lagutkina AD, Nemov AS, Nenashev AP. Shimansky SA. Conceptual Model of a Quasi-Force-Free Magnet of Small Volume with Inertial Retention of Its End Part. *Tech. Phys. Lett.* 2021;47: 573–576.
- 4. Johnson GR, Cook WH. A constitutive model and data for metals subjected to large strains, high strain rates and high. In: *Proceedings of the 7th International Symposium on Ballistics Committee*. 1983. p.541–547
- 5. Follansbee PS, Kocks UF. A constitutive description of the deformation of copper based on the use of the mechanical threshold stress as an internal state variable. *Acta Metallurgica*. 1988;1(36): 81–93.
- 6. Zerilli FJ, Armstrong RW. Dislocation-mechanics-based constitutive relations for material dynamics calculations. *Journal of Applied Physics*. 1987;5(61): 1816–1825.
- 7. Preston DL, Tonks DL, Wallace DC. Model of plastic deformation for extreme loading conditions. *Journal of Applied Physics*. 2003;1(93): 211–220.
- 8. Korkmaz ME, Günay M, Verleysen P. Investigation of tensile Johnson-Cook model parameters for Nimonic 80A superalloy. *J. Alloys Compd.* 2019;801: 542–549.
- 9. Grazka M, Janiszewski J. Identification of johnson-cook equation constants using finite element method. *Eng. Trans.* 2012;60: 215–223.
- 10. Liu W, Zhou H, Li J, Meng Z, Xu Z, Huang S. Comparison of Johnson-Cook and Cowper-Symonds models for aluminum alloy sheet by inverse identification based on electromagnetic bulge. *Int. J. Mater. Form.* 2022;15: 10.
- 11. Kolsky H. An investigation of the mechanical properties of materials at very high rates of loading. *Proceedings of the Physical Society. Section B.* 1949;11(62): 676–700.
- 12. Novikov SA. Razrusheniye materialov pri vozdeystvii intensivnykh udarnykh nagruzok. *Sorosovskiy obrazovatelnyy zhurnal*. 1999;8: 116–121. (In-Russian)

- 13. Bragov AM, E. Kadoni LK. Sovremennyye metody dinamicheskikh ispytaniy materialov. *Vestnik Nizhegorodskogo universiteta im. N.I. Lobachevskogo*. 2011;5(4): 2039–2040. (In-Russian) 14. Taylor G. The use of flat-ended projectiles for determining dynamic yield stress. *Proceedings of the Royal Society of London A*. 1948;194: 289–299.
- 15. Nie H, Suo T, Wu B, Li Y, Zhao H. A versatile split Hopkinson pressure bar using electromagnetic loading. *Int. J. Impact Eng.* 2018;116: 94–104.
- 16. Avriel E, Lovinger Z, Nemirovsky R, Rittel D. Investigating the strength of materials at very high strain rates using electro-magnetically driven expanding cylinders. *Mech. Mater.* 2018;117: 165–180. 17. Zhang H, Ravi-Chandar K. On the dynamics of necking and fragmentation I. Real-time
- and post-mortem observations in Al 6061-O. *Int. J. Fract.* 2006;142: 183–217.
- 18. Guo Y, Du B, Liu H, Ding Z, Zhao Z, Tang Z, Suo T, Li Y. Electromagnetic Hopkinson bar: A powerful scientific instrument to study mechanical behavior of materials at high strain rates. *Rev. Sci. Instrum.* 2020;91(8): 081501.
- 19. Krivosheev SI. Pulsed magnetic technique of material testing under impulsive loading. *Technical Physics*. 2005;3(50): 334–340.
- 20. Ostropiko E, Magazinov S, Krivosheev S. Uniaxial Magnetic Pulse Tension of TiNi Alloy with Experimental Strain Rate Evaluation. *Experimental Mechanics*. 2022;6(62): 1027–1036.
- 21. Magazinov SG, Krivosheev SI, Adamyan YE, Alekseev DI, Titkov VV, Chernenkaya LV. Adaptation of the magnetic pulse method for conductive materials testing. *Materials Physics and Mechanics*. 2018;40(1): 117–123.
- 22. Chandar KR, Knauss WG. Dynamic crack-tip stresses under stress wave loading -A comparison of theory and experiment. *International Journal of Fracture*. 1982;3(20): 209–222.
- 23. Ostropiko ES, Krivosheev SI, Magazinov SG. Analytical evaluation of magnetic pulse deformation of tini alloy. *Letters on Materials*. 2021;1(11): 55–60.
- 24. Krivosheev SI, Korovkin NV, Slastenko VK, Magazinov SG. Destruction of brittle materials by microsecond pressure pulses at their formation by magnetic pulse method. *International Journal of Mechanics*. 2015;9: 293–299.
- 25. Ma CC, Freund LB. The extent of the stress intensity factor field during crack growth under dynamic loading conditions. *Journal of Applied Mechanics, Transactions ASME*. 1986;2(53): 303–310.

THE AUTHORS

Krivosheev S.I.

e-mail: ksi.mgd@gmail.com

Magazinov S.G.

e-mail: magazinov_sg@mail.ru

Voloshin K.V. 🗓

e-mail: kir_vol@mail.ru

Shneerson G.A.

e-mail: gashneerson@mail.ru

Zhukov D.V.

e-mail: s_zhukov51@bk.ru

Synthesis and characterization of iron-doped TiO₂ nanotubes for dye-sensitized solar cells

Submitted: January 11, 2023

Accepted: November 24, 2023

Approved: March20, 2023

B. Samran (1) 1, E.N. Timah (1) 2, P. Thongpanit (1) 1, S. Chaiwichian (1) 3 \(\sime \)

¹ Nakhon Phanom University, Nakhon Phanom, Thailand ² Trinity International School, Bangkok, Thailand

Abstract. Titanium dioxide nanotubes as materials for energy conversion were successfully synthesized, characterized and tested for dye-sensitized solar cells (DSSC). The TiO₂ nanotubes were grown by one face anodization at room temperature on titanium sheets of 0.25 mm thickness and 99.7 % purity. The electrolyte was composed of ethylene glycol, ammonium fluoride (0.3 wt. % NH₄F), deionized water (2 vol. % deionized water) and Fe(NO₃)₃ as dopant source with varying concentrations of 2, 4, 6 and 10 mM. The X-ray diffraction (XRD), scanning electron microscopy (SEM), atomic force microscopy (AFM) and ultraviolet–visible spectrometry (UV-vis) techniques were used to characterize the TiO₂nanotubes. Finally, the samples were tested in dye-sensitized solar cells and their conversion efficiencies were calculated. According to the results, amorphous TiO₂ was transformed into the crystalline anatase phase after heat treatment. Under the given experimental conditions, our optimal results were obtained for the titanium dioxide nanotubes (TNTs) at 6 mM of iron (III) nitrate. The maximum DSSC conversion efficiency was 4.66 % for the TNTs of 6 mM Fe(NO₃)₃. The findings of this research provide significant guidelines for current and future research in the development of renewable energy.

Keywords: renewable energy; dye-sensitized solar cells; TiO₂ nanotubes; iron (III) nitrate

Acknowledgements. The authors would like to greatly thank the Thailand Science Research and Innovation, Fundamental Fund: FF 2022, the Division of Physics, Faculty of Science, Nakhon Phanom University, Muang District, Nakhon Phanom and Faculty of Industry and Technology, Rajamangala University of Technology Isan for support.

Citation: Samran B, Timah EN, Thongpanit P, Chaiwichian S. Synthesis and characterization of iron-doped TiO₂ nanotubes for dye-sensitized solar cells. *Materials Physics and Mechanics*. 2023;51(7): 15-21. DOI: 10.18149/MPM.5172023 3.

Introduction

The first dye-sensitized solar cells (DSSCs) were fabricated by O'Regan and Gratzel [1]. As a renewable sources of energy, DSSCs have several advantages such as low production cost, simple preparation method and relatively high efficiency [2]. Titanium dioxide (TiO₂) has semiconducting properties, which has attracted its usage in solar cell fabrication. Titanium dioxide has several other beneficial properties such as low toxicity, high photocatalytic activity, resistance to corrosion, excellent dielectric effect, chemical stability, availability and low cost. These amazing properties have made TiO₂ to have a wide range of applications such as in gas sensing, photocatalysis, hydrogen generation, photovoltaic, and water purification [3–5].

The use of titanium dioxide nanotubes (TNT) in solar cells and photocatalysis has grown of recent due to the benefits of slower rates of charge recombination and higher efficiencies [6–9]. To overcome the large energy band gap (3.2 eV) of titanium dioxide (TiO₂), doping with foreign elements has been employed successfully [10]. In 2009, Dholam and Patel reported the use of sputtering and sol-gel techniques to dope TiO₂ nanostructures with iron (Fe) [11]. Amongst many other techniques that have been used for synthesizing TNT for DSSCs, DC Anodization is much suitable because of its low cost and simplicity [12,13]. A number of substances have been used as key components of the electrolyte during anodization. In 2009, Sreekantanet al. [14] reported the use of an electrolyte composed of sodium sulfate, ammonium fluoride, sulfuric acid and sodium hydroxide. Later in 2011, Omidvar et al. [15] also reported the use of sulfuric acid and phosphoric acid in an electrolyte composed of deionized (DI) water and ammonium fluoride. In 2012, H. Li et al. [16] successfully used an electrolyte containing DI water, ethylene glycol and ammonium fluoride (NH₄F). This electrolyte composition will be used in this work.

The purpose of this paper is to synthesis Fe-doped TNTs and determine their efficiencies in DSSCs by varying the amount of dopant. The TNTs will be prepared by DC anodization using ethylene glycol and ammonium fluoride electrolyte. The samples will be characterized by X-Ray diffraction (XRD) and scanning electron microscopy (SEM), atomic force microscopy (AFM) and ultraviolet – visible spectrometry (UV-vis) techniques.

Experimental procedure

TiO₂ nanotubes were grown by DC anodization method at 50 V for 2 hours at room temperature. Titanium sheets of 0.25 mm thickness and 99.7 % purity purchased from Sigma Aldrich were first polished with abrasive papers. After polishing, the Ti foils were degreased ultrasonically in isopropanol, deionized water and ethanol. The electrolyte was composed of ethyleneglycol (EG), ammonium fluoride (0.3 wt. % NH₄F), deionized water (2 vol. % D.I. H₂O) and iron (III) nitrate. The concentration of Fe(NO₃)₃ was varied from 2, 4, 6 to 10 mM. The electrolyte was kept for 5 hours before anodization to ensure homogeneity. The anodization apparatus is a two-electrode configuration with a piece of highly pure platinum counter electrode.

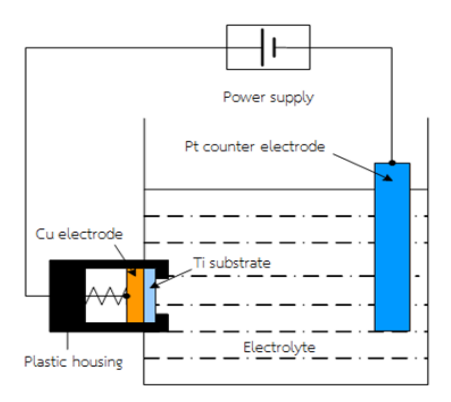


Fig. 1. The schematic diagram of a single-face anodization process

Figure 1 shows the schematic diagram of the anodization process. This set up allows only one face of the Ti foil to be in contact with the electrolyte. Three sets of samples were studied, (a) as anodized without annealing or calcination (b) anodized once and calcinated at 450 °C and (c) re-anodized after calcination at 450 °C. Characterization was done using XRD, SEM, AFM, UV-vis and tested in DSSCs. For the DSSCs, TiO₂ nanotubes photoelectrodes were immersed in 0.5 mM solution of N719 dye in a mixture of acetonitrile/tert-butanol (1:1)

at 25 °C for 24 hours. A transparent conducting oxide (TCO) glass was used as counter electrode. A platinum catalyst was deposited on the TCO glass by coating with drops of platinum solution (H_2PtCl_6). The TCO glass was heated for 30 min at 80 °C. Then, TiO₂ nanotubes photoelectrode and Pt counter electrode were assembled into a sandwich. The TiO₂ nanotubes arrays were finally assembled into DSSCs and their *IV*-characteristics were measured. The photovoltaic properties of the DSSCs were characterized by the four most important parameters, which are the short-circuit current density (J_{sc}), open-circuit voltage (V_{oc}), fill factor (FF) and the conversion efficiency (η). The equations of DSSCs are shown as follows[17]:

$$FF = \frac{V_m I_m}{V_{oc} I_{sc}},\tag{1}$$

$$\eta = \frac{V_m I_m}{P_{in}} = \frac{V_{oc} I_{sc} FF}{P_{in}},\tag{2}$$

where $I_{\rm m}$ and $V_{\rm m}$ are respectively the current density and voltage at the optimal operationpoint that gives the maximum output power, and $P_{\rm in}$ is the power of the incident light.

Results and discussion

Figure 2 shows the XRD patterns of uncalcinated Fe-doped nanotubes. The peaks at (002), (101), (102), (110), (103) and (112) are characteristic crystal faces of Ti metal. It indicates that the TiO₂ remains in the amorphous phase even for different dopant concentrations. In Fig. 3, the XRD patterns of Fe-doped TNTs annealed at 450 °C are displayed. The diffraction peaks emerging at scattering angles $2\theta = 25.3$, 48.7, 53.5 and 55.2° correspond to the anatase phase (A). This shows that the crystalline structure of TiO₂ has been transformed from its original amorphous phase after calcination into the anatase phase. These results are in agreement with the work of J.Y. Lin [18].

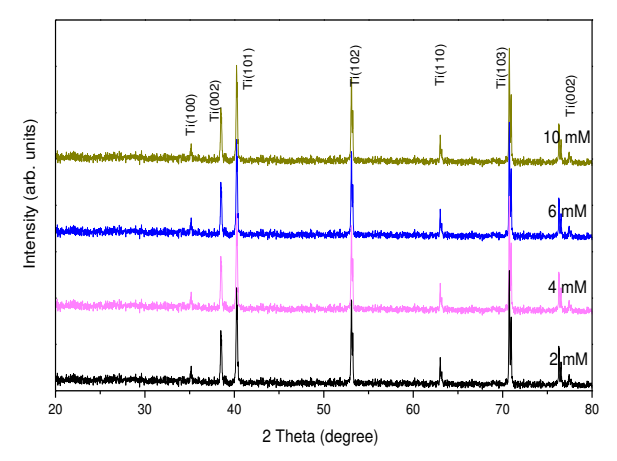


Fig. 2. XRD patterns for Fe-doped TNTs before annealing

Fig. 3. XRD patterns for Fe-doped TNTs after annealing

The SEM images of the different samples after calcination at 450 °C are shown in Fig. 4. It is observed that as the concentration of dopant substance changes, so too is the surface morphology of the samples. There seems to be an increasing disorder in the array of the nanotubes with increasing dopant concentration. At a-Fe(NO₃)₃ concentration of 10 mM, the alignment of the nanotubes are significantly destroyed, as seen in Fig. 4(d). This result is supported by the work of Xiabo Chen et al. [19].

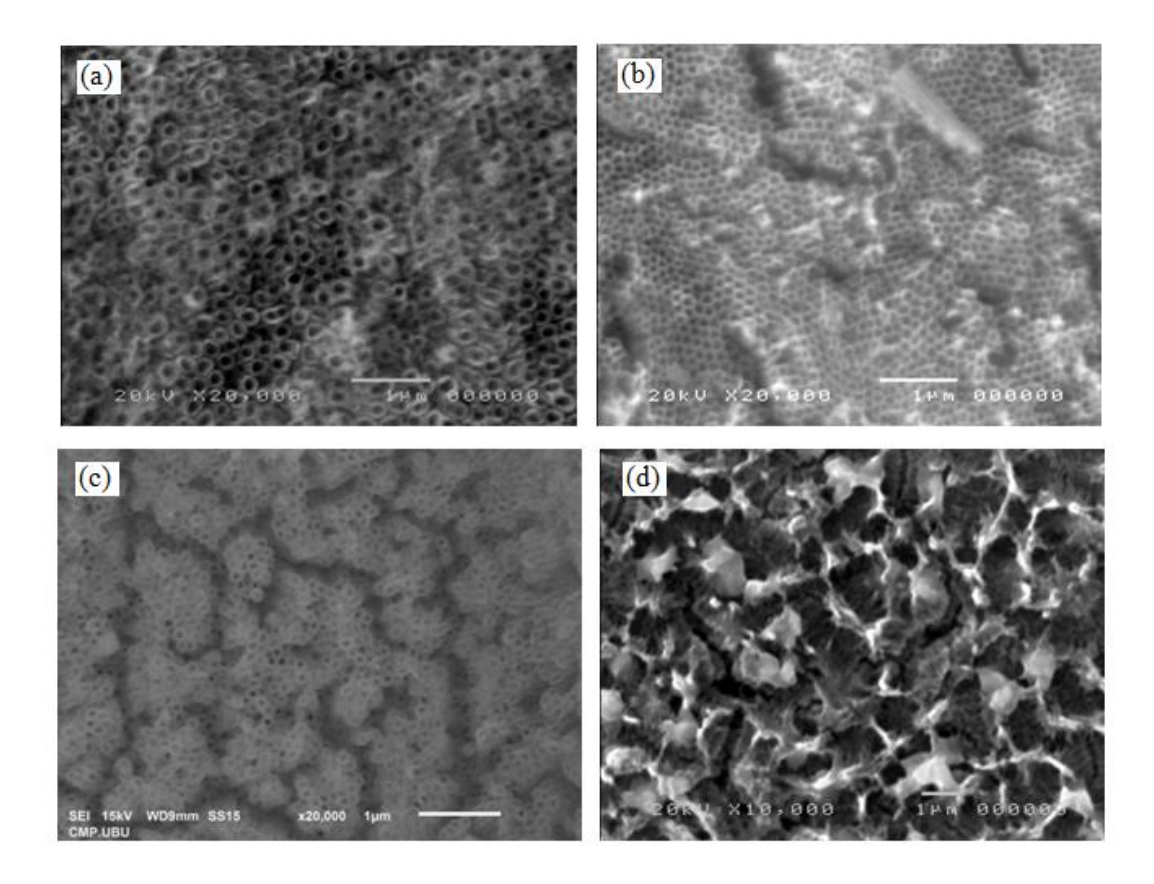


Fig. 4. SEM imagesofFe-doped TNTs with different concentrations of iron (III) nitrate: (a) 2 mM, (b) 4 mM, (c) 6mM and (d) 10 mM

Could re-anodization after annealing improve the photo-response of the nanotubes? We tried to answer this question by re-anodizing the 6 mM sample, and studied it using SEM, AFM and UV-vis techniques. The SEM image in Fig. 5 shows the surface morphology with lots of cracks and a disordered array of nanotubes. This disorder is also confirmed by the AFM images in Fig. 6. Although the nanotubes appear thicker in diameter, their array is highly non-uniform. The energy band gap of the 6 mM re-anodized sample was determined from the UV-vis spectrum, as shown in Fig. 7. The data at a cut-off wavelength of 388 nm yielded an energy band gap value of 3.20 eV. This value is still as high as that of the pour TiO₂ and would therefore result in a lower efficiency. From the results in Figs. 5-7, we can conclude that it is not recommended to re-anodize the samples after calcinations.

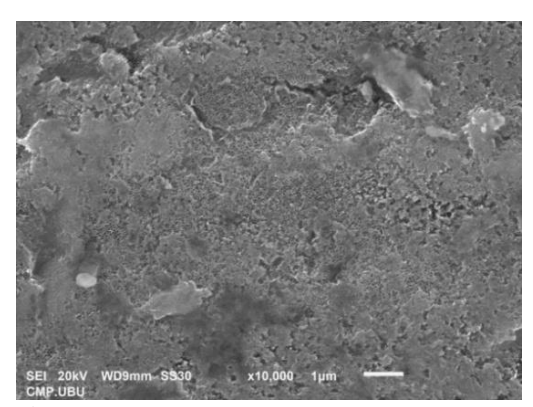


Fig. 5. SEM images of 6 mM sample reanodized after annealing at 450 °C

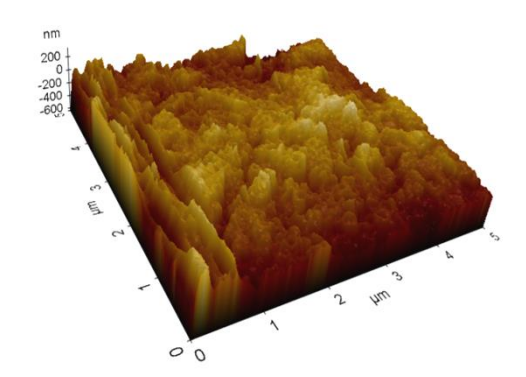


Fig. 6. AFM images of 6 mM sample reanodized after annealing at 450 °C

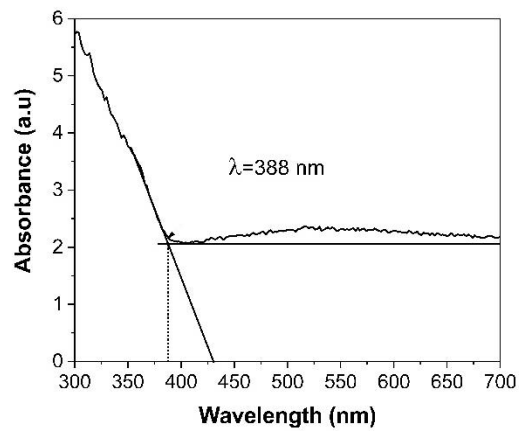


Fig. 7. UV-Visspectrum of 6 mM sample re-anodized after annealing

The IV characteristic in Fig. 8 shows a plot of current density versus voltage, while Table 1 displays the photocatalytic performance of the Fe-doped TNTs in DSSCs. It is observed from both Fig. 8 and Table 1 that as dopant concentration increases, the cell efficiency and photocatalytic performance increases as well. The dopant element, Fe, plays the role of charge traps which hinders charge career recombination. As the concentration of Fe(NO₃)₃ increases, more Fe ions displaces Ti ions in the lattice structure. Intermediate energy bands are created, which leads to a lowering of the energy band gap. This results in a shift in optical absorption from the UV region into the visible light spectrum. This is in line with the work of U. Tipparachet al. [20]. The highest cell efficiency of 4.66 % is obtained for aFe(NO₃)₃ concentration of 6 mM. At a higher concentration of 10 mM, the cell efficiency drops dramatically to 2.22 %. As seen from the SEM images in Fig. 4(d), many cracks develop as dopants concentration increases. The arrangement of the nanotubes becomes more disorderly. These conditions lead to more charge carrier recombination and a consequent decrease in photocatalytic performance and cell efficiency.

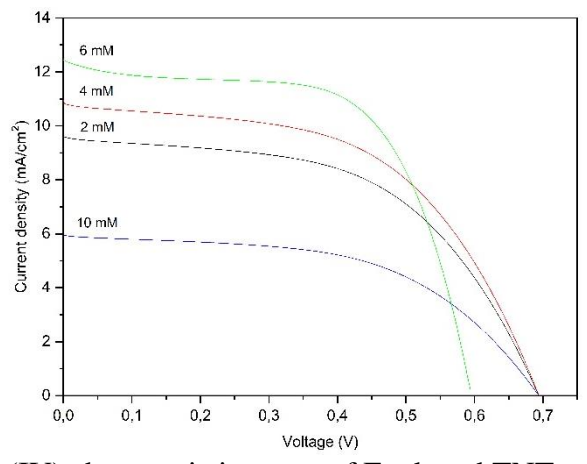


Fig. 8. Current-voltage (IV) characteristic curve of Fe-doped TNTs with varying amounts of Fe(NO₃)₃: (a) 2 mM, (b) 4 mM, (c) 6 mM and (d) 10 mM

Table 1. Photocatalytic Performance of Fe-doped TNTs with different concentrations of Fe(NO₃)₃

				(-/-
Samples	J _{sc} , mA/cm ²	V_{oc}, V	FF	η, %
2 mM	9.61	0.59	0.63	3.58
4 mM	10.96	0.68	0.54	4.04
6 mM	12.44	0.69	0.56	4.66
10 mM	5.95	0.67	0.50	2.22

Conclusions

In this work, Fe-doped titanium dioxide nanotubes were synthesized by DC anodization using a 50 V supply. The composition of the electrolyte was as follows: ethyleneglycol (EG), ammoniumfluoride (0.3 wt. % NH₄F), deionizedwater (2 vol. % deionizedwater), and Fe(NO₃)₃as dopant source with varying concentrations of 2, 4, 6 and 10 mM. The samples were studied before calcination and after calcination at 450 °C. The SEM images were used to study the surface morphology of the samples and revealed the structural arrangement of the nanotubes. The XRD patterns were used to investigate the crystalline phases of Ti and TiO₂. Anatase phases were observed after annealing at 450° C. The photocatalytic performance was studied in DSSCs and showed increased activity with dopant concentration. The highest cell efficiency of 4.66 % was obtained for aFe(NO₃)₃ concentration of 6 mM, after which the cell efficiency dropped. From the results of SEM, AFM and UV-vis studies on the 6 mM sample, we strongly recommend not to re-anodize after annealing, as this does not improve the photoresponse of the TNTs. Titanium dioxide nanotubes have a wide range of applications such as in photocatalysis, photovoltaics, hydrogen generation, water purification and fuel cells. The results of this work would serve as a guideline for further research in this field of study.

References

- 1. Aboulouard A, Gultekin B, Can M, Erol, M, Jouaiti A, Elhadadi B, Demic S. Dyesensitized solar cells based on titanium dioxide nanoparticles synthesized by flame spray pyrolysis and hydrothermal sol-gel methods: a comparative study on photovoltaic performances. *Journal of Materials Research and Technology*. 2020;9(2): 1569–1577.
- 2. Shamsudin NH, Shafie S, Ab Kadir MZA, Ahmad F, Sulaiman Y, Chachuli SAM, Razali MC. Flexible back-illuminated dye sensitised solar cells (DSSCs) with titanium dioxide/silver nanoparticles composite photoanode for improvement of power conversion efficiency. *Optik.* 2023;272: 170237.
- 3. Ahmad I, Jafer R, Abbas SM, Ahmad N, Iqbal J, Bashir S, Khan MH. Improving energy harvesting efficiency of dye sensitized solar cell by using cobalt-rGO co-doped TiO₂ photoanode. *Journal of Alloys and Compounds*. 2022;891: 162040.
- 4. Gutiérrez Y, Losurdo M, González F, Everitt HO, Moreno F. Nanoplasmonic photothermal heating and near-field enhancements: a comparative survey of 19 metals. *The Journal of Physical Chemistry C*. 2020;124(13): 7386–7395.
- 5. Joshi DN, Ilaiyaraja P, Sudakar C, Prasath RA. Facile one-pot synthesis of multi-shaped silver nanoparticles with tunable ultra-broadband absorption for efficient light harvesting in dye-sensitized solar cells. *Solar Energy Materials & Solar Cells*. 2018;185: 104–110.
- 6. Jin L, Wang YW, Wu J, Su CY, Zhou H, Xu HY. Properties of oxidation quantum dots-CdO/TiO₂ heterostructures constructed as DSSC photoanodes. *Materials Science in Semiconductor Processing*. 2022;147: 106720.
- 7. Shaikh SF, Kwon HC, Yang W, Mane RS, Moon J. Performance enhancement of mesoporous TiO₂-based perovskite solar cells by ZnS ultrathin-interfacial modification layer. *Journal of Alloys Compounds*. 2018;738: 405–414.
- 8. Krasinkova MV. Single-walled carbon nanotube as a nanoscale quantum system. *Materials Physics and Mechanics*. 2020;44: 103–109.
- 9. Srinivasa Moorthy S, Manonmani K. Fabrication and characterization of TiO₂ particulate filled glass fiber reinforced polymer composite. *Materials Physics and Mechanics*. 2013;13: 28–34.
- 10. Wang JK, Nie XJ, Wang W, Zhao ZL, Li L, Zhang ZQ. Single-layer graphene-TiO₂ nanotubes array heterojunction as photoanode to enhance the photoelectric of DSSCs. *Optik.* 2021;242: 167245.
- 11. Ismael M. Enhanced photocatalytic hydrogen production and degradation of organic pollutants from Fe (III) doped TiO₂ nanoparticles. *Journal of Environmental Chemical Engineering*. 2020;8(2): 103676.

- 12. Chandra Pradhan S, Soman SJ. Effect of thickness on charge transfer properties of conductive polymer based PEDOT counter electrodes in DSSC. *Results in Surfaces and Interfaces*. 2021;5: 100030.
- 13. Ahmed U, Alizadeh M, Rahim NA, Shahabuddin S, Ahmed MS, Pandey AK. A comprehensive review on counter electrodes for dye sensitized solar cells: A special focus on Pt-TCO free counter electrodes. *Solar Energy*. 2018;174: 1097–1125.
- 14. Gulati K, Martinez RDO, Czerwiński M, Michalska-Domańska M. Understanding the influence of electrolyte aging in electrochemical anodization of titanium. *Advances in Colloid and Interface Science*. 2022;302; 102615.
- 15. Yuferov YV, Popov ID, Zykov FM, SuntsovAY, Baklanova IV, ChukinAV, Zhidkov IS. Study of the influence of anodizing parameters on the photocatalytic activity of preferred oriented TiO₂ nanotubes self-doped by carbon. *Applied Surface Science*. 2022;573: 151366.
- 16. Montakhab E, Rashchi F, Sheibani S. Modification and photocatalytic activity of open channel TiO₂ nanotubes array synthesized by anodization process. *Applied Surface Science*. 2020;534: 147581.
- 17. Wei X, Wang C, Ding S, Yang K, Tian F, Li F. One-step synthesis of Ag nanoparticles/carbon dots/TiO₂ nanotube arrays composite photocatalyst with enhanced photocatalytic activity. *Journal of Environmental Chemical Engineering*. 2021;9(1): 104729.
- 18. Motola M, Hromadko L, Prikryl J, Sopha H, Krbal M, Macak JM. Intrinsic properties of high-aspect ratio single-and double-wall anodic TiO₂ nanotube layers annealed at different temperatures. *Electrochimica Acta*. 2020;352: 136479.
- 19. Nakpan P, Aeimbhu A. Fabrication of titanium dioxide nanotubes by difference the anodization voltage and time. *Materials Today: Proceedings*. 2021;47: 3436–3440.
- 20. Purushothaman N, Elansezhian R, Raviprakash AV. Synthesis and characterisation of nano TiO₂ film for enhancing antireflection properties. *Advances in Materials and Processing Technologies*. 2022;8(1): 29–36.

THE AUTHORS

Samran B. 🗓

e-mail: buagun@hotmail.com

Thongpanit P. 🗓

e-mail: p.thongpanit@npu.ac.th

Timah E.N.

e-mail: timahe@yahoo.com

Chaiwichian S.

e-mail: saranyou530531117@gmail.com

A kinetic model of the stress-induced void evolution in pentagonal whiskers and rods

Submitted: October 17, 2023

Approved: November 11, 2023

Accepted: November 27, 2023

A.S. Khramov (1) 1, S.A. Krasnitckii (1) 2 , A.M. Smirnov (1) 1, M.Yu. Gutkin (1) 1,3,4

¹ ITMO University, St. Petersburg, Russia

² St. Petersburg State University, St. Petersburg, Russia

³ Peter the Great St. Petersburg Polytechnic University, St. Petersburg, Russia

Abstract. A kinetic model of stress-induced vacancy diffusion in pentagonal whiskers and rods is suggested to investigate the void evolution there. In the framework of the model, the Gibbs-Thompson boundary conditions are employed to identify the free surface effect on the vacancy flux while the elastic fields of the wedge disclination are involved to reveal the contribution of the bulk effect. It is shown that the void evolution mode in the hollow pentagonal whiskers and rods is strongly determined by the initial internal and external radii as well as the materials parameters describing the response of both the residual stress and the surface tension. The void evolution diagram and kinetic curves are demonstrated to elucidate the critical and optimal parameters of this phenomenon.

Keywords: pentagonal whiskers; pentagonal rods; multiply twinned particles; residual stress; stress relaxation; disclination; hollow nanostructures; stress-induced diffusion

The article was prepared based on the report presented at the Symposium "Micromechanics of Functional Materials" at the XIII All-Russian Congress on Theoretical and Applied Mechanics.

Acknowledgements. This work was supported by the Russian Science Foundation (grant No. 22-11-00087, https://rscf.ru/en/project/22-11-00087/).

Citation: Khramov AS, Krasnitckii SA, Smirnov AM, Gutkin MY. A Kinetic Model of the Stress-Induced Void Evolution in Pentagonal Whiskers and Rods. *Materials Physics and Mechanics*. 2023;51(7): 22-33. DOI: 10.18149/MPM.5172023 4.

Introduction

Pentagonal crystal (PC) structures are deemed to be essential for enhanced performance in photonic, plasmonic and catalytic applications [1,2]. Their properties, prescribed not only by {111} faceting but also by cyclic twinning, evince more effective performance than their single-crystal analogs [3–5]. For most PCs such as pentagonal whiskers (PWs) or rods [6], plates [7], and decahedral particles (DhPs) [8], the five-fold cyclic twinning is common. The more complex multiply cyclic twinning corresponds to the class of icosahedral particles (IcPs) [9]. Besides, the cyclic twinning is responsible for inhomogeneous residual stress-strain states in PCs that significantly impact upon their functional properties [10–12].

Recently, much attention has been focused on the fabrication of hollow PC structures with tunable properties [13–17]. The fact that the hollowing process in PCs is strongly affected

© A.S. Khramov, S.A. Krasnitckii, A.M. Smirnov, M.Yu. Gutkin, 2023.

Publisher: Peter the Great St. Petersburg Polytechnic University

This is an open access article under the CC BY-NC 4.0 license (https://creativecommons.org/li-censes/by-nc/4.0/)

by the residual stress caused by multiply twinning has been demonstrated in series of experiments [18-21]. For instance, Romanov et al. [18] observed voids in large CdTe PWs with diameter 1-10 mm. Later Yasnikov and Vikarchuk [19] employed the electrodeposition technique to produce both hollow and solid Cu PCs to investigate the size effect in the void formation. They observed the voids in relatively large PCs, while relatively small PCs remained free of voids. These experiments were explained by the higher level of the strain energy stored by the inhomogeneous residual stress in the larger PCs. Another example of stress-induced process of hollowing was described by Lu et al. [20] investigating the galvanic replacement reaction of both single-crystalline and multiply twinned Ag nanoparticles with HAuCl4 in organic medium. The authors demonstrated that, under the galvanic replacement process, the single-crystalline Ag nanocubes evolved into nanoboxes while the multiply twinned Ag nanoparticles evolved into either pentagonal nanorings or nanocages of decahedral and icosahedral shapes. Similar results were obtained by Huang et al. [21] in examining the void growth phenomenon in single-crystalline and multiply twinned Pd nanoparticles placed in the Cu-acetylacetonate atmosphere. The authors reported that they synthesized hollow PdCu alloyed particles from the multiply twinned precursors in contrast to the void-free Pd/Cu coreshell particles produced from the single-crystalline precursors. Thus, to control the void evolution in PCs, it is essential to incorporate the residual stress effects into both the synthesis protocols and theoretical modeling.

The residual stress in PCs can be described within the disclination concept [22–24]. According to this concept, PWs and DhPs are considered as elastic bodies containing a positive partial wedge disclination with strength ~ 0.128 rad, while IcPs as elastic spheres containing a Marks-Ioffe stereo disclination with strength ~ 0.0613 sr that models the presence of six positive partial wedge disclinations with strength ~ 0.128 rad. It is worth noting that, within the disclination concept, various stress relaxation phenomena in PCs such as dislocation generation [25,26], crack initiation [27], formation of the phase inhomogeneities [28] and the misfit layers [29] has received the theoretical description in [30–35]. The phenomenon of the void evolution in the PCs has been elucidated in the large volume of the theoretical works as well.

Historically, the theoretical research concerning the void evolution phenomenon in PCs has focused on the interaction of point defects with wedge disclinations. The stress-induced diffusion of vacancies in vicinity of wedge disclinations was elucidated in the pioneer works [36–38].

Latter Mikhailin and Romanov [39] employed an elastic model and a molecular dynamic simulation to investigate the bulk vacancy migration to the disclination core placed in the center of a circular crystal plate. The numerical simulation demonstrated that the initial amorphization of the disclination core occurs and subsequently results in the nucleation of a cavity. Besides, it was revealed that incorporating the surface effects in the energy balance of the elastic plate leads to appropriate agreement with computer simulation results for the cavity formation phenomenon.

Romanov and Samsonidze [40] suggested a kinetic model of the point defects diffusion driven by the stress state of a wedge disclination in an elastic cylinder. The disclination core was considered as a perfect sink for point defects while the cylinder surface as a perfect source of them. The original profile of the point defects concentration inside the body was presumed to be relevant to the elastic disturbance of the disclination to introduce the initial and boundary conditions. The asymptotic expression for the point defects diffusion flux toward the disclination core was obtained in two limiting cases of (i) the initial stage, when the absorption of point defects in vicinity of the disclination prevails, and (ii) the final stage, when the steady-state condition is achieved.

Osipov and Ovid'ko [41] investigated the migration of substitutional atoms to triple junction disclinations in alloyed materials. The concentration of substitutional atoms in vicinity of a disclination core was derived with the assumption of the parabolic growth. It was inferred

that the split of the disclination, which was induced by the diffusion process, is one of the main factors responsible for the growth of a nucleus of amorphous phase under mechanical alloying.

Nazarov [42] analyzed the grain boundary diffusion affected by triple junction disclinations. He demonstrated that the stress gradients, induced by the disclination configurations, may explain anomalously high values of grain boundary diffusivity in nanocrystalline materials. To better understand the effects of a disclination on the grain boundary diffusion, Murzaev and Nazarov [43,44] implemented the molecular dynamic simulation of the grain boundary containing a partial disclination. They showed that the numerically calculated grain boundary diffusivity in disclinated nanocrystalline materials is at least two orders higher than in the disclination-free polycrystals.

Romanov et al. [18] examined the void formation in PWs and IcPs as a channel of residual stress relaxation. Within the quasi-equilibrium energetic approach, the critical conditions of a void formation in PCs were determined in terms of the change of surface and disclination strain energies due to the void growth. Using the stress fields of wedge disclinations in elastic bodies with spherical surfaces that were found by Kolesnikova at al. [45], Krasnitckii et al. [46] later considered a similar problem for DhPs. In spite of the fact that the energetic approach has quite limited applications (as it does not include the kinetic aspects of the problem), the optimal size of voids prescribed by the stress relaxation models in [18,46] is in agreement with experimental observations of hollow PCs [18,19].

Vlasov et al. introduced the most thorough formulation of non-steady stress-induced diffusion problems concerning the formation of impurity atmospheres in vicinity of triple junction disclinations [47,48] as well as the growth of void and phase nuclei in PWs [49,50] and IcPs [51,52]. For the case of void growth in PWs, Vlasov et al. [49] managed to derive the strict analytical solutions for the void radius rate. Besides, it was demonstrated [52] that, at the initial stage, when the disturbance induced by the body external surface is negligible, the nucleus radius rate in vicinity of wedge and stereo disclinations varies as $\sim t^{1/2}$ (hereinafter t is the time of the process) in contrast to that in vicinity of edge dislocations and tips of mode I cracks, varying as $\sim t^{1/3}$ and $\sim t^{2/5}$, respectively.

Later Tsagrakis et al. [53] considered the void growth phenomena in IcPs with accounting for size effects within the gradient elasticity theory. The gradient solution for a stereo disclination was found to provide nonsingular profiles of the vacancy velocity and the vacancy concentration inside IcPs. The authors showed that the gradient elastic effects are essential to consider when the internal length parameter is of the same order of magnitude as the particle radius, otherwise these effects can be neglected.

It is worth noting that the aforementioned kinetics models have a serious limitation. In fact, they are unable to incorporate the influence of surface tension in the void evolution process in PCs. Recently Krasnitckii et al. [54] have overcome this limitation by involving the surface tension on the inner and outer surfaces of hollow IcPs in the form of the linearized Gibbs-Tompson conditions. The corresponding stress-assisted diffusion problem under the steady-state approximation was solved to consider the void evolution kinetics driven by both the surface and bulk stress effects. It was shown that the void evolves in either the shrinking mode, if the vacancy flux induced by the Gibbs-Tompson effects is predominant, or the growing mode, if the pressure-induced vacancy flux prevails, or the stabilizing mode, if the contributions of these fluxes are equal.

The present work is aimed at extending the general formalism of the model suggested in [54] to investigate the stress-induced vacancy diffusion as well as the void evolution phenomena in PWs under the Gibbs-Tompson curvature effects. It represents (i) a solution of the steady-state problem of vacancy diffusion for a hollow cylindrical body, (ii) an analysis of the void evolution kinetics in a PW, and (iii) an evaluation of the critical and optimal parameters of the void equilibrium state.

Model

Consider a hollow PW as a long hollow cylindrical body containing a positive partial wedge disclination of strength $\omega \approx 0.128$ rad (Fig. 1(a)). The wedge disclination is responsible for the hydrostatic compression in the inner region of the cylinder and for the hydrostatic tension in its outer region. This volumetric strain stimulates both the generation of vacancies at the stretched surface of the PW and subsequent migration of the vacancies inward the compressed region, where they can coagulate with formation of a central cylindrical void. The stress-assisted vacancy diffusion can be described by the second Fick low with a drift term [54]:

$$\frac{1}{D}\frac{\partial C}{\partial t} = \Delta C + \frac{1}{kT}\nabla C \cdot \nabla W_{int} + \frac{C}{kT}\Delta W_{int}, \qquad (1)$$

where C is the relative (dimensionless) concentration of vacancies inside the cylinder, D is the diffusivity of vacancies, k is the Boltzmann constant, T is the absolute temperature, $W_{int} = P \delta v$ is the interaction energy of a vacancy with the wedge disclination, P is the hydrostatic pressure exerted by the wedge disclination stress tensor σ (P = -1/3 tr σ), and δv is the vacancy relaxation volume ($\delta v < 0$). The hydrostatic pressure P reads [24]:

$$P = -\frac{G\omega}{3\pi} \frac{1+\nu}{1-\nu} \left[\frac{1}{2} + \ln\frac{r}{a} + \frac{a_{\nu}^2}{a^2 - a_{\nu}^2} \ln\frac{a_{\nu}}{a} \right],\tag{2}$$

where G is the shear modulus, v is the Poisson coefficient, a_v and a are the internal and external radii, respectively, of the hollow cylinder, and r is the radial coordinate.

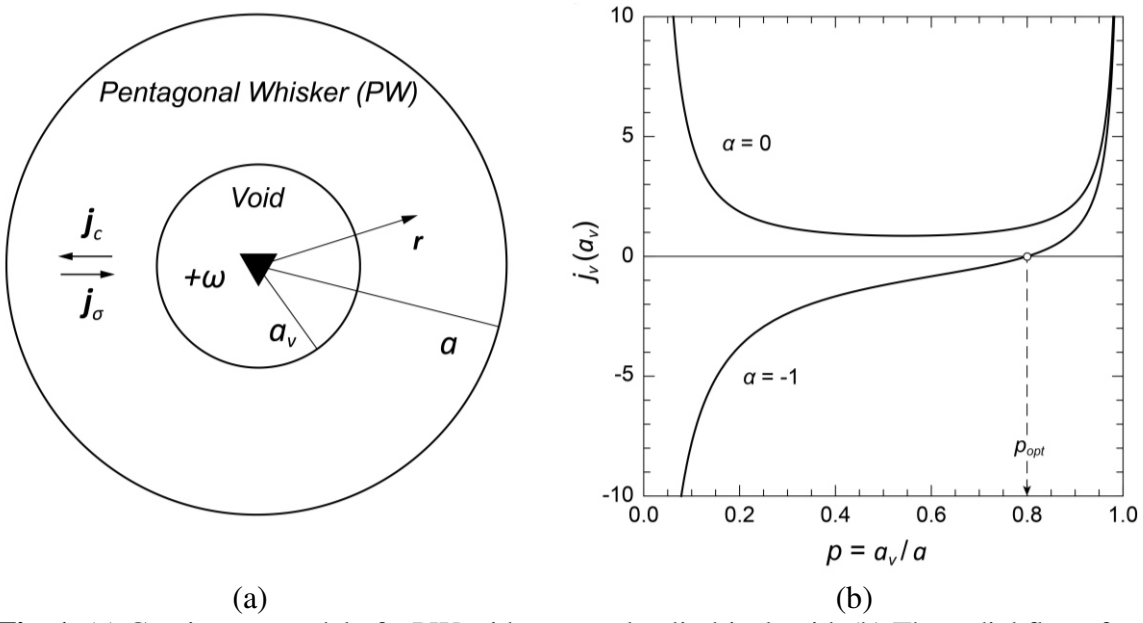


Fig. 1. (a) Continuum model of a PW with a central cylindrical void. (b) The radial flux of vacancies $j_v(a_p)$ through the void surface in dependence of the normalized void radius p for $\alpha = 0$ (single-crystalline tubes) and $\alpha = -1$ (PWs). The radial flux is given in units of C_0D/Ω

Substituting Eq. 2 in the diffusion equation Eq. 1, for the steady-state process $(\partial C/\partial t \approx 0)$ in the case of the cylindrical symmetry, one can come to the following equation:

$$\frac{d^2C}{dr^2} + \frac{1-\alpha}{r} \frac{dC}{dr} = 0,$$
(3)

where α is the dimensionless complex which defines the disclination stress contribution to the diffusion process:

$$\alpha = \frac{G\omega}{3\pi} \frac{1+\nu}{1-\nu} \frac{\delta \nu}{kT} \,. \tag{4}$$

In addition to the bulk effects accompanying the void growth in PWs, the surface effects viz. surface tension should be also taken into consideration. Actually, the surface tension produces a negative pressure (positive hydrostatic stress) on the inner surface while the outer surface is affected by a positive pressure (negative hydrostatic stress). From this point of view, the vacancy concentration at the inner surface can be bigger than at the outer one. It means that the vacancy flux inside PWs can be either inhibited or even inversed by the surface tension. The latter phenomenon exerts the void shrinking with its subsequent collapse. The impact of the surface tension on the void evolution can be taken into account in the linearized form of the Gibbs-Thompson boundary conditions as follows [55]:

$$C\big|_{r=a_p} = C_0 \left(1 + \frac{\beta}{a_v} \right), \qquad C\big|_{r=a_p} = C_0 \left(1 - \frac{\beta}{a} \right), \tag{5a,b}$$

where C_0 is the equilibrium concentration of vacancies near the flat surface, $\beta = \gamma \Omega / (kT)$ is the length parameter, γ is the specific surface energy, Ω is the atomic volume.

The solution of the diffusion equation (Eq. 3) with regard to the boundary conditions (Eqs. 5) is given by

$$C = C_0 \left(1 + \beta \frac{a(a^{\alpha} - r^{\alpha}) - a_{\nu}(r^{\alpha} - a_{\nu}^{\alpha})}{a a_{\nu}(a^{\alpha} - a_{\nu}^{\alpha})} \right).$$
 (6)

It is worth noting that Eq. 6 coincides with the solution of the diffusion problem for the defect-free cylindrical shells given in [55], if the parameter α tends to zero.

Results

The void evolution phenomenon in hollow PWs is strongly determined by the migration of vacancies. Inside the PWs, the migration of vacancies can be described in terms of the radial flux as follows:

$$j_{\nu} = j_{c} + j_{\sigma} \,, \tag{7}$$

where j_c is the vacancy flux caused by the vacancy concentration gradient between the inner and outer surfaces of the PWs,

$$j_c = -\frac{D}{\Omega} \nabla C \,, \tag{8}$$

and j_{σ} is the stress-induced vacancy flux caused by the elastic field of the wedge disclination,

$$j_{\sigma} = -\frac{D}{\Omega} \frac{C}{kT} \nabla W_{int} \,. \tag{9}$$

The radial vacancy flux in Eq. 7 can be rewritten with respect to the concentration profile (given by Eq. 6) in the following form:

$$j_{\nu}(r) = \frac{\alpha C_0 D}{\Omega} \frac{(a_{\nu} + \beta) a^{1+\alpha} - (a - \beta) a_{\nu}^{1+\alpha}}{a a_{\nu} (a^{\alpha} - a_{\nu}^{\alpha}) r}.$$
 (10)

To investigate the void evolution phenomenon, one can consider the dependencies of the radial vacancy flux through the inner surface $j_v(a_v)$ on the radii ratio $p = a_v/a$ shown in Fig. 1(b) for different values of α . The void evolution mode is defined by the sign of the total vacancy flux at the void surface in Eq. 10. If the flux is negative, the inward stress-induced flux prevails so that vacancies are absorbed by the void, thus provoking the void growth mode. When the flux is positive, the outward concentration flux is predominant so that vacancy emission from the void evincing the void shrinkage mode is expected. Besides, if the vacancy flux turns to

According to Fig. 1(b), the relatively small voids (when $p < p_{eq}$) in hollow PWs with $\alpha = -1$ tend to grow until reaching the optimal radius p_{opt} . On the contrary, the relatively large voids (when $p > p_{eq}$) tend to shrink to the optimal radius p_{opt} . In the case of defect-free single-crystalline tubes with $\alpha = 0$, the vacancy flux is positive for any radii ratio p, hence the void growth mode occurs to transform tubes into solid rods.

Since the void evolution mode in PWs is mainly determined by the sign of the vacancy flux at the void, one can derive the critical mode condition from the vanishing flux equation $j_{\nu}(a_{\nu}) = 0$ in the form:

$$\frac{a_{v} + \beta}{a - \beta} = \left(\frac{a_{v}}{a}\right)^{\alpha + 1}.$$
(11)

Introducing dimensionless variables, one can rewrite Eq. 11 with regard to the mass conservation law [54], $a^2 - a_v^2 = a_0^2$, as follows:

$$\alpha = \log_p \frac{p \, b_0 + \Delta}{p(b_0 - \Delta)},\tag{12}$$

where $p = a_v / a$, $\Delta = (1 - p^2)^{1/2}$, $b_0 = a_0 / \beta$, and a_0 is the radius of a solid PW.

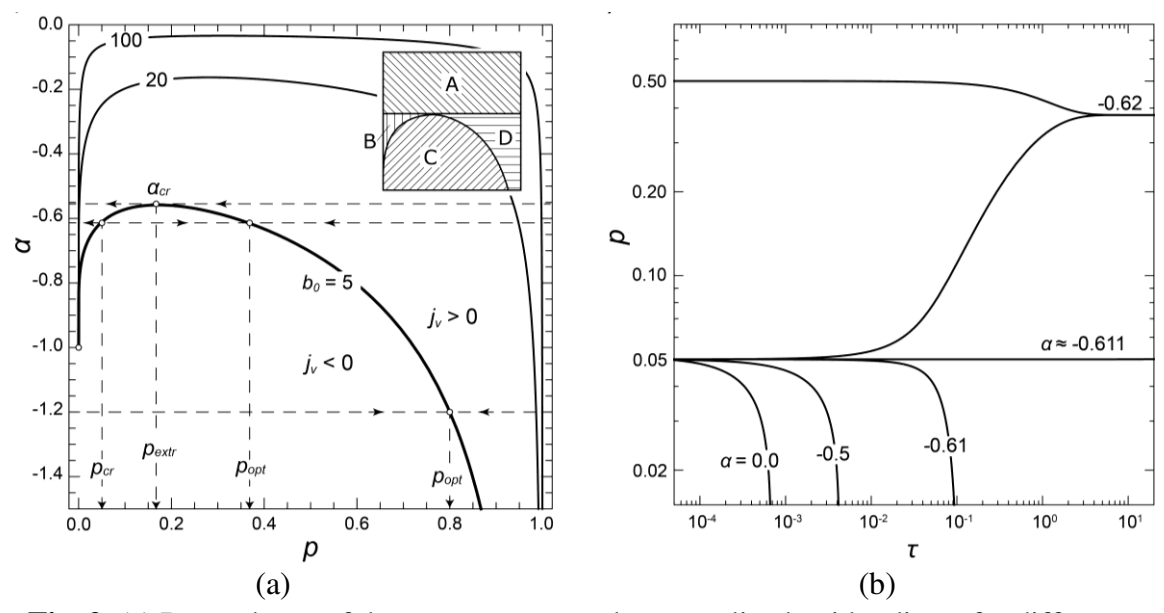


Fig. 2. (a) Dependence of the parameter α on the normalized void radius p for different values of $b_0 = 5$, 20 and 100. The inset in the upper right corner indicates the regions A, B, C and D corresponding to different scenarios of void evolution. (b) Dependence of the normalized void radius p on the dimensionless time τ given for different values of the initial void radius $p_0 = 0.05$ and 0.5, and the parameter $\alpha = 0.0, -0.5, -0.61, -0.62$, and $\alpha \approx -0.611$

Figure 2(a) demonstrates the curves $\alpha = f(p)$ given by Eq. 12 for different values of the parameter $b_0 = 5$, 20 and 100. These curves define the parameters α and p of hollow PWs for which $j_v(a_v) = 0$, i.e. the void equilibrium mode takes place. The area below the curves $(\alpha < f(p))$ corresponds to the void growth mode when $j_v(a_v) < 0$, while the area above them $(\alpha > f(p))$ to the void shrinkage mode when $j_v(a_v) < 0$. It is worth noting that the area above curves reduces if the parameter b_0 increases.

The void evolution scenarios in the hollow PWs are determined by the roots of the equation $\alpha = f(p)$ for a given value of α (see Fig. 2(a)). For example, the equation $\alpha = f(p)$ has no roots for $\alpha_{cr} < \alpha \le 0$ so the void shrinkage mode is valid for any p, and hence the void of any

size is unstable. For $\alpha = \alpha_{cr}$, there is the only root $p = p_{extr}$ corresponding to the unstable equilibrium state of the void, i.e. any perturbation of its radius results in the transition to the shrinkage mode. The cases of $p = p_{cr}$ and $p = p_{opt}$ can be elucidated as the unstable and stable equilibrium void states, respectively. For $\alpha < -1$, the equation $\alpha = f(p)$ has the only one root, $p = p_{opt}$, relating to the stable equilibrium state of the void. To obtain the stable equilibrium, the voids with p from the range of 0 must grow, while those with <math>p from the range of $p_{opt} must shrink.$

Thus, the voids in PWs should be unstable and have a tendency to shrinkage if either $\alpha_{cr} < \alpha \le 0$ for any void radius (see region A in Fig. 2(a)) or $-1 \le \alpha < \alpha_{cr}$ for pre radius less than a critical one (see region B in Fig. 2(a)). In contrast, the stable void can evolve via either shrinkage or growth if $\alpha < -1$ for any void radius and $-1 \le \alpha < \alpha_{cr}$ for void radius larger than the critical value (see regions C and D in Fig. 2(a)).

Turning now to the kinetic aspects of the void evolution in hollow PWs, the growth rate is defined by the vacancy flux at the void surface:

$$\frac{da_{v}}{dt} = -\Omega j_{v}(a_{v}). \tag{13}$$

The Eq. 13 can be derived as follows:

$$\frac{dp}{d\tau} = -\frac{\alpha \Delta^4}{p^2} \frac{(1 - \Delta/b_0) p^{1+\alpha} - (p + \Delta/b_0)}{1 - p^{\alpha}},$$
(14)

where $\tau = C_0 D t / a_0^2$ is the dimensionless time.

The numerical solution of the void evolution equation (Eq. 14) is illustrated in Fig. 2(b) for $b_0 = 5$ (in this case, $\alpha_{cr} \approx -0.558$, see Fig. 2(a)). According to Fig. 2(b), for the given initial normalized radius $p_0 = 0.05$ of the void, some different scenarios of its evolution can occur. For $\alpha = 0.0$ and -0.5 (> $\alpha_{cr} \approx -0.558$), the void tends to shrink with subsequent collapse (see region A in Fig. 2(a)). Similar pathway is expected in the case when $\alpha = -0.61$ (< $\alpha_{cr} \approx -0.558$) and the initial radius p_0 of the void is less than critical value $p_{cr} \approx 0.051$ (region B). Moreover, the time for the void collapse is mainly determined by α : the smaller the value of α , the longer the void shrinking process. As is seen from Fig. 2(b), for even smaller $\alpha = -0.62$, the void tends to take the optimal size via either its growth (for $p_0 = 0.05$ corresponding to region C) or shrinkage (for $p_0 = 0.5$ corresponding to region D). It is worth noting that, for $\alpha \approx -0.611$, the normalized radius $p_0 = 0.05$ of the void coincides with the critical one, p_{cr} , so the void occurs in the state of unstable equilibrium when any perturbation of its radius causes either shrinking or growing.

Let us now examine the critical and optimal conditions of the void evolution process in PWs. As was mentioned above, the nucleation of stable voids in solid PWs is possible if the absolute value of parameter α exceeds that of some critical value α_{cr} only. The latter one strongly depends on the ratio of the solid PW radius a_0 to the length parameter β . The parameter α characterizes the bulk effects in solid PWs attributed to the wedge disclination stress while the parameter β describes the role of surface effects (the bigger the surface energy γ the bigger β). Fig. 3(a) illustrates the dependence of α_{cr} on the solid PW radius a_0 for different values of the length parameter $\beta = 5$, 10, and 20 nm. As is seen from Fig 3(a), the critical value α_{cr} first sharply increases for $0 < a_0 < 200$ nm and then gradually tends to zero for $a_0 > 200$ nm. Besides, for a given value of the solid PW radius a_0 , the critical value α_{cr} decreases with an increase in β . It means that, in PWs of the same size (for example, at $a_0 = 100$ nm), the void nucleation is more likely to occur in the PWs with smaller surface tension ($\alpha_{cr} \approx -0.15$ for $\beta = 5$ nm whereas $\alpha_{cr} \approx -0.55$ for $\beta = 20$ nm).

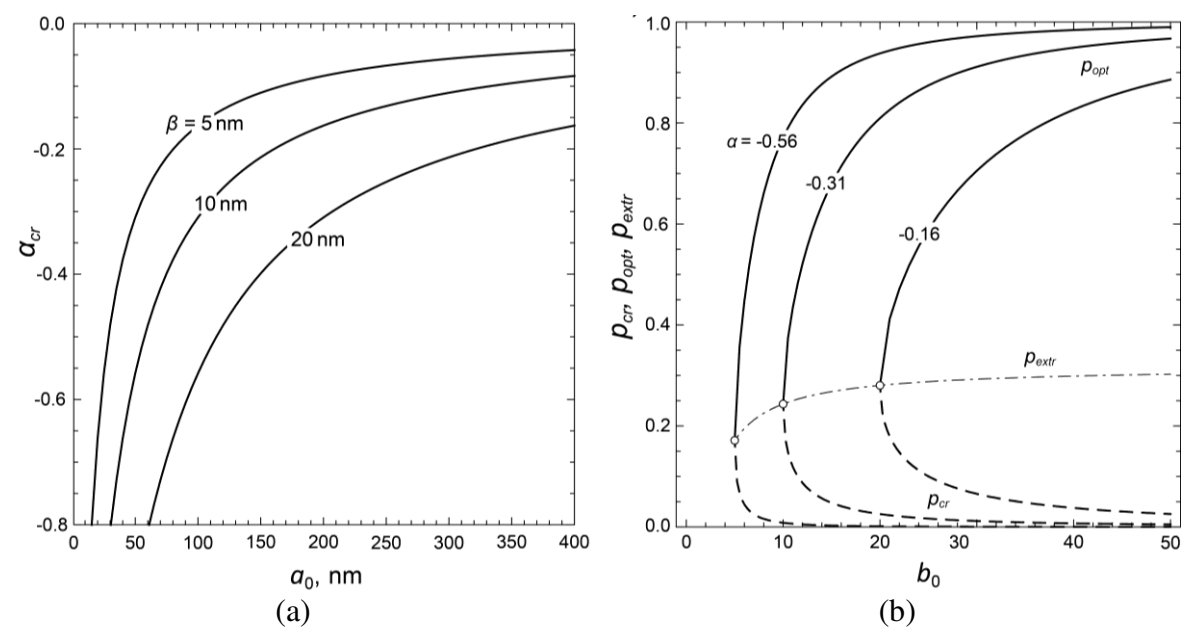


Fig. 3. (a) Dependence of the critical value α_{cr} on the solid PW radius a_0 for different values of the parameter $\beta = 5$, 10 and 20 nm. (b) The dependences of the normalized void radii p_{cr} (solid curves), p_{opt} (dushed curves), and p_{extr} (dushed-and-dotted curve) on the dimensionless parameter b_0 for $\alpha = -0.16$, -0.31, and -0.56

In contrast to the case of $\alpha_{cr} < \alpha \le 0$, when the void initiation failed, the barrier-controlled nucleation of voids in solid PWs can occur if the normalized radius of void nucleus exceeds its critical value p_{cr} at $-1 \le \alpha < \alpha_{cr}$. In this case, the void nucleus tends to grow until it reaches the optimal size and $p = p_{opt}$. As it was mentioned above, the values of parameters p_{cr} and p_{opt} are strongly determined by the material parameters α and $b_0 = a_0 / \beta$ demonstrating the role of size effect in the void evolution phenomenon. The dependences of the characteristic normalized radii of voids in PWs, p_{cr} , p_{extr} , and p_{opt} , on the value of b_0 are shown in Fig. 3b for different values of α . As is seen from Fig. 3(b), the critical and optimal normalized radii coincide with the extremal value p_{extr} if α takes the critical value. When b_0 increases, p_{cr} decreases while p_{opt} increases. In the limiting cases, when $\alpha \to -1$ or $b_0 \to +\infty$, the critical normalized radius of the void vanishes, the optimal one tends to 1.0 (the case of an infinitely thin-wall tube), and the extremal one tends to a constant value ~ 0.3 .

In the case of $\alpha < -1$, the barrier-less nucleation of voids in PWs should occur. Indeed, the contribution of the surface tension to void evolution is negligible with regard to the impact of the disclination stress field. As a result, the void nucleus is expected to grow in order to take a stable state with its optimal normalized radius p_{opt} .

Conclusions

In summary, the void evolution kinetics in PWs has been reconsidered with regard to the curvature surface effect. In doing so, the linearized Gibbs-Thompson boundary conditions are incorporated in the boundary-value problem of stress-assisted vacancy diffusion inside a hollow cylindrical body. It is shown that the vacancy flux is mainly determined by the dimensionless parameters α indicating the impact of the bulk stress state of the wedge disclination, and β describing the effect of the surface tension on the vacancy diffusion. With assuming that the direction of the vacancy flux completely prescribes the void shrinkage or growth modes in hollow PWs, various void evolution scenarios have been revealed with respect to the initial void radius $a_{v,0}$ and the dimensionless parameters α and $b_0 = a_0 / \beta$ (where a_0 is the radius of a

solid PW) which reflect the contributions of the bulk stress and surface effects, respectively, to the void evolution process.

According to the first scenario, in PWs with $\alpha_{cr} < \alpha < 0$, the void of any size is unstable, i.e. it tends to shrink with the subsequent collapse. Hence, the void nucleation is completely inhibited by the surface effects.

In PWs with $-1 \le \alpha < \alpha_{cr}$, the voids of size smaller than a critical one are not stable and tend to shrink, in contrast to the voids of size larger than the critical one tend to reach the stable state with the optimal radius $a_{v,opt}$.

When $\alpha < -1$, the voids of any size have the tendency to reach the stable state via either growing (if $a_v < a_{v,opt}$) or shrinking (if $a_v > a_{v,opt}$). Hence, the bulk stress effect prevails and stimulates the void nucleation to occur.

Finally, the critical and optimal parameters of the void evolution scenarios are identified with respect to the bulk and surface effects. It is shown that the critical parameter α_{cr} increases with an increase in the solid PW radius a_0 as well as with a decrease in the length parameter β . That is the bigger the PW size the less the influence of the surface tension and hence the barrier for void nucleation. Besides, the critical radius of void nucleus $a_{v,cr}$ also declines with an increase in the solid PW size. As for the optimal radius $a_{v,opt}$ of a stable void, the rise of both the parameters b_0 and $|\alpha|$ leads to an increase in the optimal radius of the void. Moreover, in the limiting cases when $b_0 \to +\infty$ and $\alpha \to -\infty$, the hollow PWs could evolve in thin-wall pentagonal tubes.

One of the most significant findings to emerge from this model is that the surface effects such as surface tension is essential to incorporate in the problem of the void evolution in PWs if the material parameter $\alpha > -1$. When $\alpha < -1$, the surface effect on the void nucleation can be neglected.

References

- 1. Hamans RF, Parente M, Garcia-Etxarri A, Baldi A. Optical properties of colloidal silver nanowires. *The Journal of Physical Chemistry C*. 2022;126(20): 8703-8709.
- 2. Lyu Z, Shang Y, Xia Y. Shape-Controlled Synthesis of Copper Nanocrystals for Plasmonic, Biomedical, and Electrocatalytic Applications. *Accounts of Materials Research*. 2022;3(11): 1137–1148.
- 3. Carbo-Argibay E, Rodriguez-Gonzalez B. Controlled Growth of Colloidal Gold Nanoparticles: Single-Crystalline versus Multiply-twinned Particles. *Israel Journal of Chemistry*. 2016;56(4): 214–226.
- 4. Marks LD, Peng L. Nanoparticle shape, thermodynamics and kinetics. *Journal of Physics: Condensed Matter.* 2016;28(5): 053001.
- 5. Ji G, Ji A, Lu N, Cao Z. Formation and morphology evolution of icosahedral and decahedral silver crystallites from vapor deposition in view of symmetry misfit. *Journal of Crystal Growth*. 2019;518: 89–94.
- 6. Zhao H, Eggeman AS, Race CP, Derby B. Geometrical constraints on the bending deformation of Penta-twinned silver nanowires. *Acta Materialia*. 2020;185: 110–118.1
- 7. Yoo Y, Kim SI, Han S, Lee H, Kim J, Kim HS, Ahn JP, Kang T, Choo J, Kim B. Epitaxially aligned submillimeter-scale silver nanoplates grown by simple vapor transport. *Nanoscale*. 2019;11(37): 17436–17443.
- 8. Zhou S, Zhao M, Yang TH, Xia Y. Decahedral nanocrystals of noble metals: Synthesis, characterization, and applications. *Materials Today*. 2019;22: 108-131.
- 9. Wang H, Zhou S, Gilroy KD, Cai Z, Xia Y. Icosahedral nanocrystals of noble metals: synthesis and applications. *Nano Today*. 2017;15: 121–144.
- 10. Kuo CH, Lamontagne LK, Brodsky CN, Chou LY, Zhuang J, Sneed BT, Sheehan MK, Tsung CK. The effect of lattice strain on the catalytic properties of Pd nanocrystals. *ChemSusChem.* 2013;6(10): 1993–2000.

- 11. Mychinko M, Skorikov A, Albrecht W, Sánchez-Iglesias A, Zhuo X, Kumar V, Liz-Marzán L, Bals S. The Influence of Size, Shape, and Twin Boundaries on Heat-Induced Alloying in Individual Au@ Ag Core–Shell Nanoparticles. *Small.* 2021;17(34): 2102348.
- 12. Huang J, Liu Q, Yan Y, Qian N, Wu X, Ji L, Li X, Li J, Yanga D, Zhang H. Strain effect in Pd@PdAg twinned nanocrystals towards ethanol oxidation electrocatalysis. *Nanoscale Advances*. 2022;4(1): 111–116.
- 13. Han L, Xiong P, Bai J, Che S. Spontaneous formation and characterization of silica mesoporous crystal spheres with reverse multiply twinned polyhedral hollows. *Journal of the American Chemical Society*. 2011;133(16): 6106–6109.
- 14. Huang H, Zhang L, Lv T, Ruditskiy A, Liu J, Ye Z, Xia Y. Five-Fold twinned Pd nanorods and their use as templates for the synthesis of bimetallic or hollow nanostructures. *ChemNanoMat*. 2015;1(4): 246–252.
- 15. Zhou X, Qi W, Li Y. Simple Synthesis of Ru Decahedral Hollow Nanocages with Face-Centered Cubic Structure. *Journal of Nanoscience and Nanotechnology*. 2021;21(10): 5302–5306. 16. Wang W, Shi Y, Chen Z, Zhao M, Cao Z, Lyu Z, Chen R, Xiao K, Chi M, Xia Y. Synthesis and Characterization of Pt-Ag Icosahedral Nanocages with Enhanced Catalytic Activity toward Oxygen Reduction. *ChemNanoMat*. 2022;8(9): e202200186.
- 17. Krasnitckii SA, Gutkin MY. Review on theoretical models of void evolution in crystalline particles. *Reviews on Advanced Materials and Technologies*. 2021;3(1): 96–126.
- 18. Romanov AE, Polonsky IA, Gryaznov VG, Nepijko SA, Junghanns T, Vitrykhovski NJ. Voids and channels in pentagonal crystals. *Journal of Crystal Growth*. 1993;129: 691–698.
- 19. Yasnikov IS, Vikarchuk AA. Voids in icosahedral small particles of an electrolytic metal. *Journal of Experimental and Theoretical Physics Letters*. 2006;83(1): 42–45
- 20. Lu X, Tuan HY, Chen J, Li ZY, Korgel BA, Xia Y. Mechanistic studies on the galvanic replacement reaction between multiply twinned particles of Ag and HAuCl4 in an organic medium. *Journal of the American Chemical Society*. 2007;129(6): 1733–1742.
- 21. Huang J, Yan Y, Li X, Qiao X, Wu X, Li J, Shen R, Yang D, Zhang H. Unexpected Kirkendall effect in twinned icosahedral nanocrystals driven by strain gradient. *Nano Research*. 2020; 13: 2641–2649.
- 22. Wit RDe. Partial disclinations. Journal of Physics. C. Solid State Physics. 1972;5: 529–534.
- 23. Romanov AE, Kolesnikova AL. Application of disclination concept to solid structures. *Progress in Material Science*. 2009;54: 740–769.
- 24. Romanov AE, Kolesnikova AL. Elasticity Boundary-Value Problems for Straight Wedge Disclinations. A Review on Methods and Results. *Reviews on Advanced Materials and Technologies*. 2021;3(1): 55–95.
- 25. Saito Y. Crystal structure and habit of silicon and germanium particles grown in argon gas. *J. Cryst. Growth.* 1979;47(1): 61–69.
- 26. Chen Y, Huang Q, Zhao S, Zhou H, Wang J. Interactions between Dislocations and Penta-Twins in Metallic Nanocrystals. *Metals*. 2021; 11(11): 1775.
- 27. Yasnikov IS. On the problem of the formation of an open sector instead of a twin boundary in electrolytic pentagonal small particles. *JETP Letters*. 2013;97(9): 513–516.
- 28. Alam MJ, Tsuji M, Matsunaga M, Yamaguchi D. Shape changes in Au–Ag bimetallic systems involving polygonal Au nanocrystals to spherical Au/Ag alloy and excentered Au core Ag/Au alloy shell particles under oil-bath heating. *CrystEngComm*. 2011;13(8): 2984–2993.
- 29. Yasnikov IS. The formation of regions free of twin boundaries at the periphery of electrolytic pentagonal small particles. *Technical Physics Letters*. 2014; 40: 411–413.
- 30. Dorogin LM, Kolesnikova AL, Romanov AE. Misfit layer formation in icosahedral nanoparticles. *Technical Physics Letters*. 2008;34: 779–781.
- 31. Gutkin MY, Panpurin SN. Equilibrium ensembles of quantum dots in atomically inhomogeneous pentagonal nanowires. *Physics of the Solid State*. 2014;56: 1187–1194.

- 32. Gutkin MY, Kolesnikova AL, Krasnitckii SA, Dorogin LM, Serebryakova VS, Vikarchuk AA, Romanov AE. Stress relaxation in icosahedral small particles via generation of circular prismatic dislocation loops. *Scripta Materialia*. 2015;105: 10–13.
- 33. Gutkin MY, Kolesnikova AL, Yasnikov IS, Vikarchuk AA, Aifantis EC, Romanov A E. Fracture of hollow multiply-twinned particles under chemical etching. *European Journal of Mechanics-A/Solids*. 2018;68: 133–139.
- 34. Krauchanka MY, Krasnitckii SA, Gutkin MY, Kolesnikova AL, Romanov AE. Circular loops of misfit dislocations in decahedral core-shell nanoparticles. *Scripta Materialia*. 2019;167: 81–85.
- 35. Krauchanka MY, Krasnitckii SA, Gutkin MY, Kolesnikova AL, Romanov AE. Circular loops of misfit dislocations in decahedral core-shell nanoparticles. *Scripta Materialia*. 2019;167: 81–85.
- 36. Vlasov NM, Lyubov BY. Spreading of a finite low-angle tilt boundary due to non-conservative motion of dislocations. *Sov. Physics of Metals and Metallurgy*. 1975;40(6): 1162–1168.
- 37. Lyubov BY, Vlasov NM. Sov. Some effects of interaction between point and extended defects. *Physics of Metals and Metallurgy*. 1979;47(1): 140–157.
- 38. Vlasov NM, Lyubov BYa. Impurity atmosphere condensation at the wedge disclination. *Reports of the USSR Academy of Sciences*. 1981;259(2): 348–351.
- 39. Mikhailin AI, Romanov AE. Amorphization of disclination core. *Sov. Physics of the Solid State*. 1986; 28(2): 601–603.
- 40. Romanov AE, Samsonidze GG. Diffusion in the elastic field of a wedge disclination. *Sov. Technical Physics Letters.* 1988;14(14): 585–586.
- 41. Osipov AV, Ovid'ko IA. Diffusion-induced decay of disclinations and solid state amorphization in mechanically alloyed materials. *Applied Physics A*. 1992;54: 517–519.
- 42. Nazarov AA. Grain-boundary diffusion in nanocrystals with a time-dependent diffusion coefficient. *Physics of the Solid State*. 2003;45: 1166–1169.
- 43. Murzaev RT, Nazarov AA. Energies of formation and activation for migration of grain-boundary vacancies in a nickel bicrystal containing a disclination. *The Physics of Metals and Metallography*. 2006;102: 198–204.
- 44. Nazarov AA, Murzaev RT. Computer simulation of the interaction of junction disclinations in nanomaterials with grain boundary vacancies. *Solid State Phenomena*. 2008;137: 1–8.
- 45. Kolesnikova AL, Gutkin MY, Proskura AV, Morozov NF, Romanov AE. Elastic fields of straight wedge disclinations axially piercing bodies with spherical free surfaces. *International Journal of Solids and Structures*. 2016;99: 82–96.
- 46. Krasnitckii SA, Gutkin MY, Kolesnikova AL, Romanov AE. Formation of a void as stress relaxation mechanism in decahedral small particles. *Letters on Materials*. 2022;12(2): 137–141.
- 47. Vlasov NM, Zaznoba V. Diffusion processes near triple joints of special grain boundaries. *Physics of the Solid State*. 1999;41: 55–58.
- 48. Vlasov NM, Fedik II. Hydrogen segregation in the area of threefold junctions of grain boundaries. *International Journal of Hydrogen Energy*. 2002;27(9): 921–926.
- 49. Vlasov NM, Fedik II. Diffusion-induced relaxation of residual stresses. *Doklady Physics*. 2000; 45(11): 623–626.
- 50. Vlasov NM, Dragunov YG. Phase transformations in pentagonal nanocrystals. *Technical Physics*. 2013;58: 218–222.
- 51. Vlasov NM, Dragunov YG. Formation of zirconium hydride in the vicinity of stereo disclinations. *Technical Physics*. 2013;58(6): 892–895.
- 52. Vlasov NM, Zaznoba VA. Kinetics of migration (deposition) of fission products and interstitial impurities to sinks with different singularities. *Physics of the Solid State*. 2014;56(3): 518–521.
- 53. Tsagrakis I, Yasnikov IS, Aifantis EC. Gradient elasticity for disclinated micro crystals. *Mechanics Research Communications*. 2018;93: 159–162.

54. Khramov AS, Krasnitckii SA, Smirnov AM, Gutkin M. The Void Evolution Kinetcs driven by residual stress in icosahedral particles. *Material Physics and Mechanics*. 2022;50(3): 401–409. 55. Podolyan OM, Zaporozhets TV. Void formation and collapse in nanowires. *Ukrayins'kij Fyizichnij Zhurnal*. 2011;56(9): 933–943.

THE AUTHORS

Khramov A.S.

e-mail: 242531@niuitmo.ru

Smirnov A.M.

e-mail: andrei.smirnov@niuitmo.ru

Krasnitckii S.A.

e-mail: Krasnitsky@inbox.ru

Gutkin M.Yu. 🗓

e-mail: m.y.gutkin@gmail.com

Toughening of nanocrystalline alloys due to grain boundary segregations: finite element modeling

Submitted: November 12, 2023

Approved: November 30, 2023

Accepted: December 14, 2023

A.G. Sheinerman ^{1 ™}, R.E. Shevchuk ²

¹ Institute for Problems of Mechanical Engineering RAS, St. Petersburg, Russia

² JSC "I.I. Polzunov Scientific and Development Association on Research and Design of Power Equipment",

St. Petersburg, Russia

⊠ asheinerman@gmail.com

Abstract. We propose a two-dimensional (2D) model that describes toughening of nanocrystalline metallic alloys due to grain boundary (GB) segregations. Within the model, brittle GB segregations lead to the formation of satellite GB cracks near the tip of the main crack. These cracks affect the stress concentration in the vicinity of the main crack tip and lead to toughening. We performed 2D finite element simulations of crack growth in a representative volume that incorporates GB fragments without segregations and with segregations. In these simulations, GBs are modeled as interface elements, and the effect of GB segregations manifests itself in a strong reduction of the cohesive strength of these elements. We demonstrate that GB segregations in nanocrystalline alloys can increase the fracture energy and thereby toughen these solids.

Keywords: nanocrystalline alloys; grain boundaries; segregations; toughening

Acknowledgements. The work was supported by the Russian Science Foundation (project 22-21-00056).

Citation: Sheinerman AG, Shevchuk RE. Toughening of nanocrystalline alloys due to grain boundary segregations: finite element modeling. *Materials Physics and Mechanics*. 2023;51(7): 34-41. DOI: 10.18149/MPM.5172023_5.

Introduction

The unique mechanical properties of nanocrystalline metallic materials, such as ultrahigh strength, have made them a subject of intensive research last years (see, e.g., reviews [1-6]). Of special interest are nanocrystalline alloys with grain boundary (GB) segregations, which make these nanocrystalline solids stable against grain growth [7-11]. In addition, GB solute segregations can affect the mechanical properties of nanocrystalline alloys, including their strength, hardness and fracture toughness. For example, experiments [12-14] indicate that GB segregations can dramatically increase strength and hardness of nanocrystalline alloys. An improvement of these mechanical properties was explained by the action of various mechanisms, such as inactivation of GB dislocation sources [15-17], resistance to dislocation propagation across grains [18], and suppression of GB sliding [17,19].

In parallel with strength and hardness, GB segregations in nanocrystalline alloys influence the fracture toughness of these alloys. Since such segregations are commonly brittle, they can in some cases reduce the fracture toughness of nanocrystalline alloys [20-22]. Meanwhile, recent experiments [22] demonstrated the possibility of increasing the fracture

© A.G. Sheinerman, R.E. Shevchuk, 2023.

Publisher: Peter the Great St. Petersburg Polytechnic University

toughness and ductility of nanocrystalline Pt-Au alloys due to the formation of segregations. In these experiments, GB segregations of Au increased toughness at moderate (5 at. %) Au concentration and reduced it at high (10 at. %) Au concentration. The toughening associated with the GB segregations of Au was related [22] to the formation of secondary nanocracks at GBs containing brittle GB segregations.

Also, recent two-dimensional (2D) finite element (FE) simulations [23] of crack advance along grain or interphase boundaries that form a two-dimensional hexagonal lattice within an elastic-viscoplastic constitutive model demonstrated the possibility of fracture toughness enhancement at a moderate (up to 10-40 %) fraction of brittle boundaries followed by a drop of fracture toughness at a higher fraction of such boundaries. The toughening associated with brittle boundaries was attributed [23] to the combination of various toughening mechanisms, such as crack deflection, crack branching, the formation of secondary cracks and enhanced plastic deformation near the crack tip. However, the contributions of separate toughening mechanisms to the fracture toughness enhancement were not evaluated. Also, other FE simulations studied similar effects of toughening [24-29] associated with the structural inhomogeneities, such as bimodal grain size distribution [24], the formation of elongated grains [25], or inhomogeneous residual stresses [27].

More recently, the contribution of crack deflection to the fracture toughness of nanocrystalline alloys with GB segregations has been theoretically studied within a 2D analytical model [30]. It appeared [30] that crack deflection can increase the fracture toughness by up to 30–35 %, and the maximum toughening is achieved if segregations are very brittle and occupy a moderate proportion of GBs. The aim of the present paper is to reveal the effects of secondary (satellite) nanocracks formed near the tip of the main crack due to the presence of brittle GB segregations on the fracture energy and toughness of nanocrystalline alloys. In the following, we suggest a 2D model that describes the toughening effect of the satellite nanocracks and describe the results of our FE simulations of the fracture energy of nanocrystaline alloys with GB segregations.

Model

Consider the effect of GB segregations on the fracture energy and toughness of nanocrystalline alloys. To do so, within our 2D model, we examine a bar of infinite length and a rectangular cross section under the plane strain state and introduce a precrack with the initial half-length l_0 =0.4 µm, which is much smaller than the dimensions of the bar (Fig. 1). The bar is supposed to be loaded by a tensile load that corresponds to specified constant displacements at the upper and lower boundaries, and the direction of the initial crack is assumed to be normal to the direction of the applied load (Fig. 1). A symmetry condition is set on the left boundary of the bar, that is, the displacement in the direction normal to the boundary is prohibited, and the right boundary is assumed to be free. The displacements at the upper and lower boundaries are set small enough to prevent the cracking of GBs far from the crack tip, and the material is assumed to be linearly elastic and elastically isotropic.

In the vicinity of the tip of the initial crack, on the way of its further advance during the bar tension, there is a region simulating the grain structure. In order to reduce computational costs, the rest of the bar far from the crack tip is modeled as a homogeneous material, due to the relatively low influence of this region on the critical parameters of crack growth.

To generate a representative volume of the grain structure with the size Δa_{max} =0.4 µm located near the precrack tip, algorithms were used to construct a Voronoi diagram. The characteristic average grain width is assumed to be 50 nm, which corresponds to the experimental values for the nanocrystalline Pt-Au alloy with GB segregations [22].

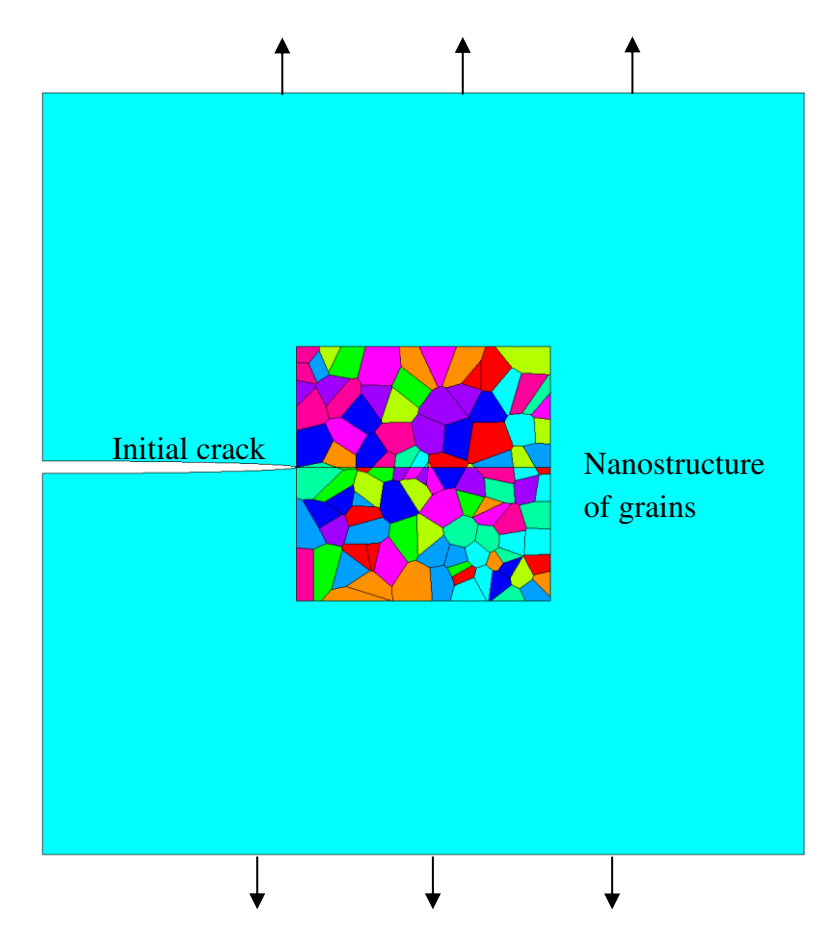


Fig. 1. Finite element model in the region near the initial crack tip, containing a nanostructure of grains

All calculations were performed in the ANSYS FE analysis system. The Young modulus E and Poisson's ratio v of the solid were put equal to the characteristic values of those for the Pt-10Au (at. %) nanocrystalline alloy examined in [22]: E=145 GPa, v=0.4 [31]. To construct a computational model of grains and a homogeneous region of the bar, flat elements in the plane strain state were used. To increase the accuracy of numerical calculations, when constructing a finite element mesh, finite elements with a quadratic function for approximating the displacements were used.

For simplicity, here we do not consider the effect of crack deflection on fracture toughness (assuming that the initial crack stays flat during growth) and focus on the effect of the secondary nanocracks at GBs (whose formation near the precrack tip is enhanced due to the presence of brittle GB segregations) on the growth of the initial crack. To simulate the formation of nanocracks at GBs as well as the growth of the initial crack, we define interface elements of the CZM (cohesive zone model) type at GBs and on the extension of the main crack; in the unloaded state, their thickness is equal to zero. During loading of the bar, the interface elements are elastically deformed along with the grains, and when the jump of displacements exceeds a critical value, they fracture.

The interface elements divide two contacting surfaces and are characterized by the surface potential that describes the additional total energy of the surfaces (per their unit area) associated with their separation and sliding. The surface potential φ is defined in the form originally proposed in [32] as

$$\varphi(\delta_n, \delta_t) = e\sigma_{max}\bar{\delta}_n \left[1 - (1 + \Delta_n)e^{-\Delta_n}e^{-\Delta_t^2}\right],\tag{1}$$

where $\Delta_n = \delta_n/\bar{\delta}_n$, $\Delta_t = \delta_t/\bar{\delta}_t$, σ_{max} is cohesive strength of the interface, δ_n and δ_t are the normal and tangential jumps of displacements at the interface element, respectively, and $\bar{\delta}_n$ and $\bar{\delta}_t$ are parameters. The maximum value of the surface potential $\varphi_{max} = \varphi(\delta_n \to \infty, \delta_t) = e\sigma_{max}\bar{\delta}_n$ corresponds to the specific work of normal separation of the two surfaces. The surface potential $\varphi(\delta_n, \delta_t)$ decreases with the normal separation δ_n at $\delta_n > \bar{\delta}_n$. This implies that once the relation $\delta_n > \bar{\delta}_n$ is satisfied, the contacting surfaces are energetically favored to be separated, and thus, the fracture at an interface element occurs in the region where $\delta_n > \bar{\delta}_n$. We put $\bar{\delta}_n = 1$ nm, $\bar{\delta}_t = 2$ nm.

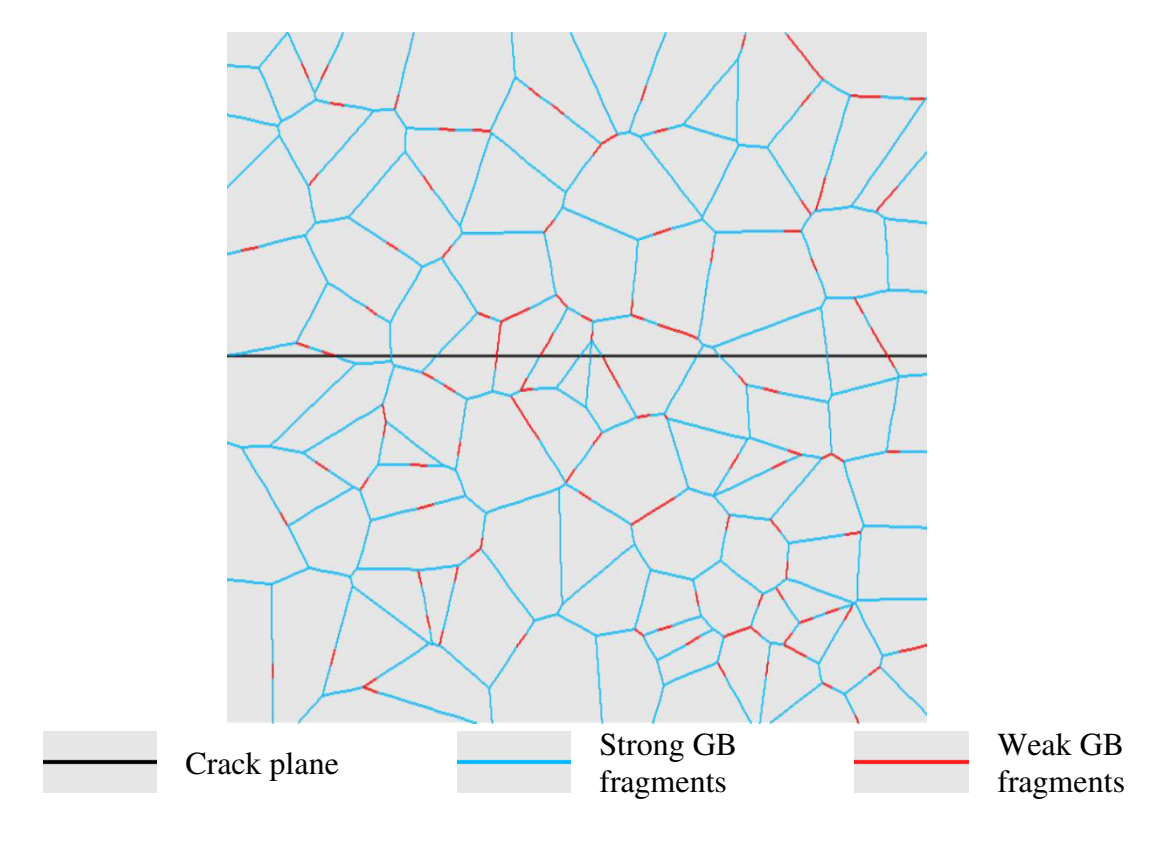


Fig. 2. The geometry of strong and weak GB fragments in the representative volume

GB segregations in the grain structure are modeled as interface elements with a strongly reduced cohesive strength σ_{max} (see Fig. 2). Focusing on the case where the fragments of GBs with segregations are very brittle, we set the value σ_{max} for the "weak" interface elements (that model GB segregations) to be 5 times smaller than that for "strong" interface elements (without GB segregations).

Let us denote the proportion c of weak GB fragments (containing GB segregations) as the ratio of the total length of weak GB fragments to the total length of GBs in the representative volume. The location of weak GB fragments is chosen randomly depending on their proportion c. Figure 2 illustrates one of the possible arrangements of strong and weak GB fragments for the case c = 15 %.

The simulation of main crack growth was carried out as follows. The bar is loaded using kinematic boundary conditions, and thus the initial stress field appears in the bar. Then, sequentially, element by element, the interface elements that make up the region in which the main crack propagates are removed. During the growth of the main crack, the interface elements in GBs can be destroyed when the critical parameters (the jumps of displacements at the elements) exceed critical values, and, thus, new nanocracks can form. The removal of interface elements was carried out using the Ekill method, which reduces the stiffness of the

required final element to a negligible value. Each step of the solution is recorded, and at all iterations of the numerical solution the value of the strain energy E, which is released during the growth of the main crack, is calculated. The magnitude of the specified displacements at the upper and lower boundaries is fixed, and so a change in the strain energy can only be caused by an increase in the length of the main crack, as well as by the formation of new nanocracks at GBs. The energy release rate G in the course of main crack growth is given by G = -dE/da, where a is the crack length.

Results

Figure 3 plots the dependences of the energy release rate G on the crack length increment Δa within the representative volume at various proportions c of weak GB fragments, calculated for some random configurations. The reason for the sharp decrease of the parameter G as the crack tip penetrates into the heterogeneous region and its increase as the crack exits the heterogeneous region is the formation of GB nanocracks as the main crack grows. The non-monotonic character of the curves in Fig. 3 in the interval $0.12 < \Delta a < 0.32 \,\mu m$ is related to the approaching the main crack tip to GB nanocracks or moving it away from such nanocracks.

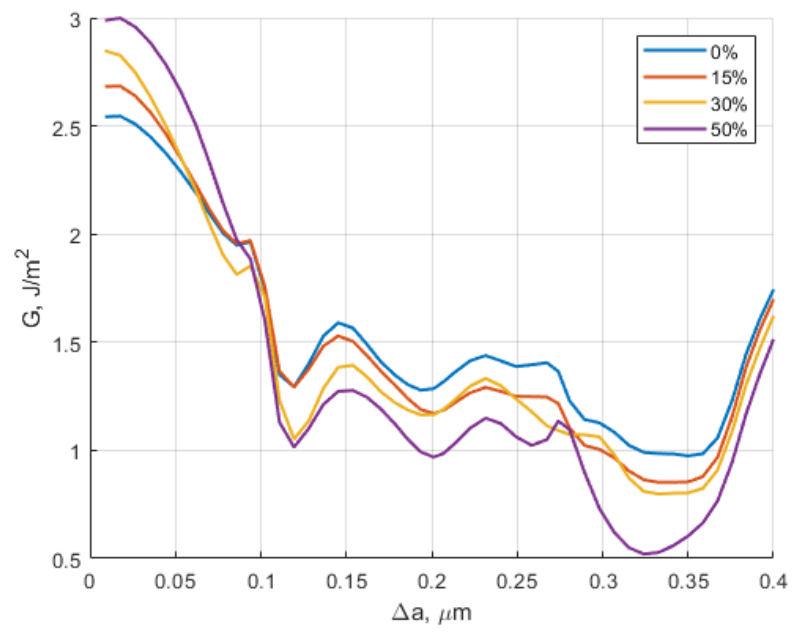


Fig. 3. Energy release rate G as a function of crack length increment Δa , for various values of the proportion c of weak GB fragments

In the absence of GB nanocracks, the critical condition for main crack growth has the form $G = G_{c0}$, where G_{c0} is the intrinsic fracture energy, which is determined by the surface energy of the solid. On the other hand, to a remote observer, the crack advances in a homogeneous medium and is characterized by the energy release rate G_0 that depends on the applied load and the crack length. Macroscopically, the crack growth condition has the form $G_0 = G_c$, where G_c is the effective fracture energy that accounts for the effect of GB nanocracks. As a result, when the energy release rate G is close to the intrinsic fracture energy G_{c0} , we have: $G_c / G_{c0} = G_0 / G$. To calculate the fracture toughness associated with crack growth over strong and weak GBs, we will consider the strongest GB along which crack propagation is most difficult and calculate the fracture energy as $G_c = \max\{(G_0 / G)G_{c0}, l_0 \le a \le l_0 + \Delta a_{\max}\}$.

Using such a calculation procedure, the fracture energy G_c was calculated for c=0,15, 30 and 50 %. Due to the influence of the random location of weak GB fragments on the results obtained, for each value of c, the values of the fracture energy G_c were averaged for 10 different arrangements of weak GB fragments. In this case, the geometry of GBs remains unchanged, and only the location of weak GBs varies.

Figure 4 shows the normalized fracture energy $G_c/G_c(c=0)$ for different proportions c of weak GB fragments. It is seen in Fig. 4 that fracture energy increases with c, and for c=50 %, an increase in the fracture energy is around 18 %. Since the fracture energy G_c is proportional to the squared fracture toughness, K_{IC}^2 , this corresponds to an increase in the fracture toughness by approximately 9 %. This implies that the formation of nanocracks at weak GBs with segregations can toughen nanocrystalline alloys and the maximum fracture toughness can be achieved when the proportion of GBs with segregations is sufficiently high. At the same time, the proportion of GBs with segregations should not exceed the values at which such brittle boundaries form clusters leading to catastrophic fracture.

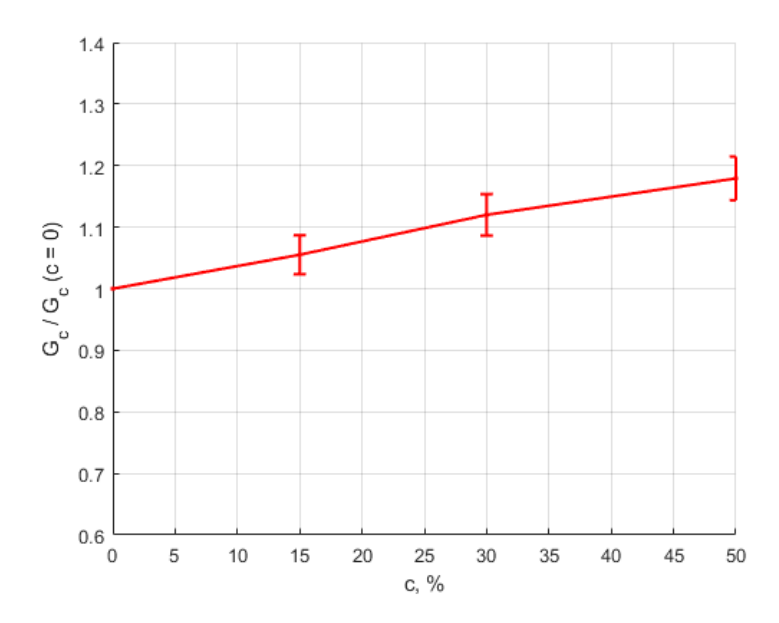


Fig. 4. Normalized fracture energy $G_c / G_c (c = 0)$ vs the proportion c of weak GB fragments

Concluding remarks

Thus, in the present paper, we have proposed a 2D model that describes the toughening due to GB solute segregations in nanocrystalline alloys. Within the model, we focused on the toughening associated with the formation of GB nanocracks at the sites for GB segregations near the tip of the main crack. These nanocracks affect the growth of the main crack and can lead to toughening. The toughening associated with the GB nanocracks is not high. For the case where GB segregations occupy 50 % of the total GB length, the fracture energy increases due to GB segregations by 18 %, which corresponds to 9 % increase in fracture toughness. However, together with other toughening mechanisms, such as crack deflection [23,30] and crack branching [23], a high enough proportion of GB segregations can considerably toughen nanocrystalline alloys [23,30]. The model is valid for the case where the fraction of the GB segregations does not exceed the values at which such brittle GBs form clusters leading to catastrophic fracture. The results of the model correlate with the experimental observations [22] of Pt-Au alloys, where GB segregations of Au led to toughening.

References

- 1. Meyers MA, Mishra A, Benson DJ. Mechanical properties of nanocrystalline materials. *Progr. Mater. Sci.* 2006;51: 427–556.
- 2. Ovid'ko IA, Valiev RZ, Zhu YT. Review on superior strength and enhanced ductility of metallic nanomaterials. *Progr. Mater. Sci.* 2018;94: 462–540.
- 3. Haché M, Cheng C, Zou Y. Nanostructured high-entropy materials. *J. Mater. Res.* 2020;35: 1051–1075.
- 4. Kushwaha AK, John M, Misra M, Menezes PL. Nanocrystalline materials: Synthesis, characterization, properties, and applications. *Crystals*. 2021;11: 1317.
- 5. Li H, Wang P, Wen C. Recent progress on nanocrystalline metallic materials for biomedical applications. *Nanomaterials*. 2022;12: 2111.
- 6. Valiev RZ, Straumal B, Langdon TG. Using severe plastic deformation to produce nanostructured materials with superior properties. *Ann. Rev. Mater. Res.* 2022;52: 357–382.
- 7. Liu F, Kirchheim R. Nano-scale grain growth inhibited by reducing grain boundary energy through solute segregation. *J. Cryst. Growth.* 2004;264: 385–391.
- 8. Chookajorn T, Murdoch HA, Schuh CA. Design of stable nanocrystalline alloys. *Science*. 2012;337: 951–954.
- 9. Lejček P, Všianská M, Šob M. Recent trends and open questions in grain boundary segregation. *J. Mater. Res.* 2018;33: 2647–2660.
- 10. Tuchinda N, Schuh CA. Grain size dependencies of intergranular solute segregation in nanocrystalline materials. *Acta Mater*. 2022;226: 117614.
- 11. Perrin AE, Schuh CA. Stabilized nanocrystalline alloys: The intersection of grain boundary segregation with processing science. *Ann. Rev. Mater. Res.* 2021;51: 241–268.
- 12. Kim JG, Enikeev NA, Seol JB, Abramova MM, Karavaeva MV, Valiev RZ, Park CG, Kim HS. Superior strength and multiple strengthening mechanisms in nanocrystalline TWIP steel. *Sci. Rep.* 2018;8: 11200.
- 13. Ke X, Ye J, Pan Z, Geng J, Besser MF, Qu D, Caro A, Marian J, Ott RT, Wang YM, Sansoz F. Ideal maximum strengths and defect-induced softening in nanocrystalline-nanotwinned metals. *Nat. Mater.* 2019;18: 1207–1214.
- 14. Hu J, Shi YN, Sauvage X, Sha G, Lu K, Grain boundary stability governs hardening and softening in extremely fine nanograined metals. *Science*. 2017;355: 1292–1296.
- 15. Valiev RZ, Enikeev NA, Murashkin MY, Kazykhanov YU, Sauvage X. On the origin of the extremely high strength of ultrafine-grained Al alloys produced by severe plastic deformation. *Scripta Mater.* 2010;63: 949–952.
- 16. Chang KI, Hong SI. Effect of sulphur on the strengthening of a Zr-Nb alloy. *J. Nucl. Mater.* 2008;373: 16–21.
- 17. Sheinerman AG. Strengthening of nanocrystalline alloys by grain boundary segregations. *Mater. Phys. Mech.* 2022;50(2): 193–199.
- 18. Turlo V, Rupert TJ. Grain boundary complexions and the strength of nanocrystalline metals: Dislocation emission and propagation. *Acta Mater.* 2018;151: 100–111.
- 19. Pan Z, Sansoz F. Heterogeneous solute segregation suppresses strain localization in nanocrystalline Ag-Ni alloys. *Acta Mater*. 2020;200: 91100.
- 20. Babicheva RI Bachurin DV, Dmitriev SV, Zhang Y, Kok SW, Bai L, Zhou K. Elastic moduli of nanocrystalline binary Al alloys with Fe, Co, Ti, Mg and Pb alloying elements. *Philos. Mag.* 2016;96: 1598–1612.
- 21. Babicheva RI, Dmitriev SV, Bachurin DV, Srikanth N, Zhang Y, Kok SW, Zhou K. Effect of grain boundary segregation of Co or Ti on cyclic deformation of aluminium bi-crystals. *Int. J. Fatigue*. 2017; 102: 270–281.
- 22. Heckman NM, Foiles SM, O'Brien CJ, Chandross M, Barr CM, Argibay N, Hattar K, Lu P, Adams DP, Boyce BL. New nanoscale toughening mechanisms mitigate embrittlement in binary nanocrystalline alloys. *Nanoscale*. 2018;10: 21231.

- 23. Chiu E, Demkowicz MJ, Srivastava A. Toughening of interface networks through the introduction of weak links. *Acta Mater*. 2021;215: 117090.
- 24. Molkeri A, Srivastava A, Osovski S, Needleman A. Influence of grain size distribution on ductile intergranular crack growth resistance. *J. Appl. Mech.* 2020;87: 031008.
- 25. Osovski S, Needleman A, Srivastava A. Intergranular fracture prediction and microstructure design. *Int. J. Fract.* 2019;216: 135–148.
- 26. Guo X, Chang K, Chen L, Zhou M. Determination of fracture toughness of AZ31 Mg alloy using the cohesive finite element method. *Eng. Fract. Mech.* 2012;96: 401–415.
- 27. De La Osa MR, Estevez R, Olagnon C, Chevalier J, Tallaron C. Cohesive zone model for intergranular slow crack growth in ceramics: influence of the process and the microstructure. Model. *Simul. Mater. Sci. Eng.* 2011;19: 074009.
- 28. Abid N, Pro JW, Barthelat F. Fracture mechanics of nacre-like materials using discrete-element models: Effects of microstructure, interfaces and randomness. *J. Mech. Phys. Sol.* 2019;124: 350–365.
- 29. Pro JW, Barthelat F. Discrete element models of fracture in tooth enamel: Failure mode competition and statistical effects. *J. Mech. Phys. Sol.* 2020;137: 103868.
- 30. Sheinerman AG. Modeling the effect of grain boundary segregations on the fracture toughness of nanocrystalline and ultrafine-grained alloys. *Metals*. 2023;13: 1295.
- 31. Kelly PF. Properties of Materials. CRC Press; 2014.
- 32. Xu XP, Needleman A. Numerical simulations of fast crack growth in brittle solids. *J. Mech. Phys. Sol.* 1994;42: 1397–1434.

THE AUTHORS

Sheinerman A.G. 🗓

e-mail: asheinerman@gmail.com

Shevchuk R.E.

e-mail: re.shevchuk@gmail.com

Elastic properties of additively produced metamaterials based on lattice structures

Submitted: September 4, 2023

Approved: September 25, 2023

Accepted: November 3, 2023

A.I. Borovkov ¹, L.B. Maslov ¹, M.A. Zhmaylo ¹, F.D. Tarasenko ¹, L.S. Nezhinskaya ¹

Abstract. The paper considers seven types of lattice structures of different topologies, which are periodic unit cells of metamaterials to be manufactured by additive technologies. We carried out finite-element analysis of lattice structures with varying thicknesses of elementary beams comprising the cells and varying initial symmetric shapes. The effective elastic properties of metamaterials as continuous media were calculated by the method of direct numerical homogenization with periodic boundary conditions. The dependences between elastic properties and characteristic parameters determining the topology of cells were established. Some types of lattices were found to exhibit auxetic properties in a certain range of topological parameters.

Keywords: metamaterials; lattice structures; elastic moduli; finite element analysis; homogenization

Acknowledgements. This work has been supported by the Russian Science Foundation grant No. 23-19-00882, https://rscf.ru/project/23-19-00882/.

Citation: Borovkov AI, Maslov LB, Zhmaylo MA, Tarasenko FD, Nezhinskaya LS. Elastic properties of additively produced metamaterials based on lattice structures. *Materials Physics and Mechanics*. 2023;51(7): 42-62. DOI: 10.18149/MPM.5172023_6.

Introduction

Over the last decade, additive technologies, as a group of manufacturing technologies with a wide range of capabilities and few limitations, have made it possible to produce complex metal and polymer parts and components that could not previously be produced by conventional material processing technologies [1]. Metamaterials, whose physical and mechanical properties can be controlled by changing the shape and parameters of a unit cell, are an example of such structures.

Metamaterials are understood as artificially designed multiscale structures formed by periodically repeating basic cells of relatively small size, fine-tuned to ensure that the physical and mechanical behaviour of the structure at the macro-level is that of a continuous material. A characteristic example of a metamaterial is a periodic lattice structure, which is formed by duplicating a unit cell in the directions of three non-coplanar vectors on which a parallelepiped describing the boundary of the unit cell is built [2]. Such a structure has a three-dimensional periodic topology, whose step of repetition depends on the geometric dimensions of the unit cell. The metamaterials can also include porous media with a complicated multiscale system of pore channels [3].

© A.I. Borovkov, L.B. Maslov, M.A. Zhmaylo, F.D. Tarasenko, L.S. Nezhinskaya, 2023. Publisher: Peter the Great St. Petersburg Polytechnic University

Since typical unit cells have complex topology, the parts integrating metamaterials can only be manufactured by additive technologies, primarily powder-based laser 3D printing. It is the specific topology and variable shape of the elementary structural cell that gives the metamaterial unique physical and mechanical properties at the macro-level, unattainable for conventional homogeneous materials. In this case, the elastic properties of the metamaterial at the macro-level are assumed to be the effective properties of the structural cell as a part of a periodic array along three axes of the global coordinate system. Thus, a metamaterial can be characterized as an additively produced material consisting of a large number of unit cells whose size is much smaller than the size of a part made of the metamaterial.

The effective physical and mechanical properties of the metamaterial, which are considerably different from the properties of the solid material from which the periodic structure is fabricated, can be determined using the homogenization procedure performed for the representative volume element (RVE) of the metamaterial [4]. In the case of a metamaterial formed by arrays of unit cells along three Cartesian axes, the RVE is a structure of minimal volume, containing the characteristic geometry of the material repeating with a certain step, so it can be regarded as a periodicity cell from the standpoint of theory of heterogeneous and composite materials.

The dependences of effective elastic properties of metamaterials on the topological features of the structure at the meso-level are a popular subject for research in mechanics of heterogeneous continuous media [5]. The main objective of this research is to establish the approaches to designing the mechanical properties of the structure by varying the topology of the unit cell by new unconventional techniques [6]. In particular, the numerical analysis of the mechanical properties of the unit cell was carried out in [7] by the homogenization method with varying topological parameters of the unit cell.

Recent developments in the field of metamaterials for special applications are outlined in [8], covering ultra-lightweight, ultra-stiff and ultra-strong materials, with emphasis placed on metamaterials with negative compressibility and negative stiffness. The current understanding of the structure and mechanical behaviour of cellular materials with low effective density, and how they can be used in the design of engineering structures, is discussed in [9].

Numerous studies deal with the influence of topological properties of metamaterials on their mechanical performance, considering different types of unit cells with varied effective porosity [10]. Some papers introduce hypotheses about the analytical dependences between the mechanical constants and the effective porosity obeying a power law [11]. However, such dependencies do not take into account a wide range of parameters of the unit cell.

Beam theories based on the Bernoulli–Euler model have been applied to evaluating the macroscopic properties of lattice struts, allowing to predict some of the properties without virtual tests [12]. The analytical description of the mechanical behaviour of unit cells using the Timoshenko beam theory is presented in [13]. However, the applicability of these approaches is strongly limited to regular cells of relatively simple shape represented in the beam formulation.

An important point in the study of additively manufactured metamaterials is the influence of technological processes during their fabrication. In particular, a significant decrease in the mechanical strength was detected for samples built diagonally with respect to the printing direction, accompanied by transformation of the material microstructure during heat treatment [14].

A notable trend in research is to determine the effective distribution of topological parameters of a metamaterial over the volume of a product. In this case, the focus shifts from the search for the optimal shape and size of the unit cell to the search for the optimal distribution of the physical and mechanical parameters within the product to achieve their smooth spatial variation [15]. This approach allows to tailor certain areas of the product to the given operating conditions and control the macroscopic properties of the material depending on the internal forces in a particular area of the structure [16].

A separate extremely interesting class is represented by metamaterials with negative effective Poisson's ratio, the so-called auxetics [17]. According to [18], unit cells capable of generating the auxetic effect are divided into three main groups based on the mechanism underlying that effect: re-entrant cells, chiral cells, and rotating cells. Importantly, the first group is the most promising from the standpoint of manufacturing technologies, including additive manufacturing, since the cells of the second group have a more complex structure, and the cells of the third group comprise structures connected through hinges, so they should be produced by other types of manufacturing technologies. A detailed analysis of the approaches to design of cell struts for auxetic metamaterials and examples of numerical analysis of their mechanical behaviour are given in [19].

As evident from the reviewed literature, interest in metamaterials has been growing steadily over the recent years, and the directions of research are diverse. While there are multiple approaches to studying the mechanical characteristics in this type of structures, the main issue has not been fully resolved. Building on our previous works on lattice structures [20], in this paper, we adopt homogenization methods to carry out numerical calculations of elastic anisotropic properties of metamaterials formed by different types of unit cells, subsequently analysing the relationship between the metamaterial's elastic moduli and topology parameters.

Materials and Methods

The geometry of metamaterials has a periodic structure similar to conventional metallic materials grains formed by crystal lattices. We focus on metamaterials formed by typical lattice structures in this study, and the research methods are based on composite mechanics, elasticity theory of anisotropic media and computational mechanics.

Theoretical aspects of homogenization. Homogenization is a method for estimating the equivalent macroscopic properties of a homogeneous material in such a way that at the global level they are equivalent to the properties of the heterogeneous metamaterial. Such properties of the metamaterial are called effective properties. The results obtained for one cell can be generalized for the whole material due to its periodic structure.

The stresses and strains averaged over a representative volume element are determined by the following formulas:

$$\langle \sigma_{ij} \rangle = \frac{1}{V} \int_{V} \sigma_{ij} dV, \langle \varepsilon_{ij} \rangle = \frac{1}{V} \int_{V} \varepsilon_{ij} dV, \langle \gamma_{ij} \rangle = \frac{1}{V} \int_{V} \gamma_{ij} dV,$$
where *V* is the volume of the RVE.

The stresses and strains averaged over the RVE of the metamaterial as assumed to be a homogeneous orthotropic material are related by the equations of generalized Hooke's law written in terms of the principal axes of material symmetry X, Y and Z of the stress and strain tensors:

$$E_{x}\langle \varepsilon_{xx}\rangle = \langle \sigma_{xx}\rangle - \nu_{xy}\langle \sigma_{yy}\rangle - \nu_{xz}\langle \sigma_{zz}\rangle,$$

$$E_{y}\langle \varepsilon_{yy}\rangle = -\nu_{yx}\langle \sigma_{xx}\rangle + \langle \sigma_{yy}\rangle - \nu_{yz}\langle \sigma_{zz}\rangle,$$

$$E_{z}\langle \varepsilon_{zz}\rangle = -\nu_{zx}\langle \sigma_{xx}\rangle - \nu_{zy}\langle \sigma_{yy}\rangle + \langle \sigma_{zz}\rangle,$$

$$G_{xy}\langle \gamma_{xy}\rangle = \langle \sigma_{xy}\rangle,$$

$$G_{yz}\langle \gamma_{yz}\rangle = \langle \sigma_{yz}\rangle,$$

$$G_{xz}\langle \gamma_{xz}\rangle = \langle \sigma_{xz}\rangle,$$
(2)

here E_x , E_y and E_z are the effective Young's moduli of the unit cell; v_{xy} , v_{yx} , v_{yz} , v_{zy} , v_{xz} and v_{zx} are the effective Poisson's ratios; G_{xy} , G_{yz} and G_{xz} are the effective shear moduli.

The expressions of the effective Poisson's ratios can be formulated as follows:

$$\nu_{xy} = \frac{\langle \varepsilon_{yy} \rangle}{\langle \varepsilon_{xx} \rangle}, \nu_{yx} = \frac{\langle \varepsilon_{xx} \rangle}{\langle \varepsilon_{yy} \rangle}, \nu_{yz} = \frac{\langle \varepsilon_{zz} \rangle}{\langle \varepsilon_{yy} \rangle}, \nu_{zy} = \frac{\langle \varepsilon_{yy} \rangle}{\langle \varepsilon_{zz} \rangle}, \nu_{zx} = \frac{\langle \varepsilon_{xx} \rangle}{\langle \varepsilon_{zz} \rangle}, \nu_{xz} = \frac{\langle \varepsilon_{zz} \rangle}{\langle \varepsilon_{xx} \rangle}.$$
(3)

According to the properties of orthotropic material models, only nine of the twelve material constants are independent, since there are three additional relationships between Poisson's ratios and Young's moduli:

$$E_x \nu_{yx} = E_y \nu_{xy}, E_y \nu_{zy} = E_z \nu_{yz}, E_z \nu_{xz} = E_x \nu_{zx}. \tag{4}$$

The compliance matrix [C] relating strains and stresses is based on material constants E_x , E_y , E_z , G_{xy} , G_{yz} , G_{xz} , v_{xy} , v_{yz} and v_{xz} and has the form:

$$[C] = \begin{pmatrix} \frac{1}{E_x} & -\frac{v_{yx}}{E_y} & -\frac{v_{zx}}{E_z} & 0 & 0 & 0\\ -\frac{v_{xy}}{E_x} & \frac{1}{E_y} & -\frac{v_{zy}}{E_z} & 0 & 0 & 0\\ -\frac{v_{xz}}{E_x} & -\frac{v_{yz}}{E_y} & \frac{1}{E_z} & 0 & 0 & 0\\ 0 & 0 & 0 & \frac{1}{G_{xy}} & 0 & 0\\ 0 & 0 & 0 & 0 & \frac{1}{G_{yz}} & 0\\ 0 & 0 & 0 & 0 & 0 & \frac{1}{G_{xz}} \end{pmatrix}.$$

$$(5)$$

In addition to form (2), Hooke's law can be written in the form, which is more common for continuum mechanics as an expression of stress through strain:

$$\begin{pmatrix}
\langle \sigma_{xx} \rangle \\
\langle \sigma_{yy} \rangle \\
\langle \sigma_{zz} \rangle \\
\langle \sigma_{xy} \rangle \\
\langle \sigma_{yz} \rangle \\
\langle \sigma_{xz} \rangle
\end{pmatrix} = \begin{pmatrix}
D_{11} & D_{12} & D_{13} & 0 & 0 & 0 \\
D_{21} & D_{22} & D_{23} & 0 & 0 & 0 \\
D_{31} & D_{32} & D_{33} & 0 & 0 & 0 \\
0 & 0 & 0 & D_{44} & 0 & 0 \\
0 & 0 & 0 & 0 & D_{55} & 0 \\
0 & 0 & 0 & 0 & 0 & D_{66}
\end{pmatrix} \cdot \begin{pmatrix}
\langle \varepsilon_{xx} \rangle \\
\langle \varepsilon_{yy} \rangle \\
\langle \varepsilon_{zz} \rangle \\
\langle \gamma_{xy} \rangle \\
\langle \gamma_{xz} \rangle
\end{pmatrix}, (6)$$

where [D] is the stiffness matrix that corresponds to the 4th-rank tensor of elastic moduli and is the inverse of the compliance matrix:

$$[D] = [C]^{-1}. (7)$$

Six numerical tests are required to determine the independent constants: three uniaxial tension tests and three shear tests. When each test is considered separately, relation (6) takes a simplified form, where $\langle \sigma_{ij}^x \rangle$, $\langle \sigma_{ij}^y \rangle$ and $\langle \sigma_{ij}^z \rangle$ are the stresses in uniaxial tensile tests along axes X, Y and Z respectively, $\langle \sigma_{ij}^{xy} \rangle$, $\langle \sigma_{ij}^{yz} \rangle$ and $\langle \sigma_{ij}^{xz} \rangle$ are the stresses in the shear tests in planes XY, YZ and ZX respectively (here $i, j \in \{x, y, z\}$):

$$A \begin{pmatrix} D_{11} \\ D_{21} \\ D_{31} \\ 0 \\ 0 \end{pmatrix} = \begin{pmatrix} \langle \sigma_{xx}^{x} \rangle \\ \langle \sigma_{yy}^{x} \rangle \\ \langle \sigma_{zz}^{x} \rangle \\ 0 \\ 0 \end{pmatrix}, A \begin{pmatrix} D_{12} \\ D_{22} \\ D_{32} \\ 0 \\ 0 \\ 0 \end{pmatrix} = \begin{pmatrix} \langle \sigma_{xx}^{y} \rangle \\ \langle \sigma_{yy}^{y} \rangle \\ \langle \sigma_{yy}^{y} \rangle \\ \langle \sigma_{zz}^{y} \rangle \\ 0 \\ 0 \\ 0 \end{pmatrix}, A \begin{pmatrix} D_{13} \\ D_{23} \\ D_{33} \\ 0 \\ 0 \\ 0 \end{pmatrix} = \begin{pmatrix} \langle \sigma_{xx}^{z} \rangle \\ \langle \sigma_{yy}^{z} \rangle \\ \langle \sigma_{zz}^{z} \rangle \\ 0 \\ 0 \\ 0 \end{pmatrix}, A \begin{pmatrix} D_{13} \\ D_{23} \\ D_{33} \\ 0 \\ 0 \\ 0 \\ 0 \end{pmatrix} = \begin{pmatrix} \langle \sigma_{xx}^{z} \rangle \\ \langle \sigma_{yy}^{z} \rangle \\ \langle \sigma_{zz}^{z} \rangle \\ 0 \\ 0 \\ 0 \end{pmatrix}, A \begin{pmatrix} D_{13} \\ D_{23} \\ D_{23} \\ D_{23} \\ 0 \\ 0 \\ 0 \end{pmatrix} = \begin{pmatrix} \langle \sigma_{xx}^{z} \rangle \\ \langle$$

$$A \begin{pmatrix} 0 \\ 0 \\ 0 \\ D_{44} \\ 0 \\ 0 \end{pmatrix} = \begin{pmatrix} 0 \\ 0 \\ \langle \sigma_{xy}^{xy} \rangle \\ 0 \\ 0 \end{pmatrix}, A \begin{pmatrix} 0 \\ 0 \\ 0 \\ 0 \\ D_{55} \\ 0 \end{pmatrix} = \begin{pmatrix} 0 \\ 0 \\ 0 \\ 0 \\ \langle \sigma_{yz}^{yz} \rangle \\ 0 \end{pmatrix}, A \begin{pmatrix} 0 \\ 0 \\ 0 \\ 0 \\ D_{66} \end{pmatrix} = \begin{pmatrix} 0 \\ 0 \\ 0 \\ 0 \\ \langle \sigma_{xz}^{xz} \rangle \end{pmatrix}, \tag{9}$$

where A is the value of longitudinal strain along one of the principal orthotropy axes or under shear in one of the principal orthotropy planes. The value of A here and below is taken equal to 0.001.

The averaged stresses during numerical homogenization are taken as the ratio of the force F_k , arising under deformation of the unit cell and applied to its face, to the area of this face S:

$$\left\langle \sigma_{ij}^{k}\right\rangle = \frac{F_{k}}{S},\tag{10}$$

where $i, j \in \{x, y, z\}, k \in \{x, y, z, xy, yz, xz\}.$

The index k in formula (10) corresponds to the test conducted: x is the tension along the X axis, y is the tension along the Y axis, z is the tension along the Z axis, xy is the shear in the XY plane, yz is the shear in the YZ plane, xz is the shear in the XZ plane.

The unknown components of the stiffness matrix D_{ij} can be obtained based on the results of the six tests:

$$[D] = \begin{pmatrix} D_{11} & D_{12} & D_{13} & 0 & 0 & 0 \\ D_{21} & D_{22} & D_{23} & 0 & 0 & 0 \\ D_{31} & D_{32} & D_{33} & 0 & 0 & 0 \\ 0 & 0 & 0 & D_{44} & 0 & 0 \\ 0 & 0 & 0 & 0 & D_{55} & 0 \\ 0 & 0 & 0 & 0 & 0 & D_{66} \end{pmatrix}.$$

$$(11)$$

Next, the compliance matrix components can be found in accordance with Eq. (7). After that, all unknown elastic constants can be found from Eq. (5):

$$E_{x} = \frac{1}{c_{11}}, E_{y} = \frac{1}{c_{22}}, E_{z} = \frac{1}{c_{33}},$$

$$G_{xy} = \frac{1}{c_{44}}, G_{yz} = \frac{1}{c_{55}}, G_{xz} = \frac{1}{c_{66}},$$

$$v_{xy} = -\frac{c_{21}}{c_{11}}, v_{xz} = -\frac{c_{31}}{c_{11}}, v_{yz} = -\frac{c_{32}}{c_{22}}.$$
(12)

Because the metamaterial is a periodic structure, numerical experiments should be performed with boundary conditions different from the traditional ones. Periodic boundary conditions adequately describe the three-dimensional symmetry of the structure, also providing a more physical deformation of the material, since they reflect the direct mutual influence of deformation of the given cell on its neighbouring cells.

The periodic boundary conditions show the same displacements of each pair of nodes on opposite faces of the unit cell of size $L_x \times L_y \times L_z$. Three tensile tests and three shear tests were conducted to determine the material parameters under the boundary conditions described above.

The following periodic boundary conditions have to be satisfied on pairs of opposite sides of the RVE, respectively, to perform three numerical uniaxial tensile tests sequentially along the X, Y, and Z axes.

Tension along the *X* axis:

$$\mathbf{u}|_{x=0} - \mathbf{u}|_{x=L_x} = A\mathbf{i}, \, \mathbf{u}|_{y=0} - \mathbf{u}|_{y=L_y} = 0, \, \mathbf{u}|_{z=0} - \mathbf{u}|_{z=L_z} = 0.$$
(13)

Tension along the *Y* axis:

$$\mathbf{u}|_{x=0} - \mathbf{u}|_{x=L_x} = 0, \, \mathbf{u}|_{y=0} - \mathbf{u}|_{y=L_y} = A\mathbf{j}, \, \mathbf{u}|_{z=0} - \mathbf{u}|_{z=L_z} = 0.$$
(14)

Tension along the Z axis:

$$\mathbf{u}|_{x=0} - \mathbf{u}|_{x=L_x} = 0, \, \mathbf{u}|_{y=0} - \mathbf{u}|_{y=L_y} = 0, \, \mathbf{u}|_{z=0} - \mathbf{u}|_{z=L_z} = A\mathbf{k}.$$
(15)

where \mathbf{u} is the displacement vector of RVE points; \mathbf{i} , \mathbf{j} and \mathbf{k} are the coordinate system basis vectors along axes X, Y and Z.

The following periodic boundary conditions have to be satisfied on pairs of opposite sides of the RVE to perform three shear tests sequentially in the XY, YZ and XZ planes.

Shear in the *XY* plane:

$$\mathbf{u}|_{x=0} - \mathbf{u}|_{x=L_x} = A\mathbf{j}, \, \mathbf{u}|_{y=0} - \mathbf{u}|_{y=L_y} = A\mathbf{i}, \, \mathbf{u}|_{z=0} - \mathbf{u}|_{z=L_z} = 0.$$
 (16)

Shear in the YZ plane:

$$\mathbf{u}|_{x=0} - \mathbf{u}|_{x=L_x} = 0, \, \mathbf{u}|_{y=0} - \mathbf{u}|_{y=L_y} = A\mathbf{k}, \, \mathbf{u}|_{z=0} - \mathbf{u}|_{z=L_z} = A\mathbf{j}.$$
(17)

Shear in the XZ plane:

$$\mathbf{u}|_{x=0} - \mathbf{u}|_{x=L_x} = A\mathbf{k}, \, \mathbf{u}|_{y=0} - \mathbf{u}|_{y=L_y} = 0, \, \mathbf{u}|_{z=0} - \mathbf{u}|_{z=L_z} = A\mathbf{i}.$$
(18)

Estimation of elastic properties of metamaterial in non-principal axes. Changing the direction of the local axes of the unit cell allows estimating the characteristics of the metamaterial in a different direction, which can have a positive effect on changing the parameters of the unit cell and the metamaterial as a whole. Specifically, the values of the elastic characteristics of the unit cell may turn out to be higher along the rotated axes, making it possible to arrange the lattice structure more rationally within the designed product and render it more resistant to applied loads. This section considers the behaviour of lattice properties when local axes of the unit cell are rotated relative to the initial orientation of the metamaterial axes (Fig. 1).

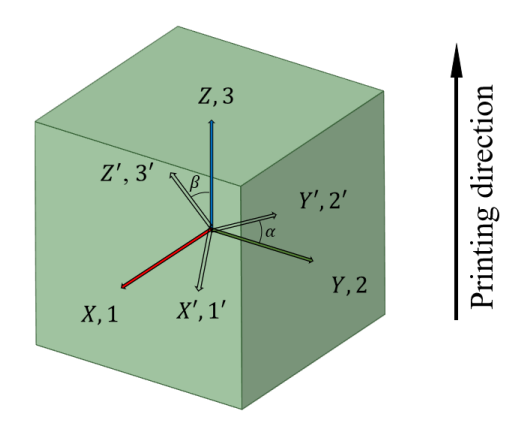


Fig. 1. Axis layout and printing direction

We "rotate" the stiffness matrix in the equation, corresponding to the 4th-rank elastic moduli tensor. The deformation directions remain unchanged.

The combination of two rotations around three orthogonal vectors X, Y, Z is taken as the rotation tensor. However, it does not seem possible to rotate a 6×6 matrix by a 3×3 rotation matrix. Instead, the 4th-rank tensor must be recovered for this purpose from the 6×6 matrix by the Voigt notation rule explained below:

the Voigt notation rule explained below:
$$\begin{pmatrix} C_{11} \rightarrow C_{1111} & C_{12} \rightarrow C_{1122} & C_{13} \rightarrow C_{1133} & C_{14} \rightarrow C_{1123} & C_{15} \rightarrow C_{1131} & C_{16} \rightarrow C_{1112} \\ C_{21} \rightarrow C_{2211} & C_{22} \rightarrow C_{2222} & C_{23} \rightarrow C_{2233} & C_{24} \rightarrow C_{2223} & C_{24} \rightarrow C_{2231} & C_{26} \rightarrow C_{2212} \\ C_{31} \rightarrow C_{3311} & C_{32} \rightarrow C_{3322} & C_{33} \rightarrow C_{3333} & C_{34} \rightarrow C_{3323} & C_{35} \rightarrow C_{3331} & C_{36} \rightarrow C_{3312} \\ C_{41} \rightarrow C_{2311} & C_{42} \rightarrow C_{2322} & C_{43} \rightarrow C_{2333} & C_{44} \rightarrow C_{2323} & C_{45} \rightarrow C_{2331} & C_{46} \rightarrow C_{2312} \\ C_{51} \rightarrow C_{3111} & C_{52} \rightarrow C_{3122} & C_{53} \rightarrow C_{3133} & C_{54} \rightarrow C_{3123} & C_{55} \rightarrow C_{3131} & C_{56} \rightarrow C_{3112} \\ C_{61} \rightarrow C_{1211} & C_{62} \rightarrow C_{1222} & C_{63} \rightarrow C_{1233} & C_{64} \rightarrow C_{1223} & C_{65} \rightarrow C_{1231} & C_{66} \rightarrow C_{1212} \end{pmatrix}$$
The 4th-rank elastic moduli tensor C_{ijkl} is symmetric with respect to the first and second

pairs of indices:

$$C_{ijkl} = C_{iikl} = C_{ijlk}. (20)$$

The elements can be written as a 6×6 matrix using the following index substitution:

$$11 \to 1; 22 \to 2; 33 \to 3; 23, 32 \to 4; 13, 31 \to 5; 12, 21 \to 6.$$
 (21)

As one Cartesian coordinate system x_1 , x_2 , x_3 is converted to another Cartesian coordinate system x'_1, x'_2, x'_3 , the components of the elastic moduli tensor are transformed as follows (the Einstein notation for summation over repeated indices is used here):

$$C'_{ijkl} = n_{i\alpha} n_{j\beta} n_{k\gamma} n_{l\delta} C_{\alpha\beta\gamma\delta}, \tag{22}$$

where n_{mn} are the directional cosines between the m, n axes, which can be determined from the formula:

$$n_{mn} = \frac{x_m \cdot x_n}{|x_m||x_n|}. (23)$$

In our case, the axes are rotated by the angle α lying in the range from 0 to 2π with the step 0.02π around the Z axis and by the angle β in the range from $-\pi/2$ to $\pi/2$ with the step 0.01π in the case of rotation around the rotated Y axis. The rotation matrices are constructed by the angles given at each step:

$$P_{z} = \begin{pmatrix} \cos\alpha & -\sin\alpha & 0\\ \sin\alpha & \cos\alpha & 0\\ 0 & 0 & 1 \end{pmatrix},\tag{24}$$

angles given at each step.
$$P_{z} = \begin{pmatrix} \cos\alpha & -\sin\alpha & 0\\ \sin\alpha & \cos\alpha & 0\\ 0 & 0 & 1 \end{pmatrix}, \qquad (24)$$

$$P_{y} = \begin{pmatrix} \cos\beta & 0 & \sin\beta\\ 0 & 1 & 0\\ -\sin\beta & 0 & \cos\beta \end{pmatrix}. \qquad (25)$$

Thus, the rotated axes can be calculated by the formula:

$$x_i' = P_y \cdot P_z \cdot x_i, i \in \{1, 2, 3\}. \tag{26}$$

The matrix of elastic moduli C'_{ijkl} is calculated from Eq. (22) in the local (rotated) coordinate system. After that, the values of elastic constants in the rotated coordinate system can be obtained by Eq. (12).

Calculating the moduli values for each of the specified angle values, we obtain a circular diagram reflecting the dependence of the considered mechanical characteristics on the direction of local axes. For convenience, matrix transformations, orthogonal rotation and other related calculations are performed with the code in MATLAB package. Such transformations were performed for each type of unit cell.

Geometric models for unit cells of the metamaterial. Geometric models of unit cells of the metamaterial are designed assuming that the basic cells can be formed by rods of different diameters and have different volume fractions of solid material. SolidWorks computer-aided design system was used to build the geometric models [21].

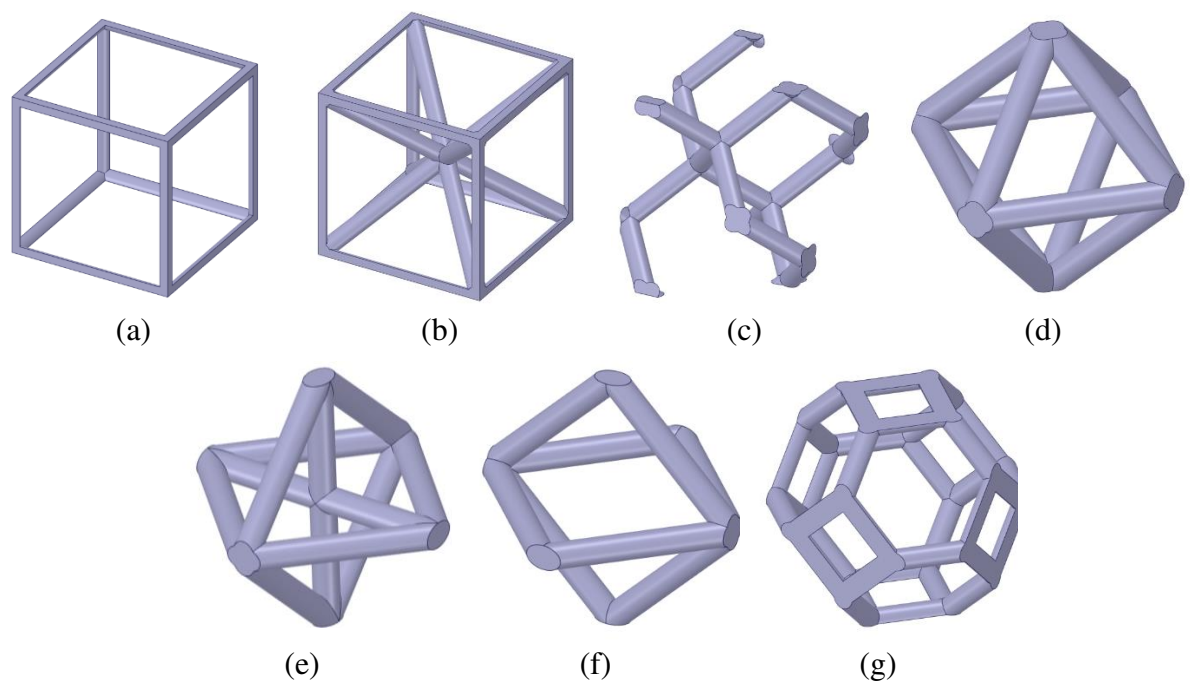


Fig. 2. Unit cells of metamaterials: (a) cell of type 1, (b) cell of type 2, (c) cell of type 3, (d) cell of type 4, (e) cell of type 5, (f) cell of type 6, (g) cell of type 7

Each cell type has the overall dimensions of $10 \times 10 \times 10$ mm. The 3D view of the designed unit cells is shown in Fig. 2. The topology of the cells was chosen as the most interesting and promising for further research. The designs presented in Fig. 2 are based on a single rod 1.0 mm in diameter.

Several modifications of the structure geometry are adopted to comprehensively analyse the influence of the metamaterial unit cell topology, as well as to correctly compare the lattices with each other.

We primarily focus on the effect of the volume fraction of the lattice structure material and the effect of the ratio of the unit cell dimensions L_x , L_y and L_z on the macroscopic properties of the metamaterial. The analysis in this section aimed to establish the dependence of the macroscopic properties of the metamaterial on its effective density for each of the seven cell types considered.

Several modifications of the structure geometry are adopted to comprehensively analyse the influence of the metamaterial unit cell topology, as well as to correctly compare the lattices with each other.

We primarily focus on the effect of the volume fraction of the lattice structure material and the effect of the ratio of the unit cell dimensions L_x , L_y and L_z on the macroscopic properties of the metamaterial. The analysis in this section aimed to establish the dependence of the macroscopic properties of the metamaterial on its effective density for each of the seven cell types considered.

The effective density of metamaterial is understood as the ratio of the volume of solid material contained in a unit cell to the volume of a parallelepiped with the characteristic size $L_x \times L_y \times L_z$. The volume fraction varies from 0.01 to 1, where 1 corresponds to solid material. The mechanical characteristics were calculated by taking 10 points in the range from 0.01 to 0.1, and then another 24 points with a constant step of 0.0375. Figures 3–9 show the geometric shapes for each of the cell types for the four volume fractions of the material.

Cells with the characteristic size $L_x = L_y = L_z = 10$ mm are considered above. Departing from the traditional understanding of a cubic unit cell, we introduce a range of variation for one of the geometrical parameters, the value of length L_x . Let us estimate the variation trends of the metamaterial parameters with varying ratio of unit cell sizes. The value of length L_x varies from 10 to 1 mm with the step of 1 mm for each cell under consideration.

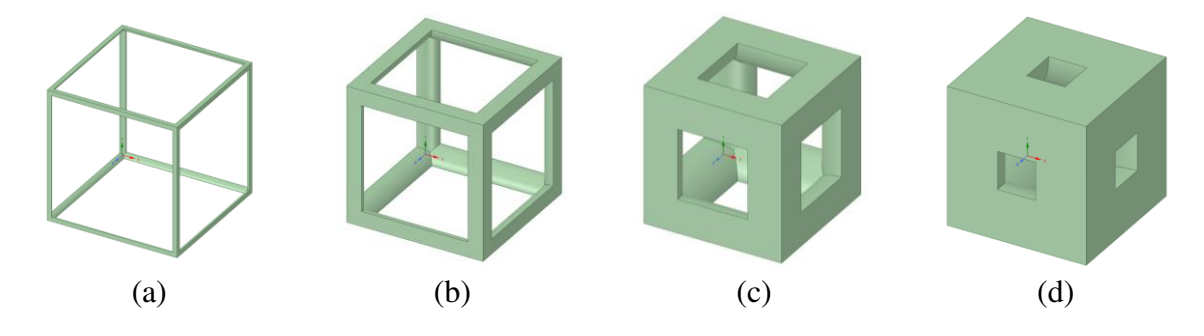


Fig. 3. Unit cell of type 1 with different volume fractions of the material: (a) 0.01; (b) 0.1; (c) 0.4; (d) 0.7

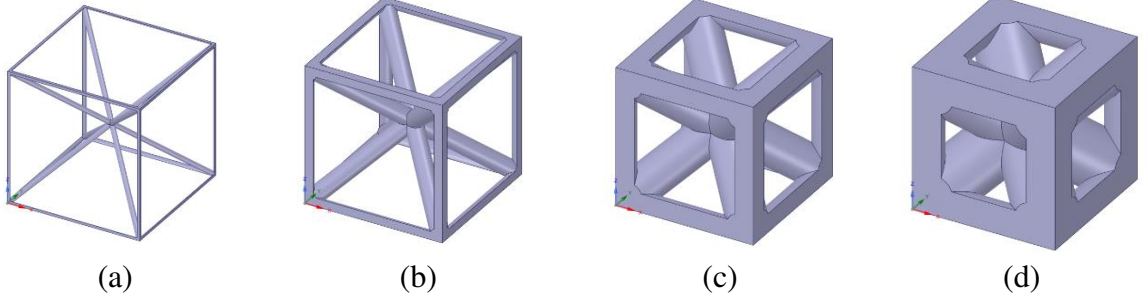


Fig. 4. Unit cell of type 2 with different volume fractions of the material: (a) 0.01; (b) 0.1; (c) 0.4; (d) 0.7

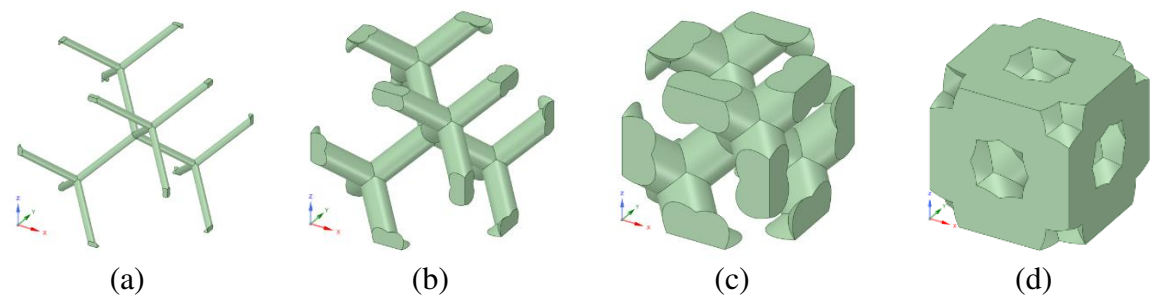


Fig. 5. Unit cell of type 3 with different volume fractions of the material: (a) 0.01; (b) 0.1; (c) 0.4; (d) 0.7

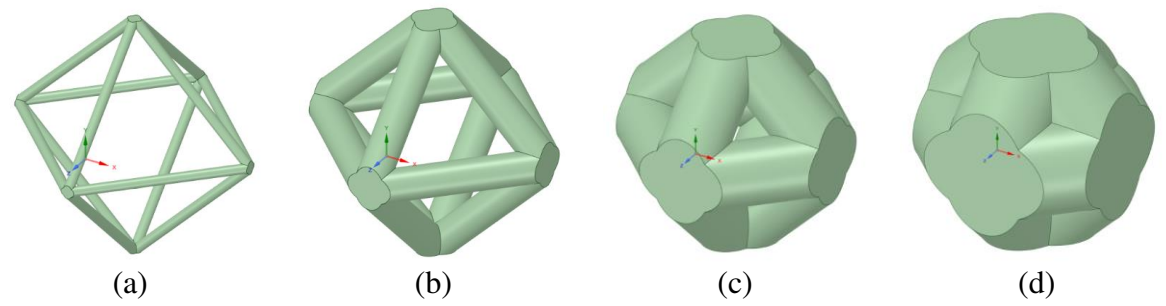


Fig. 6. Unit cell of type 4 with different volume fractions of the material: (a) 0.01; (b) 0.1; (c) 0.4; (d) 0.7

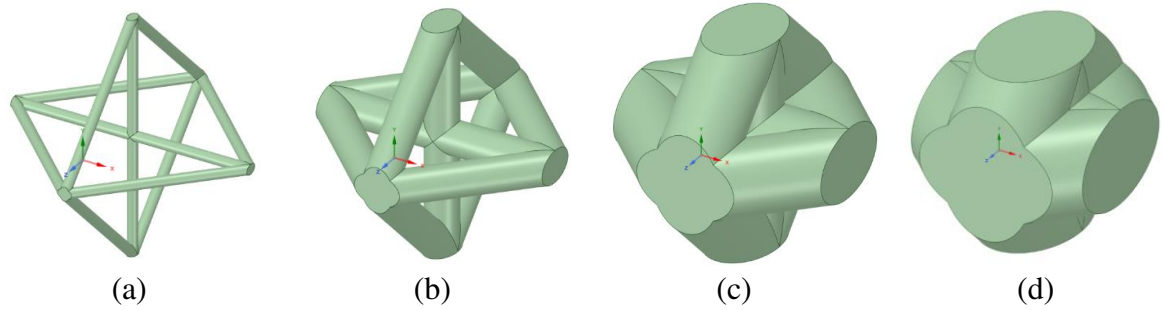


Fig. 7. Unit cell of type 5 with different volume fractions of the material: (a) 0.01; (b) 0.1; (c) 0.4; (d) 0.7

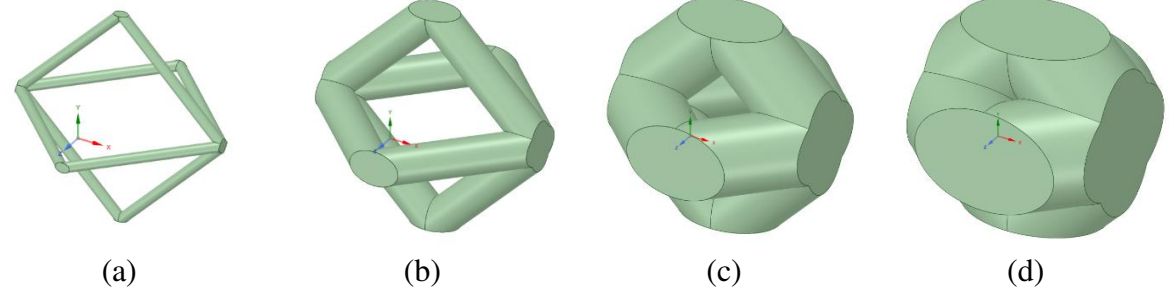


Fig. 8. Unit cell of type 6 with different volume fractions of the material: (a) 0.01; (b) 0.1; (c) 0.4; (d) 0.7

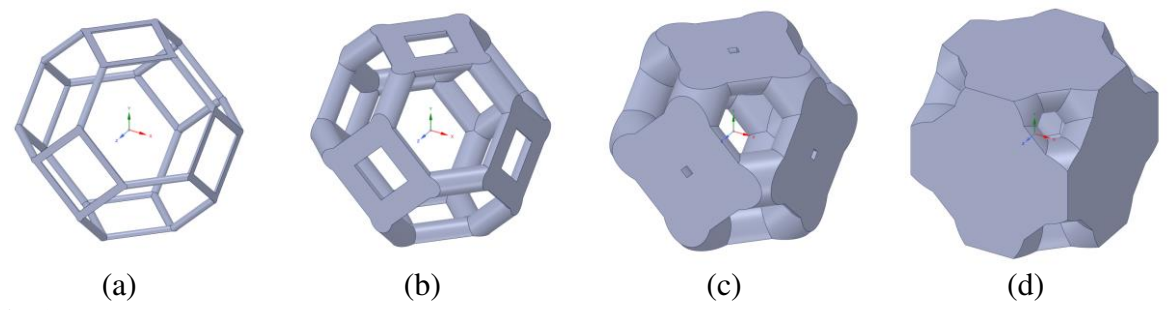


Fig. 9. Unit cell of type 7 with different volume fractions of the material: (a) 0.01; (b) 0.1; (c) 0.4; (d) 0.7

Figures 10–16 show the 3D view for four topologies of each type of unit cells with $L_x \in \{10, 7, 4, 1\}$. For correct analysis of the results, homogenization was performed at a fixed volume fraction of 0.05.

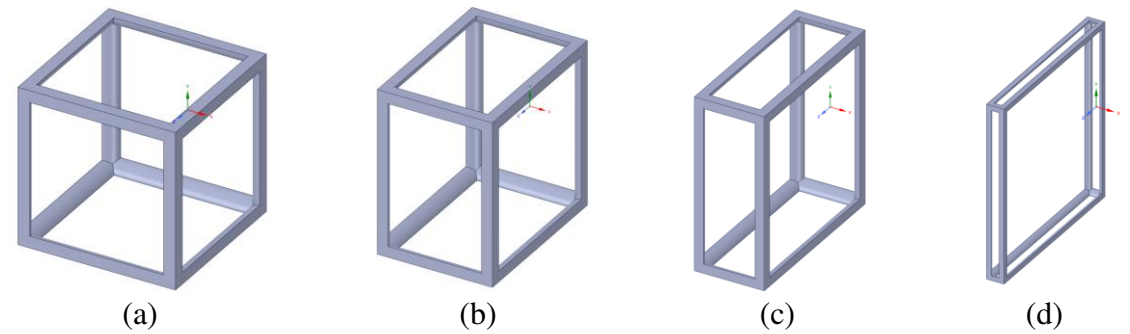


Fig. 10. Unit cell of type 1 with varying dimension L_{χ} : (a) 10 mm, (b) 7 mm, (c) 4 mm, (d) 1 mm

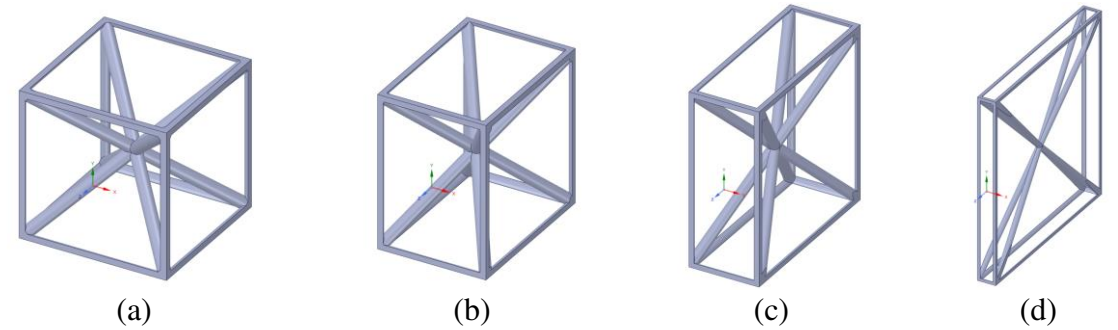


Fig. 11. Unit cell of type 1 with varying dimension L_x : (a) 10 mm, (b) 7 mm, (c) 4 mm, (d) 1 mm

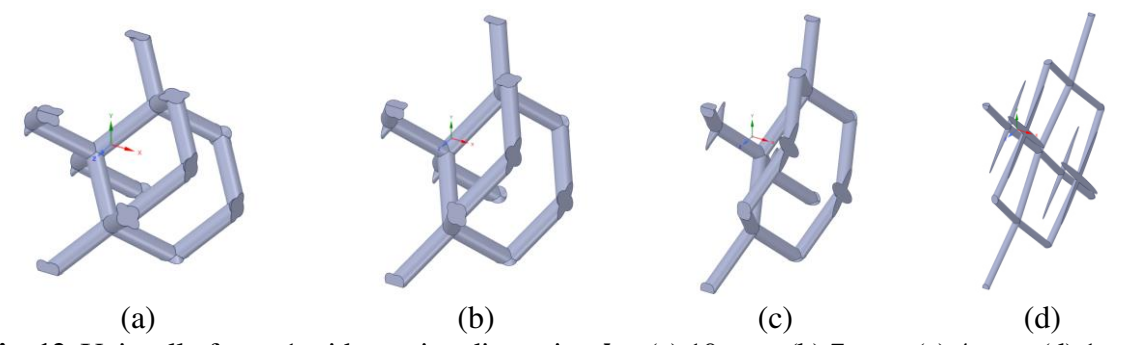


Fig. 12. Unit cell of type 1 with varying dimension L_{χ} : (a) 10 mm, (b) 7 mm, (c) 4 mm, (d) 1 mm

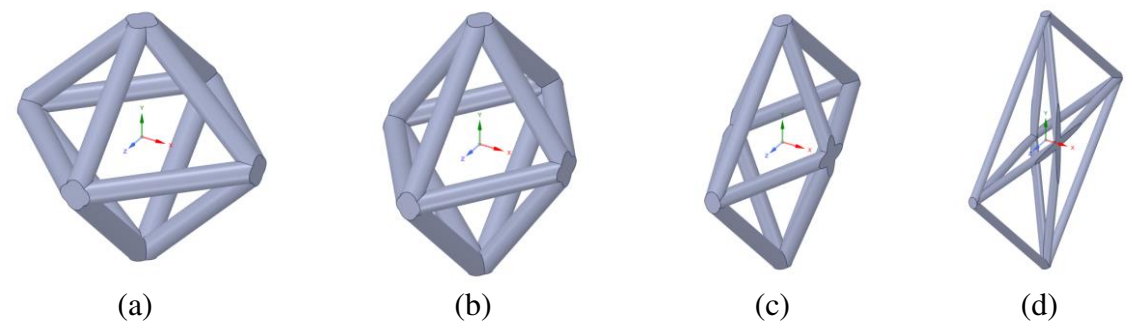


Fig. 13. Unit cell of type 1 with varying dimension L_{χ} : (a) 10 mm, (b) 7 mm, (c) 4 mm, (d) 1 mm

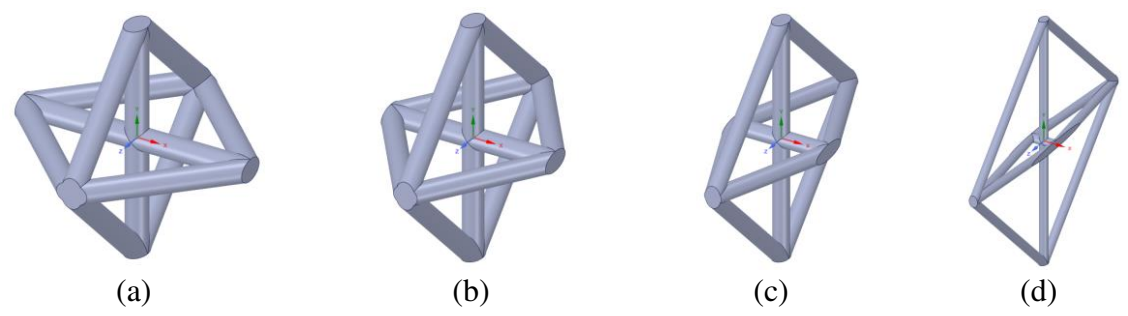


Fig. 14. Unit cell of type 1 with varying dimension L_x : (a) 10 mm, (b) 7 mm, (c) 4 mm, (d) 1 mm

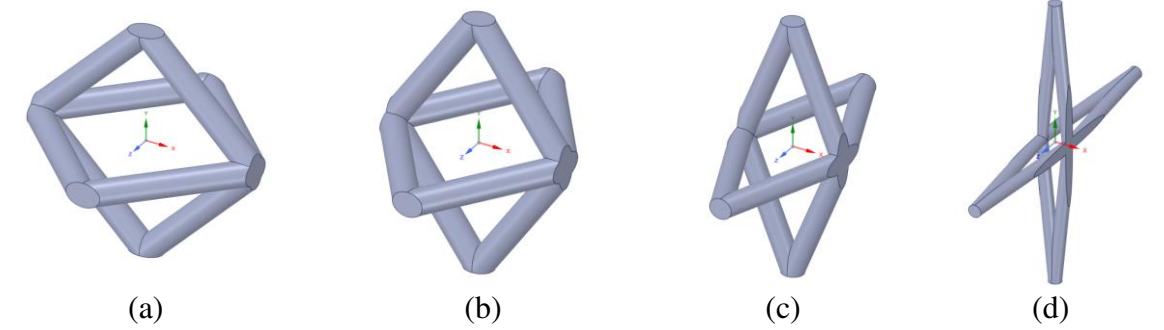


Fig. 15. Unit cell of type 1 with varying dimension L_x : (a) 10 mm, (b) 7 mm, (c) 4 mm, (d) 1 mm

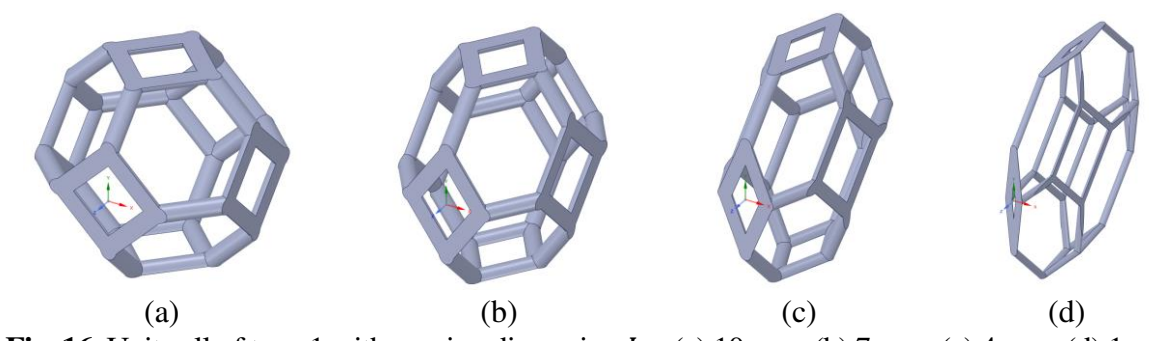


Fig. 16. Unit cell of type 1 with varying dimension L_{χ} : (a) 10 mm, (b) 7 mm, (c) 4 mm, (d) 1 mm

Finite element models of metamaterial unit cells. A series of finite element models were developed based on the presented three-dimensional geometric models (Figs. 3–16). The models are formed by tetrahedral finite elements with first-order displacement interpolation. The classical finite element method in displacements with variational formulation based on the weighted residuals method or the principle of minimum potential energy is used for the three-dimensional problem of elasticity theory [22].

The homogenization process for the metamaterial is carried out according to the algorithm described above using the finite element analysis system ANSYS Material Designer. The characteristic problems of elasticity theory are solved in a static formulation using the considered periodic boundary conditions (13)–(18).

The computational domain of each type of metamaterial represents one unit cell. The maximum size of the finite element of the computational mesh is 1 mm. The characteristic mesh size depends on the thickness of the rod forming the unit cell, covering the range from 0.005 to 1 mm and selected for each cell type individually taking into account the volume fraction of the solid material.

Typical examples of finite element meshes are shown in Figs. 17 and 18. The numbers of elements and nodes in the numerical models are given in Table 1 for unit cells of types 1–7 with 0.4 vol. % of the material as a typical example.

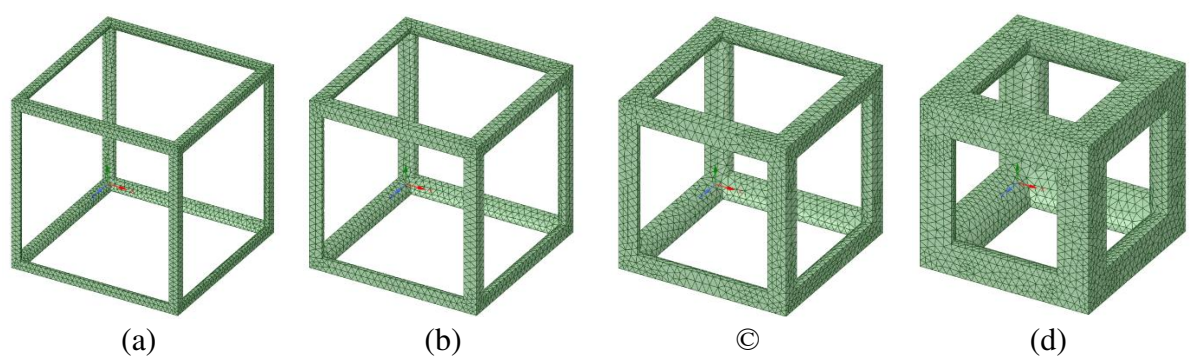


Fig. 17. Finite element mesh for unit cells of type 1 with different volume fractions of the material: (a) volume fraction 0.025, mesh size 0.3 mm, (b) volume fraction 0.05, mesh size 0.4 mm, (c) volume fraction 0.1, mesh size 0.45 mm, (d) volume fraction 0.25, mesh size 0.5 mm

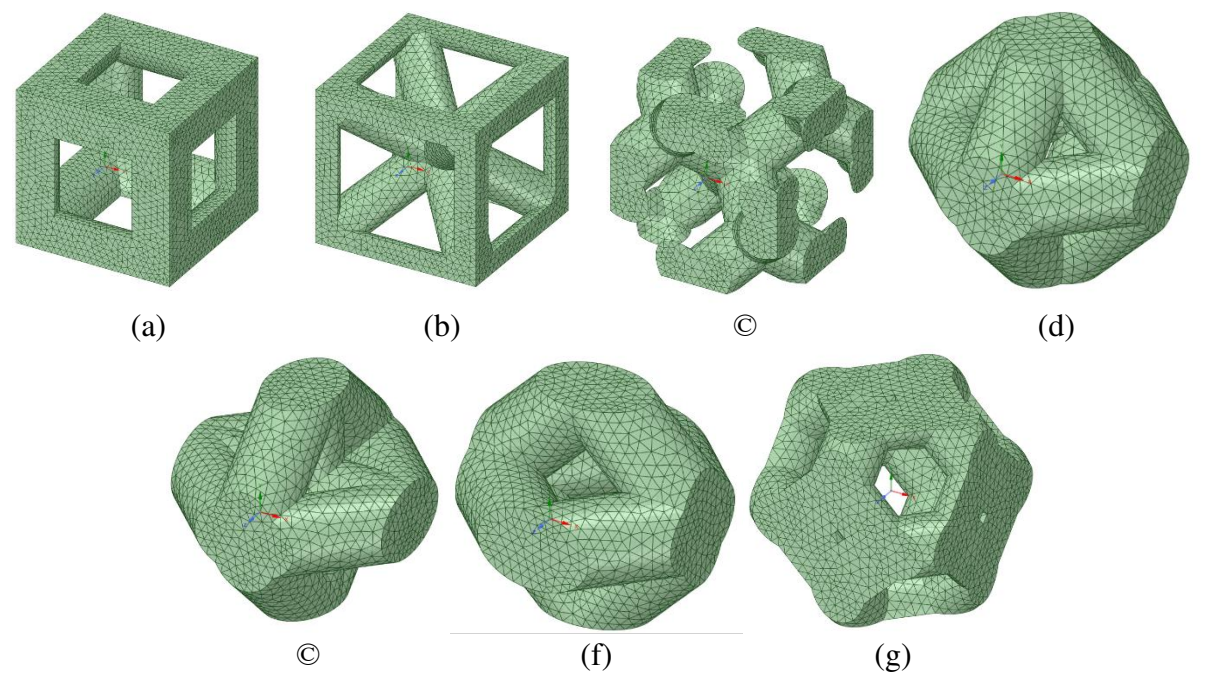


Fig. 18. Finite element mesh for unit cells of types 1–7 with 0.4 vol.% of the material: (a) type 1, (b) type 2, (c) type 3, (d) type 4, (c) type 5, (f) type 6, (g) type 7

Table 1. Mesh statistics for finite element models of unit cells with 0.4 vol. % of the material

Unit cell type	Number of elements	Number of nodes		
1	40 743	63 706		
2	37 920	59 799		
3	32 162	50 098		
4	28 606	42 551		
5	30 609	45 272		
6	30 245	44 863		
7	33 133	51 415		

Representative elements are considered to check the adequacy and correctness of the introduced periodic boundary conditions (13)–(18). Provided that the elasticity theory problem is well-posed for a periodic composite material with periodic boundary conditions, the homogenization problem can be solved numerically for a representative volume element consisting of $1 \times 1 \times 1$ basic or unit cells. However, it is certainly possible to study the

behaviour of the RVEs consisting of $3 \times 3 \times 3$ and $5 \times 5 \times 5$ unit cells, since they can be considered as the representative volume elements of larger size (Fig. 19).

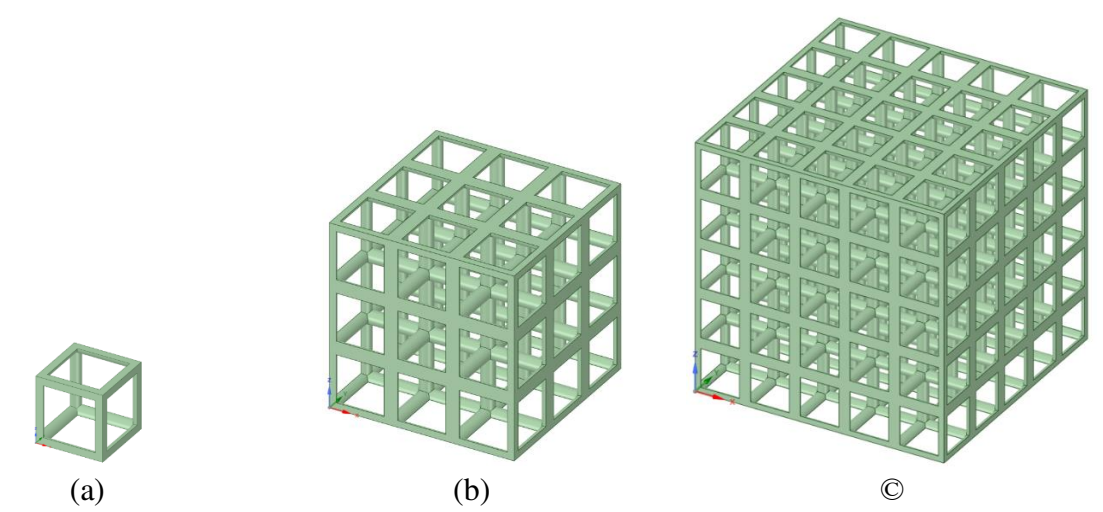


Fig. 19. Representative volume elements with different numbers of unit cells: (c) $1 \times 1 \times 1$ unit cells, (b) $3 \times 3 \times 3$ unit cells, (c) $5 \times 5 \times 5$ unit cells

This step is necessary for checking whether the periodic boundary conditions adopted are well-posed and the overall methodology is sound. Because the RVE is large-sized, a larger number of finite elements have to be processed (Table 2), which significantly increases the computational cost of the research. Therefore, it seems reasonable to assess the influence of the number of unit cells in the RVE on the values of the obtained elastic characteristics of the metamaterial.

Table 2. Mesh statistics for finite element models of representative volume elements formed by different numbers of unit cells

	· ·			
Number of unit cells in RVE		Number of elements	Number of nodes	
	$1 \times 1 \times 1$	5 450	10 533	
Ī	$3 \times 3 \times 3$	119 466	208 914	
ſ	$5 \times 5 \times 5$	574 758	980 132	

Mechanical properties of the material. Finally, to formulate the problem of elasticity theory for the case of additively manufactured materials, we should tailor the mechanical properties to account for potential anisotropy. Our study considers the metamaterials produced additively from AlSi₁₀Mg by selective laser melting (SLM) with the powder particle size less than 150 μ m. The material and the technique can be used to produce parts with thin structural elements and complex geometry, also well suited for manufacturing of lightweight products.

Table 3. Mechanical properties of additively manufactured AlSi₁₀Mg alloy

Mechanical property type	Direction				
	X/XY	Y/YZ	Z/XZ		
Young's modulus, Gpa	82.5	76.7	76.8		
Shear modulus, Gpa	23.8	27.1	21.4		
Poisson's ratio 0.32		0.32	0.33		

The values of technical elastic properties of the solid material obtained by selective melting 0 are given in Table 3. The orientation of coordinate system axes and printing direction are shown in Fig. 1. As seen from Table 3, adopting the SLM technology for producing

metamaterials yields a slightly pronounced orthotropy of the properties, which is taken into account when selecting a non-isotropic model of the material for numerical analysis.

Results and Discussion

This section presents the computational results for the elastic properties of metamaterials of all types with varying volume fraction of solid material within the unit cell. We also carried out an analysis of Young's moduli values depending on the rotation of the local axes relative to the principal axes of material symmetry, as well as analysis of the effect of compression of the unit cell shape along one of the coordinate axes.

Verification of boundary conditions. To verify the adequacy and correctness of the mathematical formulation of the problem and periodic boundary conditions imposed on pairs of nodes of the mesh, the effective mechanical properties of the structures consisting of $1 \times 1 \times 1$, $3 \times 3 \times 3$ and $5 \times 5 \times 5$ unit cells of type 1 were evaluated (Fig. 19). The volume fraction of the material of the analysed cells was taken equal to 0.1. In our opinion, verifying only one type of metamaterial should be sufficient to draw the required conclusions, since the results for the rest of the cells should be similar due to the uniformity of the used algorithm. The computations are performed on an Intel Core i7 CPU (10^{th} generation) workstation with 64 Gb DDR4 RAM. The duration of analysis for the models with $1 \times 1 \times 1$, $3 \times 3 \times 3$ and $5 \times 5 \times 5$ cells was 40, 181 and 810 seconds, respectively.

The computational results for the three cases of the metamaterial RVE are presented in Table 4. The relative differences are given in the table compared to the $5 \times 5 \times 5$ structure.

Table 4. Young's moduli for different	ent numbers of unit	cells in representativ	e volumes of type 1
metamaterial			
	DITE 11 4 4 4	DITE 11 0 0 0	DITE 14 5 5 5

Machanical property type	RVE with $1 \times 1 \times 1$	RVE with $3 \times 3 \times 3$	RVE with $5 \times 5 \times 5$
Mechanical property type	unit cells	unit cells	unit cells
E_1 , Mpa	3 366.2	3 366.1	3 366.4
E_2 , Mpa	3 137.8	3 137.9	3 138.2
E_3 , Mpa	3 140.2	3 140.6	3 140.9
Relative difference for E_1 , %	0.006	0.009	_
Relative difference for E_2 , %	0.013	0.010	_
Relative difference for E_3 , %	0.022	0.009	_

As seen from Table 4, the relative differences in Young's moduli between the three RVEs is less than 0.03 %, which is within the numerical errors of finite element analysis. At the same time, the computations for the RVE consisting of $5 \times 5 \times 5$ unit cells take more than 15 times longer compared to the computations for the RVE with $1 \times 1 \times 1$ unit cells.

Thus, it is safe to assume that the mathematical model is correct and subsequent computations can be performed with the periodic boundary conditions (13)–(18) without compromising the accuracy of the results for an RVE consisting of one unit cell with the characteristic size of $10 \times 10 \times 10$ mm.

Results for the case of rods with fixed diameter. The computational time for one metamaterial unit cell is about 3 minutes depending on the geometric complexity. The results of finite element homogenization for unit cells of types 1–7 at fixed diameter of rods are presented in Table 5.

Since the rod diameters of all unit cells of the metamaterials are the same and equal to 1 mm, the volume fraction of the material in each of the unit cells is different (Table 6). This should be taken into account in the comparative analysis of elastic moduli. We can approximately consider Young's and shear moduli to be proportional to the material volume fraction for small values.

Nevertheless, only the simplest structure of type 1 contains a significantly lower volume fraction of the material, while the other cells are filled with the base material by about the same 4.1–6.9 %.

Mechanical	Unit cell of						
property type	of type 1	of type 2	of type 3	of type 4	of type 5	of type 6	type 7
E_1 , Mpa	665.4	908.2	80.3	594.3	897.3	59.5	231.3
E ₂ , Mpa	619.3	863.4	78.9	595	854.7	56	240.2
E_3 , Mpa	620	863.9	79.5	593.6	595.8	55.6	234.3
<i>G</i> ₁₂ , Mpa	2.7	422.8	82.9	386.9	5.4	372.2	62.2
<i>G</i> ₂₃ , Mpa	2.6	428.9	84	421.9	415.4	2.6	62.9
<i>G</i> ₃₁ , MPa	2.6	417.5	82.2	359.3	352.6	344.9	61.7
$ u_{12}$	0.03	0.29	0.47	0.33	-0.2	0.9	0.4
ν_{13}	0.03	0.29	0.46	0.28	0.5	0.9	0.4
$ u_{23}$	0.03	0.29	0.49	0.37	0.6	-0.9	0.4

Table 5. Effective elastic moduli of metamaterials with different types of unit cells at fixed rod diameter (1 mm)

Table 6. Volume fraction of material for rod diameter of 1 mm

Unit cell type	Unit cell of	Unit cell of	Unit cell of				
Omit cen type	type 1	of type 2	of type 3	of type 4	of type 5	type 6	type 7
Volume fraction	0.022	0.069	0.049	0.059	0.053	0.041	0.059

We can conclude from these preliminary computations that the effective elastic properties of the metamaterial depend significantly on the geometry of the unit cell forming the periodic structure of the metamaterial. Cells of types 1, 2 and 5 exhibit the highest stiffnesses along the principal orthotropy axes. The geometry of these cells contains the rods that are parallel to the loading axes, making the material more resistant to tension–compression.

Cells of types 2 and 4 exhibit the highest shear stiffness, determined by the shear modulus, apparently due to the presence of transverse rods connecting the diagonal nodes of the lattice. Metamaterials based on type 5 and 6 cells also have rather high shear stiffnesses, but only in two planes, which is due to incomplete symmetry of the cells with respect to the coordinate planes.

Metamaterials based on types 3 and 6 cells have the lowest values of Young's and shear moduli along the axes of the global coordinate system. A possible explanation for this is that these cell types are formed mainly by diagonal rods and, therefore, do not have high stiffness in the considered directions. Nevertheless, it can be hypothesized that the properties may be higher in other directions (this point is discussed below).

The simplest cell of type 1 exhibits the highest stiffness along the three principal directions due to its characteristic cubic shape with no additional diagonal rods. However, its shear stiffness as well as its Poisson's ratio are minimal. The significant difference in Young's moduli along the Z axis for the cell of type 5 compared to the same parameter along the X and Y axes is due to the absence of the rod in the unit cell in this direction.

Interestingly, the metamaterials based on cells of types 5 and 6 have auxetic properties, which is confirmed by the negative values of Poisson's ratio in certain planes. Both positive and negative values of Poisson's ratio are rather high for these cell types. Analysing the geometry of these cells, we can assume that diagonally arranged rods lead to the auxetic effect, and the metamaterials themselves can be classified as auxetics based on re-entrant cells.

The computations ultimately confirm that all types of metamaterials exhibit material symmetry of elastic properties with respect to the three orthotropy planes. The structural anisotropy is in this case apparently complemented by the initial non-isotropy of the material properties due to additive manufacturing by selective laser melting.

The volume fraction of the material in the unit cell of the metamaterial can serve as an additional criterion of efficiency along with the elastic properties. We assume that a metamaterial with a lower content of initial material but higher stiffness is more efficient than a metamaterial with similar elastic properties but lower porosity. We should also note that the

presence of a system with branched pore channels in metamaterials can be a crucial factor in some applications, in particular for biomedicine [23].

Effect of material volume fraction on metamaterial properties. Let us start the analysis of the effective properties of the metamaterial formed by different types of cells by considering the comparative graphs illustrating the differences in the variation of Young's moduli, shear moduli, and Poisson's ratio at the same value of the material volume fraction. Figure 20 shows the variations of elastic constants of the metamaterial as functions of porosity. The results are given as curves of the dependences of Young's moduli, shear moduli and Poisson's ratios along the principal axes of orthotropy on the volume fraction of the initial material.

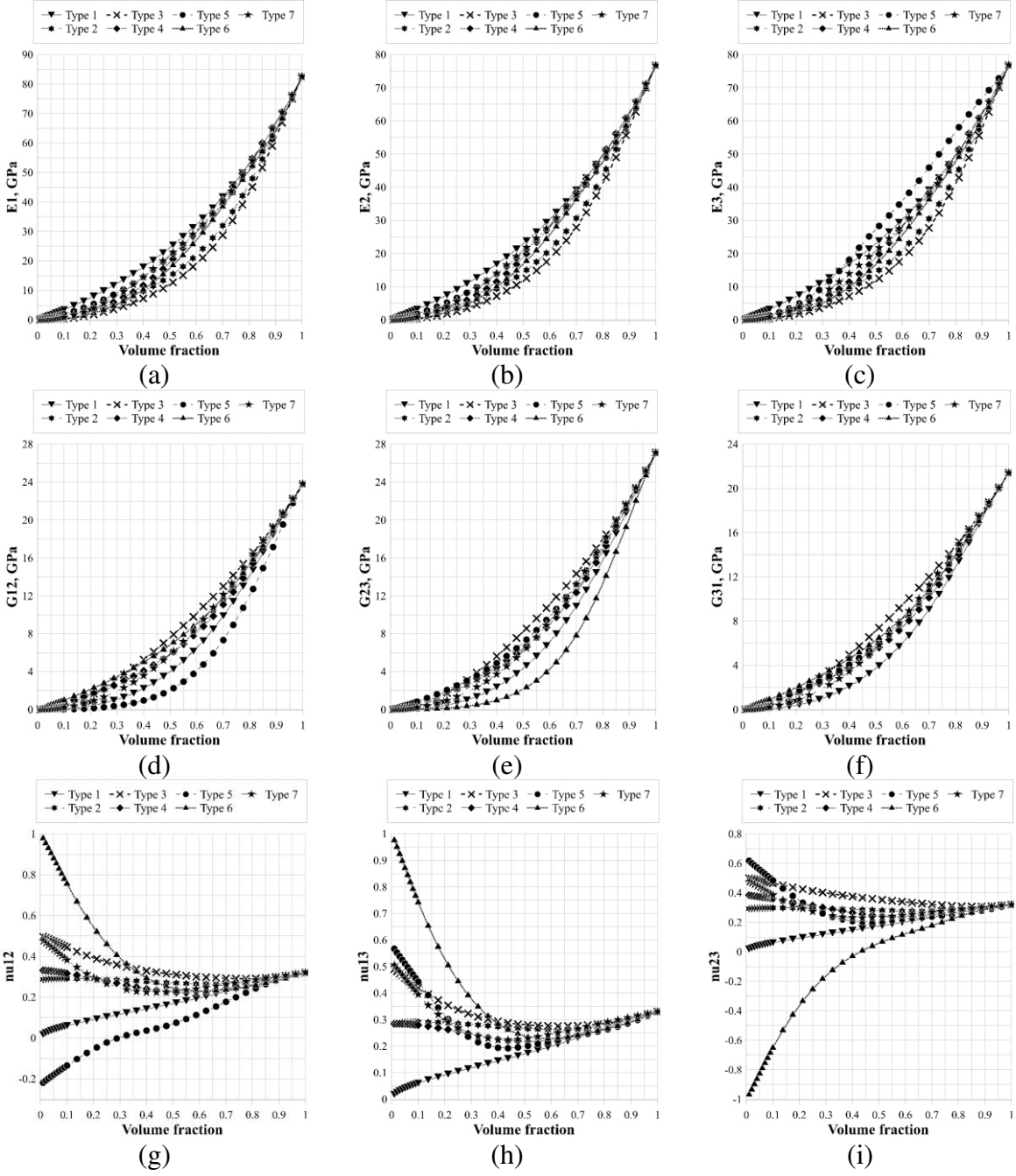


Fig. 20. Dependences of elastic constants of metamaterials formed by cells of type 1–7 on the volume fraction of solid material: (a) Young's modulus E_1 , (b) Young's modulus E_2 , (c) Young's modulus E_3 , (d) shear modulus G_{12} , (e) shear modulus G_{23} , (f) shear modulus G_{31} , (g) Poisson's ratio v_{12} , (h) Poisson's ratio v_{13} , (i) Poisson's ratio v_{23}

The dependences for most cell types have a typical nonlinear character, generally corresponding to the behaviour of porous structures with varied porosity 0. This behaviour, however, is apparently inverted, since by definition porosity and volume fraction of the material sum to 1. As follows from the theory of composites, the Young's and shear elastic moduli of the metamaterial vary from zero to the corresponding values of the solid material following some nonlinear relationship. The degree of non-isotropy associated with additive manufacturing increases slightly with increasing relative density.

The values of the mechanical characteristics of metamaterials strongly depend on the type of unit cell. We can observe from the computations that the nature of the dependence coincides with the intuitive understanding of the metamaterial behaviour, correlated with the basic concepts of deformable solid mechanics. The mechanical characteristics grow with an increase in the volume fraction, tending to the values of the moduli in the solid AlSi₁₀Mg alloy. However, as seen from Figure 20, the mechanical characteristics vary at a different rate in each of the unit cells given the same variation rate of effective density.

Analysing the curves, we see a distinct dependence of the mechanical characteristics of the metamaterial on the volume fraction of the base material. When comparing the elastic moduli in each direction for all the considered cell types, the cells with the highest and the lowest elastic modulus along each of the axes are distinguished. In particular, the largest Young's modulus along the axes X and Y is observed in the cell of type 1, along the axis Z – by the cell of type 1 (at lower values of volume fraction) and by the cell of type 5 (at medium values of volume fraction) and by the cells of types 5 and 6 (at volume fraction close to 1). The lowest elastic modulus along each of the axes is observed in the cell of type 3.

The dependence of the parameters on the relative density of the material is similar for all of the cell types, but due to the lack of complete symmetry of some types of basic cells, some differences occur, mainly when considering the Young's modulus along Z axis. It is also important to mention that metamaterials based on the cells of types 3 and 4 demonstrate the effect of "sagging" of Young's modulus values at the volume fractions of 0.3–0.8. This effect might be useful in terms of selecting the optimal combination of mass and stiffness properties.

It is also interesting to note that auxetic behaviour occurs for the metamaterials of types 5 and 6, and this effect takes place over the whole considered range of the volume fraction.

Effect of unit cell asymmetry on metamaterial properties. The effect of gradual contraction of the cell along one coordinate axis (X) is demonstrated in Fig. 21 in the form of dependences of Young's and shear moduli and Poisson's ratio on the side length of the periodicity cell along the X axis. The effect of the difference of the sides of the unit cell is shown above in Figs. 10–16.

The results of finite element homogenization of the cells with different aspect ratios suggest that Young's modulus evidently decreases along the X axis with the decrease in the value of the unit cell side L_x . The reason for this is the decrease in the effective cross-sectional area perpendicular to the X axis due to the decrease in the thickness of the rod. The values of elastic moduli along the other two axes increase. This fact can be explained, on the contrary, by the increase in the effective cross-sectional area perpendicular to the Y and Z axes. The rate of decrease of E_x is higher than the rate of increase of E_y and E_z . In the cells of types 1 and 2 the character of Young's modulus variation along each of the axes is close to linear.

It is important to mention that the basic mechanical characteristics of the metamaterial are close to isotropic before the decrease in L_x . The cell of type 6 shows a significant increase in Young's moduli along the Y and Z axes, with a slight decrease in Young's moduli along the X axis. In contrast, the cells of types 3 and 7 exhibit a relatively low growth of Young's moduli E_2 and E_3 and a significant decrease of E_1 with a less than twofold decrease in the parameter L_x . However, a decrease in Young's moduli along each of the three axes occurs with a further decrease in the parameter L_x .

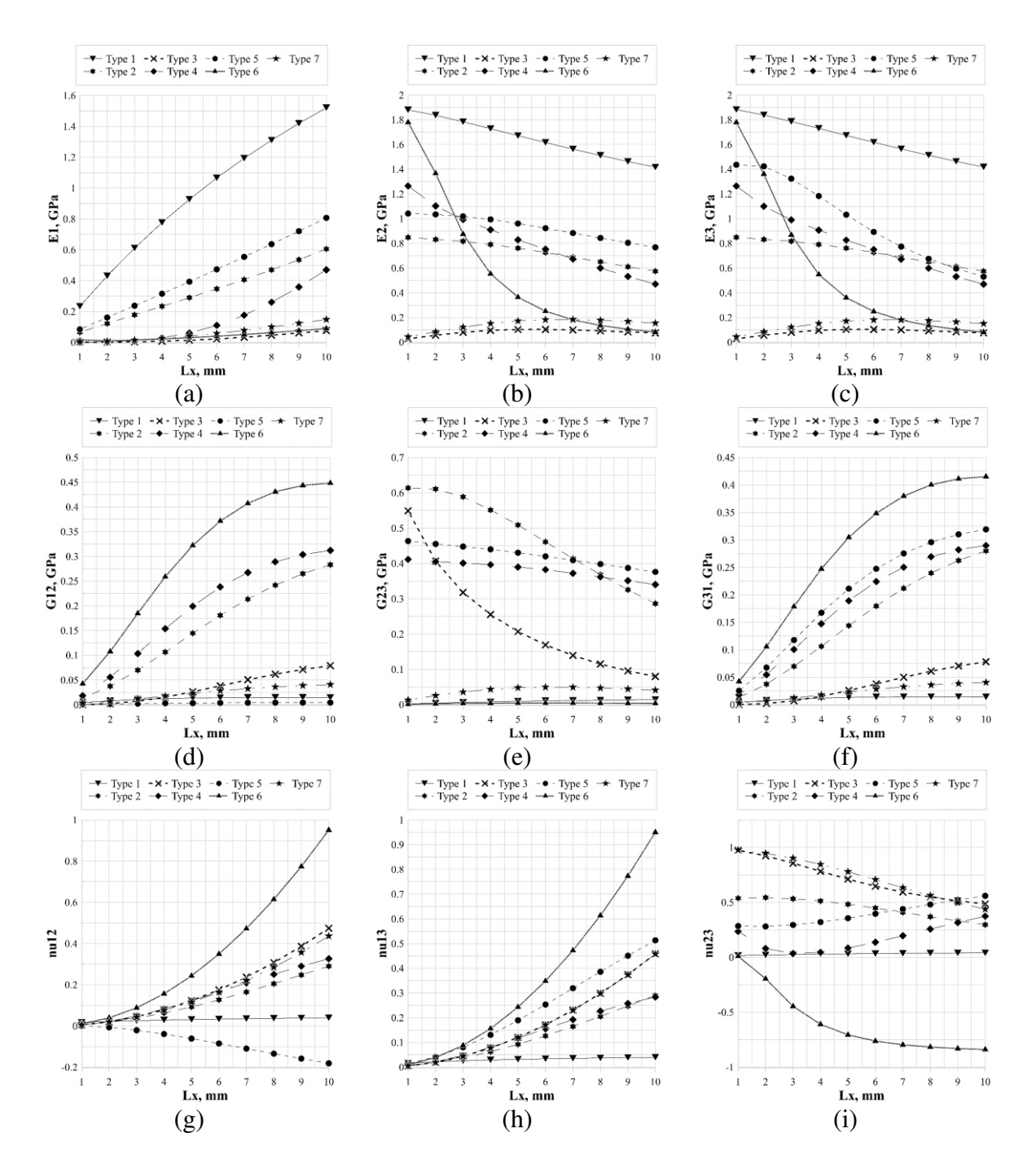


Fig. 21. Dependences of elastic properties on the length of cell side L_x for metamaterial formed by unit cells of types 1–7: (a) Young's modulus E_1 , (b) Young's modulus E_2 , (c) Young's modulus E_3 , (d) shear modulus G_{12} , (e) shear modulus G_{23} , (f) shear modulus G_{31} , (f) Poisson's ratio v_{12} , (g) Poisson's ratio v_{13} , (i) Poisson's ratio v_{23}

Since the mechanical characteristics of cells with different values of the parameter L_x were computed at a fixed material volume fraction and a constant unit cell mass, an increase in Young's moduli along the Y and Z axes can be achieved without increasing the amount of material. Thus, the stiffness of the metamaterial can be tailored to the desired level by varying the aspect ratios of the unit cell.

Elastic moduli of the metamaterial in the rotated coordinate system. Due to their geometrical features, metamaterials might have a high degree of anisotropy and have different values of mechanical characteristics in different directions. The paper considers unit cells of

each type at 0.4 vol. % (Fig. 18), and an algorithm for determining the elastic moduli in different directions is developed using Eqs. (12), (22). Surface diagrams are given as a typical example for the values of Young's modulus in different directions of the local coordinate system (Fig. 22). Such diagrams can be interpreted as the average stiffness at an arbitrary stretching direction of the metamaterial.

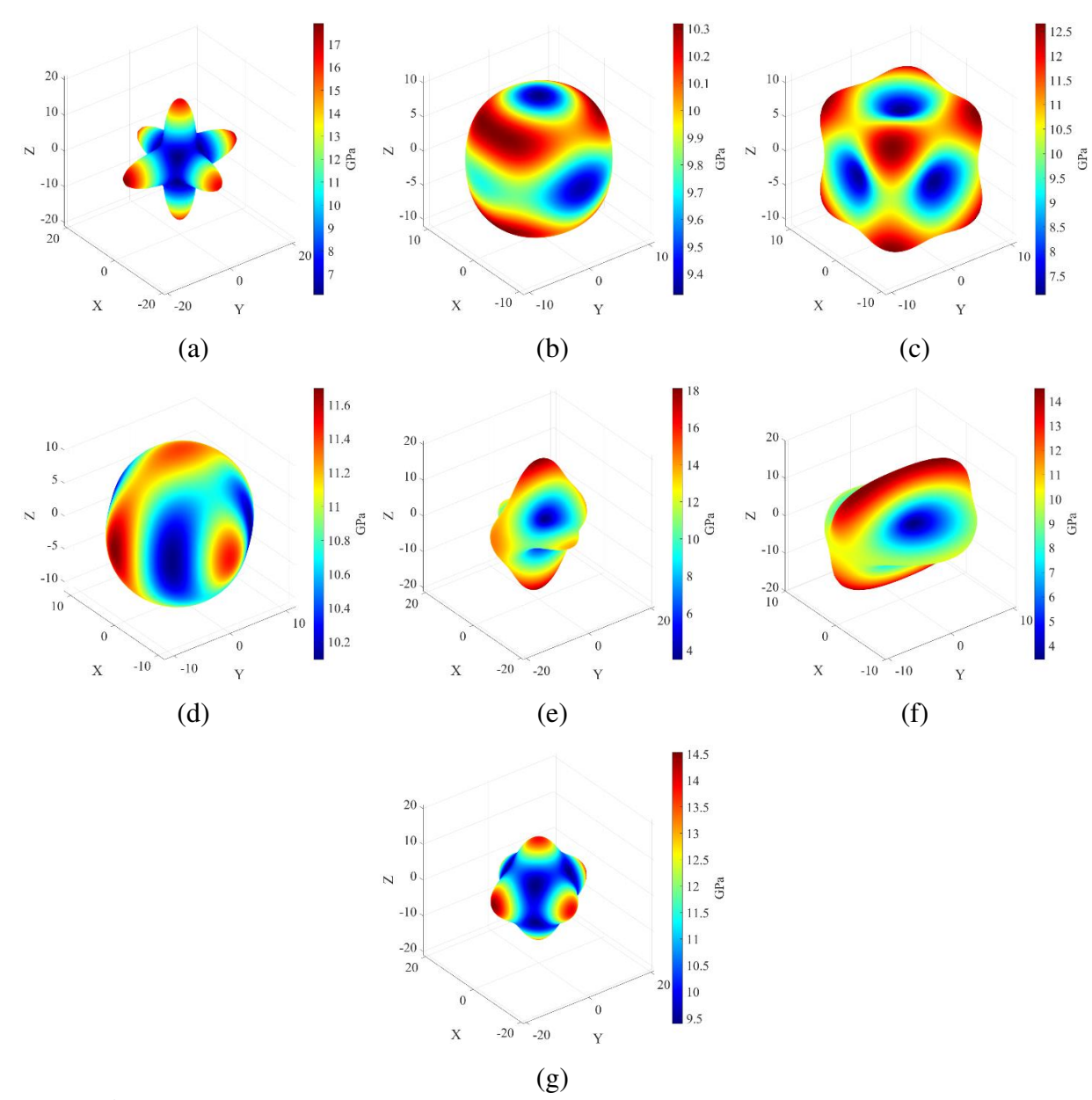


Fig. 22. Young's modulus of the metamaterial formed by cells of different types with 0.4 vol. %: (a) type 1, (b) type 2, (c) type 3, (d) type 4, (e) type 5, (f) type 6, (g) type 7

As follows from the diagrams (Fig. 22), the character of the modulus distribution depends significantly on the type of unit cell. In particular, cells of types 1 and 7 have significantly higher Young's moduli in the directions of the principal axes. Conversely, however, the cell of type 3 has a higher Young's modulus value in the diagonal direction. The diagrams for cells of types 5 and 6 show a lower amount of symmetry planes, reflecting the geometric properties of these cells, while the modulus values cover a much wider range compared to other unit cell types. Cell of types 2 and 4 have less pronounced anisotropy compared to other types of unit cells. Cells of types 5 and 6, demonstrating auxetic properties, also have a characteristic, different from classical metamaterials, appearance of circular diagrams of the Young's modulus.

Depending on the cell type, Young's modulus both increases and decreases in the direction of each of the orthogonal axes, which is well-observed in the diagrams above. Thus, cells of types 1, 5 and 7 exhibit a decrease in Young's moduli by 2–11 times in each direction when the axes are rotated. Cells of types 2, 3, 4 and 9 exhibit an increase in Young's moduli by 1.5–2.5 times for each of the axes.

Analysing the diagrams presented above for the cells whose rods are aligned with the global axes, it is possible notice an interesting feature. If we consider such rotation, which makes the axes aligned with the diagonals of the unit cell, the values taken by the diagonal components of the elastic moduli tensor decrease significantly, as well as the spread in the values of all tensor components. Conversely, a significant increase of some components corresponding to the loading direction in the new axes is observed for other cells when the direction of the changes, which suggesting that the axes are oriented more rationally under homogeneous loading.

Conclusion

Analysis of the properties of lattice structures is a burgeoning area of research in mechanics. This article describes an approach to studying the macroscopic mechanical properties of metamaterials. We formulated and verified a number of assumptions about the relationship between mechanical properties and topological parameters, such as the type of unit cell, volume fraction of material, geometrical parameters of the RVE.

We aimed to determine the overall influence of the topology of a heterogeneous periodic structure on the values of macroscopic mechanical characteristics in a metamaterial. We found the topology parameters estimating the influence that each of them has on the results of the obtained elastic moduli of the porous material.

Analysing the influence of the RVE aspect ratios, we found a significant decrease in Young's moduli in the direction of the axis along which the geometric size of the cell varied; on the other hand, a significant increase in Young's moduli along the other two axes was observed as well.

The diagrams illustrate the influence of anisotropy of the additive material used to produce the metamaterial cells on the resulting mechanical properties. Varying the direction of the local axes allows to better assess the mechanical capabilities of the unit cells by monitoring their stiffness in other directions.

Studies on a range of dependences should allow to design materials with specific mechanical properties, required for developing modern advanced industrial products based on continuum mechanics, mechanics of heterogeneous media and composites, computational mechanics and mathematical modelling, biomedical and advanced manufacturing technologies.

References

- 1. Lewandowski JJ, Mohsen S. Metal additive manufacturing: A review of mechanical properties. *The Annual Review of Materials Research*. 2016;46(1): 151–186.
- 2. Hanks B, Berthel J, Frecker M, Simpson TW. Mechanical properties of additively manufactured metal lattice structures: Data review and design interface. *Additive Manufacturing*. 2020;35: 101301.
- 3. Maslov LB. Dynamic Model of a Periodic Medium with Double Porosity. *Mechanics of Solids*. 2018;53: 184–194.
- 4. Omairey SL, Dunning PD, Sriramula S. Development of an ABAQUS plugin tool for periodic RVE homogenisation. *Engineering with Computers*. 2019;35: 567–577.
- 5. Christensen J, Kadic M, Kraft O. Vibrant times for mechanical metamaterials. *MRS Communications*. 2015;5(3): 453–462.
- 6. Oraib A, Rowshanc R, Rashid K. Topology-mechanical property relationship of 3D printed strut, skeletal, and sheet based periodic metallic cellular materials. *Additive Manufacturing*. 2018;19: 167–183.

- 7. Bin RS, Mazedur RM. Modeling elastic properties of unidirectional composite materials using Ansys Material Designer. *Procedia Structural Integrity*. 2020;28: 1892–1900.
- 8. Zadpoor AA. Mechanical meta-materials. *Materials Horizons*. 2016;3(5): 371–381.
- 9. Gibson LJ, Ashby MF. *Cellular solids: structure and properties*. Cambridge University Press. 1997. 10. Hedayati R, Sadighi M, Mohammadi-Aghdam M, Zadpoor A. Mechanical behavior of additively manufactured porous biomaterials made from truncated cuboctahedron unit cells.

International Journal of Mechanical Sciences. 2016;106: 19–38.

- 11. Deshpande V, Ashby M, Fleck N. Foam topology: bending versus stretching dominated architectures. *Acta Materialia*. 2001;49(6): 1035–1040.
- 12. Zadpoor AA, Hedayati R. Analytical relationships for prediction of the mechanical properties of additively manufactured porous biomaterials. *Journal of Biomedical Materials Research Part A.* 2016;104(12): 3164–3174.
- 13. Hedayati R, Sadighi M, Mohammadi-Aghdam M, Zadpoor A. Mechanical properties of regular porous biomaterials made from truncated cube repeating unit cells: analytical solutions and computational models. *Material Science and Engineering*. 2016;60: 163–183.
- 14. Wauthle R, Vrancken B, Beynaerts B, Jorissen K, Schrooten J, Kruth J-P, Van Humbeeck J. Effects of build orientation and heat treatment on the microstructure and mechanical properties of selective laser melted Ti6Al4V lattice structures. *Additive Manufacturing*. 2015;5: 77–84.
- 15. Wang Y, Zhang L, Daynes S, Zhang H, Feih S, Wang MY. Design of graded lattice structure with optimized mesostructures for additive manufacturing. *Materials and Design*. 2018;142: 114–123. 16. Loh GH, Pei E, Harrison D, Monzón MD. An overview of functionally graded additive manufacturing. *Additive Manufacturing*. 2018;23: 34-44.
- 17. Lee J-H, Singer JP, Thomas EL. Micro/Nanostructured Mechanical Metamaterials. *Advanced Materials*. 2012;24(36): 4782–4810.
- 18. Kolken HMA, Zadpoor AA. Auxetic mechanical metamaterials. RSC Advances. 2017;7(9): 5111–5129.
- 19. Wallbanks M, Khan MF, Bodaghi M, Triantaphyllou A, Serjouei A. On the design workflow of auxetic metamaterials for structural applications. *Smart Materials and Structures*. 2021;31(2): 023002.
- 20. Zhmaylo M, Maslov L, Borovkov A, Tarasenko F. Finite element homogenization and experimental evaluation of additively manufactured lattice metamaterials. *Journal of the Brazilian Society of Mechanical Sciences and Engineering*. 2023;45: 299.
- 21. *SolidWorks Help*. Available from: https://help.solidworks.com/2023/English/SolidWorks/sldworks/r_welcome_sw_online_help.htm [Accessed 11th August 2022].
- 22. Maslov LB. *Finite element poroelastic models in biomechanics*. St. Petersburg: Lan' Publ. House; 2023. (In-Russian)
- 23. Maslov LB. Biomechanical model and numerical analysis of tissue regeneration within a porous scaffold. *Mechanics of Solids*. 2020;55(7): 1115–1134.

THE AUTHORS

A.I. Borovkov 🗓

e-mail: borovkov@compmechlab.com

L.B. Maslov 🗓

e-mail: leonid-maslov@mail.ru

M.A. Zhmaylo 🗓

e-mail: zhmaylo@compmechlab.com

F.D. Tarasenko 🗓

e-mail: tarasenko@compmechlab.ru

L.S. Nezhinskaya 🗓

e-mail: nezhinskaya.l@compmechlab.ru

Modal and harmonic analysis of the rotor system involving four different materials by finite element code: Ansys workbench

Submitted: September 21, 2022

Approved: February 22, 2023

Accepted: July 13, 2023

N.E.B. Afane ¹ ¹, S. Zahaf ¹ ² [∞], M. Dahmane ¹ ³, A. Belaziz ¹ ⁴, R. Noureddine ¹ ⁵

¹ National Polytechnic School of Oran, Oran, Algeria

² University of Djilali Bounaama-Khamis Meliana, Ain Defla, Algeria

³ Higher National School of Hydraulics, Blida, Algeria

⁴Mechanical Research Center Constantine (CRM), Constantine, Algeria

⁵University of Oran 2 Mohamed Ben Ahmed, Oran, Algeria

⊠ samir.zahaf@univ-dbkm.dz

Abstract. This article presents the study of the Jeffcott rotor shaft system, diameter 32 mm, length 1000 mm with a disc in the middle of an exterior diameter 250 and 30 mm thickness for four different materials namely (JIS-S45C steels, 38CrMoAl steels, structural steels, titanium steels (Ti-6AL-4V)), for a case simply supported, and it is important to determine the natural frequencies, critical speeds and amplitudes of the rotor system (von Mises stress, principal stress, maximum shear stress, lifetime). This characteristic is found by using the parametric design tool ANSYS Workbench. Modal, harmonic cases are realized for the single-rotor system. The results obtained for this analysis are useful for design of rotor system and to facilitate engineering applications and allied researches by presenting a detailed comparative picture based on dynamic analysis of Jeffcott rotor. The authors covered modal, harmonic response along with natural frequencies and whirling speeds at different modes. Resonance occurrence speeds are also analyzed using the Campbell diagram. The harmonic response is investigated, with added material (0.1 kg) on the disc, to reveal the von Mises stress, normal elastic strain, total displacement, maximum shear stress and life cycle number. FEA is carried out to estimate critical speeds for these four materials. The results of this study indicated that the critical speeds are superiors for 38CrMoAl steel, (1858.7, 1859.4, 8468.1 rpm) and lower for the steels of JIS-S45C (1784.2, 1784.9, 8147.7 rpm) by contribution the two steels (structural steels, titanium alloy (Ti-6Al-4V)). The natural frequencies of the Jeffcott rotor are also higher for 38CrMoAl steels and are equal for the two materials (Titanium alloy (Ti-6Al-4V), JIS-S45C) and minimum for structural steels. On the other hand, the results of the harmonic analysis indicated that the vibration severity is very lower for 38CrMoAl steels material (9435.2 MPa) and very higher for structural steels material (55134 MPa). The rotary machines undergoing high stress severity and deformation severity are recommended to use 38CrMoAl steels. Rotor dynamic analysis of Jeffcott rotor with four materials, JIS-S45C, 38CrMoAl, structural steel, titanium alloy materials are highly recommended with the less severity of vibration. Choose JIS-S45C and 38CrMoAl materials for higher whirling speeds compared to structural steel, titanium alloy materials. The rotary machines undergoing higher operating speeds like propeller shafts, turbine and compressor are recommended to use JIS S45C and 38CrMoAl.

Keywords: rotor; natural frequency; critical speeds; amplitudes; phase angle; damping; Von Mises stress; strain elastic; total displacement

Citation: Afane NEB, Zahaf S, Dahmane M, Belaziz A, Noureddine R. Modal and harmonic analysis of the rotor system involving four different materials by finite element code: Ansys workbench. *Materials Physics and Mechanics*. 2023;51(7): 63-98. DOI: 10.18149/MPM.5172023 7.

© N.E.B. Afane, S. Zahaf, M. Dahmane, A. Belaziz, R. Noureddine, 2023.

Publisher: Peter the Great St. Petersburg Polytechnic University

This is an open access article under the CC BY-NC 4.0 license (https://creativecommons.org/li-censes/by-nc/4.0/)

Introduction

Rotor Dynamics is a branch of physics which deals with study of behaviour of rotating systems under application of dynamic forces. Rotor is part of system i.e. disks, blades or couplings mounted on shaft is called as rotor. Rotor is used to convert one form of energy into another form hence rotational energy must be maximum, so we must reduce vibrational energy as much as possible, so they have wide range of applications in many industries as well as household applications so we need to analyse the system to prevent catastrophic failures.

Applications such as centrifugal pumps, generators, motors, compressors, blowers, sewing machine, steam turbines, gas turbines, aero engines, main and tail rotors of helicopters. In rotating system, flexural vibrations are main cause as compared to torsional vibration and axial vibration.

Unbalance in rotor gives raise to forces and moments in rotor, this generates flexural vibration in rotor. The vibrations perpendicular to the axis of rotation, such vibrations are known as flexural vibrations. Whirling is one of the main cause for failures of rotating systems due unbalance of rotor i.e. due to the manufacturing defects center of gravity of shaft doesn't coincide with axis of rotation, misalignment of rotor shaft and bearings, due to loose supports or if the machine is operated at critical speeds may lead to catastrophic failure of system.

Generally, rotors rotate at high speeds, when the natural frequency of the system is equal to the critical speed resonance occur. Resonance is the most common problem in rotating systems. In a rotating system, if there is some percentage of vibration in the machine, these vibrations are magnified by resonance. At these critical speeds the amplitude of vibration goes on increasing this cause rotor to bend and twist so this cause rubs or wear and tear and collide with adjacent parts of system hence excessive force are developed and hence leads to failure. So determination of natural frequency, critical speeds and amplitudes of vibrations are very important in rotor dynamics. As a designer by changing mass, stiffness, position of disk etc. such design modification to change critical speeds of system to operate in a suitable environment. To reduce whirling amplitudes, we must avoid rotating at critical speeds of the system, or squeeze film damper is suitable. By using damper, whirling amplitudes are reduced as well as reduces forces on the supports [1].

Tai et al. [2] analysed steady state response of a single rub-impact rotor system. The harmonic balance method with pseudo arc-length continuation is used to obtain the analytical solutions of the stable periodic motion. The changed of frequency response due to unbalance at first natural frequency was discussed. Nanfei Wang and Dongxiang Jiang [3] described vibration response characteristics of a dual rotor unbalance. The governing equation of dual rotor system with unbalance was numerically derived by using Runge Kutta method. The rotor test rig model was conducted to experimentally validate the responses due to the rotating unbalance. Juan Xu et al. [4] presented vibration characteristics of unbalance responses for motorized spindle system using mathematical and simulation models at high excitation frequencies. SM Ghoneam et al. [5] studied the dynamic analysis of a rotor system with active magnetic bearings. This system consists of a flexible shaft with a rigid disk and flexible bearings. Natural frequencies of rotor active magnetic bearings system are evaluated using Ansys Workbench and finite element based on Matlab code. Natural frequencies and mode shapes are evaluated in the case of free-free system and with AMB stiffness at rotational speed Ω =0. The results show that the natural frequencies increase with the increase of bearing stiffness. The higher modes do not differ much when the bearing stiffness increases. Stiffness of AMB increases with the increase in both current and number of turns, and decreases with the increase in the air gap. Comparison between results that obtained from Ansys Workbench and finite element and the error percentages between them has been illustrated. Very close agreement has been obtained. The results which obtained from Ansys Workbench are more accurate.

Amit Malgol et al. [1] studied and analysed of rotor shaft system for three different position of the disk, for a simply supported case, and it is important to determine natural frequency, critical speeds and amplitudes of rotor system. This characteristic is found by using ANSYS parametric design tool. Modal, harmonic and transient cases are carried out for the single rotor system. The results obtained for this analysis are useful for design of rotor system. The results obtained from analytical method have close agreement with the results obtained from ANSYS results.

Emna Sghaier et al. [6] created a new mathematical model for the dynamic behavior of the rotating machines at non-stationary regime shows coupling between the lateral and torsional degrees of freedom. It also shows strong non-linearities. The results of the simulations show that the model help to better understand the behavior of the rotating machinery. It shows the interaction between the rotational behavior and the lateral one, especially in the vicinity of the critical speed.

Yuanchang Chen et al. [7] studied a comprehensive experimental and numerical study based on three modal tests and a correlated finite element simulation to study the complex curvature mode shapes and mode coupling dynamics for a three bladed wind turbine assembly. Three tests are conducted: Test 1, ten accelerometers are deployed on the whole assembly under impact excitation; Test 2, nine accelerometers are deployed on a single blade under impact excitation; and Test 3, a non-contact 3D Scanning Laser Doppler Vibrometer (SLDV) test is performed on a single blade under shaker excitation. The results show that this model has an excellent correlation with both experimental mode shapes from the SLDV test and dynamic response from the impact test. All blade modes below 100 Hz are studied, and experimental and numerical modes give close frequency and well correlated mode shapes.

Mohamed Amine Dabachi et al. [8] studied the durability of Darrieus-type floating wind turbine blades with three-stage rotors under extreme load conditions. Considering the applied stresses, perfect long-term durability is required. FEM allows the selection of materials (fiber, matrix), fiber architectures (plies, tissues), and the optimization of lay-up sequences that minimize the sensitivity to mechanical stresses applied to the structures. The results show that the composite materials, with proper ply orientation, are the best choice to achieve these characteristics. These characteristics result in a high strength-to-weight ratio, which reduces the total weight of the blade and the centrifugal forces acting on it.

Arnab Bose et al. [9] analyzed the natural and whirl frequencies of a slant-cracked functionally graded rotor-bearing system using finite element analysis for the flexural vibrations. The functionally graded shaft is modelled using two nodded beam elements formulated using the Timoshenko beam theory. The flexibility matrix of a slant-cracked functionally graded shaft element has been derived using fracture mechanics concepts, which is further used to develop the stiffness matrix of a cracked element. Material properties are temperature and position dependent and graded in a radial direction following power-law gradation. A Python code has been developed to carry out the complete finite element analysis to determine the Eigenvalues and Eigenvectors of a slant-cracked rotor subjected to different thermal gradients. The analysis investigates and further reveals significant effect of the power-law index and thermal gradients on the local flexibility coefficients of slant-cracked element and whirl natural frequencies of the cracked functionally graded rotor system.

For mathematical modelling, D'Alembert's Principle was used to derive the equation of motion and ANSYS was used to simulate the response. Apart from those studies on analysis of vibration response due to rotating unbalance, Sudhakar and Sekhar et al. [10] identified unbalance fault in a rotor bearing system using equivalent loads minimization and vibration minimization method. Unbalance fault was experimentally identified for one rotating speed and three unbalance conditions. The maximum discrepancy was 23% in unbalance identification process. Using different method, Akash Shrivastava and Amiya Ranjan Mohanty et al. [11] also

identified unbalance in a rotor system. Three different rotating speeds and four unbalance conditions were presented using a joint input estimation. The maximum discrepancy between actual and estimated unbalance reported is 10 %. In the present study, Jeffcott rotor is simulated using FEM by ANSYS, and the Whirl map diagrams are plotted. The analytical results are reported with backward whirl when the rotor is coasting down.

Pavlenko et al. [12] aimed to investigating rotor dynamics of multistage centrifugal machines with ball bearings by using the computer programs "Critical frequencies of the rotor" and "Forced oscillations of the rotor," which are implemented the mathematical model based on the use of beam finite elements. Free and forces oscillations of the rotor for the multistage centrifugal oil pump NPS 200-700 are observed by taking into account the analytical dependence of bearing stiffness on rotor speed, which is previously defined on the basis of results' approximation for the numerical simulation in ANSYS by applying 3D finite elements. The calculations found that characteristic and constrained oscillations of rotor and corresponded to them forms of vibrations, as well as the form of constrained oscillation on the actual frequency for acceptable residual unbalance are determined.

Ralston Fernandes et al. [13] presented a methodology for conducting a 3-D static fracture analysis with applications to a gas turbine compressor blade. An open crack model is considered in the study, and crack-tip driving parameters are estimated by using 3-D singular crack-tip elements in ANSYS. The static fracture analysis is verified with a special purpose fracture code (FRANC3D). Results demonstrate that for the applied loading condition, a mixed mode crack propagation is expected. In the modal analysis study, increasing the depth of the crack leads to a decrease in the natural frequencies of both the single blade and bladed disk system, while increasing the rotational velocity increases the natural frequencies. The presence of a crack also leads to mode localization for all mode families, a phenomenon that cannot be captured by a single blade analysis.

Hyung-Chul Jung et al. [14] presented a rotor dynamic modelling and analysis of a radial inflow turbine rotor-bearing system. One of the challenging aspects of radial turbine design and manufacturing is vibration and stability. In this rotor dynamic analysis of a 1 kWe radial inflow turbine, a computer model is constructed for a rotating shaft with a row of rotor blades supported by two ball bearings. The modal and harmonic analyses are performed with the model to determine the design for safe operation of the turbine. The design parameters of the shaft length and diameter, and the distance between two bearings were varied to identify the critical speeds and unbalance response. A parametric study is then conducted on variations in unbalanced force and bearing stiffness.

Work objective and overall methodology

The scientific research objective for this study and the overall methodology as shown in Fig. 1. This article presents the study of the Jeffcott rotor shaft system for four different materials (JIS-S45C steels, 38CrMoAl steels, standard steels, titanium alloy steels (Ti-6AL-4V)), for a case simply supported, and it is important to determine the natural frequencies, critical speeds and amplitudes of the rotor system (von Mises stress, principal stress, maximum shear stress, lifetime). This characteristic is found by using the parametric design tool ANSYS Workbench. Modal, harmonic cases are realized for the single-rotor system. The results obtained for this analysis are useful for the design of the rotor system. In the present work, the dynamic analysis of the rotor is presented with a Jeffcott rotor with a single unbalance mass equal to 0.1 kg. The unbalance mass is symmetrical is mounted on a flexible rotor (see Fig. 2) and on a rigid bearing support and the work is analyzed with the ANSYS Workbench software.

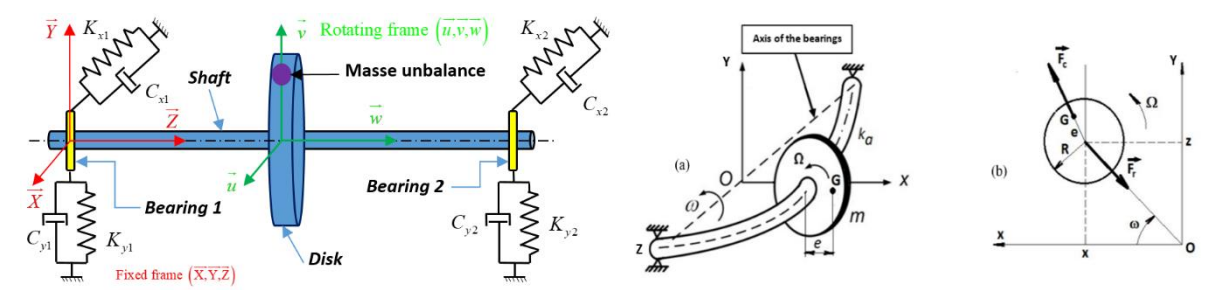


Fig. 1. Dynamic rotor system studied [15]

Fig. 2. LAVAL/JEFFCOTT model (a) and plan of oscillations (xoz) (b)

 $\overrightarrow{F_c}$ - centrifugal inertial force due to unbalance, $\overrightarrow{F_r}$ - restoring force due to shaft flexibility, e - unbalance eccentricity, R - shaft radius.

In this context, the dynamic characteristics have been analyzed and evaluated where the critical speeds are reported on the basis of the modal analysis, the unbalanced response of the harmonic response, neglecting the gyroscopic effect.

Fundamental equation

The general form of equation of motion for all vibration problems is given by, $[M]{\ddot{u}} + [C]{\dot{u}} + [K]{u} = {f},$ (1)

where, symmetric mass matrix $[M] = {m \choose 0}m$, symmetric damping matrix $[C] = {c \choose -2m\omega} {c \choose 0}$, symmetric stiffness matrix $[K] = {K \choose 0} {K \choose 0}$, external force vector $\{f\} = {-mg \sin \theta \choose -mg \cos \theta} = f(t)$, generalized coordinate vector in rotordynamics $\{u\}$.

This equation of motion can be expressed in the following general form [3].
$$[M]\{\ddot{u}\} + ([C] + [G])\{\dot{u}\} + ([K] + [B])\{u\} = \{f\}. \tag{2}$$

The above-mentioned equation (2) describes the motion of an axially symmetric rotor, which is rotating at constant spin speed Ω about its spin axis. This equation is just similar to the general dynamic equation except it is accompanied by skew-symmetric gyroscopic matrix, [G] and skew-symmetric circulatory matrix [B]. The gyroscopic and circulatory matrices [G]and [B] are greatly influenced by rotational velocity Ω . When the rotational velocity Ω , tends to zero, the skew-symmetric terms present in equation (2) vanish and represent an ordinary stand still structure. The gyroscopic matrix [G] contains inertial terms and that are derived from kinetic energy due to gyroscopic moments acting on the rotating parts of the machine. If this equation is described in rotating reference frame, this gyroscopic matrix [G] also contains the terms associated with Carioles acceleration.

The circulatory matrix [B] is contributed mainly from internal damping of rotating elements [16]. The concept of rotor dynamics can be easily demonstrated with the help of generalized Laval-Jeffcott rotor modal, as shown in Fig. 2.

The generalized Laval-Jeffcott rotor consists of a long, flexible mass less shaft with flexible bearings on both the ends. The bearings have support stiffness of K_x and K_y associated with damping C_x and C_y in x and y direction respectively. There is a massive disk of mass, m located at the center of the shaft. The center of gravity of the disk is offset from the shaft geometric center by an eccentricity of e. The motion of the disk center is described by two translational displacements, (x, y) as shown in Fig. 2 and 3. We consider that:

- 1. Lateral vibrations are damped;
- 2. The model is symmetrical;
- 3. Gravity and the gyroscopic effect are neglected;
- 4. The rotational speed Ω is constant;
- 5. The oscillations take place in the plane perpendicular to the plane of equilibrium of the system.

Let's go back to the JEFFCOTT model and consider the flexible and isotropic bearings, i.e. the characteristics are identical in the 2 directions Ox and Oy as shown in Fig. 3.

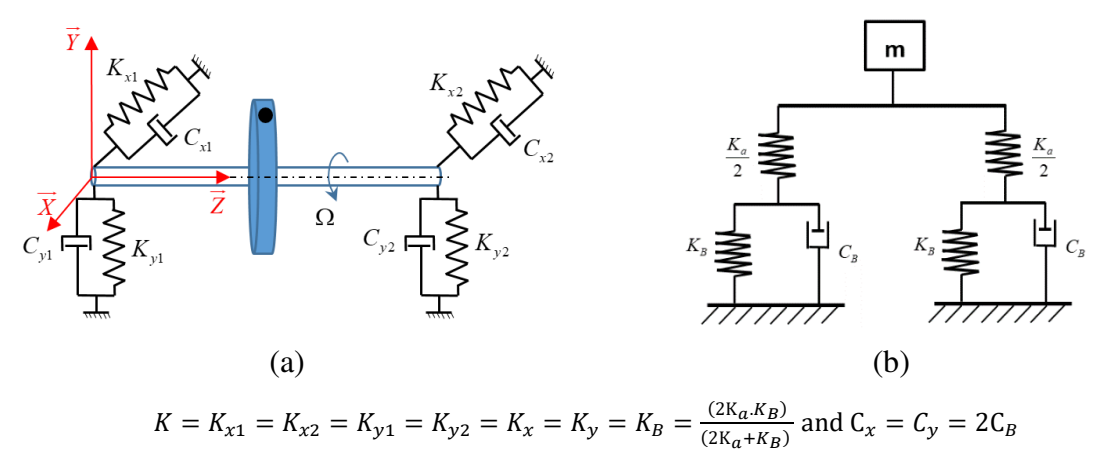


Fig. 3. Model with flexible and isotropic bearings (a), and oscillator in each direction (b)

When the rotor is rotating at constant rotational speed, the equation of motion for the mass center can be derived from Newton's law of motion, and it is expressed in the following form.

$$m\frac{d^2}{dt^2}(x + e\cos(\Omega t + \phi_e)) = -C_x\dot{x} - K_x x \tag{3}$$

$$m\frac{d^2}{dt^2}(y + e\sin(\Omega t + \phi_e)) = -C_y\dot{y} - K_yy$$
(4)

The above equations can be re-written as,

$$m\ddot{x} + C_{x}\dot{x} + K_{x}x = me\Omega^{2\cos(\Omega t + \phi_{e})},$$

$$m\ddot{y} + C_{y}\dot{y} + K_{y}y = me\Omega^{2}\sin(\Omega t + \phi_{e}),$$
(5)
(6)

$$m\ddot{y} + C_{y}\dot{y} + K_{y}y = me\Omega^{2}\sin(\Omega t + \phi_{e}), \tag{6}$$

where, is the phase angle of the mass unbalance. The above equations of motions show that the motions in X and Y direction are both dynamically and statically decoupled in this model. Therefore, they can be solved separately.

Determination of natural frequencies. For this simple rotor model, the undamped natural frequency, damping ration and the damped natural frequency of the rotor model for X and Y direction can be calculated from.

$$\omega_{nx} = \sqrt{\frac{K_x}{m}}, \zeta_x = \frac{c_x}{2m\omega_{nx'}}, \omega_x = \omega_{nx}\sqrt{1 - \zeta_x^2}, \omega_{ny} = \sqrt{\frac{K_y}{m}}, \zeta_y = \frac{c_y}{2m\omega_{ny'}}, \omega_y = \omega_{ny}\sqrt{1 - \zeta_y^2}$$
 (7)

Steady state response to unbalance. For a single unbalance force, as present in this case, that can be set to zero. Therefore, the equations (5) and (6) becomes,

$$m\ddot{x} + C_{\chi}\dot{x} + K_{\chi}x = me\Omega^{2}\cos(\Omega t), \tag{8}$$

$$m\ddot{y} + C_{\nu}\dot{y} + K_{\nu}y = me\Omega^2 \sin(\Omega t). \tag{9}$$

Then the solution for the response is,

$$|x| = \frac{me\Omega^2}{\sqrt{[(K_x - \Omega^2 m)^2 + (\Omega C_x)^2]}},\tag{10}$$

$$|x| = \frac{me\Omega^2}{\sqrt{[(K_x - \Omega^2 m)^2 + (\Omega C_x)^2]}},$$

$$|y| = \frac{me\Omega^2}{\sqrt{[(K_y - \Omega^2 m)^2 + (\Omega C_y)^2]}}.$$
(11)

Rotor-Dynamic Analysis: modal and harmonic

Modal analysis. The role of Modal analysis is to facilitate the investigations pertaining to the vibration characteristics (natural frequencies and mode shapes) of a mechanical structure or component, showing the movement of different parts of the structure under dynamic loading conditions. Modal Analysis offers different modes with natural frequencies and, one can obtain the critical speeds from the whirl map diagram, which are useful to review the stability and resonance occurrence possibility. Its use can be observed in different fields such as rotor dynamic analysis for a hydraulic turbine [17] to chaotic vibration reduction in a centrifugal pump [18]. Modal fitting of different vibration modes and use of frequency response functions facilitate virtual manufacturing setup for the use of structural dynamics concepts [19]. In context to modal analysis, Jeffcott rotor equations of motion are as under, covering forces [20,21].

Harmonic response analysis. The role of harmonic response analysis is to determine responses towards balanced and unbalanced excitations. Many researchers have explored and admired the effectiveness of harmonic response analysis to find results based on various vibration parameters [22-24]. To perform a harmonic analysis of an unbalanced excitation; the effect of the unbalanced mass is represented by the forces in the two perpendicular directions to the spinning axis. For a single mass unbalance, the angle a will be zero and one will get the following expressions for the forces in the XY plane, as shown in Fig. 4:

$$F_x = F_c \cos \Omega \, t = F_c e^{j\Omega t},\tag{12}$$

$$F_{x} = F_{c} \cos \Omega t = F_{c} e^{j\Omega t},$$

$$F_{y} = F_{c} \sin \Omega t = F_{c} \cos \left(\Omega t - \frac{\pi}{2}\right),$$
(12)

where, The Z-axis is a spinning axis, m = unbalance mass, $\Omega = \text{rotational velocity}$, r = radiusof the eccentric mass, ω = angular velocity of in rad/sec.

Mathemanical modeling

To perform the simulations, is necessary to obtain the mathematical model of the rotor-bearing system, where was used Finite Element Method. Initially it was found the kinetic energy, potential and forces that were applied to the elements of the system, as described by [25].

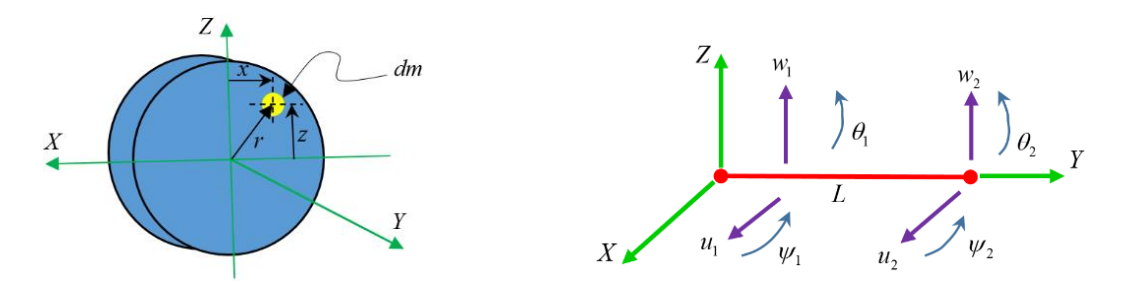


Fig. 4. Representation of disk [27] **Fig. 5.** Modeling of one dimensional (1D) rotor [29]

Finite elements method. According to Rao [26], these methods allow more accurate predictions, reducing the cost of experiments and simulation, thus achieving cheaper and more accurate designs before testing prototypes. Through this method can be found matrices of mass, stiffness, damping, the gyroscopic effect mass and unbalanced. In this method is used the energy equations for each element, and without the generalized coordinates, but with the degrees of freedom available in the element. For the derivation of the equations of motion of the rotor, just apply the Lagrange equation in the kinetic energy, potential and forces of the system, as described by [27]. The general equation is given as:

$$\frac{d}{dt}\left(\frac{\partial T}{\partial \delta}\right) - \frac{\partial T}{\partial \delta} + \frac{\partial U}{\partial \delta} = F,\tag{14}$$

where $(N(1 \le i \le N))$ is the number of degree of freedom, δ is the displacement vector and ° indicates differentiation in relation to time. These equation follows a procedure used by [28]. In the case of the disc element, as it has four degrees of freedom, u, w, θ and ψ , Fig. 4.

Assuming that the kinetic energy of the disc is obtained using Lagrange has to the following equation:

$$\frac{d}{dt} \left(\frac{\partial T_D}{\partial \delta'} \right) - \frac{\partial T_D}{\partial \delta} = [M_D] \{ \delta'' \} + \Omega[C_D] \{ \delta' \}, \tag{15}$$

where $[M_D]$ is the classical mass matrix and $[C_D]$ is the gyroscopic matrix.

In 1D finite element, the shaft is modeled as a beam which has a constant circular crosssection. If the element has two nodal, it will form the 8- order matrix. Each of the nodal has 4 degrees of freedom: 2 displacements and 2 slopes in both x-y plane and y-z planes (Fig. 5), therefore nodal displacement vector can be written in the equation [29]. To shaft matrices, first is shown that this have to be divided through nodes, as shown in Fig. 5:

$$\delta = [u_1, w_1, \theta_1, \Psi_1, u_2, w_2, \theta_2, \Psi_2]^T. \tag{16}$$

The relationship between displacement and slope are:

$$\theta = \frac{\delta w}{\delta y},\tag{17}$$

$$\Psi = -\frac{\delta u}{\delta v}.\tag{18}$$

Displacements δu and δw in accordance with movements in the X and Y directions written by the equation:

$$\delta u = [u_1, \Psi_1, u_2, \Psi_2]^T, \tag{19}$$

$$\delta w = [w_1, \theta_1, w_2, \theta_2]^T. \tag{20}$$

Displacements in the finite element are formed from:

$$u = N_1(y)\delta u, (21)$$

$$w = N_2(y)\delta w. (22)$$

 $N_1(y)$ and $N_2(y)$ are the function of displacements for the beam that are subjected to bending loads:

$$N_{1}(y) = \left[1 - \frac{3y^{2}}{L^{2}} + \frac{2y^{3}}{L^{3}}; -y + \frac{2y^{2}}{L} - \frac{y^{3}}{L^{2}}; \frac{3y^{2}}{L^{2}} - \frac{2y^{3}}{L^{3}}; \frac{y^{2}}{L} - \frac{y^{3}}{L^{2}}\right],$$

$$N_{2}(y) = \left[1 - \frac{3y^{2}}{L^{2}} + \frac{2y^{3}}{L^{3}}; y - \frac{2y^{2}}{L} + \frac{y^{3}}{L^{2}}; \frac{3y^{2}}{L^{2}} - \frac{2y^{3}}{L^{3}}; -\frac{y^{2}}{L} + \frac{y^{3}}{L^{2}}\right].$$
Kinetic energy of the shaft can be calculated as [29]:

$$N_2(y) = \left[1 - \frac{3y^2}{L^2} + \frac{2y^3}{L^3}; y - \frac{2y^2}{L} + \frac{y^3}{L^2}; \frac{3y^2}{L^2} - \frac{2y^3}{L^3}; -\frac{y^2}{L} + \frac{y^3}{L^2}\right]. \tag{24}$$

$$T = \frac{\rho S}{2} \int_0^L \left[\delta \dot{u}^T N_1^T N_1 \delta \dot{u} + \delta \dot{w}^T N_2^T N_2 \delta \dot{w} \right] dy + \frac{\rho I}{2} \int_0^L \left[\delta \dot{u}^T \frac{dN_1^T}{dy} \frac{dN_1}{dy} \delta \dot{u} + \delta \dot{w}^T \frac{dN_2^T}{dy} \frac{dN_2}{dy} \delta \dot{w} \right] dy - 2\rho I \Omega \int_0^L \delta \dot{u}^T \frac{dN_1^T}{dy} \frac{dN_2}{dy} \delta w dy + \rho I L \Omega^2,$$

$$(25)$$

where ρ is the density, S is the cross-sectional area of the beam, and N shape functions, I is the area moment of inertia of the beam cross-section about the neutral axis, Ω angular velocity and L is the length of the element. Making the necessary integrations and applying Lagrange, is obtained. Substitution of equation (23) and (24) into equation (25), then [27]:

$$T = \frac{1}{2}\delta\dot{u}^T M_1 \delta\dot{u} + \frac{1}{2}\delta\dot{w}^T M_2 \delta\dot{w} + \frac{1}{2}\delta\dot{u}^T M_3 \delta\dot{u} + \frac{1}{2}\delta\dot{w}^T M_4 \delta\dot{w} + \Omega\delta\dot{u}^T M_5 \delta w + \rho IL\Omega^2, \quad (26)$$

where M_1 and M_2 are the classical mass matrix, M_3 and M_4 are generated due to a secondary effect of rotor inertia, and M_5 is generated due to gyroscopic. By applying the Lagrange equation, then [27]:

$$\frac{d}{dt}\left(\frac{\partial T}{\partial \dot{\delta}}\right) - \frac{\partial T}{\partial \delta} = (M + M_S)\ddot{\delta} + C\dot{\delta},\tag{27}$$

where [M] is the classical mass matrix, $[M_s]$ effect of inertia matrix and $[C_s]$ gyroscopic matrix. Where M and M_s are obtained from M_1, M_2, M_3, M_4 and C from M_5 , thus [27]:

$$M = \frac{\rho SL}{420} \begin{bmatrix} 156 & 0 & 0 & -22L & 54 & 0 & 0 & 13L \\ 0 & 156 & 22L & 0 & 0 & 54 & -13L & 0 \\ 0 & 22L & 4L^2 & 0 & 0 & 13L & -3L^2 & 0 \\ -22L & 0 & 0 & 4L^2 & -13L & 0 & 0 & -3L^2 \\ 54 & 0 & 0 & -13L & 156 & 0 & 0 & 22L \\ 0 & 54 & 13L & 0 & 0 & 156 & -22L & 0 \\ 0 & -13L & -3L^2 & 0 & 0 & -22L & 4L^2 & 0 \\ 13L & 0 & 0 & -3L^2 & 22L & 0 & 0 & 4L^2 \end{bmatrix},$$
 (29)

$$M_{S} = \frac{\rho I}{30L} \begin{bmatrix} 36 & 0 & 0 & -3L & -36 & 0 & 0 & -3L \\ 0 & 36 & 3L & 0 & 0 & -36 & 3L & 0 \\ 0 & 3L & 4L^{2} & 0 & 0 & -3L & -L^{2} & 0 \\ -3L & 0 & 0 & 4L^{2} & 3L & 0 & 0 & -L^{2} \\ -36 & 0 & 0 & 3L & 36 & 0 & 0 & 3L \\ 0 & -36 & -3L & 0 & 0 & 36 & -3L & 0 \\ 0 & 3L & -L^{2} & 0 & 0 & -3L & 4L^{2} & 0 \\ -3L & 0 & 0 & -L^{2} & 3L & 0 & 0 & 4L^{2} \end{bmatrix},$$

$$(30)$$

$$C = \frac{\rho I\Omega}{15L} \begin{bmatrix} 36 & 0 & 0 & -3L & -36 & 0 & 0 & -3L \\ 0 & 36 & 3L & 0 & 0 & -36 & 3L & 0 \\ 0 & 3L & 4L^2 & 0 & 0 & -3L & -L^2 & 0 \\ -3L & 0 & 0 & 4L^2 & 3L & 0 & 0 & -L^2 \\ -36 & 0 & 0 & 3L & 36 & 0 & 0 & 3L \\ 0 & -36 & -3L & 0 & 0 & 36 & -3L & 0 \\ 0 & 3L & -L^2 & 0 & 0 & -3L & 4L^2 & 0 \\ -3L & 0 & 0 & -L^2 & 3L & 0 & 0 & 4L^2 \end{bmatrix}.$$

$$(31)$$

Strain energy on the shaft can be calculated by the equation [27]:

$$U = \frac{EI}{2} \int_{0}^{L} \left[\delta u^{T} \frac{d^{2}N_{1}^{T}}{dy^{2}} \frac{d^{2}N_{1}}{dy^{2}} \delta u + \delta w^{T} \frac{d^{2}N_{2}^{T}}{dy^{2}} \frac{d^{2}N_{2}}{dy^{2}} \delta w \right] dy + \frac{F_{0}}{2} \int_{0}^{L} \left[\delta u^{T} \frac{dN_{1}^{T}}{dy} \frac{dN_{1}}{dy} \delta u + \delta w^{T} \frac{dN_{2}^{T}}{dy} \frac{dN_{2}}{dy} \delta w \right] dy.$$
 (32)

Then, after integration:

$$U = \frac{1}{2}\delta u^T K_1 \delta u + \frac{1}{2}\delta w^T K_2 \delta w + \frac{1}{2}\delta u^T K_3 \delta u + \frac{1}{2}\delta w^T K_4 \delta w, \tag{33}$$

where $[K_1]$ and $[K_2]$ are the classical stiffness matrix $[K_c]$, $[K_3]$ and $[K_4]$ are the matrix due to the axial force (K_f) . The effect of shear force can be calculated by the equation [27]:

$$a = \frac{12EI}{GS_r L^2}. (34)$$

With shear modulus [27]:

$$G = \frac{E}{2(1+v)},\tag{35}$$

where v is the Poissons ratio and E is Young's modulus of the material. Then by applying Eq. (32) to the Lagrange equation [27]:

$$\frac{\partial U}{\partial \delta} = K\delta,\tag{36}$$

$$K = K_C + K_F, \tag{37}$$

where $[K_c]$ and $[K_F]$, can be calculated [27]:

$$K_{C} = \frac{EI}{(1+a)L^{3}} \begin{bmatrix} 12 & 0 & 0 & -6L & -12 & 0 & 0 & -6L \\ 0 & 12 & 6L & 0 & 0 & -12 & 6L & 0 \\ 0 & 6L & (4+a)L^{2} & 0 & 0 & -6L & (2-a)L^{2} & 0 \\ -6L & 0 & 0 & (4+a)L^{2} & 6L & 0 & 0 & (2-a)L^{2} \\ -12 & 0 & 0 & 6L & 12 & 0 & 0 & 6L \\ 0 & -12 & -6L & 0 & 0 & 12 & -6L & 0 \\ 0 & 6L & (2-a)L^{2} & 0 & 0 & -6L & (4+a)L^{2} & 0 \\ -6L & 0 & 0 & (2-a)L^{2} & 6L & 0 & 0 & (4+a)L^{2} \end{bmatrix}, (38)$$

$$K_{F} = \frac{F}{30L} \begin{bmatrix} 36 & 0 & 0 & -3L & -36 & 0 & 0 & -3L \\ 0 & 36 & 3L & 0 & 0 & -36 & 3L & 0 \\ 0 & 3L & 4L^{2} & 0 & 0 & -3L & -L^{2} & 0 \\ -3L & 0 & 0 & 4L^{2} & 3L & 0 & 0 & -L^{2} \\ -36 & 0 & 0 & 3L & 36 & 0 & 0 & 3L \\ 0 & 3L & -L^{2} & 0 & 0 & -3L & 4L^{2} & 0 \\ 0 & 3L & -L^{2} & 0 & 0 & -3L & 4L^{2} & 0 \\ -3L & 0 & 0 & -L^{2} & 3L & 0 & 0 & 4L^{2} \end{bmatrix}.$$

$$(39)$$

Moreover, the disc is the main element of the rotor system, which is characterized only by its kinetic energy. The node of the rotor has four degrees of freedom: two displacements u and w and two slopes about the x-y and y-z planes, which are θ and ψ respectively. Then if the nodal displacement vector δ of the center of the disk is [30]:

$$\delta = [u, w, \theta, \Psi]^T. \tag{40}$$

By applying the Lagrange equations, the equation for the disk:

where the first matrix is the classical stiffness matrix and the second one is the matrix due to gyroscopic effects. In this study, the effects of bearing influence are neglected so that the general equation of rotor dynamics is [30]:

$$M\ddot{\delta} + K\delta = F(t), \tag{42}$$

where δ is all nodal displacement vectors, M is the mass matrix, K is the stiffness matrix and F(t) is the force vector. 1D finite element analysis in this study uses the discretization of 3 elements and 4 nodal. Simplification scheme of the rotor with dimension in mm is shown in Fig. 6.

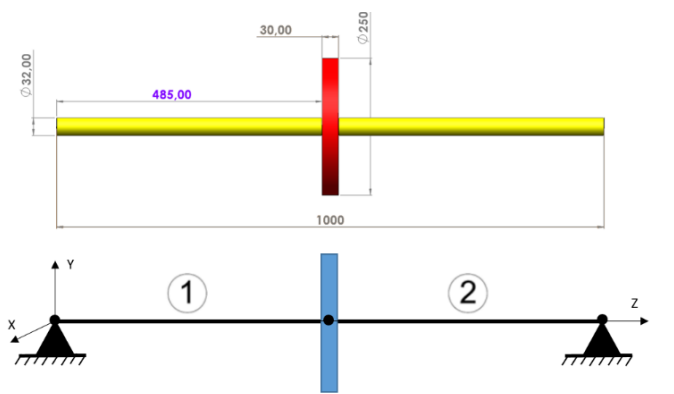


Fig. 6. Simplification scheme of the discretization in 1D finite element analysis for the rotor

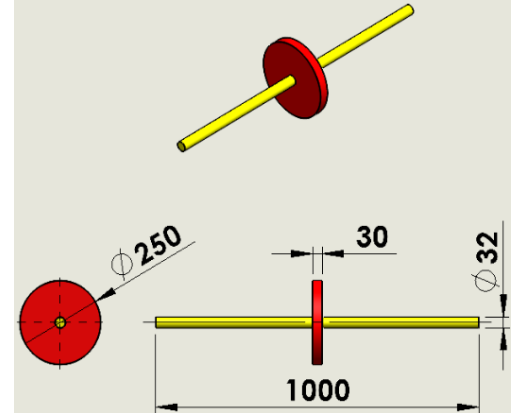


Fig. 7. Jeffcott rotor model definition drawing (using Solidworks)

To produce the equality throughout the element, the local element matrix of each element is arranged into a global matrix. Every element, which has the same number of nodal and that of degrees of freedom, is placed on the same row and column and this applies to the mass matrix, stiffness matrix and damping matrix [27]. The illustrative example of the element assembly from local elements into global element for two local elements can be seen in Fig. 6. Globalizing matrix in this way is the fastest and easy, even for a lot of elements and nodal degrees of freedom. In addition to the dimensions of each component of the rotor, the mechanical properties of the component are also required as the input data of the calculation.

As for bearing is simpler to find the matrix, because having the force equation, the matrix is obtained directly:

$$\begin{bmatrix}
F_{u} \\
F_{\theta} \\
F_{\omega} \\
F_{\psi}
\end{bmatrix} = - \begin{bmatrix}
k_{xx} & 0 & k_{xz} & 0 \\
0 & 0 & 0 & 0 \\
k_{zx} & 0 & k_{zz} & 0 \\
0 & 0 & 0 & 0
\end{bmatrix} \begin{bmatrix} u \\ \theta \\ \omega \\ \psi \end{bmatrix} - \begin{bmatrix} c_{xx} & 0 & c_{xz} & 0 \\
0 & 0 & 0 & 0 \\
c_{zx} & 0 & c_{zz} & 0 \\
0 & 0 & 0 & 0
\end{bmatrix} \begin{bmatrix} \dot{u} \\ \dot{\theta} \\ \dot{\omega} \\ \dot{\psi} \end{bmatrix}.$$
(43)

Considering the first the matrix of stiffness and the second matrix of damping, where they can be symmetric, when $k_{xx} = k_{yy}$ et $c_{xx} = c_{yy}$ or asymmetric when $k_{xx} \neq k_{yy}$ et $c_{xx} \neq c_{yy}$.

In the case of unbalanced mass matrix is also obtained directly, applying the Lagrange in the equation kinetic energy of the unbalanced mass, we obtain the following matrix.

$$\begin{bmatrix} F_u \\ F_{\omega} \end{bmatrix} = m_u d\Omega^2 \begin{bmatrix} \cos(\Omega t + \alpha) \\ \sin(\Omega t + \alpha) \end{bmatrix},\tag{43}$$

where Ω is the angular velocity and α is the angular position with respect z axis.

Analysis by 3D finite element method of the rotor dynamics system

Jeffcott rotor geometry and mechanical properties of materials. The program Solidworks, seen in Fig. 7, is used to create the Jeffcott rotor model. The shaft's dimensions are L = 1000 mm in length and d = 32 mm in diameter. Bearings on both ends of the shaft support the rotor. The center is mounted with a disc that has an offset mass of 0.1 kg. The disc has the following measurements: 250 mm in diameter, 30 mm in thickness, and an equal mass unbalance (0.1 kg). A geometric shaft center and an eccentricity of e separate the unbalance's center of gravity from each other. The CAD model and schematic design of the Jeffcott rotor are shown in Figs. 8 and 9. Table 1 depicts the material characteristics. Engineering materials utilized primarily in rotor machines, such as low-carbon steels (JIS-S45C steel, 38CrMoAl steel, structural steel, and titanium alloy steel (Ti-6AL-4V)), were included by the authors.

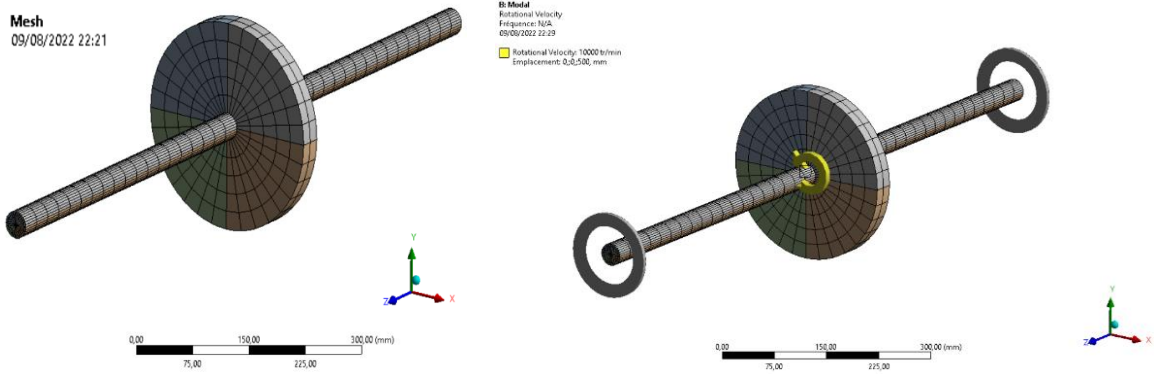


Fig. 8. Global mesh of the Jeffcott rotor model

Fig. 9. Boundary conditions of the Jeffcott rotor model: modale analysis

Sl.no:	Droportios	JIS-S45C	38CrMoAl	Structure	Ti-6Al-4V alloy	Units
51.110:	Properties	steel	steel	steel	steel	Units
1	Density	7700	7850	7850		Kg/m ³
2	Young's modulus	190	210	200	114	GPa
						Unit
3	Poisson's ratio	0,27	0.3	0.3	0.35	less
						quantity
4	Shear modulus	7.4803E+10	8.0769E+10	7.6923E+10	4.2222E+10	Pa
5	Tensile strength,	569	571	460	1170	MPa
	ultimate	2.42	420	250	1100	MD
6	Tensile strength	343	439	250	1100	MPa
7	Elongation at break	20	10	23	10	%
8	Bearing stiffness	1.6e+006	1.6e+006	1.6e+006	1.6e+006	N/mm
9	Bearing damp	23000	23000	23000	23000	N·s/mm
10	Mass	17.346	17.346	17.346	17.346	kø

Table 1. Material properties of 4 steels.

Jeffcott rotor mesh by Ansys Workbench. Given that the geometry of the product is broken down into a limited number of pieces, meshing is an essential component of ANSYS and works with computer-aided design and engineering processes. The fundamental principle of FEA is to do calculations at a finite set of points and then extrapolate the outcomes to the full volume. Every continuous object has a potentially huge number of degrees of freedom, which could make it difficult to discover solutions by FEA through the use of discretization or meshing, FEA reduces degrees of freedom from infinite to finite. The geometry for the selected Jeffcott rotor with shaft includes 8537 elements with a dimension of 7 mm and 28,682 nodes (details of which have already been disclosed). (As depicted in Fig. 8).

Boundary conditions. For modal analysis we fixed Z-axis rotation and translation and stiff behavior at both ends, displacements are employed as a constraint for modal analysis. Two displacements at the level of bearing A and B with fixed Z-axis rotation and translation and rigid behavior at both ends are utilized as a restriction for harmonic response analysis (see Figs. 9 and 10). The unbalanced forces, stresses, phase angles, and deformations are measured at the first natural frequencies because the initial resonance possibility is at the first mode.

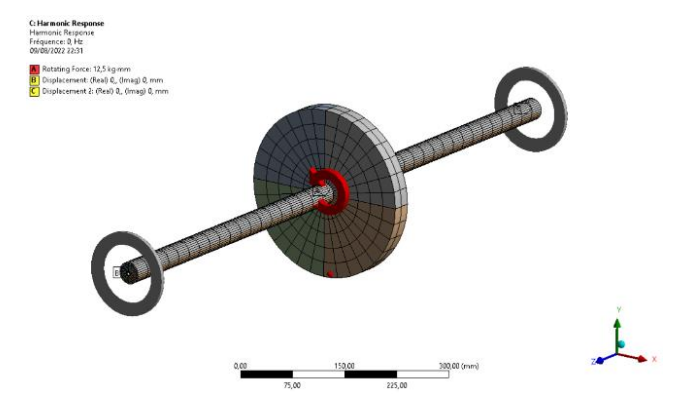


Fig. 10. Boundary conditions of the Jeffcott rotor model: harmonis response analysis

Results and Discussion

Modal Analysis. The following Tables 2-5 indicate the natural frequencies of the Jeffcott rotor for four materials and for ten different modes. In Tables 2-5, we notice that the natural frequencies in the almost four materials are similar and increase progressively, 0 Hz in the first mode, 265.27 Hz in the fifth mode, 652.73 Hz in the tenth mode, 1596.2 Hz in the fifteenth

mode, 2685 Hz in twentieth mode. In this case, we will simply extract the results in the last ten frequencies only and comment on them.

For JIS-S45C steel material. The maximum deformation for the material (*JIS-S45C* steel material) and varies from 13.948 mm at 1st mode, 18.134 mm at 2nd mode, 12.989 mm at 3rd mode, 18.045 mm at 4th mode, 27.928 mm at 5th mode, 27.887 mm at 6th mode, 15.294 mm at 7th mode, 20.07 mm at 8th mode, 19.364 mm at 9th mode, 15.293 mm at 10th mode as shown in Fig. 11.

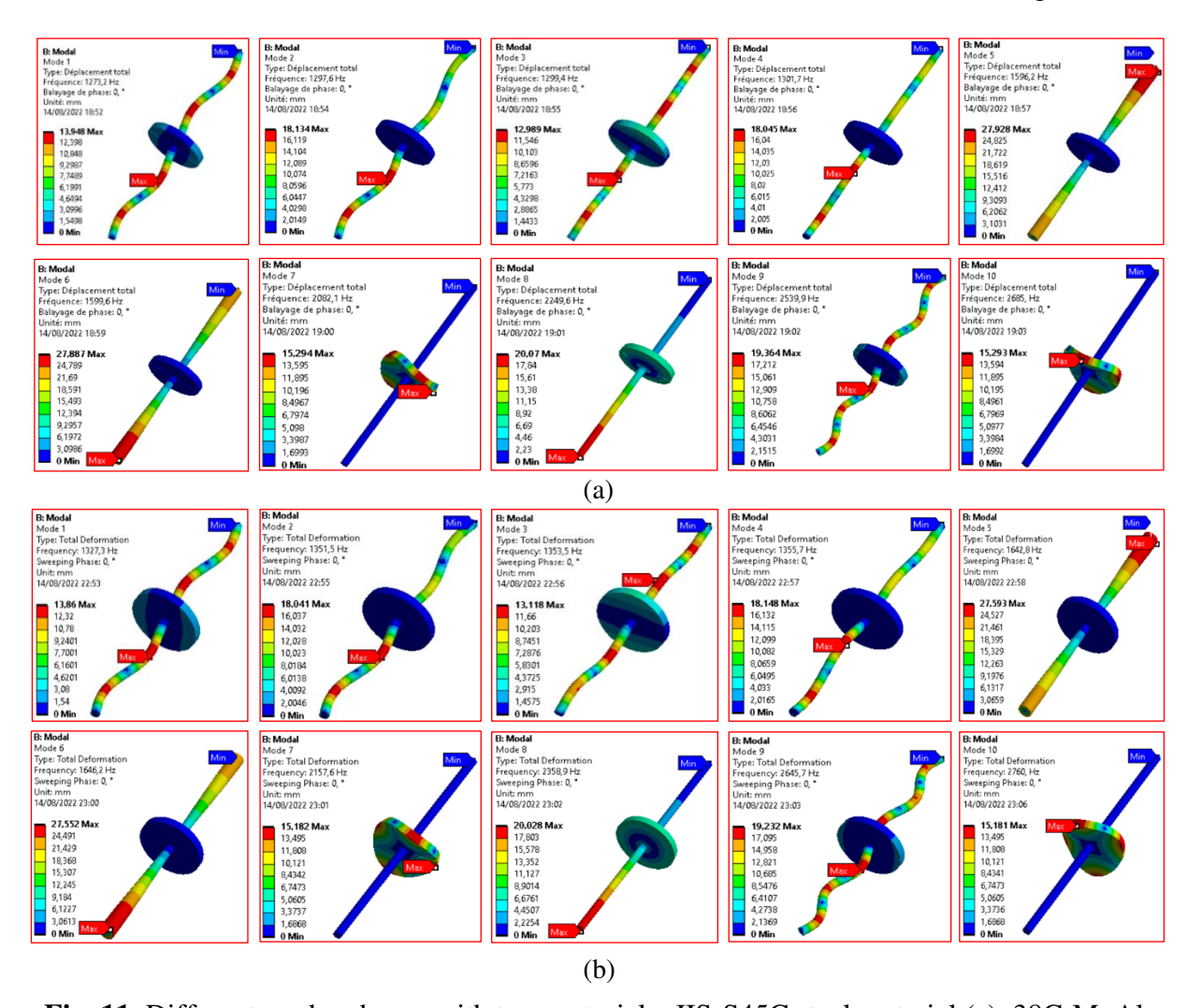


Fig. 11. Different modes shapes with two materials: JIS-S45C steel material (a), 38CrMoAl steel material (b)

For 38CrMoAl steel material. The maximum deformation for the material (38CrMoAl steel material) and varies from 13.86 mm at 1st mode, 18.041 mm at 2nd mode, 13.118 mm at 3rd mode, 18.148 mm at 4th mode, 27.593 mm at 5th mode, 27.552 mm at 6th mode, 15.182 mm at 7th mode, 20.028 mm at 8th mode, 19.232 mm at 9th mode, 15.181 mm at 10th mode as shown in Fig. 11. The natural frequencies and several modes of two materials are shown in the above Tables 2, 3 when the speed varies from 0 to10000 rpm.

For JIS-S45C steel material. The resonance occurrence possibilities are found from the whirl map diagram in the first 3 modes. 1784.2 rpm in a backward whirl at a natural frequency of 29.72 Hz, 1784.9 rpm in a forward whirl at a natural frequency of 29.765 Hz, 8147.7 rpm in the backward whirl at a natural frequency of 123.55 Hz as shown in Table. 2.

Mode	Whirl Direction	Mode Stability	Critical Speed	0, rpm	10000 rpm
1	UNDETERMINED	UNSTABLE	0, rpm	0, Hz	0, Hz
2	BW	STABLE	1784,2 rpm	29,74 Hz	29,72 Hz
3	FW	STABLE	1784,9 rpm	29,745 Hz	29,765 Hz
4	BW	STABLE	8147,7 rpm	189,64 Hz	123,55 Hz
5	FW	STABLE	0, rpm	189,66 Hz	265,27 Hz
6	BW	STABLE	0, rpm	425,59 Hz	425,14 Hz
7	FW	STABLE	0, rpm	425,79 Hz	426,24 Hz
8	BW	STABLE	0, rpm	512,33 Hz	463,43 Hz
9	FW	STABLE	0, rpm	512,69 Hz	619,19 Hz
10	FW	STABLE	0, rpm	652,73 Hz	652,73 Hz
11	BW	STABLE	0, rpm	1282,6 Hz	1273,2 Hz
12	BW	STABLE	0, rpm	1284,3 Hz	1297,6 Hz
13	FW	STABLE	0, rpm	1298,9 Hz	1299,4 Hz
14	FW	STABLE	0, rpm	1300,5 Hz	1301,7 Hz
15	BW	STABLE	0, rpm	1596,2 Hz	1596,2 Hz
16	BW	STABLE	0, rpm	1599,6 Hz	1599,6 Hz
17	BW	STABLE	0, rpm	2249,6 Hz	2082,1 Hz
18	FW	STABLE	0, rpm	2364,1 Hz	2249,6 Hz
19	BW	STABLE	0, rpm	2364,8 Hz	2539,9 Hz
20	FW	STABLE	0. rpm	2539.6 Hz	2685, Hz

Table. 2. Whirl map Campbell Diagram of JIS S45C steel material

For 38CrMoAl steel material. The resonance occurrence possibilities are found from the whirl map diagram in the first 3 modes. 1858.7 rpm in a backward whirl at a natural frequency of 30.962 Hz, 1859.4 rpm in a forward whirl at a natural frequency of 31.007 Hz, 8468.1 rpm in the backward whirl at a natural frequency of 130.94 Hz as shown in Table. 3.

Table. 3. Whirl map Campbell Diagram of 38CrMoAl steel material

Mode	Whirl Direction	Mode Stability	Critical Speed	0, rpm	10000 rpm
1	UNDETERMINED	STABLE	0, rpm	3,5879e-004 Hz	3,5879e-004 Hz
2	BW	STABLE	1858,7 rpm	30,982 Hz	30,962 Hz
3	FW	STABLE	1859,4 rpm	30,987 Hz	31,007 Hz
4	BW	STABLE	8468,1 rpm	197,51 Hz	130,94 Hz
5	FW	STABLE	0, rpm	197,53 Hz	273,46 Hz
6	BW	STABLE	0, rpm	443,38 Hz	442,93 Hz
7	FW	STABLE	0, rpm	443,59 Hz	444,04 Hz
8	BW	STABLE	0, rpm	534,24 Hz	484,63 Hz
9	FW	STABLE	0, rpm	534,62 Hz	639,49 Hz
10	FW	STABLE	0, rpm	680,55 Hz	680,55 Hz
11	BW	STABLE	0, rpm	1336,7 Hz	1327,3 Hz
12	BW	STABLE	0, rpm	1338,5 Hz	1351,5 Hz
13	FW	STABLE	0, rpm	1352,8 Hz	1353,5 Hz
14	FW	STABLE	0, rpm	1354,5 Hz	1355,7 Hz
15	BW	STABLE	0, rpm	1642,8 Hz	1642,8 Hz
16	BW	STABLE	0, rpm	1646,2 Hz	1646,2 Hz
17	BW	STABLE	0, rpm	2358,9 Hz	2157,6 Hz
18	FW	STABLE	0, rpm	2439,9 Hz	2358,9 Hz
19	BW	STABLE	0, rpm	2440,7 Hz	2645,7 Hz
20	FW	STABLE	0, rpm	2645,4 Hz	2760, Hz

Figure 12 shows the Whirl map diagram/Campbell diagram for four materials with their critical speeds is shown above. The Campbell diagram, also known as whirl speed map or a frequency interface diagram, of a simple rotor system. On the other hand, the rotor system is made by the two materials (JIS-S45C steel material, 38CrMoAl steel material), The occurrence

possibilities of operating well at response speed are found from the wirl map diagram in the 14 following modes (265.27, 425.14, 426.24, 463.43, 619.19, 652.73, 1273.2, 1297.6, 1299.4, 1301.7, 1596.2, 1599.6, 2082.1, 2249.6, 2539.9, 2685 Hz), (273.46, 442.93, 444.04, 484.63, 639.49, 680.55, 1327.3, 1351.5, 1353.5,1355.7, 1642.8, 1646.2, 2157.6, 2358.9, 2645.7, 2760 Hz) for 38CrMoAl steel material, as shown in the Table. 3. For the two materials (*JIS-S45C steel material, 38CrMoAl steel material*), the critical velocity occurrence possibilities are found from the wirl map diagram in the first 3 modes (29.72, 29.765, 123, 55Hz), (30.962, 31.007, 130.94Hz) as shown in Tables 2 and 3.

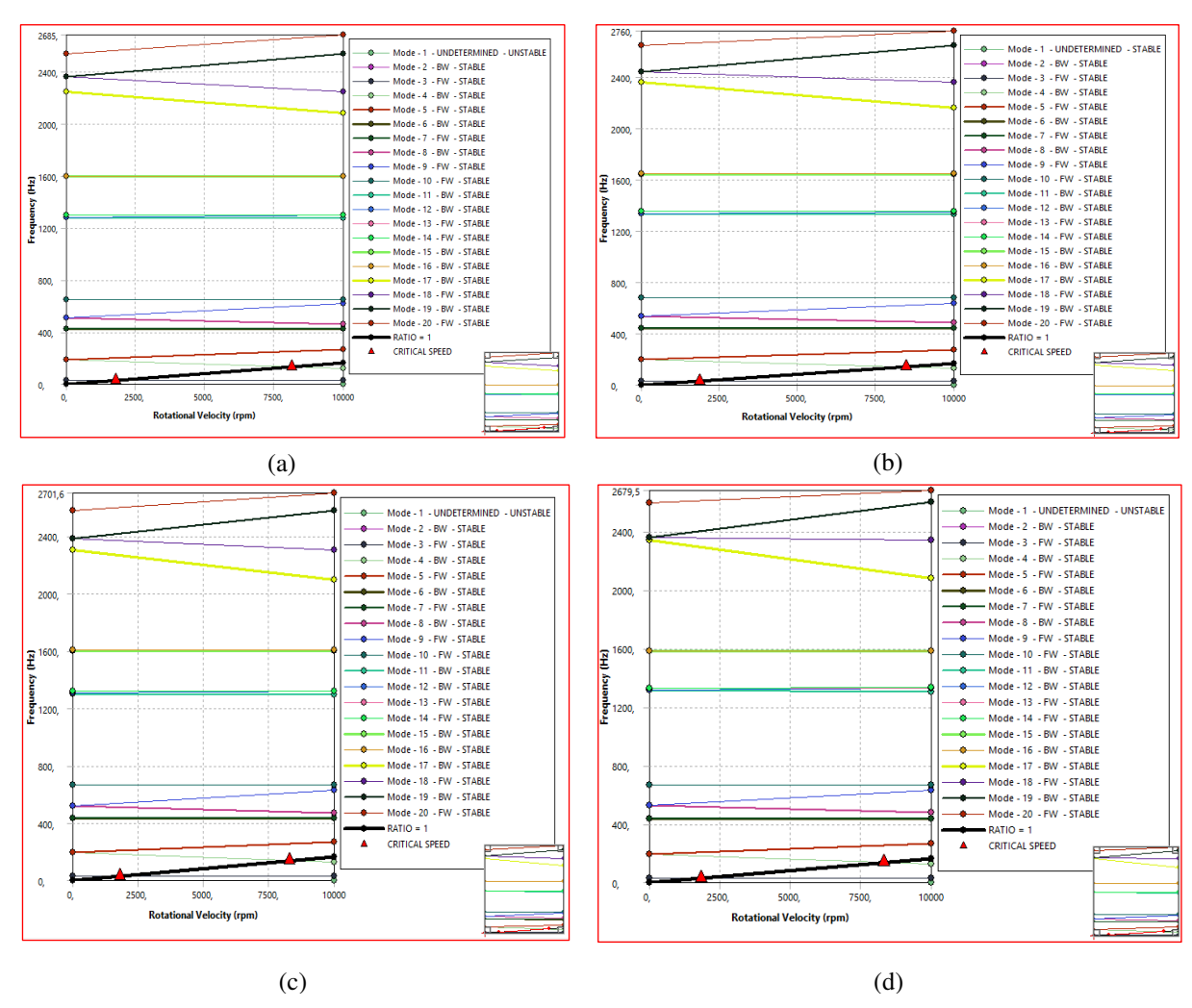


Fig. 12. Whirl map Campbell diagram with four materials: (a) JIS-S45C steel material; (b) 38CrMoAl steel material: (c) structural steel material; (d) titanium alloy (Ti-6AL-4V) material

For structure steel material: The maximum total deformation for this type of material is almost larger at each mode and varies from 437.97 mm at 1st mode, 557.88 mm at 2nd mode, 446.39 mm at 3rd mode, 585.74 mm at 4th mode, 872.55 mm at 5th mode, 871.26 mm at 6th mode, 480.07 mm at 7th mode, 633.35 mm at 8th mode, 608.17 mm at 9th mode, 480.07 mm at 10th mode. The natural frequencies and several modes of this material are shown in Table 4 and Fig. 13 when the speed varies from 0 rpm to 10,000 rpm.

The resonance occurrence possibilities are found from the whirl map diagram in the first 3 modes. 1813.9rpm in backward whirl at natural frequency of 30.2015 Hz, 1814.6 rpm in forward whirl at natural frequency of 30.261 Hz, 8275.9 rpm in the backward whirl at natural frequency of 126.51 Hz as shown in Table. 4. On the other hand, the rotor system is made by the materials (*structure steel material*). The occurrence possibilities of operating well at

response speed are found from the wirl map diagram in the 14 following modes (268.47, 432.25, 433.35, 472.16, 627.5, 664.15, 1295.1, 1318.9, 1321.4, 1323.1, 1603.2, 1606.5, 2099.3, 2302, 2582, 2701.6 Hz), as shown in the Table 4.

Table. 4. Whirl map Campbell diagram of Structural Steel material.

Mode	Whirl Direction	Mode Stability	Critical Speed	0, rpm	10000 rpm
1	UNDETERMINED	UNSTABLE	0, rpm	0, Hz	0, Hz
2	BW	STABLE	1813,9 rpm	30,236 Hz	30,215 Hz
3	FW	STABLE	1814,6 rpm	30,24 Hz	30,261 Hz
4	BW	STABLE	8275,9 rpm	192,75 Hz	126,51 Hz
5	FW	STABLE	0, rpm	192,77 Hz	268,47 Hz
6	BW	STABLE	0, rpm	432,69 Hz	432,25 Hz
7	FW	STABLE	0, rpm	432,9 Hz	433,35 Hz
8	BW	STABLE	0, rpm	521,37 Hz	472,16 Hz
9	FW	STABLE	0, rpm	521,74 Hz	627,5 Hz
10	FW	STABLE	0, rpm	664,15 Hz	664,15 Hz
11	BW	STABLE	0, rpm	1304,5 Hz	1295,1 Hz
12	BW	STABLE	0, rpm	1306,2 Hz	1318,9 Hz
13	FW	STABLE	0, rpm	1320,2 Hz	1321,4 Hz
14	FW	STABLE	0, rpm	1321,9 Hz	1323,1 Hz
15	BW	STABLE	0, rpm	1603,2 Hz	1603,2 Hz
16	BW	STABLE	0, rpm	1606,5 Hz	1606,5 Hz
17	BW	STABLE	0, rpm	2302, Hz	2099,3 Hz
18	FW	STABLE	0, rpm	2381,1 Hz	2302, Hz
19	BW	STABLE	0, rpm	2381,8 Hz	2582, Hz
20	FW	STABLE	0, rpm	2581,6 Hz	2701,6 Hz

Table. 5. Whirl map Campbell diagram of titanium alloy (Ti-6AL-4V) material.

5	Whirl Direction	Mode Stability	Critical Speed	0, rpm	10000 rpm
1	UNDETERMINED	UNSTABLE	0, rpm	0, Hz	0, Hz
2	BW	STABLE	1824,8 rpm	30,417 Hz	30,397 Hz
3	FW	STABLE	1825,5 rpm	30,422 Hz	30,442 Hz
4	BW	STABLE	8323,9 rpm	193,82 Hz	127,64 Hz
5	FW	STABLE	0, rpm	193,83 Hz	269,47 Hz
6	BW	STABLE	0, rpm	435,35 Hz	434,9 Hz
7	FW	STABLE	0, rpm	435,56 Hz	436,01 Hz
8	BW	STABLE	0, rpm	525,48 Hz	476,11 Hz
9	FW	STABLE	0, rpm	525,87 Hz	631,18 Hz
10	FW	STABLE	0, rpm	669,2 Hz	669,2 Hz
11	BW	STABLE	0, rpm	1313,6 Hz	1304,1 Hz
12	BW	STABLE	0, rpm	1315,4 Hz	1326,5 Hz
13	FW	STABLE	0, rpm	1327,7 Hz	1330,3 Hz
14	FW	STABLE	0, rpm	1329,4 Hz	1330,9 Hz
15	BW	STABLE	0, rpm	1581,2 Hz	1581,2 Hz
16	BW	STABLE	0, rpm	1584,5 Hz	1584,5 Hz
17	BW	STABLE	0, rpm	2342,6 Hz	2078,1 Hz
18	FW	STABLE	0, rpm	2359,4 Hz	2342,6 Hz
19	BW	STABLE	0, rpm	2360,1 Hz	2597,7 Hz
20	FW	STABLE	0, rpm	2597,4 Hz	2679,5 Hz

For titanium alloy (Ti-6AL-4V) material. The maximum total deformation for this type of material is almost larger at each mode and varies from 18.512 mm at 1st mode, 22.787 mm at 2nd mode, 26.196 mm at 3rd mode, 28.491 mm at 4th mode, 36.515 mm at 5th mode, 36.46 mm at 6th mode, 20.284 mm at 7th mode, 27.021 mm at 8th mode, 25.738 mm at 9th mode, 20.286 mm at 10th mode. The natural frequencies and several modes of this material are shown in Table 5 and Fig. 13 above when the speed varies from 0 rpm to 10,000 rpm.

The resonance occurrence possibilities are found from the whirl map diagram in the first 3 modes. 1824.8 rpm in backward whirl at natural frequency of 30.397 Hz, 1825.5 rpm in forward whirl at natural frequency of 30.442 Hz, 8323.9 rpm in the backward whirl at natural frequency of 127.64 Hz as shown in Table. 5.

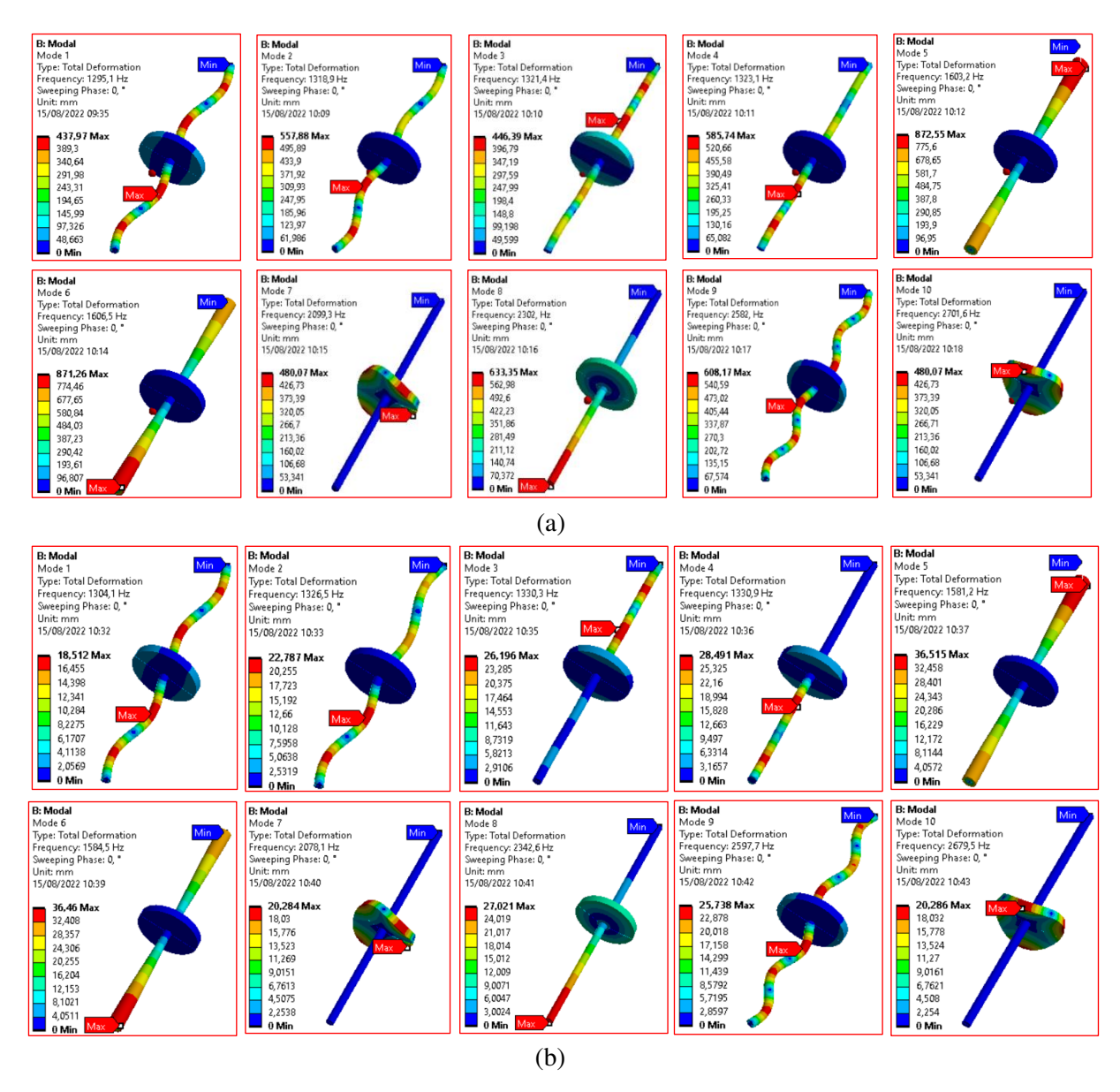


Fig. 13. Different modes shapes with two materials: (a) structural steel material, (b) titanium alloy (Ti-6AL-4V) material

On the other hand, the rotor system is made by the materials (*titanium alloy* (*Ti-6AL-4V*)). The occurrence possibilities of operating well at response speed are found from the wirl map diagram in the 14 following modes (269.47, 434.9, 436.01, 476.11, 631.18, 669.2, 1304.1, 1326.5, 1330.3, 1330.9, 1581.2, 1584.5, 2078.1, 2342.6, 2597.7, 2679.5 Hz), as shown in the Table 5.

Harmonic response analysis. Analysis of the harmonic response of a rotor allows us to determine the deformations, Von Mises stresses, principal stresses, maximum shear stresses and phase angle effect due to balanced and unbalanced forces acting on the system rotor-shaft.

Stress severity for Jeffcott rotor. The following data represents results of the harmonic response analysis of the Jeffcott rotor for the four different materials based on the stress severity.

Figure 14 explains the stresses severity due to the unbalance force for four materials. When the 0.1 kg of unbalanced mass added on the disk with the increasing, the frequencies from 270 to 2700 Hz with step size 100 Hz.

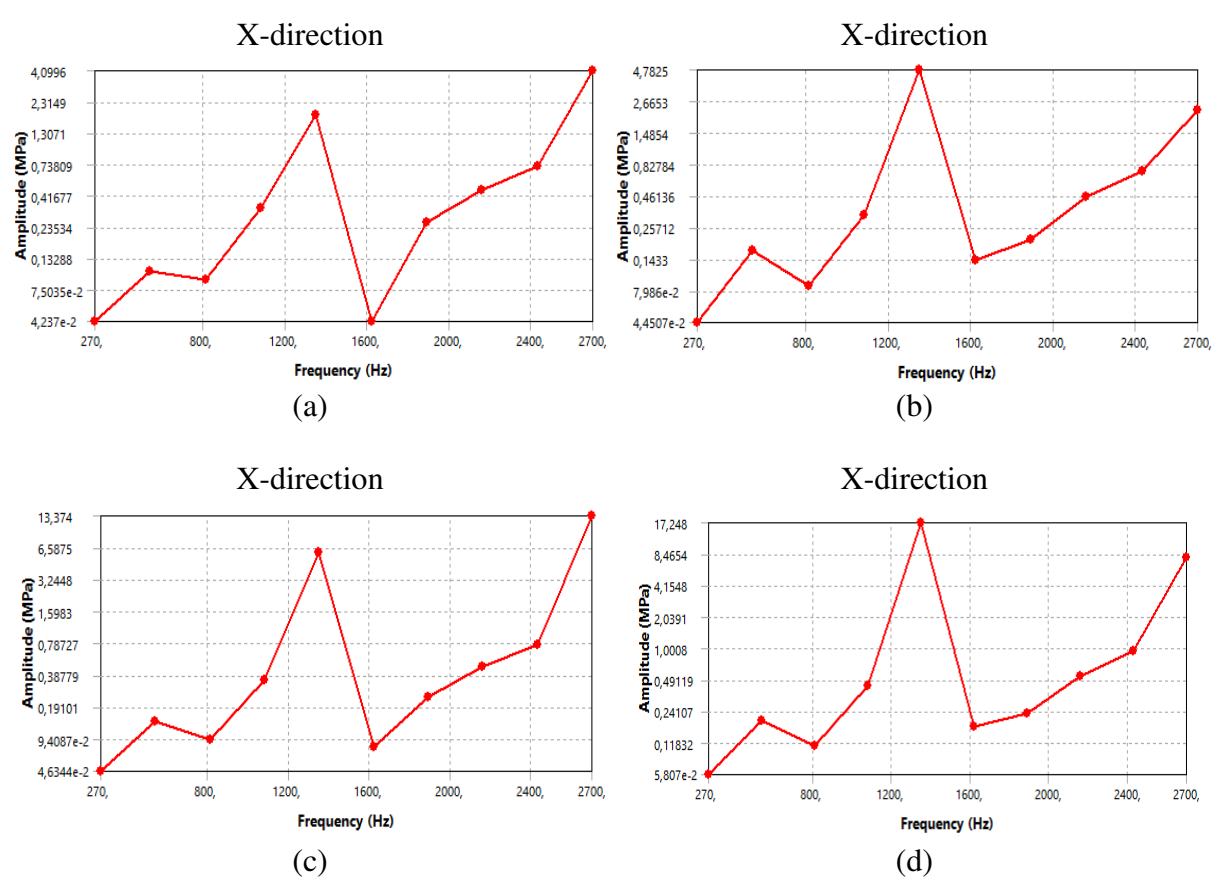


Fig. 14. Stress severity for Jeffcott rotor with 4 varieties of materials due to the unbalance forces: (a) JIS-S45C; (b) 38CrMoAl; (c) structural steel; (d) Ti-6AL-4V

For a steel material of JIS-S45C. When 0.1 kg of unbalance is added to the disk with the increase in frequencies from 270 to 2700 Hz with a step of 100 Hz, the maximum amplitude of normal stress total along X varies from 4.237E-2 MPa at 270 Hz, 1.805 MPa at 1350 Hz and 4.0996 MPa at 2700 Hz a shown in Fig. 14.

For a steel material of 38CrMoAl. When 0.1 kg of unbalance is added to the disk with the increase in frequencies from 270 to 2700 Hz with a step of 100 Hz, the maximum amplitude of normal stress total along X varies from 4.4507E-2 MPa at 270 Hz, 4.7825 MPa at 1350 Hz and 2.6653 MPa at 2700 Hz this mentioned in Fig. 14.

For a material of structural steel. When 0.1 kg of unbalance is added to the disk with the increase in frequencies from 270 to 2700 Hz with a step of 100 Hz, the maximum amplitude of normal stress total along X varies from 4.6344E-2 MPa at 270 Hz, 6.5875 MPa at 1350 Hz and 13.374 MPa at 2700 Hz a shown in Fig. 14.

For a material of titanium alloy (Ti-6AL-4V). When 0.1 kg of unbalance is added to the disk with the increase in frequencies from 270 to 2700 Hz with a step of 100 Hz, the maximum amplitude of normal stress total along X varies from 5.807E-2 MPa at 270 Hz, 17.248 MPa at 1350 Hz and 8.4654 MPa at 2700 Hz this mentioned in Fig. 14.

For a steel material of JIS-S45C. When 0.1 kg of unbalance is added to the disk with the increase in frequencies from 270 to 2700 Hz with a step of 100 Hz, the maximum amplitude of normal stress total along Y varies from 3.4435E-2 MPa at 270 Hz, 3.02MPa at 1350 Hz and 20.648 MPa at 2700 Hz a shown in Fig. 15.

For a steel material of 38CrMoAl. When 0.1 kg of unbalance is added to the disk with the increase in frequencies from 270 to 2700 Hz with a step of 100 Hz, the maximum amplitude of normal stress total along Y varies from 3.618E-2 MPa at 270 Hz, 7.3703 MPa at 1350 Hz and 7.3703 MPa at 2700 Hz this mentioned in Fig. 15.

For a material of structural steel. When 0.1 kg of unbalance is added to the disk with the increase in frequencies from 270 to 2700 Hz with a step of 100 Hz, the maximum amplitude of normal stress total along Y varies from 3.7946E-2 MPa at 270 Hz, 8.9688 MPa at 1350 Hz and 55.453 MPa at 2700 Hz a shown in Fig. 15.

For a material of titanium alloy (Ti-6AL-4V). When 0.1 kg of unbalance is added to the disk with the increase in frequencies from 270 to 2700 Hz with a step of 100 Hz, the maximum amplitude of normal stress total along Y varies from 4.8007E-2 MPa at 270 Hz, 18.335 MPa at 1350 Hz and 25.171 at 2700 Hz this mentioned in Fig. 15.

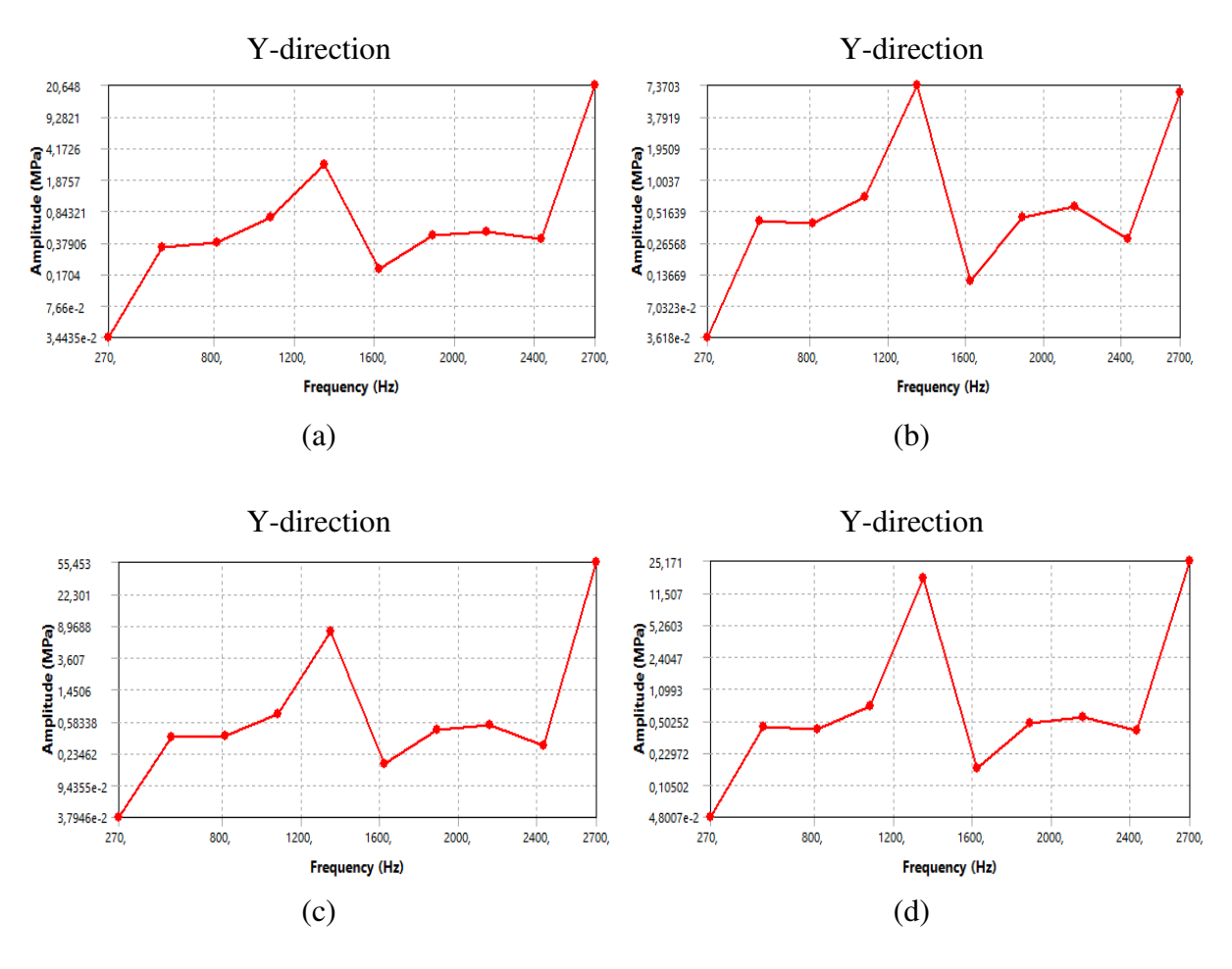


Fig. 15. Stress severity for Jeffcott rotor with 4 varieties of materials due to the unbalance forces: (a) JIS-S45C; (b) 38CrMoAl; (c) structural steel; (d) Ti-6AL-4V

For a steel material of JIS-S45C. When 0.1 kg of unbalance is added to the disk with the increase in frequencies from 270 to 2700 Hz with a step of 100 Hz, the maximum amplitude of normal stress total along Y varies from 0.3983 MPa at 270 Hz, 23.773 MPa at 1350 Hz and 46.995 MPa at 2700 Hz a shown in Fig. 16.

For a steel material of 38CrMoAl. When 0.1 kg of unbalance is added to the disk with the increase in frequencies from 270 to 2700 Hz with a step of 100 Hz, the maximum amplitude of normal stress total along Y varies from 0.3027 MPa at 270 Hz, 39.891 MPa at 1350 Hz and 21.672 MPa at 2700 Hz this mentioned in Fig. 16.

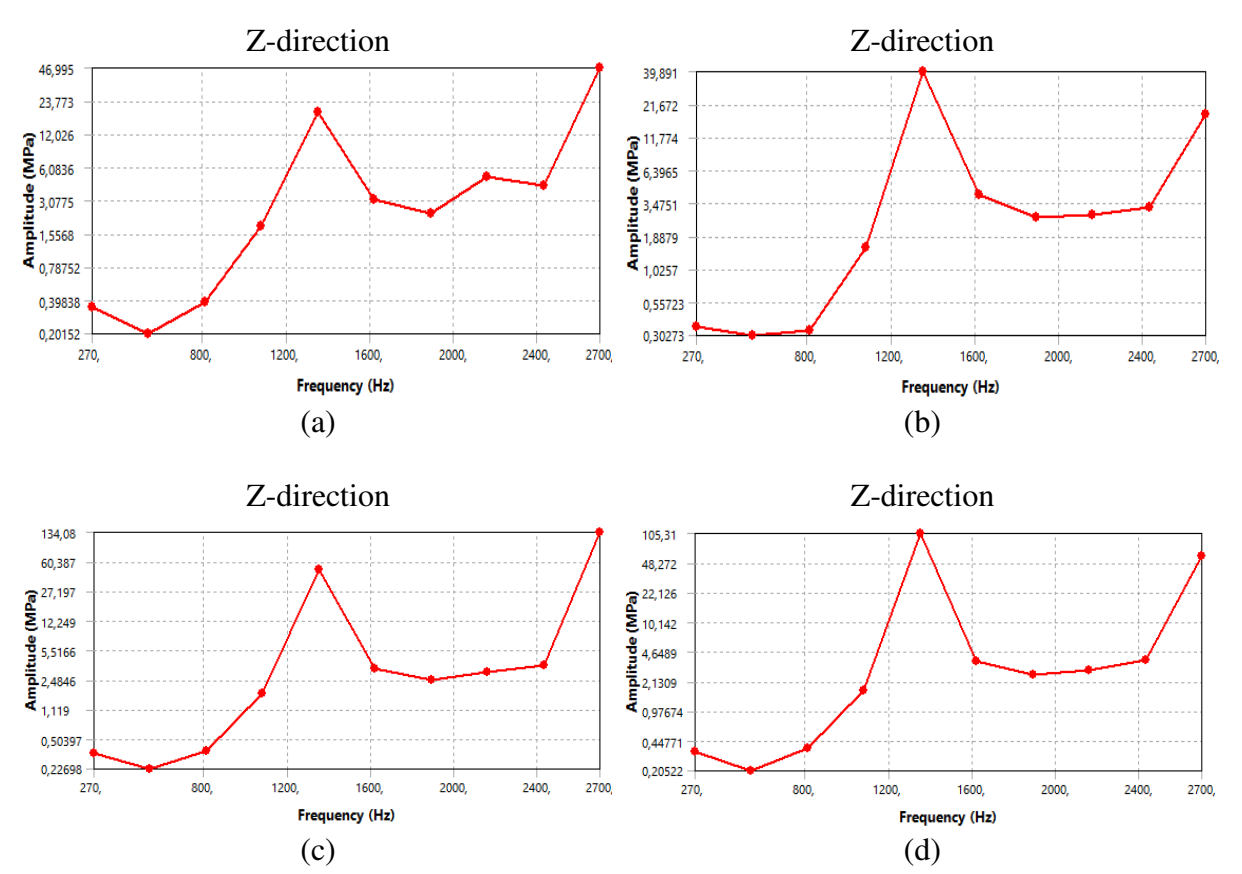


Fig. 16. Stress severity for Jeffcott rotor with 4 varieties of materials due to the unbalance forces: (a) JIS-S45C, (b) 38CrMoAl, (c) structural steel, and (d) Ti-6AL-4V

For a material of Structural Steel When 0.1 kg of unbalance is added to the disk with the increase in frequencies from 270 to 2700 Hz with a step of 100 Hz, the maximum amplitude of normal stress total along Y varies from 0.3 MPa at 270 Hz, 60.387 MPa at 1350 Hz and 134.08 MPa at 2700 Hz a shown in Fig. 16.

For a material of titanium alloy (Ti-6AL-4V). When 0.1 kg of unbalance is added to the disk with the increase in frequencies from 270 to 2700 Hz with a step of 100 Hz, the maximum amplitude of normal stress total along Y varies from 0.31 MPa at 270 Hz, 105.31 MPa at 1350 Hz and 48.272 at 2700 Hz this mentioned in Fig. 12.

Deformation severity for Jeffcott rotor. Figure 13 explains the deformation severity due to the unbalance force for four materials. When the 0.1 kg of unbalanced mass added on the disk with the increasing, the frequencies from 270 to 2700 Hz with step size 100 Hz.

For a steel material of JIS-S45C. When 0.1 kg of unbalance is added to the disk with the increase in frequencies from 270 to 2700 Hz with a step of 100 Hz, the maximum amplitude of deformation total along X varies from 0.83667 mm at 270 Hz, 0.1374 mm at 1350 Hz and 1.5277 mm at 2700 Hz a shown in Fig. 17.

For a steel material of 38CrMoAl. When 0.1 kg of unbalance is added to the disk with the increase in frequencies from 270 to 2700 Hz with a step of 100 Hz, the maximum amplitude of deformation total along X varies from 0.7506 mm at 270 Hz, 0.7506 mm at 1350 Hz and 1.0275 mm at 2700 Hz a shown in Fig. 17.

For a material of structural steel. When 0.1 kg of unbalance is added to the disk with the increase in frequencies from 270 to 2700 Hz with a step of 100 Hz, the maximum amplitude of deformation total along X varies from 0.70512 mm at 270 Hz, 0.17663 mm at 1350 Hz and 5.6242 mm at 2700 Hz a shown in Fig. 17.

For a material of titanium alloy (Ti-6AL-4V). When 0.1 kg of unbalance is added to the disk with the increase in frequencies from 270 to 2700 Hz with a step of 100 Hz, the maximum amplitude of deformation total along X varies from 1.27589 mm at 270 Hz, 1.27589 mm at 1350 Hz and 4.7221 mm at 2700 Hz a shown in Fig. 17.

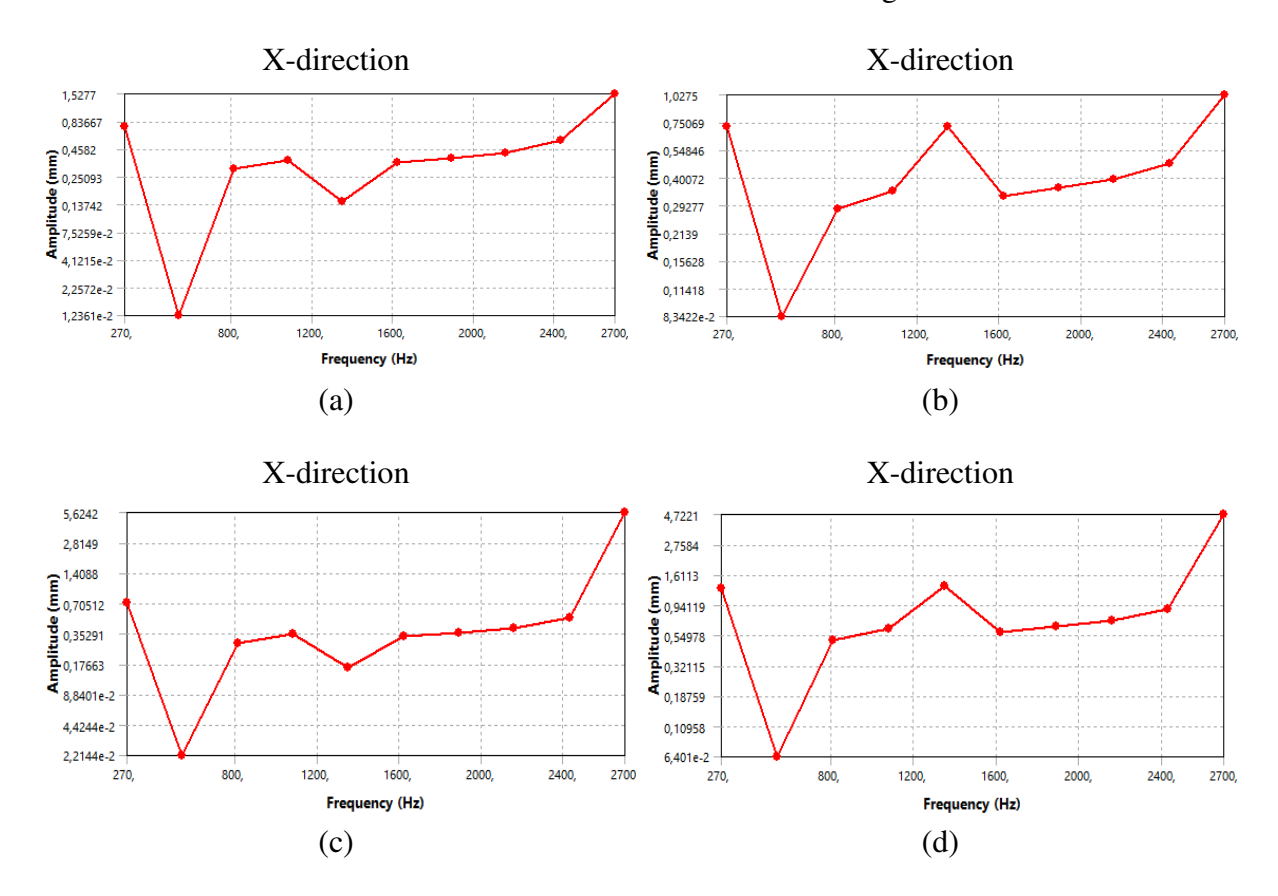


Fig. 17. Deformation severity for Jeffcott rotor with 4 varieties of materials due to the unbalance forces. (a) JIS-S45C; (b) 38CrMoAl; (c) structural steel; (d) Ti-6AL-4V

For a steel material of JIS-S45C. When 0.1 kg of unbalance is added to the disk with the increase in frequencies from 270 to 2700 Hz with a step of 100 Hz, the maximum amplitude of deformation total along Y varies from 0.84969 mm at 270 Hz, 0.1356 mm at 1350 Hz and 1.5664 mm at 2700 Hz a shown in Fig. 18.

For a steel material of 38CrMoAl. When 0.1 kg of unbalance is added to the disk with the increase in frequencies from 270 to 2700 Hz with a step of 100 Hz, the maximum amplitude of deformation total along Y varies from 0.69327 mm at 270 Hz, 0.80392 mm at 1350 Hz and 1.1093 mm at 2700 Hz a shown in Fig. 18.

For a material of Structural Steel. When 0.1 kg of unbalance is added to the disk with the increase in frequencies from 270 to 2700 Hz with a step of 100 Hz, the maximum amplitude of deformation total along Y varies from 0.72833 mm at 270 Hz, 0.18248 mm at 1350 Hz and 5.8078 mm at 2700 Hz a shown in Fig. 18.

For a material of titanium alloy (Ti-6AL-4V). When 0.1 kg of unbalance is added to the disk with the increase in frequencies from 270 to 2700 Hz with a step of 100 Hz, the maximum amplitude of deformation total along Y varies from 1.31794 mm at 270 Hz, 1.31794 mm at 1350 Hz and 4.897 mm at 2700 Hz a shown in Fig. 18.

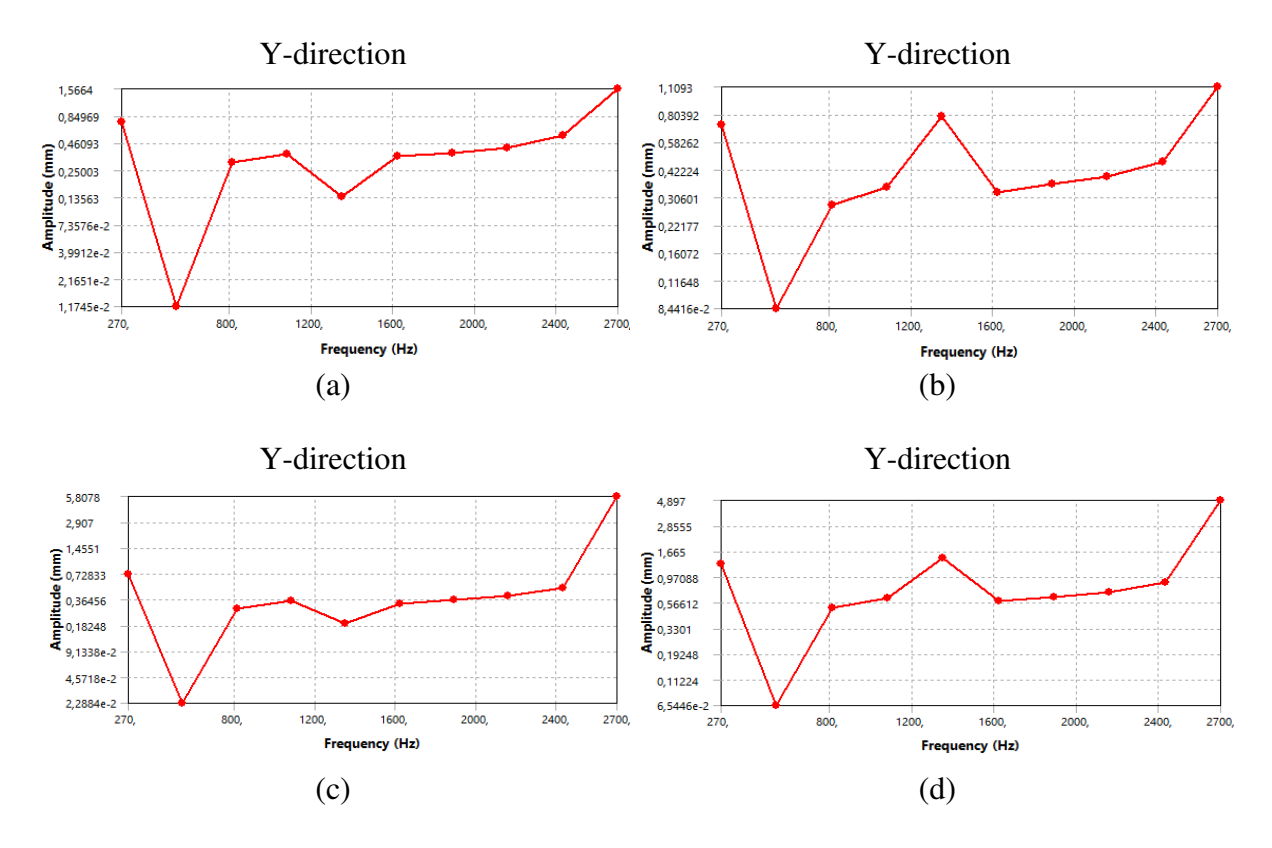


Fig. 18. Deformation severity for Jeffcott rotor with 4 varieties of materials due to the unbalance forces: (a) JIS-S45C, (b) 38CrMoAl, (c) structural steel, (d) Ti-6AL-4V

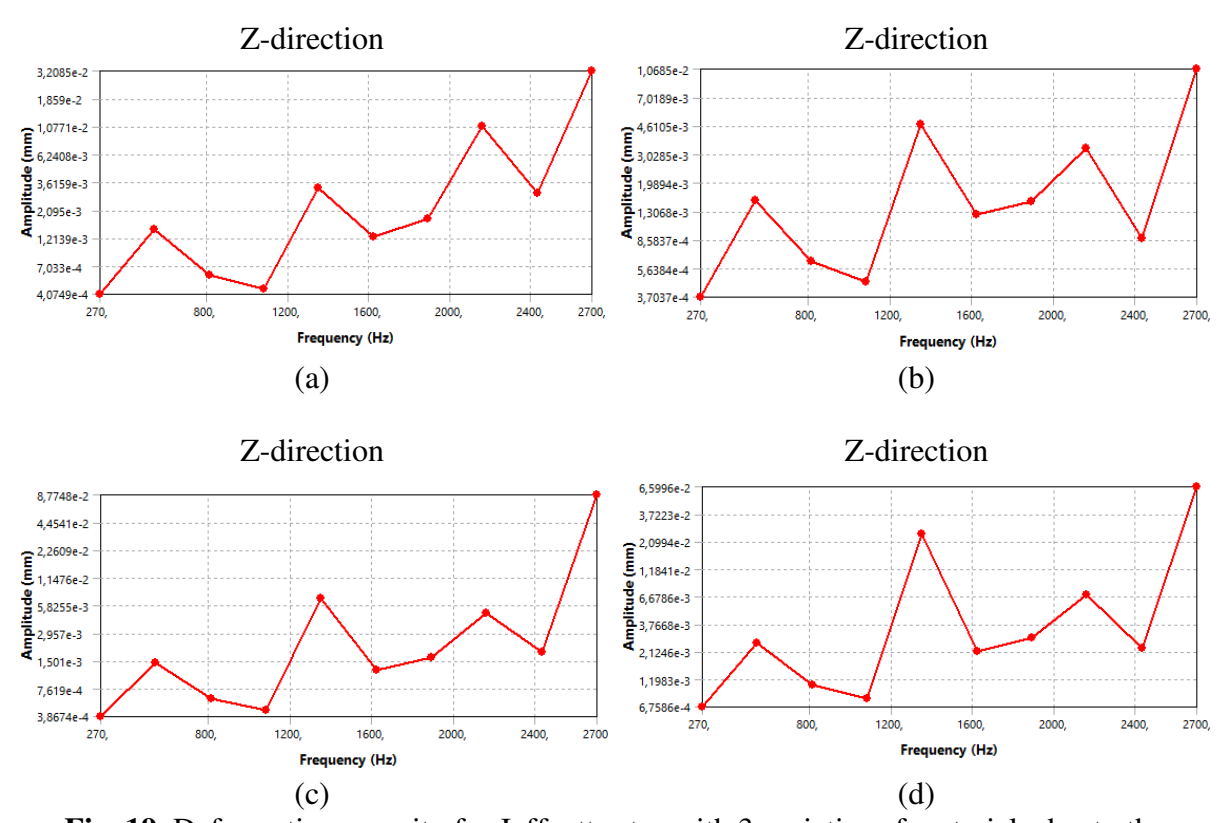


Fig. 19. Deformation severity for Jeffcott rotor with 3 varieties of materials due to the unbalance forces

For a steel material of JIS-S45C. When 0.1 kg of unbalance is added to the disk with the increase in frequencies from 270 to 2700 Hz with a step of 100 Hz, the maximum amplitude of deformation total along Z varies from 4.0779E-4 mm at 270 Hz, 3.6159E-3 mm at 1350 Hz and 3.2085E-2 mm mm at 2700 Hz a shown in Fig. 19.

For a steel material of 38CrMoAl. When 0.1 kg of unbalance is added to the disk with the increase in frequencies from 270 to 2700 Hz with a step of 100 Hz, the maximum amplitude of deformation total along Z varies from 3.7037E-4 mm at 270 Hz, 4.6105E-3 mm at 1350 Hz and 1.0685E-2 mm mm at 2700 Hz a shown in Fig. 19.

For a material of structural Steel. When 0.1 kg of unbalance is added to the disk with the increase in frequencies from 270 to 2700 Hz with a step of 100 Hz, the maximum amplitude of deformation total along Z varies from 3.8674E-4 mm at 270 Hz, 5.8255E-3 mm at 1350 Hz and 8.7748E-2 mm at 2700 Hz a shown in Fig. 19.

For a material of Titanium Alloy (Ti-6AL-4V). When 0.1 kg of unbalance is added to the disk with the increase in frequencies from 270 to 2700 Hz with a step of 100 Hz, the maximum amplitude of deformation total along Z varies from 6.7586E-4 mm at 270 Hz, 2.0994E-2 mm at 1350 Hz and 6.5996E-2 mm mm at 2700 Hz a shown in Fig. 19.

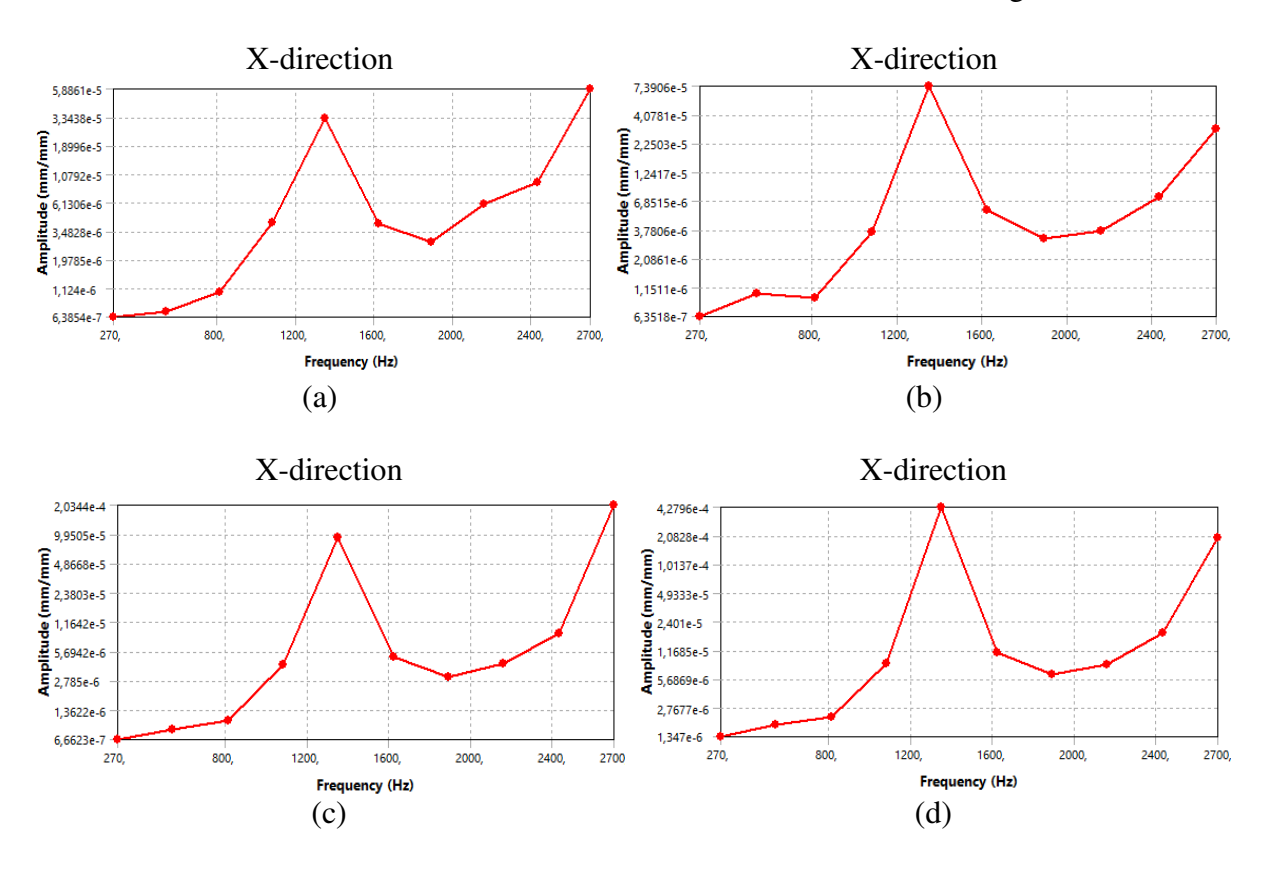


Fig. 20. Normal elastic strain severity for Jeffcott rotor with 4 varieties of materials due to the unbalance forces. (a) JIS-S45C; (b) 38CrMoAl; (c) structural steel; (d) Ti-6AL-4V

Normal elastic strain severity for Jeffcott rotor. Figure 20 explains normal elastic strain severity due to the unbalance force for four materials. When the 0.1 kg of unbalanced mass added on the disk with the increasing, the frequencies from 270 to 2700 Hz with step size 100 Hz.

For a steel material of JIS-S45C. When 0.1 kg of unbalance is added to the disk with the increase in frequencies from 270 to 2700 Hz with a step of 100 Hz, the maximum amplitude of normal elastic strain along X varies from 6.3854E-7 mm at 270 Hz, 3.3438E-5 mm at 1350 Hz and 5.8861E-5 mm at 2700 Hz a shown in Fig. 20.

For a steel material of 38CrMoAl. When 0.1 kg of unbalance is added to the disk with the increase in frequencies from 270 to 2700 Hz with a step of 100 Hz, the maximum amplitude of normal elastic strain along X varies from 6.3518E-7 mm at 270 Hz, 7.3906E-5 mm at 1350 Hz and 3.16E-5 mm at 2700 Hz a shown in Fig. 20.

For a material of structural steel. When 0.1 kg of unbalance is added to the disk with the increase in frequencies from 270 to 2700 Hz with a step of 100 Hz, the maximum amplitude of normal elastic strain along X varies from 6.6623E-7 mm at 270 Hz, 9.9505E-5 mm at 1350 Hz and 2.0344E-1 mm at 2700 Hz a shown in Fig. 20.

For a material of titanium alloy (Ti-6AL-4V). When 0.1 kg of unbalance is added to the disk with the increase in frequencies from 270 to 2700 Hz with a step of 100 Hz, the maximum amplitude of normal elastic strain along X varies from 1.347E-6 mm at 270 Hz, 4.2796E-4 mm at 1350 Hz and 2.0828E-4 mm mm at 2700 Hz a shown in Fig. 20.

For a steel material of JIS-S45C. When 0.1 kg of unbalance is added to the disk with the increase in frequencies from 270 to 2700 Hz with a step of 100 Hz, the maximum amplitude of normal elastic strain along Y varies from 6.3169E-7 mm at 270 Hz, 9.7506E-6 mm at 1350 Hz and 1.5051E-4 mm at 2700 Hz a shown in Fig. 21.

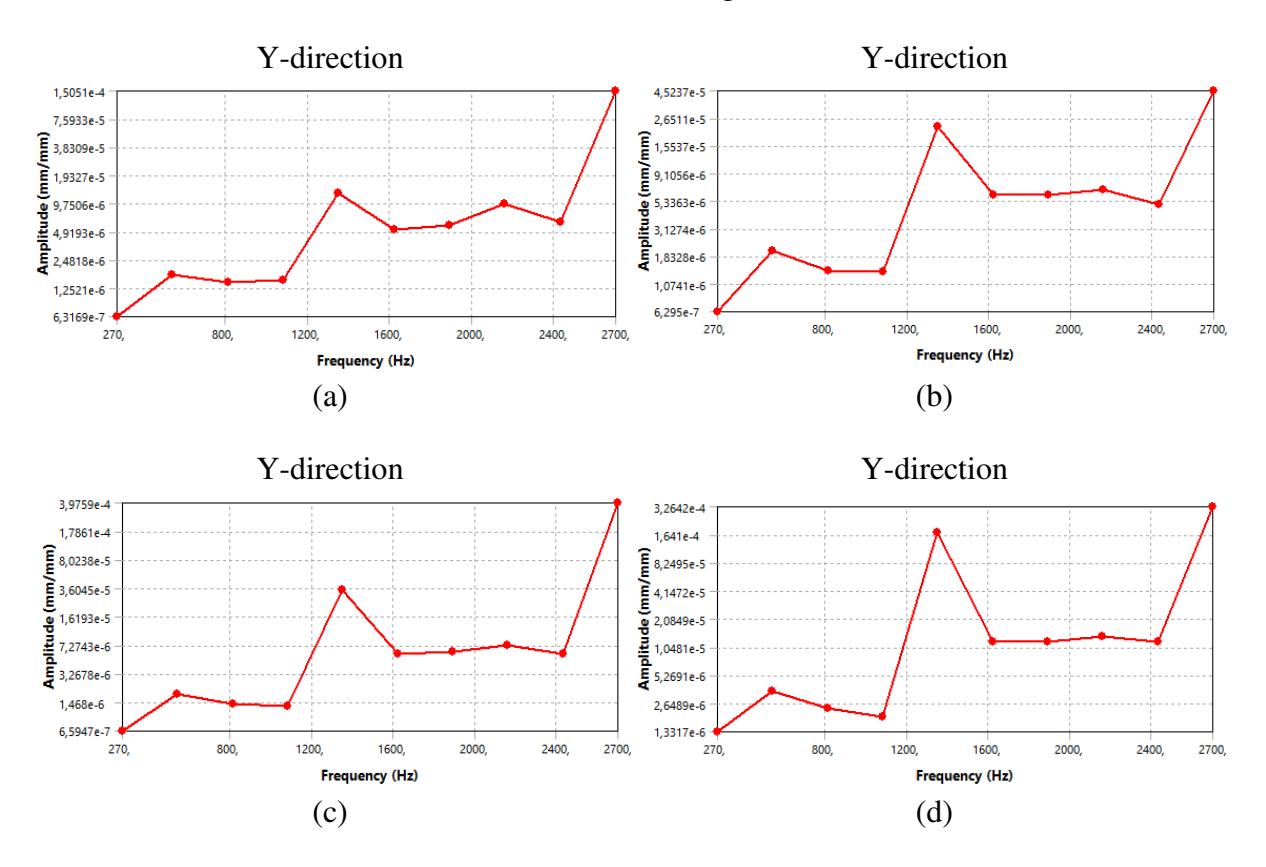


Fig. 21. Normal elastic strain severity for Jeffcott rotor with 4 varieties of materials due to the unbalance forces. (a) JIS-S45C; (b) 38CrMoAl; (c) structural steel; (d) Ti-6AL-4V

For a steel material of 38CrMoAl. When 0.1 kg of unbalance is added to the disk with the increase in frequencies from 270 to 2700 Hz with a step of 100 Hz, the maximum amplitude of normal elastic strain along Y varies from 6.295E-7 mm at 270 Hz, 2.6511E-5 mm at 1350 Hz and 4.5237E-5 mm at 2700 Hz a shown in Fig. 21.

For a material of structural steel. When 0.1 kg of unbalance is added to the disk with the increase in frequencies from 270 to 2700 Hz with a step of 100 Hz, the maximum amplitude of normal elastic strain along Y varies from 6.5947E-7 mm at 270 Hz, 3.6045E-5 mm at 1350 Hz and 3.9757E-4 mm at 2700 Hz a shown in Fig. 21.

For a material of titanium alloy (Ti-6AL-4V). When 0.1 kg of unbalance is added to the disk with the increase in frequencies from 270 to 2700 Hz with a step of 100 Hz, the maximum amplitude of normal elastic strain along Y varies from 1.3317E-6 mm at 270 Hz, 1.641E-4 mm at 1350 Hz and 3.2642E-4 mm at 2700 Hz a shown in Fig. 21.

For a steel material of JIS-S45C. When 0.1 kg of unbalance is added to the disk with the increase in frequencies from 270 Hz to 2700 Hz with a step of 100 Hz, the maximum amplitude of normal elastic strain along Y varies from 2.035E-6mm at 270 Hz, 7.1783E-5mm at 1350 Hz and 2.6707E-4mm mm at 2700 Hz a shown in Fig. 22.

For a steel material of 38CrMoAl. When 0.1 kg of unbalance is added to the disk with the increase in frequencies from 270 to 2700 Hz with a step of 100 Hz, the maximum amplitude of normal elastic strain along Y varies from 2.1237E-6 mm at 270 Hz, 1.8149E-4 mm at 1350 Hz and 9.6134E-5 mm at 2700 Hz a shown in Fig. 22.

For a material of structural steel. When 0.1 kg of unbalance is added to the disk with the increase in frequencies from 270 to 2700 Hz with a step of 100 Hz, the maximum amplitude of normal elastic strain along Y varies from 2.30E-6 mm at 270 Hz, 2.45E-4 mm at 1350 Hz and 7.308E-4 mm at 2700 Hz a shown in Fig. 22.

For a material of titanium alloy (Ti-6AL-4V). When 0.1 kg of unbalance is added to the disk with the increase in frequencies from 270 to 2700 Hz with a step of 100 Hz, the maximum amplitude of normal elastic strain along Y varies from 3.63055E-6mm at 270 Hz, 8.9358E-4 mm at 1350 Hz and 6.59265E-4 mm at 2700 Hz a shown in Fig. 22.

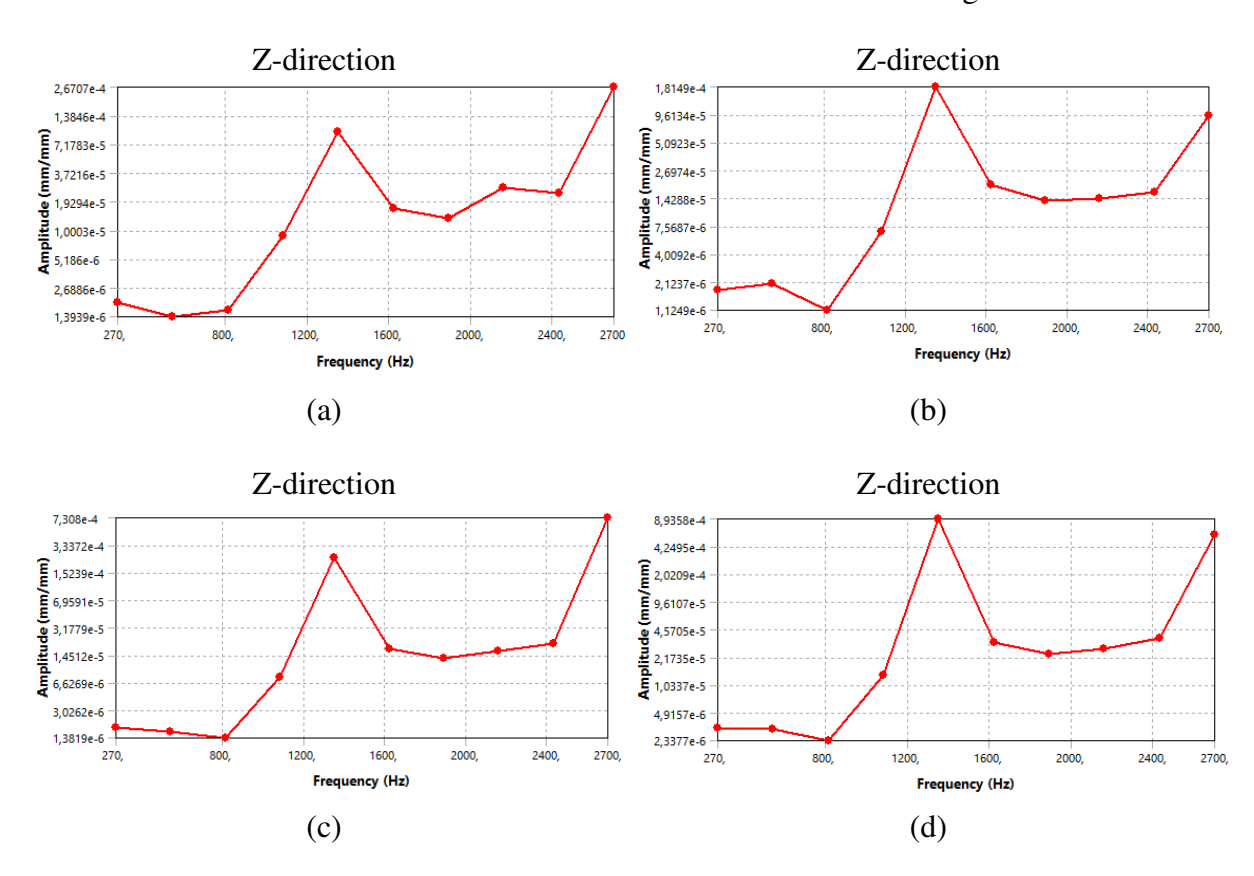


Fig. 22. Normal elastic strain severity for Jeffcott rotor with 3 varieties of materials due to the unbalance forces. (a) JIS-S45C; (b) 38CrMoAl; (c) structural steel; (d) Ti-6AL-4V

Phase angle effect on stress severity for Jeffcott rotor. Ensuing values of the four chosen materials provides the results of the harmonic response analysis for the Jeffcott rotor based on the phase angle effect with respect to the stress severity.

Figures 23-26 explains the severity of normal stresses due to the unbalance force for four materials wherein the 0.1 kg of unbalanced mass added on the disk with the increasing, the frequencies from 270 to 2700 Hz with step size 100 Hz.

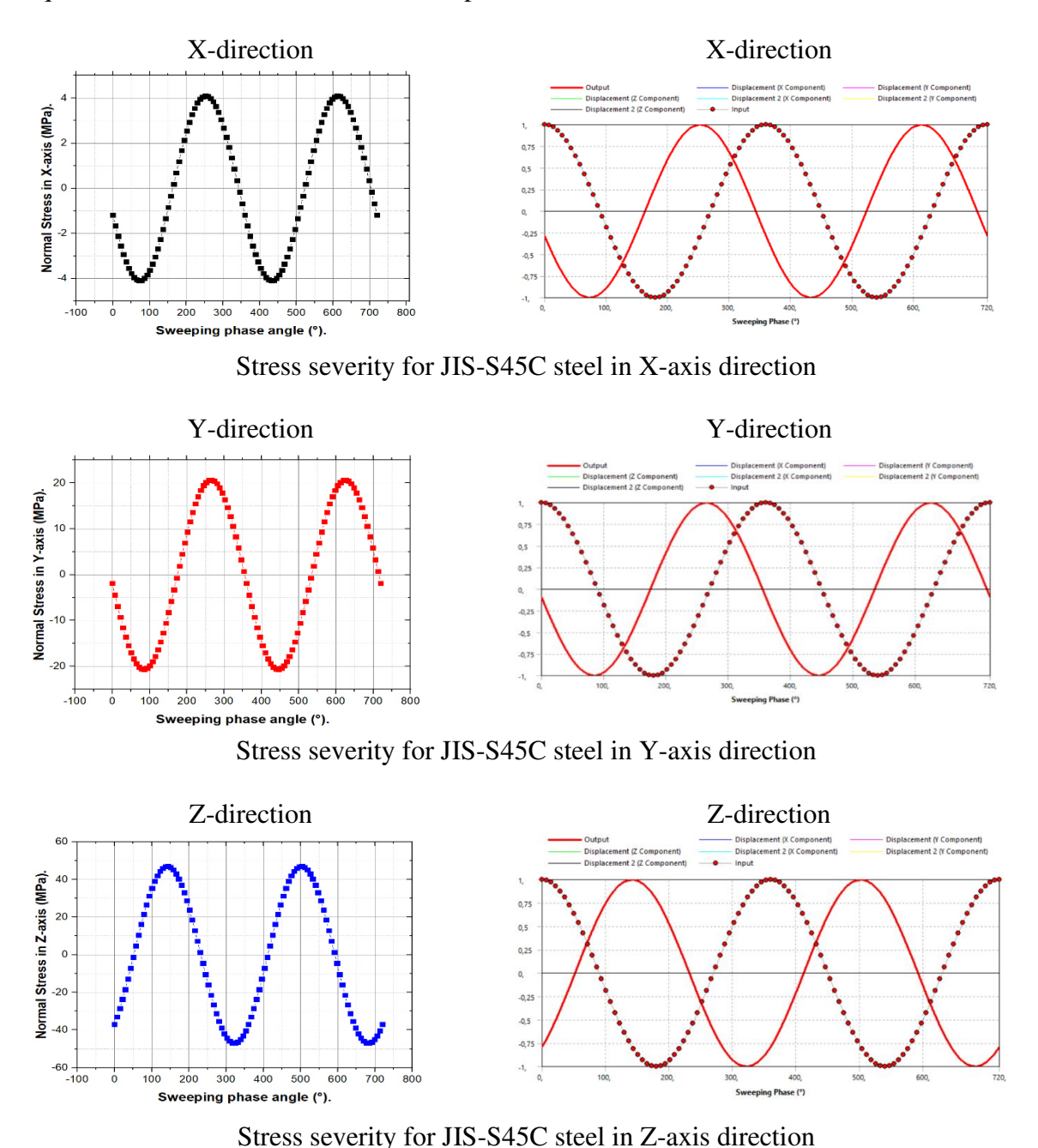


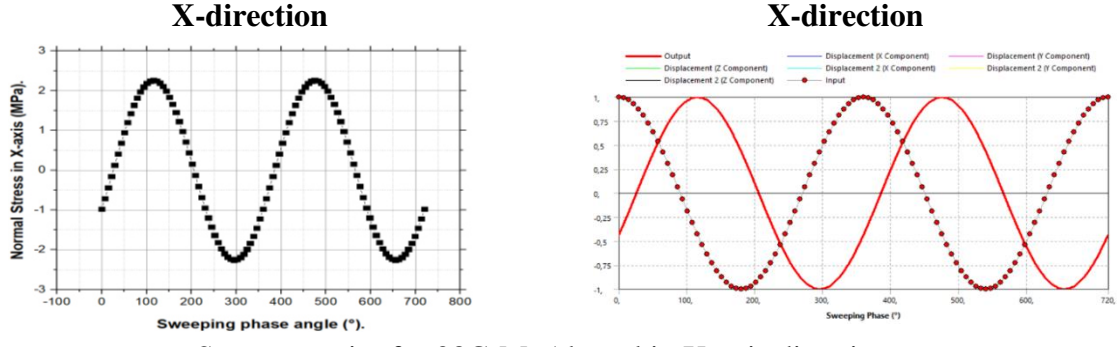
Fig. 23. Stresses severity vs phase angle for Jeffcott rotor for JIS-S45C steel material

For a steel material of JIS-S45C in X direction. The maximum normal stress is -1.186 MPa at sweep phase angle equal 0°, 4.0987 MPa at sweep phase angle equal 252°, -4.0987 MPa at sweep phase angle equals 432°, 4.0987 MPa at sweep phase angle equals 612°, -1.186 MPa at sweep phase angle equals 720° (See Fig. 23).

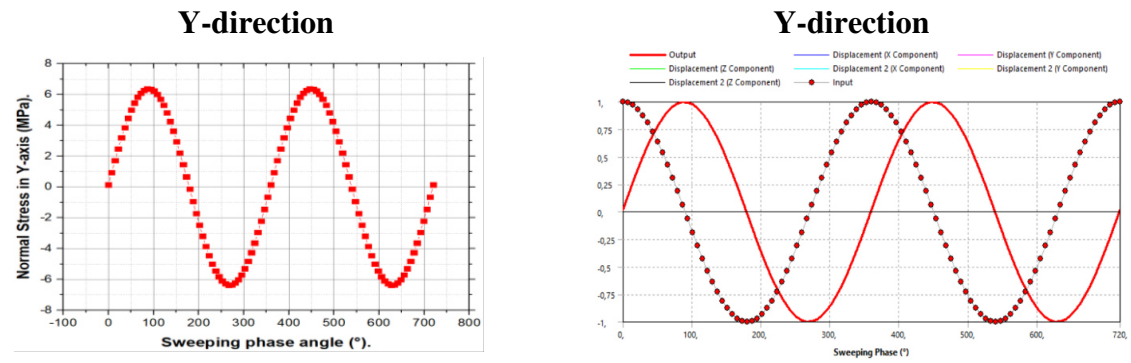
For a steel material of JIS-S45C in Y direction. The maximum normal stress is -1.8746 MPa at sweep phase angle equal 0°, 20.64 MPa at sweep phase angle equal 266.4°, -20.64 MPa at sweep phase angle equals 446.4°, 20.64MPa at sweep phase angle equals 626.4°, -1.8745 MPa at sweep phase angle equals 720° in Y direction (See Fig. 23).

For a steel material of JIS-S45C in Z direction. The maximum normal stress is - 37.009 MPa at sweep phase angle equal 0°, 46.965 MPa at sweep phase angle equal 144°, - 46.965 MPa at sweep phase angle equals 324°, 46.965 MPa at sweep phase angle equals 504°, -37.009 MPa at sweep phase angle equals 720° (see Fig. 23).

For a steel material of 38CrMoAl in X direction. The maximum normal stress is -0.97662MPa at sweep phase angle equal 0°, 2.2592MPa at sweep phase angle equal 115.2°, -2.2592MPa at sweep phase angle equals 115.2°, 2.2592MPa at sweep phase angle equals 475.2°, -0.97663MPa at sweep phase angle equals 720° (see Fig. 24).



Stress severity for 38CrMoAl steel in X-axis direction



Stress severity for 38CrMoAl steel in Y-axis direction

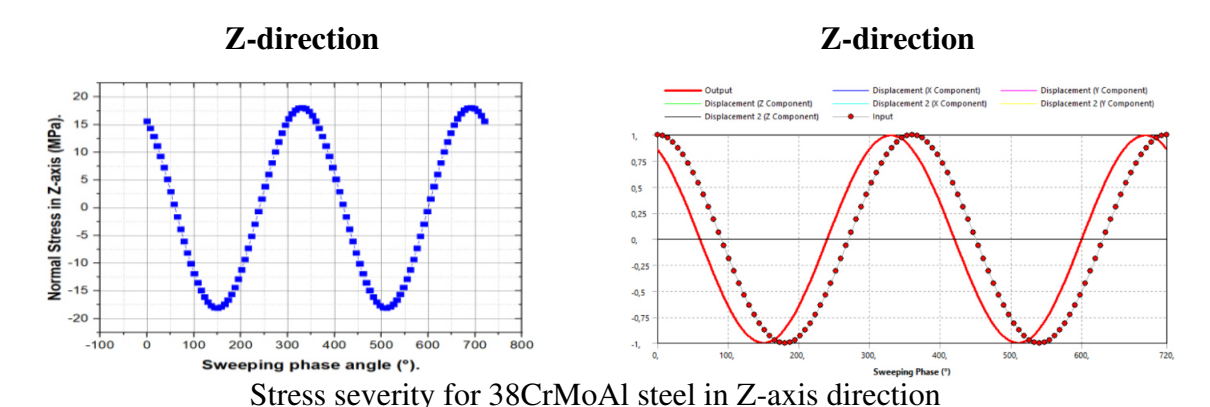


Fig. 24. Stresses severity vs phase angle for Jeffcott rotor with 38CrMoAl steel material

For a steel material of 38CrMoAl in Y direction. The maximum normal stress is -0.13911 MPa at sweep phase angle equal 0° , 6.3642 MPa at sweep phase angle equal 86.4° , -6.3642 MPa at sweep phase angle equals 266.4° , 6.3642 MPa at sweep phase angle equals 446.4° , -6.3642 MPa at sweep phase angle equals 626.4° , 6.3642 MPa at sweep phase angle equals 446.4° , 0.1391 MPa at sweep phase angle equals 720° in Y direction (see Fig. 24).

For a steel material of 38CrMoAl in Z direction. The maximum normal stress is 15.623 MPa at sweep phase angle equal 0°, -18.086 MPa at sweep phase angle equal 151.2°, -18,086 MPa at sweep phase angle equals 331.2°, -18.086 MPa at sweep phase angle equals 511.2°, -15.623 MPa at sweep phase angle equals 720° (See Fig. 24).

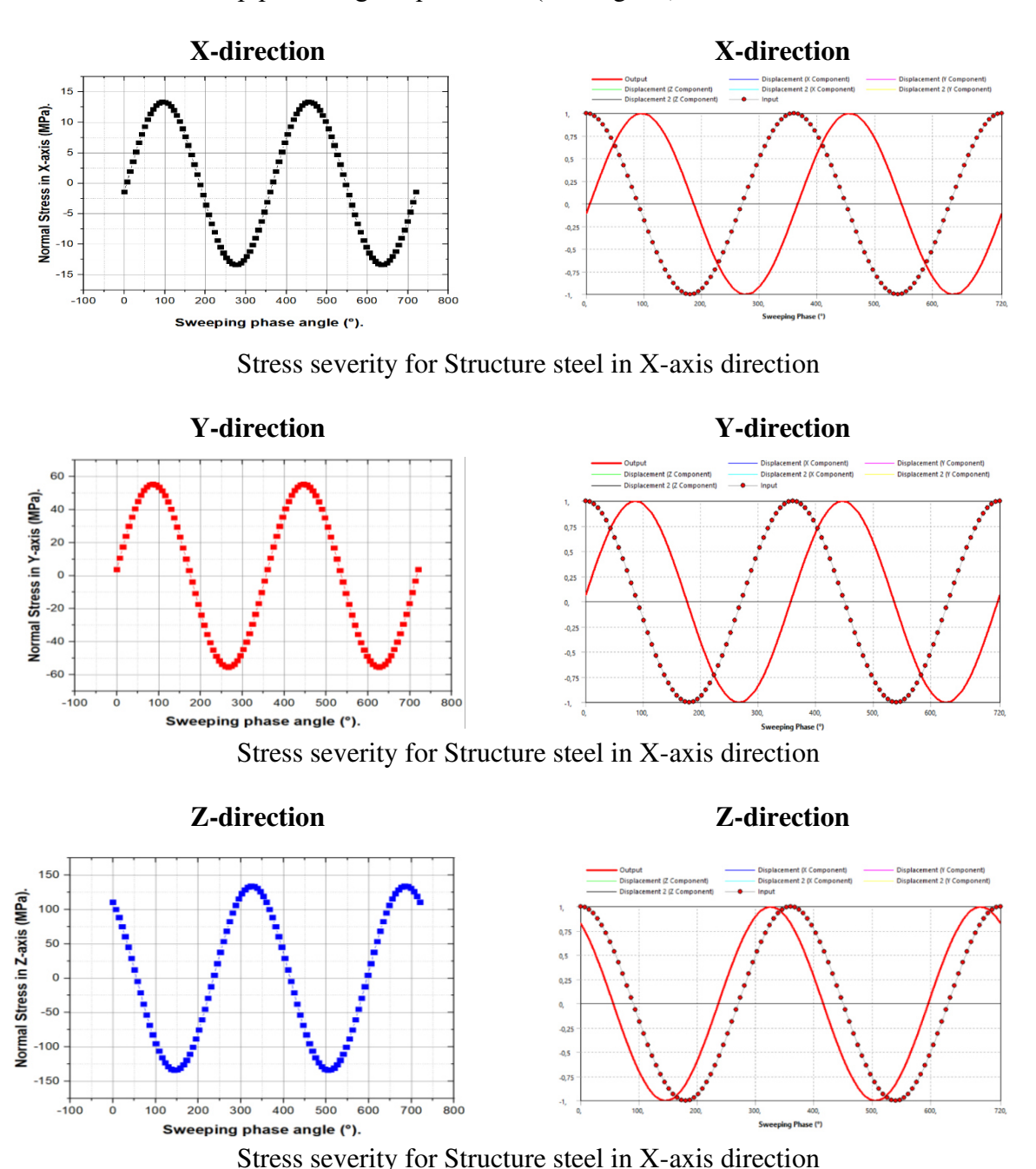


Fig. 25. Stresses severity vs phase angle for Jeffcott rotor with for Structure steel material

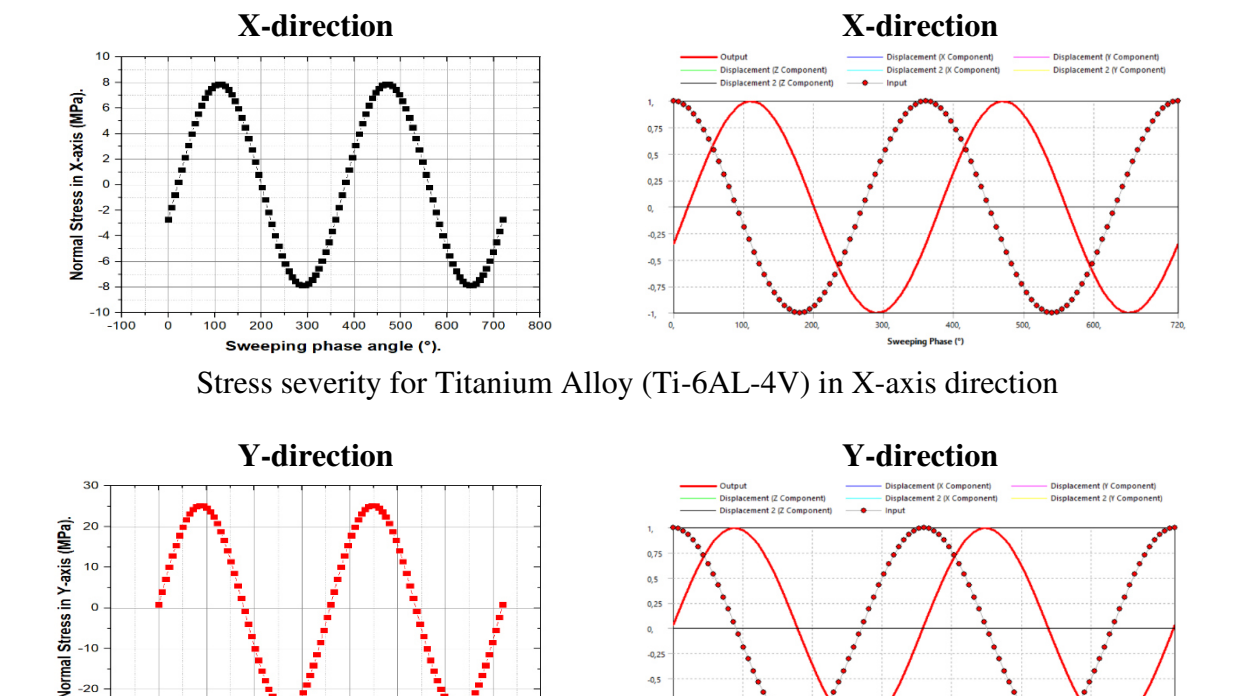
For Structural steel material in X direction. The maximum normal stress is -1.4351 MPa at sweep phase angle equal 0°, 13.36 MPa at sweep phase angle equal 93.6°, -13.36 MPa at sweep phase angle equals 273.6°, 13.36 MPa at sweep phase angle equals 453.6°, -13.33 MPa at sweep phase angle equals 640.8°, -1.4351 MPa at sweep phase angle equals 270° (See Fig. 25).

For structural steel material in Y direction. The maximum normal stress is 3.7447 MPa at sweep phase angle equal 0° , 55.452 MPa at sweep phase angle equals 266.4° , 55.452 MPa at sweep phase angle equals

446.4°, -54.982 MPa at sweep phase angle equals 633.6°, 3.7446 MPa at sweep phase angle equals 270° (see Fig. 25).

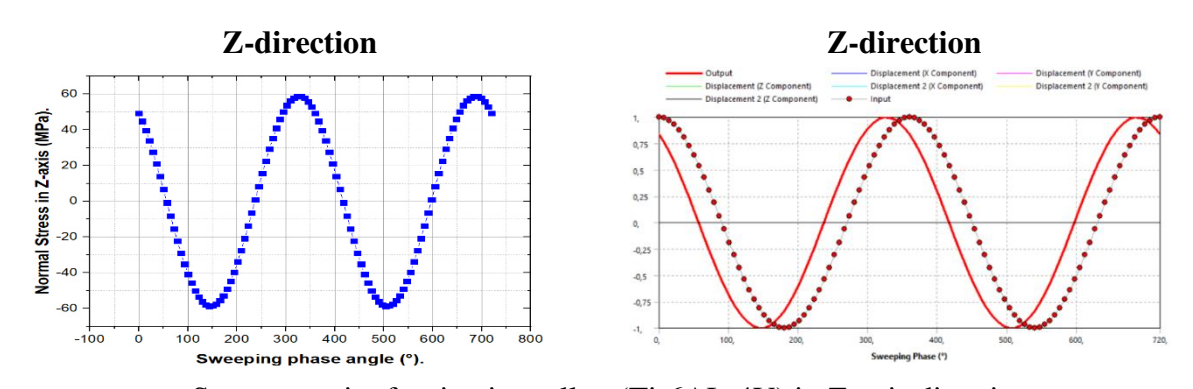
For Structural steel material in Z direction. The maximum normal stress is 110.71 MPa at sweep phase angle equal 0°, -134.02 MPa at sweep phase angle equal 144°, 134.02 MPa at sweep phase angle equals 324°, -134.02 MPa at sweep phase angle equals 504°, 110.71MPa at sweep phase angle equals 270° (see Fig. 25).

For titanium alloy (Ti-6AL-4V) material in X direction. The maximum normal stress is -2.7244 MPa at sweep phase angle equal 0°, 7.8805 MPa at sweep phase angle equal 108°, -7.8565 MPa at sweep phase angle equals 295.2°, 7.8805 MPa at sweep phase angle equals 468°, -7.8805 MPa at sweep phase angle equals 648°, -2.7244 MPa at sweep phase angle equals 270° (see Fig. 26).



Stress severity for titanium alloy (Ti-6AL-4V) in Y-axis direction

300 400



Stress severity for titanium alloy (Ti-6AL-4V) in Z-axis direction

Fig. 26. Stresses severity vs phase angle for Jeffcott rotor for Titanium Alloy (Ti-6AL-4V) material

For Titanium Alloy (Ti-6AL-4V) material in Y direction. The maximum normal stress is 0.81197MPa at sweep phase angle equal 0°, 25.16 MPa at sweep phase angle equal 86.4°, -25.16MPa at

sweep phase angle equals 266.4°, 25.16 MPa at sweep phase angle equals 446.4°, -25.16 MPa at sweep phase angle equals 626.4°, 0.8119 MPa at sweep phase angle equals 270° (see Fig. 26).

For Titanium Alloy (Ti-6AL-4V) material in Z direction. The maximum normal stress is 49.207 MPa at sweep phase angle equal 0° , -58.755 MPa at sweep phase angle equal 144° , 58.755 MPa at sweep phase angle equals 324° , -58.755 MPa at sweep phase angle equals 504° , 49.207 MPa at sweep phase angle equals 270° (see Fig. 26).

Force reaction effect on Jeffcott rotor. Figure 27 explains the force reaction in the two bearings due to the unbalance force for four materials. When the 0.1 kg of unbalanced mass added on the disk with the increasing, the frequencies from 270 to 2700 Hz with step size 100 Hz.

For a material of JIS-S45C steel. When 0.1 kg of unbalance is added to the disk with the increase in frequencies from 270 to 2700 Hz with a step of 100 Hz, the maximum amplitude of reaction force along X varies from 2228.3 N at 270 Hz, 2.124E+5 N at 1350 Hz and 9.7022E5 N at 2700 Hz a shown in Fig. 27.

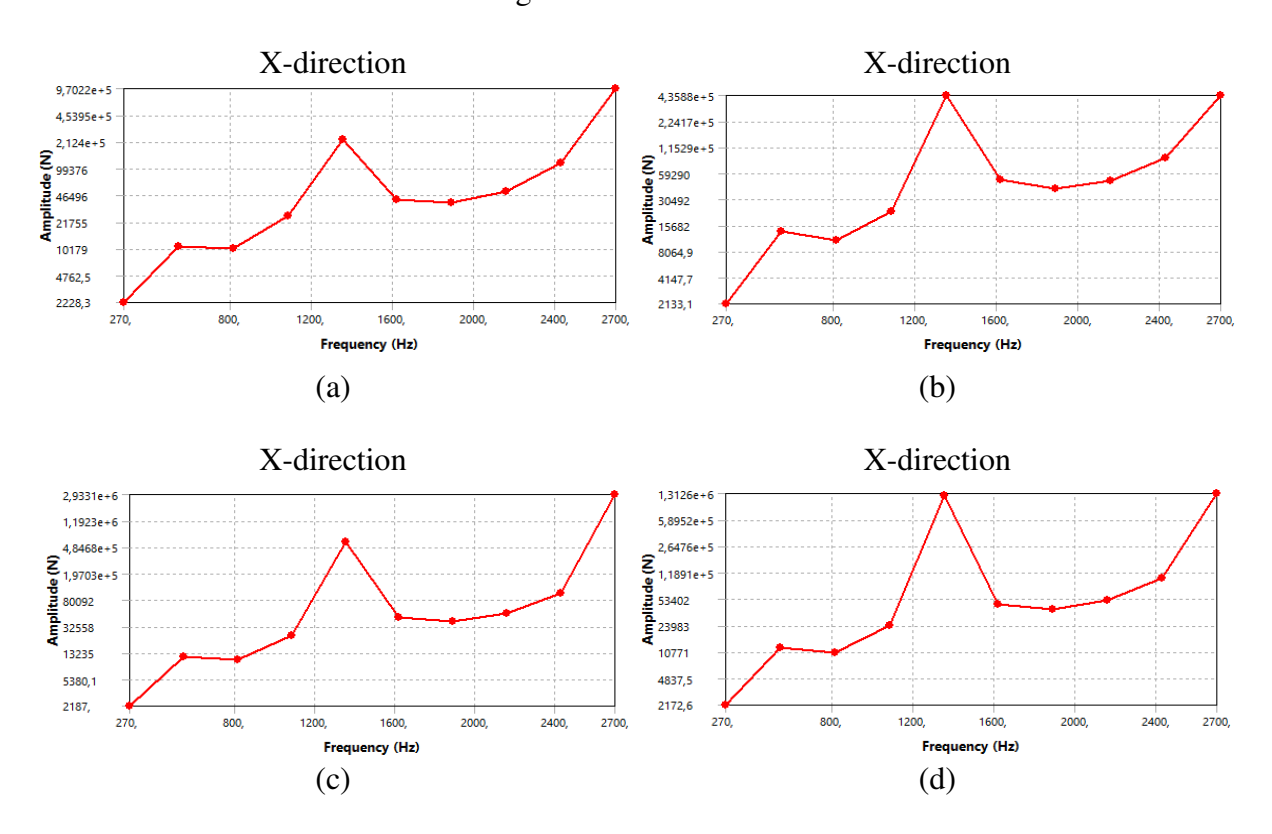


Fig. 27. Shows the Force Reaction vs phase angle for a Jeffcott rotor with 4 varieties of materials. (a) JIS-S45C; (b) 38CrMoAl; (c) structural steel; (d) Ti-6AL-4V

For a material of 38CrMoAl steel. When 0.1 kg of unbalance is added to the disk with the increase in frequencies from 270 to 2700 Hz with a step of 100 Hz, the maximum amplitude of reaction force along X varies from 2133.1 N at 270 Hz, 4.3588E+5 N at 1350 Hz and 4.3588E+5 N at 2700 Hz a shown in Fig. 27.

For a material of structural steel. When 0.1 kg of unbalance is added to the disk with the increase in frequencies from 270 to 2700 Hz with a step of 100 Hz, the maximum amplitude of reaction force along X varies from 2187 N at 270 Hz, 4.8468E+5 N at 1350 Hz and 2.9331E6 N at 2700 Hz a shown in Fig. 27.

For material of titanium alloy (**Ti-6AL-4V**). When 0.1 kg of unbalance is added to the disk with the increase in frequencies from 270 to 2700 Hz with a step of 100 Hz, the maximum amplitude of reaction force along X varies from 2172.6 N at 270 Hz, 1.3126E+6 N at 1350 Hz and 1.3126E+6 N at 2700 Hz a shown in Fig. 27.

For a material of JIS-S45C steel. When 0.1 kg of unbalance is added to the disk with the increase in frequencies from 270 to 2700 Hz with a step of 100 Hz, the maximum amplitude of reaction force along Y varies from 2225.1 N at 270 Hz, 2.1749E+5 N at 1350 Hz and 1.0018E+6 N at 2700 Hz a shown in Fig. 28.

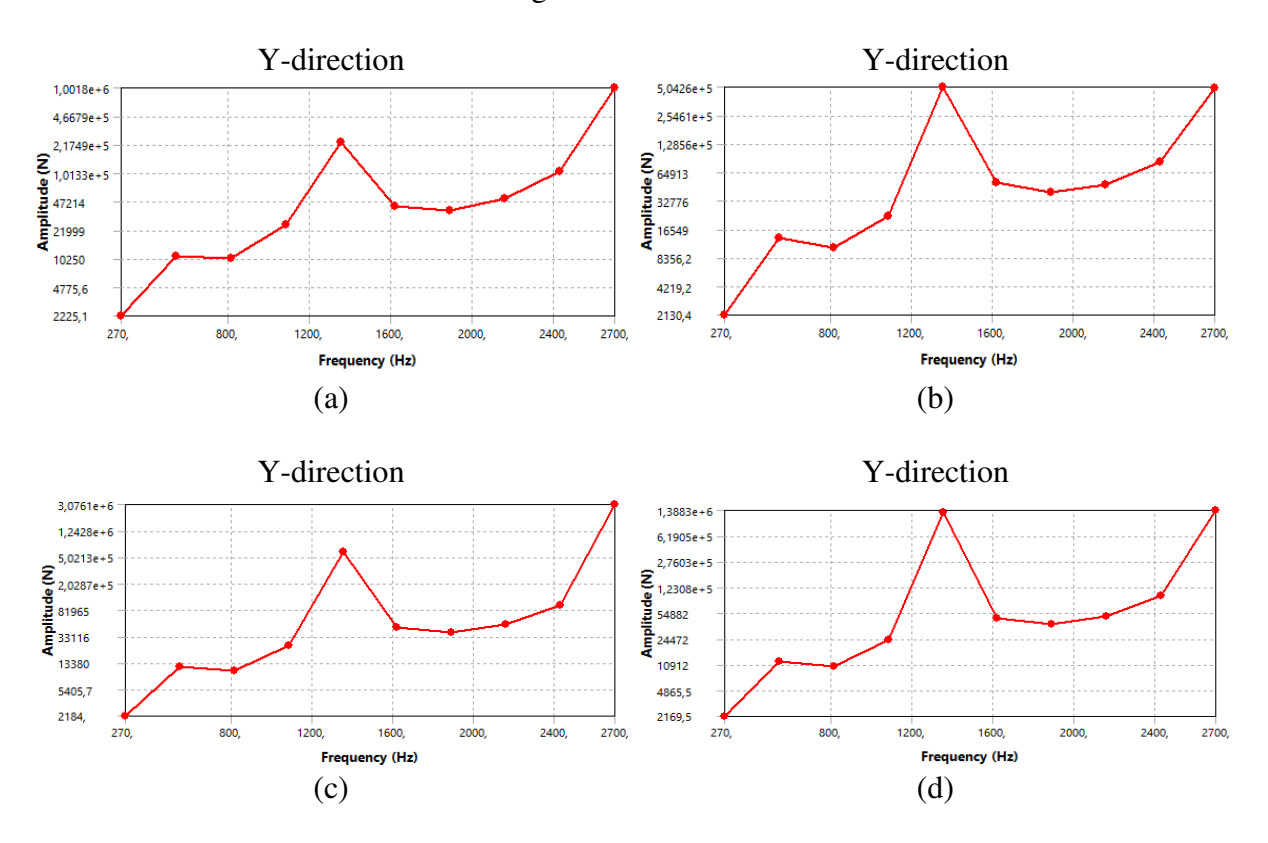


Fig. 28. Shows the deformation vs phase angle for a Jeffcott rotor with 4 varieties of materials. (a) JIS-S45C; (b) 38CrMoAl; (c) structural steel; (d) Ti-6AL-4V

For a material of 38CrMoAl steel. When 0.1 kg of unbalance is added to the disk with the increase in frequencies from 270 to 2700 Hz with a step of 100 Hz, the maximum amplitude of reaction force along Y varies from 2130.4 N at 270 Hz, 5.0426E+5 N at 1350 Hz and 5.0426 N at 2700 Hz a shown in Fig. 28.

For a material of Structural steel. When 0.1 kg of unbalance is added to the disk with the increase in frequencies from 270 to 2700 Hz with a step of 100 Hz, the maximum amplitude of reaction force along Y varies from 2184 N at 270 Hz, 5.0213E+5 N at 1350 Hz and 3.0761E+6 N at 2700 Hz a shown in Fig. 28.

For material of Titanium Alloy (**Ti-6AL-4V**). When 0.1 kg of unbalance is added to the disk with the increase in frequencies from 270 to 2700 Hz with a step of 100 Hz, the maximum amplitude of reaction force along Y varies from 2169.5N at 270 Hz, 1.3883E+6 N at 1350 Hz and 1.3883E+6N at 2700 Hz a shown in Fig. 28.

For a material of JIS-S45C steel. When 0.1 kg of unbalance is added to the disk with the increase in frequencies from 270 to 2700 Hz with a step of 100 Hz, the maximum amplitude of reaction force along Z varies from 3.212N at 270 Hz, 2278.7N at 1350 Hz and 2278.7E+6 at 2700 Hz a shown in Fig. 29.

For a material of 38CrMoAl steel. When 0.1 kg of unbalance is added to the disk with the increase in frequencies from 270 to 2700 Hz with a step of 100 Hz, the maximum amplitude of reaction force along Z varies from 2.7424 N at 270 Hz, 3787.3 N at 1350 Hz and 1533.9 N at 2700 Hz a shown in Fig. 29.

For a material of structural steel. When 0.1 kg of unbalance is added to the disk with the increase in frequencies from 270 to 2700 Hz with a step of 100 Hz, the maximum amplitude of reaction force along Z varies from 2.9805N at 270 Hz, 4425.6N at 1350 Hz and 1776.3N at 2700 Hz a shown in Fig. 29.

For material of titanium alloy (Ti-6AL-4V). When 0.1 kg of unbalance is added to the disk with the increase in frequencies from 270 to 2700 Hz with a step of 100 Hz, the maximum amplitude of reaction force along Z varies from 2.8215 N at 270 Hz, 9544.7 N at 1350 Hz and 1251.5 N at 2700 Hz a shown in Fig. 29.

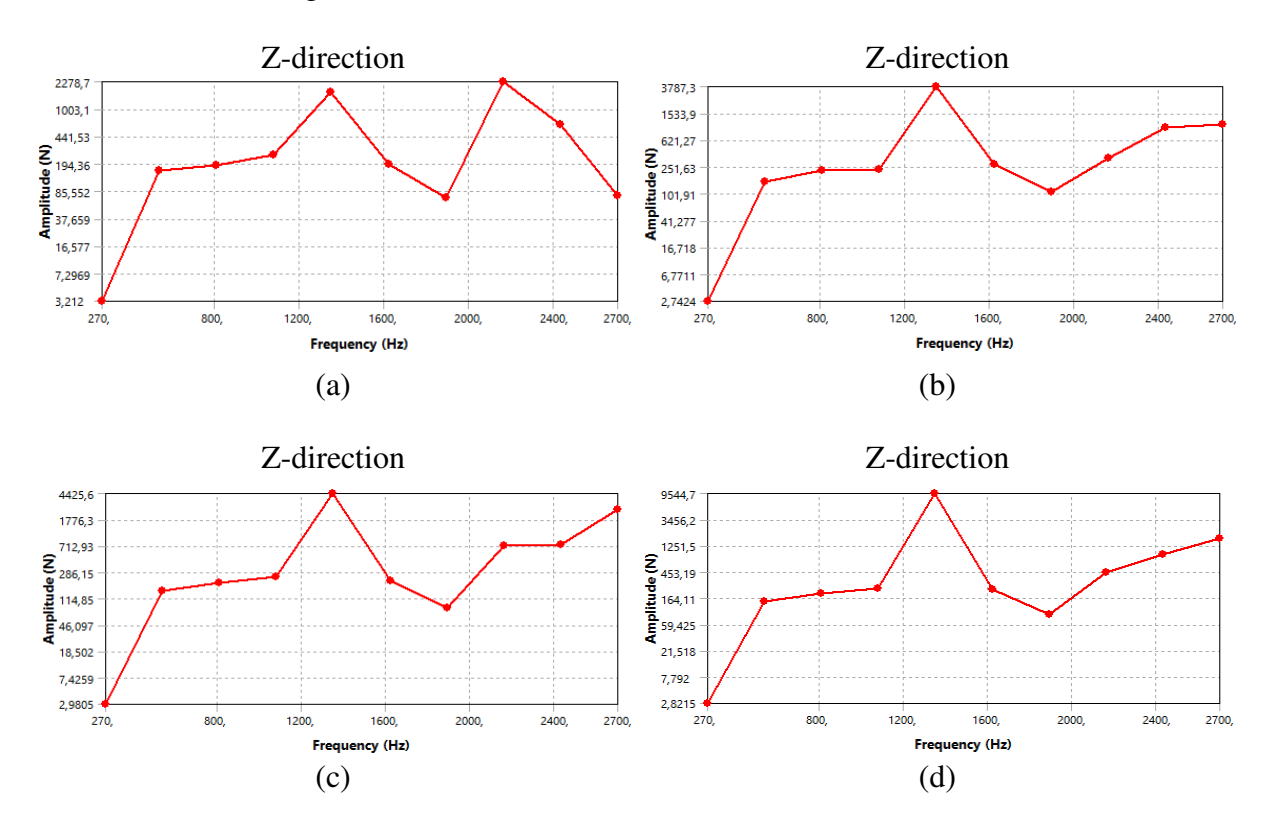


Fig. 29. Shows the force reaction for a Jeffcott rotor with 4 varieties of materials: (a) JIS-S45C; (b) 38CrMoAl; (c) structural steel; (d) Ti-6AL-4V

Distribution of equivalent stress and total displacement in rotordynamic system. Figure 30 shows the equivalent stress distribution in Jeffcott's rotor-dynamic system (JIS S45C, 38CrMoAl, structural steel, titanium alloy) for four different materials. When 0.1 kg of unbalance is added to the disc with the increase in frequencies from 270 to 2700 Hz with a step of 100 Hz, the amplitude of maximum equivalent stresses for 4 materials are equal to (18625, 9435.2, 55134, 23624 MPa) (red outline at bearing level).

On the other hand, when 0.1 kg of unbalance is added to the disk with the increase of frequencies from 270 to 2700 Hz with a step of 100 Hz, the normal plastic deformation amplitude for 4 materials (JIS S45C, 38CrMoAl, structural steel, titanium alloy) are equal to (0.1026, 0.0506, 0.2894, 0.2187 mm/mm).

We note in Fig. 30, the single-disc root-dynamic system manufactured by the two materials (JIS S45C, 38CrMoAl) show a minimum total displacement which are equal to (11.984, 5.213 mm) by contribution of the two steels (structural steel, titanium alloy).

Figure 30 shows the maximum shear stress distribution in Jeffcott's rotor-dynamic system made by four different materials (JIS S45C, 38CrMoAl, structural steel, titanium alloy). When 0.1 kg of unbalance is added to the disc with increasing frequencies from 270 to 2700 Hz with a step of 100 Hz, the maximum shear stress amplitude for 4 materials are equal to (10036, 5288, 29634, 12649 MPa) (outline in red at the bearings).

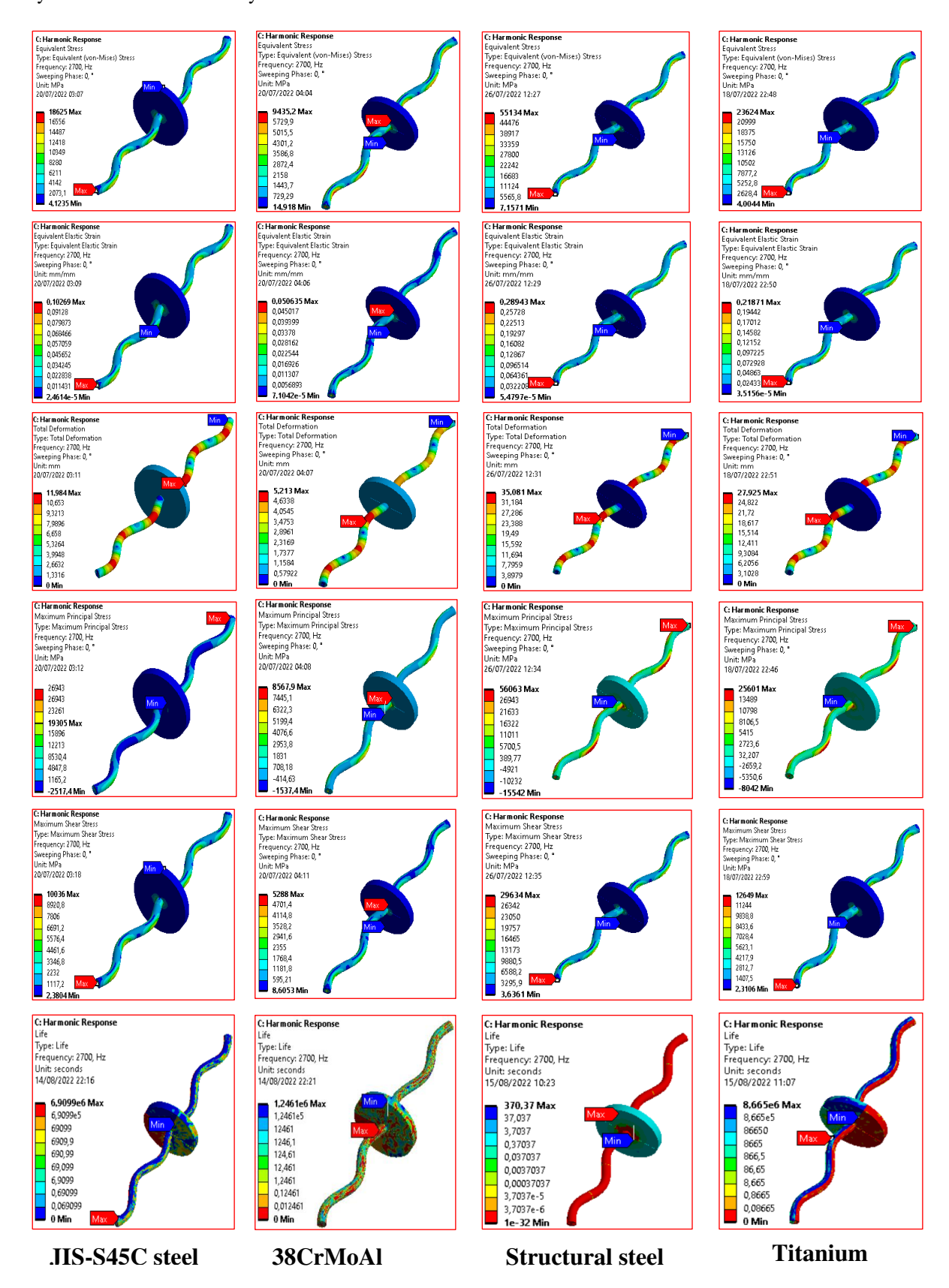


Fig. 30. Shows the von Mises stress, normal elastic strain, total displacement, maximum shear stress and life cycle number for a Jeffcott rotor with 4 varieties of materials.

On the other hand, when 0.1 kg of unbalance is added to the disc with the increase in frequencies from 270 Hz to 2700 Hz with a step of 100 Hz, the number of life cycles for the 4 materials (JIS S45C, 38CrMoAl, Structural Steel, Titanium Alloy) are equal to (6.9099e6, 1.2461e6, 370.37, 8.665e6).

Conclusions

The academic finite element method is a good tool to understand the dynamics of rotor system. It is observed that all the verification of analysis, that of numerical results for a single rotor system is very good agreement with ANSYS results. The Jeffcott rotor performed using the commercially available ANSYS Workbench software indicated that the critical velocities for four materials are 1784.2, 1784.9, 8147.7RPMs for JIS S45C steel material, 1858.7, 1859.4, 8468.1 RPMs for 38CrMoAl steel material, 1813.9, 1814.6, 8275,9 RPMs for structural steel material and 1824.8, 1825.5, 8323.9 for titanium Alloy (Ti-6AL-4V) material. The natural frequencies of the Jeffcott rotor are also higher for 38CrMoAl steels and are equal for the two materials (titanium alloy (Ti-6Aal-4V) and JIS S45C) and minimum for steel structure steels.

For JIS-S45C steel a stability of the Jeffcott rotor system found in the Campbell diagram between the two critical speeds (1784.2 rpm, 8147.7 RPM), that is to say the rotor system is turned well with a speed rotation superior to 1784.2 rpm and lower of 8147.7 rpm. On the other hand, if the rotation speed of the dynamic rotor superior the critical speed 8147.7 RPM, the rotor system is turned well (see Fig. 12).

For 38CrMoAl steel a stability of the Jeffcott rotor system found in the Campbell diagram between the two critical speeds (1858.7 rpm, 8468.1 rpm), that is to say the rotor system is turned well with a speed rotation superior of 1858.7 rpm and lower of 8468.1 rpm. On the other hand, if the rotation speed of the dynamic rotor superior the critical speed 8468.1 rpm, the rotor system is turned well (see Fig. 12).

For structural steel a stability of the Jeffcott rotor system found in the Campbell diagram between the two critical speeds (1813.9, 8275.9 rpm), that is to say the rotor system is turned well with a speed rotation superior of 1813,9rpm and lower of 8275.9 rpm. On the other hand, if the rotation speed of the dynamic rotor superior the critical speed 8275.9 rpm, the rotor system is turned well (see Fig. 12).

For titanium alloy (Ti-6AL-4V) material a stability of the Jeffcott rotor system found in the Campbell diagram between the two critical speeds (1824.8, 8323.9 rpm), that is to say the rotor system is turned well with a speed rotation superior of 1824.8rpm and lower of 8323.9 rpm. On the other hand, if the rotation speed of the dynamic rotor superior the critical speed 8323.9 rpm, the rotor system is turned well (see Fig. 12). The rotary machines undergoing higher operating speeds like propeller shafts, turbine and compressor are recommended to use JIS S45C and Ti-6AL-4V.

In the harmonic analysis, due to the unbalance force of 0.1 kg acting on the disc, the vibration severity is very high for the steel materials, and Equivalent stress is 18625 MPa for JIS S45C steel material, 9435.2 MPa for 38CrMoAl steels material, and 55134 MPa for Structural steels material, and 23624 MPa for titanium alloy (Ti-6AL-4V) material.

Not only equivalent alternating stresses but also the other stresses in the X-axis, Y-axis, and Z-axis directions are less severity for 38CrMoAl steels materials compared to the JIS S45C steels, 38CrMoAl steels and titanium alloy (Ti-6AL-4V) materials (refer Figs. 10–12). The rotary machines undergoing high stress severity and deformation severity are recommended to use 38CrMoAl steels.

Rotor dynamic analysis of Jeffcott rotor with four materials, JIS S45C, 38CrMoAl, structural steel, titanium alloy materials are highly recommended with the less severity of vibration. Choose JIS S45C and Ti-6AL-4V materials for higher whirling speeds compared to structural steel, titanium alloy materials.

The sweeping phase angle severity is found maximum on the Z-direction for all materials. Compared to the two steels (structural steels, titanium alloy), parameters such as natural

frequency, the harmonic response is far better for (JIS S45C, 38CrMoAl) and are recommended. A tabular representation is listed in Table 2 and 3.

Authors thus presented a comparative picture about dynamic analysis of Jeffcott rotor with 0.1 kg of unbalance mass is added to the disc, as a case sample application. It is expected that a study capturing the comparative status of different engineering materials along with different analyses will be useful for both researchers and practitioners. Both communities will be motivated to explore and compare different materials for diverse and better applications.

References

- 1. Malgol A, Potdar Y. Modelling and simulation of single rotor system. *Int J Latest Technol Eng Manage Appl Sci.* 2017;6(4): 163–169.
- 2. Tai X, Ma H, Liu F, Liu Y, Wen B. Stability and steady-state response analysis of a single rub-impact rotor system. *Archive of Applied Mechanics*. 2015;85(1): 133–148.
- 3. Wang N, Jiang D. Vibration response characteristics of a dual-rotor with unbalance-misalignment coupling faults: Theoretical analysis and experimental study. *Mechanism and Machine Theory*. 2018;125: 207–219.
- 4. Xul J, Zheng X, Zhang J, Liu, X. Vibration characteristics of unbalance response for motorized spindle system. *Procedia Engineering*. 2017;174: 331–340.
- 5. Ghoneam SM, Asy MA, Embaby AG, Elhadhody EA. Dynamic analysis of rotor system with active magnetic bearings using finite element method. *International Journal of Engineering Applied Sciences and Technology*. 2022;7(1): 2455–2143.
- 6. Sghaier E, Bourdon A, Remond, Dion JL, Peyret N. Dynamic behavior of very-high speed rotors at non-stationary conditions. *Proceedings of The 10th International Conference On Rotor Dynamics Iftomm.* 2019;4(63): 79–90.
- 7. Chen Y, Mendoza A.S.E, & Griffith D.T. Experimental and numerical study of high-order complex curvature mode shape and mode coupling on a three-bladed wind turbine assembly. *Mechanical Systems and Signal Processing*. 2021;160: 107873.
- 8. Dabachi MA, Rouway M, Rahmouni A, Bouksour O, Sbai SJ, Laaouidi H, Lagdani O. Numerical investigation of the structural behavior of an innovative offshore floating darrieus-type wind turbines with three-stage rotors. *Journal of Composites Science*. 2022;6(6): 167.
- 9. Bose A, Sathujoda P, Canale G. Natural frequency analysis of a functionally graded rotor-bearing system with a slant crack subjected to thermal gradients. *International Journal of Turbo & Jet-Engines*. 2021. Available from: https://doi.org/10.1515/tjeng-2021-0002
- 10. Sudhakar GNDS, Sekhar AS. Identification of unbalance in a rotor bearing system. *Journal of Sound and Vibration*. 2011;330(10): 2299–2313.
- 11. Shrivastava A, Mohanty AR. Identification of unbalance in a rotor system using a joint input-state estimation technique. *Journal of Sound and Vibration*. 2019;442: 414–427.
- 12. Pavlenko IV, Simonovskiy VI, Demianenko MM. Dynamic analysis of centrifugal machines rotors supported on ball bearings by combined application of 3D and beam finite element models. *IOP Conference Series: Materials Science and Engineering*. 2017;233(1): 012053.
- 13. Fernandes R, El-Borgi S, Ahmed K, Friswell MI, Jamia N. Static fracture and modal analysis simulation of a gas turbine compressor blade and bladed disk system. *Advanced Modeling and Simulation in Engineering Sciences*. 2016;3: 1–23.
- 14. Jung HC, Krumdieck S. Rotordynamic modelling and analysis of a radial inflow turbine rotor-bearing system. *International Journal of Precision Engineering and Manufacturing*. 2014;15: 2285–2290.
- 15. Sghaier E, Bourdon A, Remond D, Dion JL, Peyret N. Dynamic behavior of very-high speed rotors at non-stationary conditions. In: *International Conference on Rotor Dynamics*. 2018. p.79–90.
- 16. Yang XU, Lei Z, Suyuan YU. *Dynamics Analysis of very flexible Rotor. Technical Paper.* Beijing: Institute of Nuclear Energy Technology, Tsinghua University; 2004.

- 17. Egusquiza E, Valero C, Presas A, Huang X, Guardo A, Seidel U. Analysis of the dynamic response of pump-turbine impellers. Influence of the rotor. Mechanical Systems and Signal Processing. 2016;68: 330–341.
- 18. Garcia M, Laín S, Orrego S, Barbosa J, Quintero B. Hydraulic and rotor-dynamic interaction for performance evaluation on a Francis turbine. International Journal on Interactive Design and Manufacturing (IJIDeM). 2017;11(3): 623–632.
- 19. Vasquez RE. On the use of structural dynamics in virtual manufacturing. *International* Journal on Interactive Design and Manufacturing (IJIDeM). 2017;11(1): 103–114.
- 20. Newland DE, Ungar EE. Mechanical vibration analysis and computation. 1990.
- 21. Rao S.S. Vibration of continuous systems. John Wiley & Sons; 2019.
- 22. Kushwaha N, Patel V.N. Modelling and analysis of a cracked rotor: a review of the literature and its implications. Archive of Applied Mechanics. 2020;90(6): 1215–1245.
- 23. Sarmah N, Tiwari R. Dynamic analysis and identification of multiple fault parameters in a cracked rotor system equipped with active magnetic bearings: a physical model based approach. Inverse Problems in Science and Engineering. 2020;28(8): 1103-1134.
- 24. Jung H.C, Krumdieck S. Rotordynamic modelling and analysis of a radial inflow turbine rotor-bearing system. International Journal of Precision Engineering and Manufacturing. 2014;15(11): 2285–2290.
- 25. Lalanne M, Ferraris G. Rotordynamics prediction in engineering. Wiley; 1990.
- 26. Rao JS. History of rotating machinery dynamics. Springer; 2011.
- 27. Alam HS, Irasari P. Rotor-dynamic characteristic evaluation of interior permanent magnet motor using finite element method. Journal of Mechatronics, Electrical Power, and Vehicular Technology. 2014;5(1): 1–8.
- 28. Santiago DFA. Diagnostic of faults of rotating machinery using wavelet transform and artificial neural networks (Doctoral dissertation, Phd Thesis, am inas acu ldade de ngen aria ec nica). Universidade Estadual de Campinas; 2003.
- 29. Lalanne M, Ferraris G. Rotordynamics prediction in engineering. John Wiley & Sons; 1998. 30. Senko R, Silva AA, Borges JM. Dynamic and control of a rotor system based on passage through critical speeds with incorporation of smart actuators in flexible bearing device. In: Proceedings of Congresso Brasileiro de Engenharia Mecânica-COBEM. Ribeirão Preto; 2013.

THE AUTHORS

Nasreddine Afane El Bachir (10)

e-mail: afanenasreddine@gmail.com

Samir Zahaf 🗓

e-mail: samir.zahaf@univ-dbkm.dz

Mouloud Dahmane 🗓

e-mail: m.dahmane@ensh.dz

Azzeddine Belaziz (10)

e-mail: belaziz2013@gmail.com

Noureddine Rachid (1)

e-mail: noureddine.rachid@univ-oran2.dz

Evaluation of mechanical properties of ABS-based fiber composite with infill using 3D printing technology

Submitted: April 13, 2023

Approved: November 14, 2023

Accepted: December 12, 2023

P. Venkataramana [b], S.P. Jani [b], U. Sudhakar [b], M. Adam Khan [b2], K. Sravanthi [b]

¹ Marri Laxman Reddy Institute of Technology and Management, Hyderabad, India

² Kalasalingam Academy of Research and Education, Tamil Nadu, India

⊠ adamkhanm@gmail.com

Abstract. This research explores the utilization of acrylonitrile butadiene styrene (ABS) material for structural applications, addressing the growing demand for polymer composites. Employing fused filament fabrication (FFF) 3D printing with a 2 mm shell thickness, ABS samples were reinforced with basalt, hemp, and glass fibers using epoxy resin to enhance material strength. Mechanical behavior under axial, flexural, and impact loading conditions was investigated, revealing the basalt-reinforced ABS composite's superior performance with a maximum load of 9540 N - three times that of pure ABS (2975 N). The load-bearing capacity of basalt-epoxy reinforced ABS reached 880 N, surpassing glass-epoxy and hemp-epoxy variants. Impact energy was notably higher for reinforced composites (28.9-32.2 KJ/m²) compared to pure ABS (10.3 KJ/m²). The SEM analysis also carried out for better understanding of fracture surface of composites. This study recommends the application of these reinforced ABS composites in structural contexts.

Keywords: 3D printing; fibre; epoxy; mechanical load

Citation: Venkataramana P, Jani SP, Sudhakar U, Adam Khan M, Sravanthi K. Evaluation of mechanical properties of ABS-based fiber composite with infill using 3D printing technology. *Materials Physics and Mechanics*. 2023;51(7): 99–106. DOI: 10.18149/MPM.5172023_8.

Introduction

Fused deposition modelling (FDM) is a widely used 3D printing technology that has revolutionized the manufacturing industry. FDM printers use a thermoplastic filament that is melted and extruded layer by layer to create 3D objects [1]. The most commonly used material in FDM printing is acrylonitrile butadiene styrene (ABS). However, ABS has some limitations in terms of strength, stiffness, and thermal stability. To overcome these limitations, researchers have been investigating the use of fiber reinforcements in ABS for FDM printing. The addition of fibers can significantly improve the mechanical properties of the printed parts. In this literature review, we will explore the various types of fibers that can be used as reinforcement in ABS for FDM printing and the impact of fiber reinforcement on the mechanical and thermal properties of the printed parts [2,3].

In recent years, there has been a growing interest in using fiber-reinforced materials for 3D printing. The addition of fibers to a polymer matrix can enhance the mechanical properties of the printed parts, including tensile strength, flexural strength, and impact strength. There are several types of fibers that have been investigated as reinforcement in ABS for FDM printing, including carbon fibers, glass fibers, and natural fibers [4,5].

Carbon fibers are widely used as a reinforcement in composites due to their high strength, stiffness, and low weight. Several studies have investigated the use of carbon fibers as a reinforcement in ABS for FDM printing [6]. Carbon fiber-reinforced ABS (CFR-ABS) can

© P. Venkataramana, S.P. Jani, U. Sudhakar, M. Adam Khan, K. Sravanthi, 2023.

Publisher: Peter the Great St. Petersburg Polytechnic University

This is an open access article under the CC BY-NC 4.0 license (https://creativecommons.org/li-censes/by-nc/4.0/)

have a tensile strength up to 120 MPa and a modulus of elasticity up to 12 GPa, which is significantly higher than unreinforced ABS [7]. The addition of carbon fibers can also improve the thermal stability of ABS. However, the high cost of carbon fibers and the difficulty in achieving a homogeneous distribution of fibers in the polymer matrix are significant challenges in using CFR-ABS for 3D printing [8].

Glass fibers are another commonly used reinforcement in composites due to their high strength and stiffness. Several studies have investigated the use of glass fibers as a reinforcement in ABS for FDM printing [9]. Glass fiber-reinforced ABS (GFR-ABS) can have a tensile strength up to 80 MPa and a modulus of elasticity up to 7 GPa, which is significantly higher than unreinforced ABS. The addition of glass fibers can also improve the thermal stability of ABS. However, the main challenge in using GFR-ABS for 3D printing is the difficulty in achieving a homogeneous distribution of fibers in the polymer matrix [10].

Natural fibers, such as flax, hemp, and jute, have been investigated as a reinforcement in composites due to their low cost, low density, and biodegradability [11]. Several studies have investigated the use of natural fibers as a reinforcement in ABS for FDM printing [12]. Natural fiber-reinforced ABS (NFR-ABS) can have a tensile strength up to 40 MPa and a modulus of elasticity up to 4 GPa. The addition of natural fibers can also improve the thermal stability of ABS. However, the main challenge in using NFR-ABS for 3D printing is the difficulty in achieving a homogeneous distribution of fibers in the polymer matrix [13].

The novelty of this project lies in the investigation of the mechanical behavior of ABS composites reinforced with different types of fibers under different loading conditions. While ABS material is commonly used for soft and low-load applications, the addition of fiber reinforcement can enhance its strength and make it suitable for structural applications. The use of 3D printing technology for fabricating the composite samples provides an efficient and cost-effective way to produce complex geometries. The use of basalt and hemp fibers as reinforcement materials is relatively new and has not been extensively studied in comparison to traditional reinforcement materials like glass fibers. Therefore, this project offers a unique opportunity to explore the mechanical properties of ABS composites reinforced with basalt and hemp fibers in comparison to glass fibers. The study results will contribute to the knowledge of the potential of reinforced ABS composites for structural applications, offering insights into the optimal fiber type and loading conditions for achieving the desired mechanical performance.

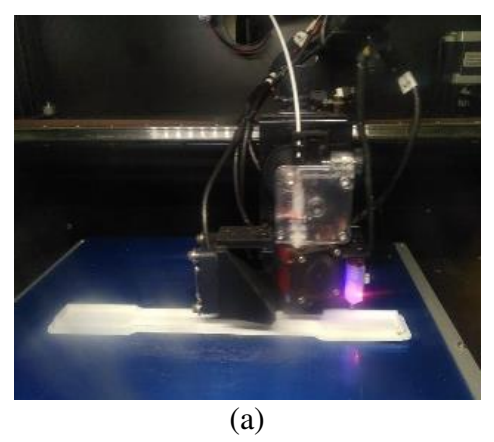
Materials and Methods

Sample development. Acrylonitrile butadiene styrene (ABS) is the common thermoplastic polymer material which is highly recommended and used for making the structural device. Most of the toys and play store devices are made using this polymeric material [14,15]. To increase the structural properties in terms of strength, the fiber reinforcement is made inside the 3D printed ABS material. In order to study the strength of 3D printed composite, a common ASTM standard test samples are used. In order to produce the test structure, the ABS wire is used to develop the test sample for tensile test, flexural test and impact test following ASTM standard. Figure 1 shows the photo image of 3D printing of ABS material (Table 1).

The test samples developed through the additive manufacturing are further post processed to fill the structure with different fiber and Epoxy SYSBOND 757 with hardener 757 (10:1) [16]. The fibre and resin in the proportion of 60:40 wt. % is used to fill in the additive – built test coupons. Three different types of fibre namely basalt, glass and hemp fibre are used as a reinforcement material mixed with the epoxy resin; and the same are filled inside the ABS structure. Standard procedure is adopted for resin – catalyst curing with fibre reinforcement. The prepared mixture / blend of fibre and epoxy was refilled as given in the photo image (Fig. 2).

After a proper curing time, the test samples are cleaned and verified to the standard dimensions. The extra projections or overflow in the ASTM standard dimensions are cleared

before the mechanical testing (tensile, flexural and impact) of samples. The samples are now designated as i. ABS + Basalt, ii. ABS + Glass and iii. ABS + Hemp combination. The final test samples are given in the following image (Fig. 3). Further, the standard procedure is used to evaluate the mechanical properties of the test samples.



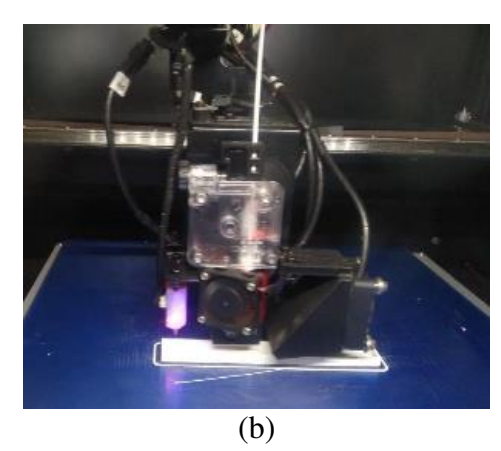


Fig. 1. 3D printing of hollow structure using ABS wire for mechanical test specimen following ASTM standard dimensions: (a) tensile test sample; (b) flexural test sample

Table 1. Printing specification

Initial layer height, mm	0.2
Top/bottom thickness, mm	0.68
Infill density, %	100
Infill pattern	Lines
Infill line direction, °	90
Bed plate temp., °C	100
Travel speed, mm/s	100
Fan speed, %	100
Adhesion Type	Skirt
Speed, mm/s	80
Thickness, mm	0.16
Temp., °C	270



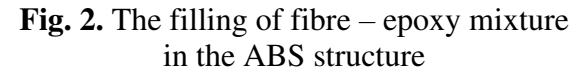


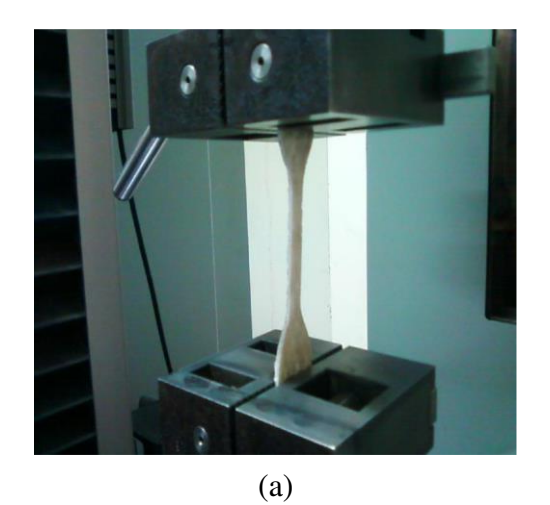


Fig. 3. Test samples after curing of fibre – epoxy resin in the ABS structure

Results and Discussion

Tensile testing. The mechanical testing of the ABS build structure with fiber – epoxy filling is compared with pure ABS 3D printed sample. The test samples are investigated to report the material behaviour under axial loading condition. The tensile testing is followed with an ASTM Standard number ASTM D638-14 for evaluation. The test samples are designated in three different groups of combination for better comparison and illustration; and the samples are as:

- 1. ABS with basalt fibre and epoxy resin (ABS + basalt);
- 2. ABS with glass fibre and epoxy resin (ABS + glass);
- 3. ABS with hemp fibre and epoxy resin (ABS + hemp).



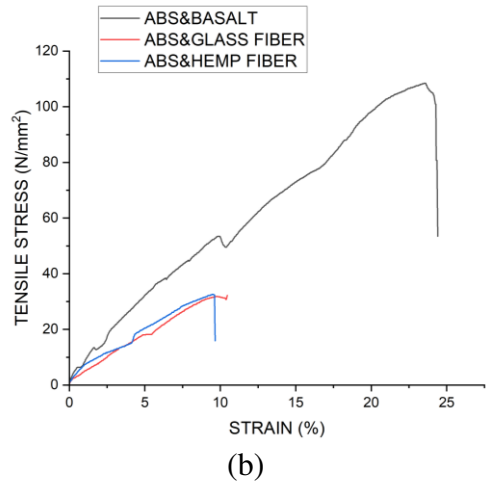


Fig. 4. Universal testing machine (a) and stress-strain graphs (b)

Figure 4 shows the mechanical testing facility for the test sample (UTM 2010 Model) and the result of test samples in the form of graph. The stress – strain curves recorded for the ABS with different fiber and epoxy resin indicate the appreciable result. The difference in yield point and fracture point are wide in range for the samples based on the reinforcement material. While comparing the individual results, the performance of the ABS material with basalt fiber maximum [17]. The maximum load for the ABS material with basalt fiber is, 9540 N as the basalt natural material has high strength compared to the other fiber material. It is three times stronger than the pure ABS 3D printed material (2975 N load) as indicated in the Fig. 5 as tensile load factor. The ABS with glass fiber (3360 N load) and hemp fiber (3240 N load) are less compared to basalt fiber material. The brittleness nature of glass fiber has induced the composite to fracture in the early stage rather than the basalt.

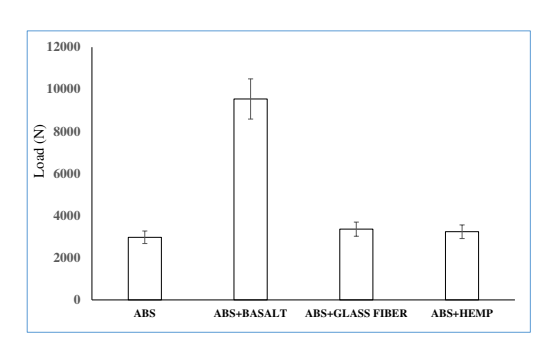


Fig. 5. Tensile load recorded for the ABS with different fibre – epoxy resin

Further, the material quality in terms of strength is evaluated for comparison. As recorded, the maximum yield load in the axial condition has increased tensile strength of different material combination. Figure 6 shows tensile strength recorded for different fiber material in the ABS material. As the load increase, the intensity of the subjected area will subsequently support to increase the strength. Therefore, the tensile strength of the material will be maximum [18,19]. On the other hand, the material behaviour in terms of young's modulus is one of the

predominant factor. The result of stress and the strain induced in the material during the axial load is used to find the modulus of the material. Figure 7 is the calculated value of modulus based on stress and strain of the material behaviour. The difference in modulus is very less compared to each material combination. For example, the hemp and glass fiber (3.2 and 3.1 KPa) is close to the basalt fiber (4.3 KPa), indicating the difference in deformation. As the elongation increases, the modulus of the material will be reduced. By the for pure ABS material the modulus recoded is 1.8 KPa where the elongation is maximum compared to the fiber reinforcement. Therefore, the load bearing capacity of the ABS material with basalt – epoxy resin reinforcement has developed a better result compared to other materials.

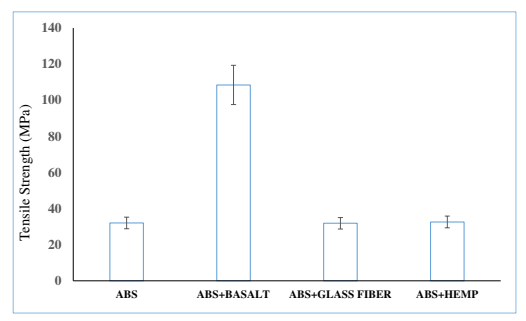


Fig. 6. Tensile strength of ABS with different fibre – epoxy resin

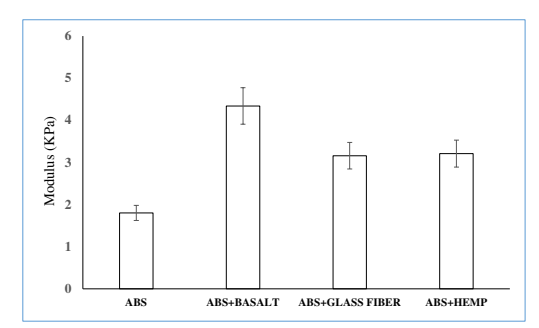


Fig. 7. Youngs modulus of ABS with different fibre – epoxy resin

Flexural test. The flexural testing of the material is made through the three point bending method following the simply supported loaded structure. The ASTM standard was followed for the flexural loading (ASTMD790-30) with a defined set of geometrical dimensions and experimental procedure. Like the tensile testing, the samples are designated as:

- 1. ABS with basalt fibre and epoxy resin (ABS + Basalt);
- 2. ABS with glass fibre and epoxy resin (ABS + glass);
- 3. ABS with hemp fibre and epoxy resin (ABS + hemp).

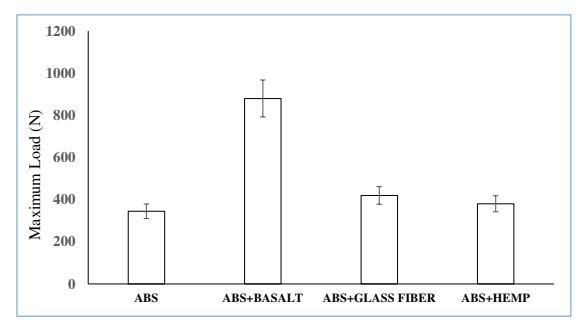


Fig. 8. Flexural load recorded for the ABS material reinforced with different types of fibre – epoxy resin

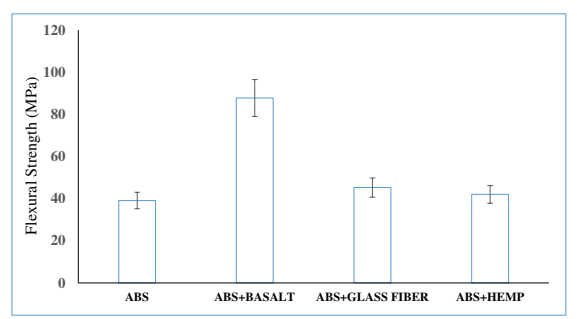


Fig. 9. Flexural strength recorded for the ABS material reinforced with different types of fibre – epoxy resin

The samples are tested and evaluated to report the flexural strength and the bending load of the material. From the experimentation, the flexural load and the strength of the material. Figure 8 indicates the maximum load for ABS with different reinforcement material. The load bearing capacity of the basalt – epoxy reinforced ABS material recorded with a maximum load of 880 N. The basalt fiber possess high strength, and it has high flexural properties just like the carbon material. The nature made basalt material (derived from the rock) has high damping energy, and it can withstand maximum load. For the glass and hemp reinforced ABS material possess two times less load compared to the basalt material. When comparing the pure ABS with fiber reinforced material; the quality of pure ABS found discouraging to select in terms of load. As the pure ABS material developed through the additive manufacturing does not have enough bonding to bear the load.

In general, the additive build materials are anisotropic in nature, and they are in need of secondary process or support to bear the load. In this case, the ABS structure with different types of fiber – epoxy resin is filled and investigated. The reinforcement has a reasonable strength compared to the ABS built material structure. From the graph (Fig. 9) the flexural strength of the material is recorded. The basalt fiber – epoxy has a maximum flexural strength of 87.7 MPa indicating the strength as in the axial loading. For the glass fiber and hemp fiber – epoxy reinforced ABS structure has less strength in the two-fold of basalt material. When the load is applied on the hatch layers, the structure is subjected to sliding of the material and it fails. At the same, the hatch layers do not have good bonding with maximum loading and make the material fracture. To increase the strength, the reinforcement in the ABS structure has supported the layer to withstand the applied load.

Impact strength. The impact strength of the above designed materials is studied to record the impact energy observed in the material. The ASTM standard was followed for the Impact (ASTM D256) with a defined set of geometrical dimensions and experimental procedure. The impact energy of the ABS structure reinforced with the basalt – epoxy resin has a maximum impact energy of 53.9 KJ/m². As mentioned in the previous section, the data recorded for the ABS with basalt – epoxy resin has two time high strength compared to the other two fibers. The glass – epoxy and hemp – epoxy has an average of 28.9 and 32.2 KJ/m² impact energy. At the same, the pure ABS structure has 10.3 KJ/m² energy. The ABS is the pure soft material which is vulnerable towards the impact load and do not have strength to face the load. However, on reinforcement of hard fiber in the ABS structure have absorbed the impact energy. From the Fig. 10 analysis, the mechanical behaviour of the material with fiber – epoxy reinforced structure results indicate that the basalt fiber has high strength in terms of tensile loading, flexural load and impact load.

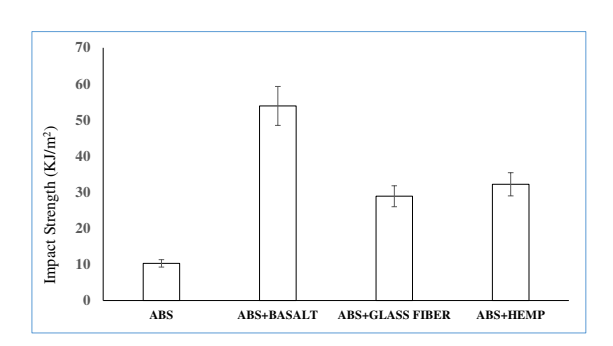


Fig. 10. Impact strength recorded for the ABS material reinforced with different types of fibre – epoxy resin

Scanning electron microscopy (SEM) analysis (Fig. 11) was conducted on fractured samples from the tensile and flexural testing of hemp-reinforced ABS composites. The examination aimed to elucidate the microstructural features and fracture surfaces, providing insights into the material's failure mechanisms. The SEM images revealed the dispersion and alignment of hemp fibers within the ABS matrix, contributing to the enhanced mechanical properties observed in the tensile and flexural tests. Fracture surfaces exhibited characteristic patterns indicative of fiber-matrix interactions, offering valuable information on the composite's structural integrity. This analysis further supports the comprehensive understanding of the mechanical behavior and performance of hemp-reinforced ABS composites in structural applications.

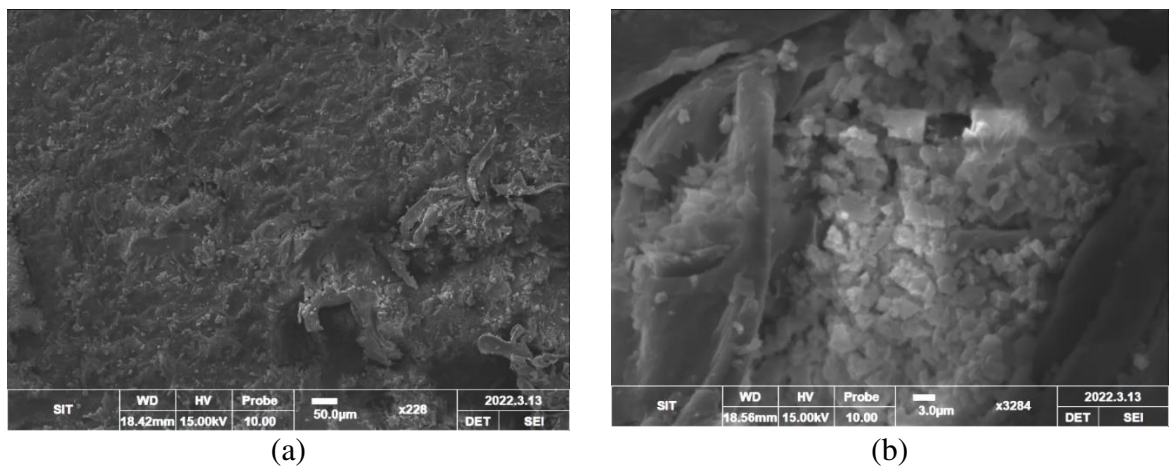


Fig. 11. Fracture image of hemp ABS fibre: (a) tensile tested sample; (b) flexural tested sample

Conclusions

The study utilized ABS material to construct a test structure, extending its application by developing three distinct fiber-epoxy reinforced ABS composites for comparative analysis. Findings indicate that fiber reinforcement significantly enhances axial load strength, with the basalt-epoxy composite demonstrating notable yielding strength. Deformation resistance, particularly towards elongation and strain rate, was improved through fiber-epoxy reinforcement, with the basalt fiber-epoxy composite displaying high resistance. In flexural strength, the basalt fiber-epoxy reinforced ABS material exhibited commendable bending strength and resistance against maximum bending load, making it suitable for structural applications. Contrarily, the soft ABS material demonstrated lower strength than its fiber-epoxy reinforced counterparts. Scanning electron microscopy (SEM) analysis confirmed the uniform distribution of fibers within the ABS matrix. The study recommends a shift in the application of soft ABS material towards mechanical loading and structural applications when reinforced with fibers and epoxy. For future work, optimizing fiber content, exploring additional composite materials, conducting durability studies, and assessing scalability for industrial applications are proposed avenues to refine and expand the application scope of fiber-reinforced ABS composites.

Reference

- 1. Jani SP, Kumar AS, Anushraj B, Mashinini PM, Uppalapati S. Development and Optimization Study of Poly-Lactic Acid Blended Carbon Particles by Fused Deposition Modelling Method. In: Innovations in Additive Manufacturing. Cham: Springer; 2022. p.121-138.
- 2. Mazzanti V, Malagutti L, Mollica F. FDM 3D printing of polymers containing natural fillers: A review of their mechanical properties. *Polymers*. 2019;11(7): 1094.
- 3. Morales MA, Atencio Martinez CL, Maranon A, Hernandez C, Michaud V, Porras A. Development and characterization of rice husk and recycled polypropylene composite filaments for 3D printing. *Polymers*. 2021;13(7): 1067.
- 4. Sanei SHR, Popescu D. 3D-printed carbon fiber reinforced polymer composites: a systematic review. J Composites Sci. 2020;4(3): 98.
- 5. Mazzanti V, Malagutti L, Mollica F. FDM 3D printing of polymers containing natural fillers: A review of their mechanical properties. *Polymers*. 2019;11(7): 1094.
- 6. Billah KMM, Lorenzana FA, Martinez NL, Wicker RB, Espalin D. Thermomechanical characterization of short carbon fiber and short glass fiber-reinforced ABS used in large format additive manufacturing. Additive Manufacturing. 2020;35: 101299.

- 7. Ahmed SW, Hussain G, Altaf K, Ali S, Alkahtani M, Abidi MH, Alzabidi A. On the effects of process parameters and optimization of interlaminate bond strength in 3D printed ABS/CF-PLA composite. *Polymers*. 2020;12(9): 2155.
- 8. Adeniran O, Cong W, Oluwabunmi K. Thermoplastic matrix material influences on the mechanical performance of additively manufactured carbon-fiber-reinforced plastic composites. *J Composite Materials*. 2022;56(9): 1391-1405.
- 9. Badogu K, Kumar R, Kumar R. 3D Printing of Glass Fiber-Reinforced Polymeric Composites: A Review. *J Institution of Engineers (India): Series C.* 2022;103(5):1285-1301.
- 10. Chabaud G, Castro M, Denoual C, Le Duigou A. Hygromechanical properties of 3D printed continuous carbon and glass fibre reinforced polyamide composite for outdoor structural applications. *Additive Manufacturing*. 2019;26: 94-105.
- 11. Mazzanti V, Malagutti L, Mollica F. FDM 3D printing of polymers containing natural fillers: A review of their mechanical properties. *Polymers*. 2019;11(7): 1094.
- 12. Parpala RC, Popescu D, Pupaza C. Infill parameters influence over the natural frequencies of ABS specimens obtained by extrusion-based 3D printing. *Rapid Prototyping J.* 2021;27(6): 1273-1285.
- 13. Ismail KI, Yap TC, Ahmed R. 3D-Printed Fiber-Reinforced Polymer Composites by Fused Deposition Modelling (FDM): Fiber Length and Fiber Implementation Techniques. *Polymers*. 2022;14(21): 4659.
- 14. Le Duigou A, Correa D, Ueda M, Matsuzaki R, Castro M. A review of 3D and 4D printing of natural fibre biocomposites. *Materials & Design*. 2020;194: 108911.
- 15. Antony S, Cherouat A, Montay G. Fabrication and characterization of hemp fibre based 3D printed honeycomb sandwich structure by FDM process. A. *Composite Materials*. 2020;27: 935-953. 16. Asokan R, Rathanasamy R, Paramasivam P, Chinnasamy M, Pal SK, Palaniappan SK. Hemp composite. In: *Green Sustainable Process for Chemical and Environmental Engineering*

and Science. Elsevier; 2023. p.89-112.

- 17. Chinnasamy V, Subramani SP, Palaniappan SK, Mylsamy B, Aruchamy K. Characterization on thermal properties of glass fiber and kevlar fiber with modified epoxy hybrid composites. *J Mater Res Technol*. 2020;9(3): 3158-3167.
- 18. Jayanth D, Kumar PS, Nayak GC, Kumar JS, Pal SK, Rajasekar R. A review on biodegradable polymeric materials striving towards the attainment of green environment. *J Polymers Environ*. 2018;26: 838-865.
- 19. Kaliyannan GV, Rathanasamy R, Kumar HKM, Raj MKA, Chinnasamy M, Pal SK, Palaniappan SK. Natural fiber-based bio-degradable polymer composite. In: *Green Sustainable Process for Chemical and Environmental Engineering and Science*. Elsevier; 2023. p.145-165. 20. ASTM D256. *Standard Test Methods for Determining the Izod Pendulum Impact Resistance of Plastics*.
- 21. ASTM D790. Standard Test Methods for Flexural Properties of Unreinforced and Reinforced Plastics and Electrical Insulating Materials.
- 22. ASTM D638. Standard Test Method for Tensile Properties of Plastics.

THE AUTHORS

Venkataramana P. 🗓

e-mail: nagakiransai123@gmail.com

Jani S.P. 🗓

e-mail: spjani10@gmail.com

Sudhakar U. @

e-mail: sudhakar uppalapati@yahoo.com

Adam Khan M. @

e-mail: adamkhanm@gmail.com

Sravanthi K. 📵

e-mail: kundhurusravanthi@gmail.com

Assessment of physical and vibration damping characteristics of sisal/PLA biodegradable composite

Submitted: April 12, 2023

Accepted: October 31, 2023

Approved: July 12, 2023

Y. Munde ¹ ¹, A.S. Shinde ¹ ¹ ¹, I. Siva ¹ ², P. Anearo ¹ ³

Abstract. Natural fiber composites have industrially attractive because of their low density, low cost, and comparable specific mechanical properties with synthetic fiber. The extrusion and injection molding method is used to fabricate the sisal fiber-reinforced PLA biodegradable composites with random fiber orientations. The fiber weight fraction varied from 0 to 30 wt. % (in the step of 10 %), and the influence of the fiber weight fraction of biocomposite on different properties was studied. The composites are tested for evaluating the physical properties, viz. density, hardness, and water absorption and vibration characteristics, viz. natural frequency and damping ratio. The density of Sisal/PLA biocomposites was seen from 1.18 to 1.23 gm/cm³ and hardness from 93.84 to 97.28. In water absorption, as the weight percentage of sisal increases, the diffusion and permeability coefficient increase and reach 2.83E-05 and 8.11E-06, respectively, for 30 % sisal loading. The fundamental natural frequencies and damping ratio of 30 wt. % sisal fiber biocomposite are 24.41 Hz and 0.1450, respectively, higher than the pure PLA. This is observed for all vibration modes, and the reason behind this is the high stiffness of fibers. These developed biodegradable composites help lower the cost of purePLA-based composites and have wise applications in packaging and allied industries.

Keywords: natural frequency; damping ratio; sisal fiber; PLA; water absorption

Citation: Munde Y, Shinde AS, Siva I, Anearo P. Assessment of physical and vibration damping characteristics of sisal/PLA biodegradable composite. *Materials Physics and Mechanics*. 2023;51(7): 107-116. DOI: 10.18149/MPM.5172023_9.

Introduction

A highly demanded and exponentially raised use of synthetic fiber reinforced composites in industries posed environmental concerns because of their non-degradable and non-renewable properties. Industries are looking to develop green materials independent of polymers derived from petroleum resources (1). Among the different biopolymers available today, i.e. polyhydroxy butyrate (PHB), poly(hy- droxyalkanoate) (PHA), polybutylene succinate (PBS), poly(lactic acid), starch, polycaprolactone (PCL), the PLA is promising to replace petroleum-based polymer in engineering applications which are renewable and biologically degradable because made from the fermentation of starch-based biomass. Initially, the high cost of PLA ed its use, but recently the cost has recentlys use, but recently the cost has fallen. The reinforcement of natural fibers in PLA producess composites with enhanced properties and also minimizes the amount of PLA required, which saves cost (2).

Several studies were carried out on the static mechanical behavior of PLA composites with a different types of natural fiber such as sisal [1,3,4], jute [5–8], Banana [4,9–13], pulp fibers (14), Pineapple Leaf (15), Ramie fabric [16,17], oil palm (18), corn (19), sugarcane bagasse (20), Grewia optiva (21), flax [22,23], kenaf (24), bamboo (25), Waste Leather Buff (26), olive pit powder (27). In comparison, many of these researchers have studied the effect of fiber loading, treatment of fiber, and fiber length on mechanical behavior in terms of tensile, flexural, and impact properties. They show that natural fibers reinforcement in PLA composites has good potential.

The literature reveals that a large quantum of research was carried out on sisal/PLA composite, but minimal work is reported on the vibration-damping behavior of biodegradable composites. The present work attempts to fabricate sisal/PLA composites using an extrusion-injection molding process with different weight fractions of sisal fiber. Experimental modal analysis will characterize the fabricated composite for physical and vibration properties.

Materials and Methods

PLA matrix and sisal fiber property details. The matrix used in this study is Ingeo biopolymer polylactic acid (PLA) of grade 3052D, supplied by Nature Works LLC, USA. This is designed for injection molding applications with a density of 1.24 g/cc, MFI 14 g/10 min (at 210 °C/2.16 Kg). Sisal fibers are obtained from the sisal plant leaves *Agave sisalana*. Fiber is extracted by a process known as decortication. The sisal fibers were obtained from Tokyo Engineering Corporation, Coimbatore, India. The chemical composition of sisal fiber includes 66-72 % cellulose, 12 % hemicellulose, 10-14 % lignin, and 11 % moisture content. The physical and mechanical properties of sisal fiber and PLA matrix are listed in Table 1.

Table 1. Properties of sisal fiber and PLA matrix

Property	Sisal fiber	PLA matrix		
Density, g/cc	1.45	1.24		
Elongation, %	2-2.5	3.5		
Tensile strength, MPa	511-635	62		
Young's modulus, GPa	9.4-22	-		
Heat distortion temperature, °C	-	55		

Manufacturing of specimens. Overnight dried sisal fibers of 3 to 5 mm, and PLA was compounded using a twin screw extruder (Make M/s Specific Engineering, Model –ZV 20) with Screw diameter 21 mm, L/D ratio 40:1, zonal temperature 165-210 °C and speed 40 rpm. Pallets were produced for 0, 10, 20, and 30 wt. % of fiber to the polymer weight. Table 2 shows the specimen coding followed in the production. Extruded pallets were dried at 90 °C for 12 hr. in a hot air-oven and then injection molded by injection molding machine (Make Ferromatik Milacron, model-OMEGA 80W) with a screw diameter of 36 mm and screw speed of 298 rpm. The molding temperature ranged from 175 to 200 °C, and a pressure of 50 bar was maintained.

Table 2. Composites formulation for specimen preparation

	1 word 20 Compositor formation for specimen proparation									
Composite designation PLA		Weight fraction of sisal fiber, %	Weight fraction of PLA matrix, %							
		0	100							
	S10	10	90							
	S20	20	80							
	S30	30	70							

Experimental studies

Measurement of density and void content. The density measurement of sisal/PLA composites as found out using Archimedes' principle. Theoretical density (ρ_t) of was calculated using Eq. (1):

$$\rho_C = \frac{1}{\left(\frac{W_f}{\rho_f} + \frac{W_m}{\rho_m}\right)},\tag{1}$$

where ρ_c , ρ_f , and ρ_m are the densities of composites, fiber and matrix, respectively. The weight fraction of fiber and matrix denoted are by W_f and W_m .

The volume of void fraction (V_v) of the sisal/PLA composites was calculated from values of experimental and theoretical densities by Eq. (2):

$$V_{v} = \frac{\rho_{t} - \rho_{e}}{\rho_{t}}.$$
 (2)

Measurement of shore D hardness. The Shore D hardness of PLA and sisal/PLA composites was measured using a digital Durometer HT-6510D. The hardness is measured as per ASTM D2240 at three different points, and the average value is reported.

Water absorption test. The specimens of sisal/PLA composites of dimensions 20 × 20 mm were used to measure water absorption as per ASTM D570. The specimens of all compositions were dried in a hot air oven at 80 °C for 12 hr. to remove moisture content. The completely dried specimen was immersed in distilled water for 7 days with an interval of 24 hr. Every 24 hr. of time, specimens were taken out from the water, wipedd out to remove excess water and immediately measured weight with an analytical weighing balance. Eq. (3) is used to calculate % of water absorption:

$$WA(\%) = \frac{W_t - W_1}{W_1},\tag{3}$$

where W_t and W_l are the weight of the specimen for a different time and the sample's initial dry weight, respectively.

The kinematics of water can be understood by calculating parameters such as the Diffusion coefficient (D) and Sorption coefficient (S) using Eqs. (4) and (5), respectively:

$$D = \frac{t^2 m^2}{16W_{\infty}^2},$$

$$S = \frac{W_{\infty}}{W_t},$$
(4)

$$S = \frac{W_{\infty}}{W_t},\tag{5}$$

where t is the initial sample thickness, m is the slope of the linear portion of the absorption curve, and W_{∞} water absorption at saturation time.

The net effect can be calculated in terms of Permeability Coefficient (P) by using Eq. (6):
$$P = D \times S$$
.

Experimental modal analysis. Experimental modal analysis has been carried out to study the effect of sisal fiber addition in PLA matrix composites on its natural frequency and damping ratio. In these experiments, a specimen is fixed in rigid support for 20 mm length, a miniature accelerometer is attached to the specimen's free end, and impulse forces are applied using an impact hammer. As a specimen triggered by hammer, the miniature accelerometer measures the displacement signal in the time domain. This time domain signal converts into the frequency domain using Fast Fourier Transform (FFT) algorithm in Bruel & Kjaer DAQ. The direct measurement of FRF was from Photon + software for various weight fraction percentages of fiber-reinforced PP composites. The coherence value was observed to be close to one, confirming the signal's data quality.

As per ASTME 756 [28], the produced composite has undergone impulse excitation analysis. Specimen of $200 \times 20 \times 3$ mm are analysed as cast and shown in Fig. 1(a). The experimental modal analysis determines the natural frequency and associated modal damping as key parameters allied with the dynamic behaviour of the composite structure. The effects of fiber loading on the free vibrational characteristics of composite beams are also investigated.

Figure 1(b) shows a free vibration test setup schematic. The specimen was held with fixed-free boundary conditions, and the excitation was carried out by an impact hammer (PCB Piezoelectric model 086C03) with a hard tip. The lightweight miniature accelerometer (Bruel & Kjaer model 352B10) is used to avoid the effect of the weight of the accelerometer on free vibrational behaviour, and it is placed with wax at the free end of the cantilever beam to acquire displacement signals. The data acquisition system (Bruel & Kjaer with Photon+ software) comprises of fast Fourier transform (FFT) algorithm to get frequency response and time domain signal. The first peaks in Frequency Response Function (FRF) curve show the natural frequency of the studied composite beam. The method employed to find the damping values of sisal fiber-reinforced PLA composites is half-power bandwidth using the FRF curves. Equation (7) was used to calculate a damping ratio.

$$\zeta = \frac{\Delta\omega}{2\omega_n},\tag{7}$$

where ζ – damping coefficient, $\Delta\omega$ – bandwidth and ω_n – natural frequency.

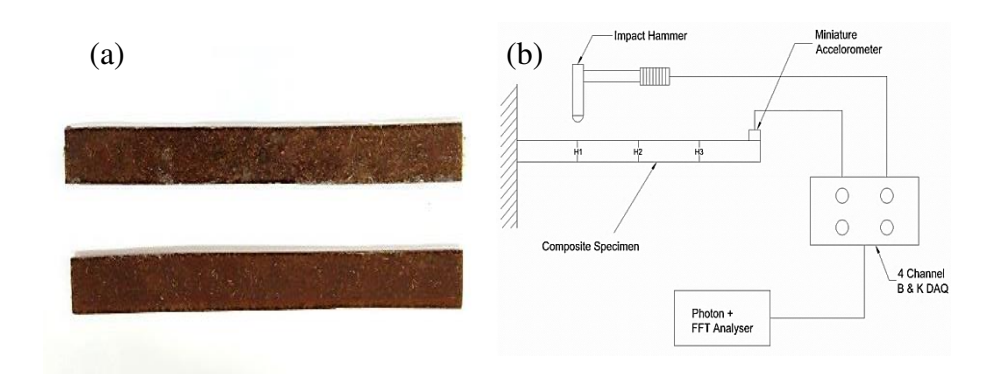


Fig. 1. (a) Test specimen (b) and test setup for experimental modal analysis

Results and Discussion

Density and void fraction. The theoretical and experimental density of the Sisal/PLA composite were obtained and shown in Table 3. For all the compositions, the experimental density was lower than that of theoretical density, and with an increase in fiber content from 10 to 30 %, the density of composites increased. This is because of the higher density of sisal fiber, which is 1.45 g/cm³, compared to pure PLA, which has 1.24 g/cm³.

The volume fractions of void content are shown in Table 2. This value indicates the difference in density of composites obtained by the experimental and theoretical methods.

The presence of voids in specimens is mainly because of air trapped during compounding, hollow spaces and incompatibility of fiber with matrix surface.

The value of void content is a maximum of 6.18 %, which clearly shows the fabrication of specimens was fairly good.

7	Fable 3. Density	and v	oid conten	t of Sisal/	PLA composites	
						_

Composition designation	Theoretical Density, g/cc	Experimental Density, g/cc	Volume fraction of voids, %
S10	1.26	1.18	6.18
S20	1.28	1.21	5.04
S30	1.30	1.23	5.23

Shore D hardness. The hardness of composite material is the resistance to indentation. Shore D hardness is the method that relatively measures hardness, a higher number indicates harder material. The value of the hardness of composite material depends on fiber dispersal into the matrix. The hardness of Sisal/PLA is shown in Table 4. Pure PLA exhibited a hardness value of 92.58 lowest, showing it is flexible material phase. Increasing fiber content increases the hardness throughout, and a maximum of was observed for S30 composites 97.28. This shows that the fiber incorporation has reduced the polymer chain's movement of PLA and increased rigidity.

Table 4. Shore D hardness of PP and sisal/PP composites

Composition designation	Shore D hardness
PLA	92.58
S10	93.84
S20	96.44
S30	97.28

Water absorption. The percentage weight gain versus the square root of time of sisal/PLA composites is shown in Fig. 2. The maximum WA of 4.67 % was seen for S30, and a minimum of 1.30 % for pure PLA. Water absorption (%) increased with an increase in fiber loading. The hydroxyl groups of sisal fiber highly contribute to gaining water. With increased fiber content, the quantity of hydroxyl groups counted to more, promoting an increase in WA. [2,23].

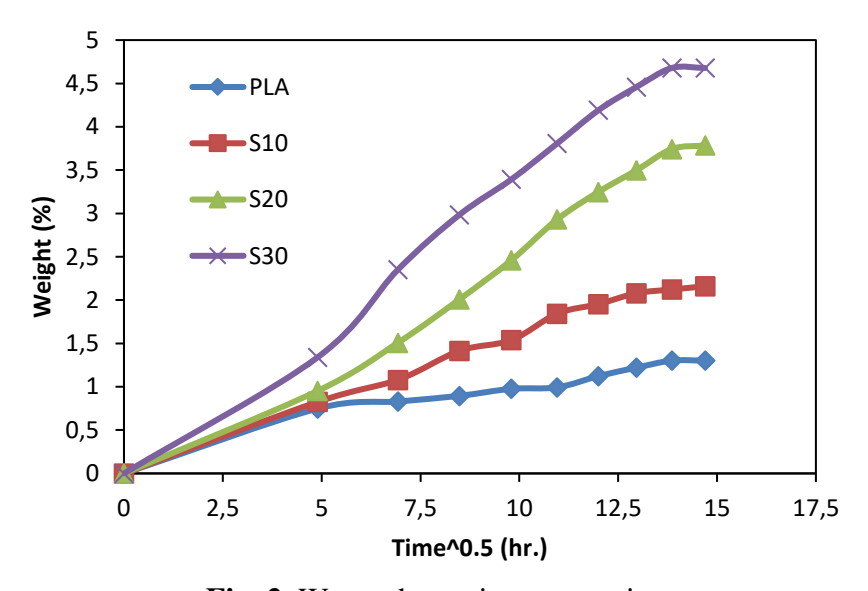


Fig. 2. Water absorption versus time

Table 5. Diffusion and permeability coefficient of the sisal/PLA composites

TOOLO OF BILLWOLD IN COLL		· · · · · · · · · · · · · · · · · · ·			
Composition designation	W_{∞}	W_t Diffusion coefficient (D)		Sorption coefficient (S)	Permeability coefficient (P)
PLA	1.302	0.748576	0.28E ⁻⁰⁵	0.575	1.59E ⁻⁰⁶
PLAS10	2.159	0.825318	1.62E ⁻⁰⁵	0.382	6.21E ⁻⁰⁶
PLAS20	3.753	0.921575	$1.78E^{-05}$	0.246	4.38E ⁻⁰⁶
PLAS30	4.678	1.340074	$2.83E^{-05}$	0.286	8.11E ⁻⁰⁶

The diffusion, sorption and permeability coefficient of pure PLA and sisal/PLA composites are depicted in Table 5. The findings discovered that the diffusion coefficient rises with increased fiber content, with the highest for S30 of 2.83E⁻⁰⁵ mm²/s. The permeability coefficient has shown similar behavior as that observed for diffusion.

Natural frequency of Sisal/PLA composites. A typical decay curve in the time domain and FRF curve, i.e. FFT of signals respectively for pure PLA shown in Figs. 3 and 4, respectively. FRF curve clearly shows the three peaks, the three modes' natural frequency. The beam deformation pattern at each peak is the mode shape which appears to be bending, second bending, and twisting. Similar signal data is obtained by triggering all specimens three times and then average natural frequency values at each mode reported.

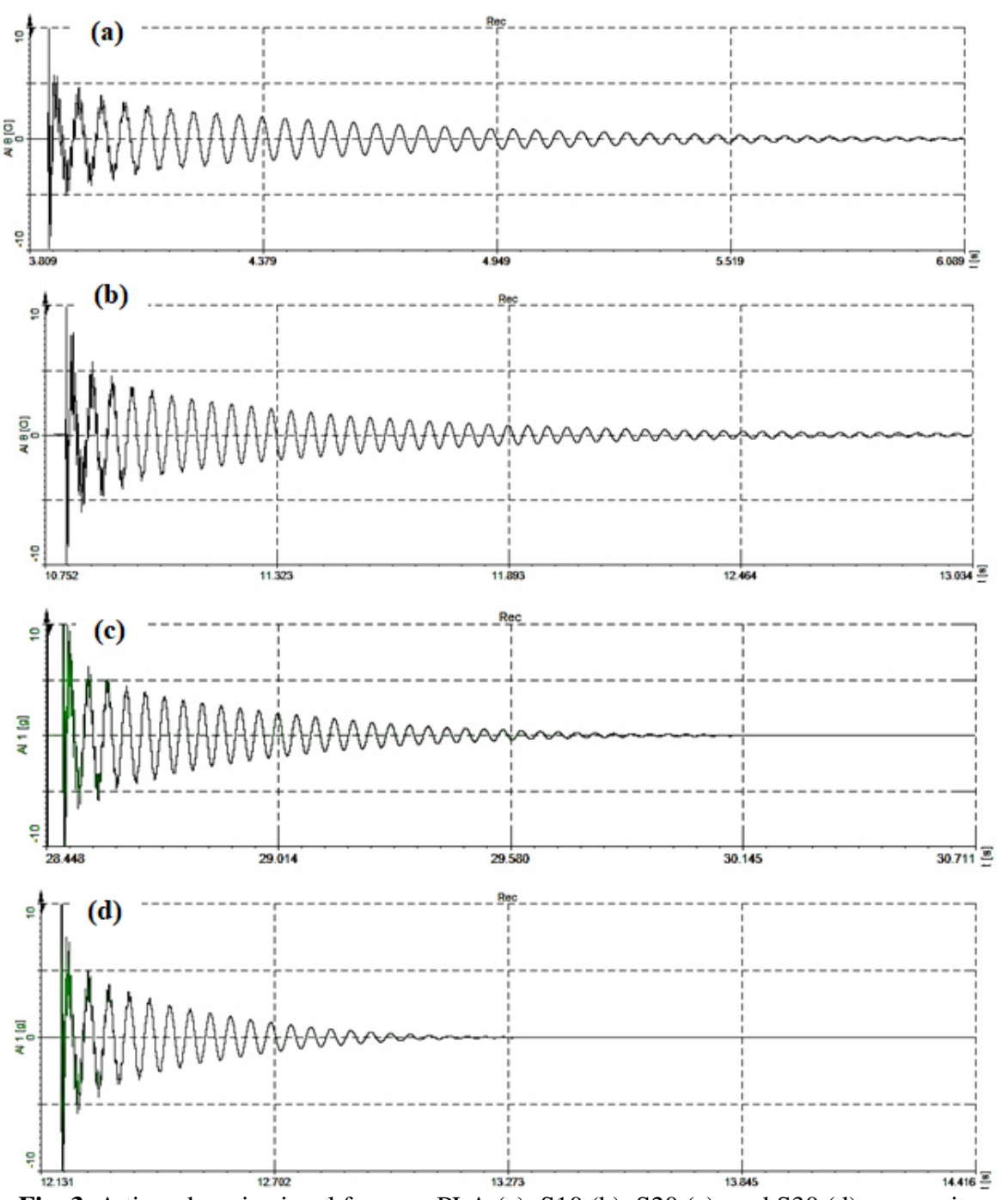


Fig. 3. A time domain signal for pure PLA (a), S10 (b), S20 (c), and S30 (d) composites

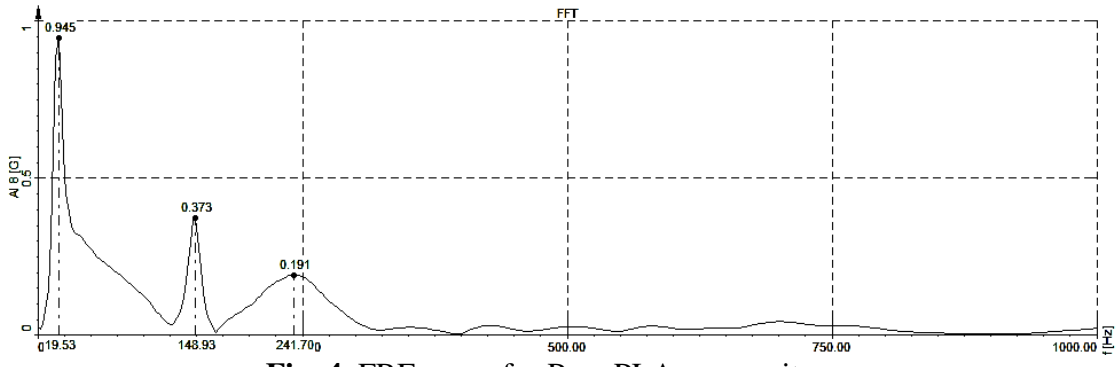


Fig. 4. FRF curve for Pure PLA composites

Figure 5 shows the influence of sisal fiber wt. % on mode one natural frequency of sisal/PLA composites. The mode 1 natural frequency of pure PLA, S10, S20, and S30 are 18.91, 20.75, 23.80, and 24.41 Hz, respectively. The mode 1 natural frequency raised by 9.7, 14.7, and 2.6 % for the subsequent addition of 10 wt. % of sisal over pure PLA.

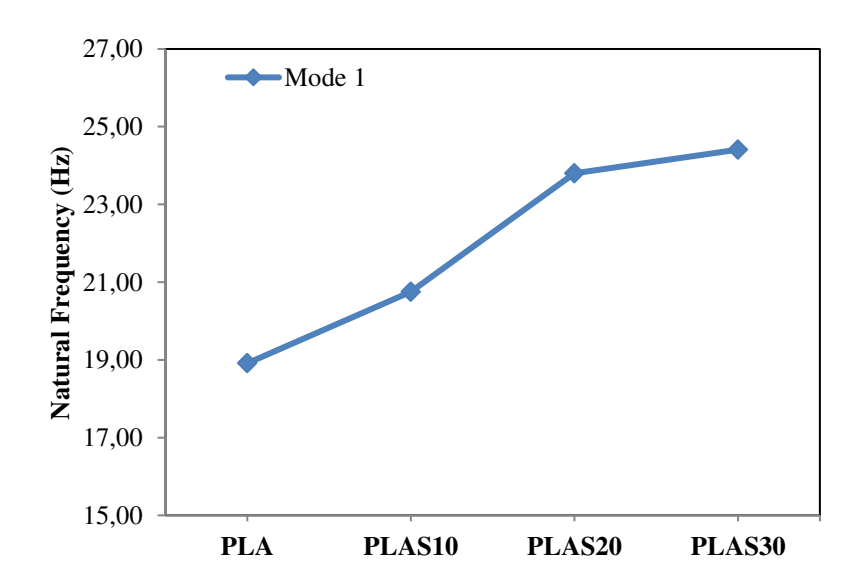


Fig. 5 Influence of fiber wt. % on the natural frequency of composites (Model)

Table 6. Influence of wt. % on natural frequency of composites

	<u> </u>							
G		Natural frequency, Hz						
Composition	Mode 1	Mode 2	Mode 3					
PLA	18.91	148.32	234.38					
S10	20.75	168.46	288.70					
S20	23.80	180.05	280.15					
S30	24.41	172.12	253.90					

Table 6 shows that natural frequencies for mode 2 and mode 3 increase with the increase in weight fraction up to 20 wt. % and then slightly decreases but is always higher than the pure PLA composites. This is because of the improved bending stiffness of Sisal/PLA with an increase in fiber content over pure PLA. Also, fiber reinforcement with an increase in fiber loading and the surface-to-surface contact area along the fiber/matrix interface that improves-surface contact area along the fiber/matrix interface improves stiffness. The decrease in natural frequency of S30 compared to S20 indicated the lowering of stiffness at high fiber content because of the

agglomeration and weakfiber—matrix interface. Similar results for nano clay-filled glass vinyl ester composites were observed by Chandradass et al. (28).

The natural frequency of S10 composites for mode 1, mode 2, and mode 3 is 20.75, 168.46, and 288.70 Hz, respectively. It indicated that the composites exhibited higher natural frequencies when it has higher modes of vibration. A similar trend was observed for pure PLA, S20, and S30 composites.

Damping ratio of sisal/PLA composites. Figure 6 shows the influence of wt. % of fiber on mode 1 damping of PLA composites. The increase in wt. % from 0 to 30 % increases the damping ratio. As fiber content increases, the composite behavior shifts from viscoelastic to elastic and causes a reduction in the damping ratio, but the improvement was observed here. The marginal improvement in damping ratio was observed for S10 and S20 over pure PLA because of higher stiffness. The maximum damping ratio of 0.1450 is obtained at S20, indicating low stiffness, and weakens fibre-matrix interface, making itlose maximum energy. Also, at higher fiber content, there is an increase in the friction at the fibre-matrix interface and interlock of fiber resulting in an increase in damping.

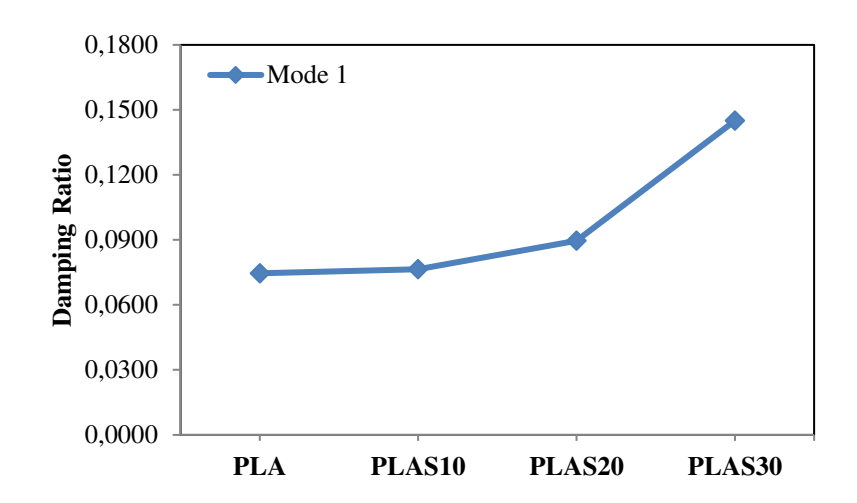


Fig. 6. Influence of wt. % on damping ratio of composites (Mode 1)

Table 7 shows the mode 2 and mode 3 damping ratio of Sisal/PLA composites. It can be seen that a trend of damping for mode 2 and mode 3 is similar to that of mode 1. For pure PLA composites, the damping ratio declined at higher modes of vibration. It is consistent with increased natural frequency at higher mode reducing the damping ratio. A similar trend was observed for S10, S20, and S30 sisal/PLA composites. A similar observation was reported for Banana polyester and sisal polyester composites (29), A Etaati et al. for hemp polypropylene composites (30).

Ta	ble '	7. Inf	luence	of w	t. %	on o	damping rat	io of	compos	ites	Mode	1, 2	. 3)

Composition	Damping ratio					
Composition	Mode 1	Mode 2	Mode 3			
PLA	0.0746	0.0094	0.0060			
S10	0.0764	0.0094	0.0055			
S20	0.0896	0.0118	0.0076			
S30	0.1450	0.0205	0.0140			

Conclusions

In the present research work, Sisal/PLA composite specimens were successfully fabricated by twin screw extrusion and injection molding methods at a different fibre weight fraction. The influence of the weight fraction of sisal fiber in PLA composites on physical and vibration-damping properties was examined. The density and Shore D hardness of PLA composites rise on fiber reinforcement, but at the same time, water absorption also rises to 4.5 % for a 30 % weight fraction of fiber. Fundamental natural frequencies and damping ratio of PLA composites were improved on fiber incorporation. The S30 composition showed the highest natural frequency and damping ratio of 24.41 Hz and 0.1450, respectively. These developed biodegradable composites help lower the cost of purePLA-based composites. The Sisal/PLA composites could be a better alternative for packaging and allied industrial applications.

References

- 1. Chaitanya S, Singh I. Processing of PLA/sisal fiber biocomposites using direct- and extrusion-injection molding. *Mater. Manuf. Process.* 2017;32(5): 468–474.
- 2. Bajracharya RM, Bajwa DS, Bajwa SG. Mechanical properties of polylactic acid composites reinforced with cotton gin waste and flax fibers. *Procedia Eng.* 2017;200: 370–376.
- 3. Rajesh G, Ratna Prasad AV, Gupta A. Mechanical and degradation properties of successive alkali treated completely biodegradable sisal fiber reinforced poly lactic acid composites. *J. Reinf. Plast. Compos.* 2015;34(12): 951–961.
- 4. Rao KMM, Rao KM, Prasad AVR. Fabrication and testing of natural fibre composites: Vakka, sisal, bamboo and banana. *Mater. Des.* 2010;31(1): 508–513.
- 5. Rajesh G, Ratna Prasad AV. Tensile Properties of Successive Alkali Treated Short Jute Fiber Reinforced PLA Composites. *Procedia Mater. Science*. 2014;5: 2188–2196.
- 6. Goriparthi BK, Suman KNS, Mohan Rao N. Effect of fiber surface treatments on mechanical and abrasive wear performance of polylactide/jute composites. *Compos Part A Appl Sci Manuf*. 2012;43(10): 1800–1808.
- 7. Hu RH, Ma ZG, Zheng S, Li YN, Yang GH, Kim HK, et al. A fabrication process of high volume fraction of jute fiber/polylactide composites for truck liner. *Int. J. Precis Eng, Manuf.* 2012;13(7):1243–1246.
- 8. Zafar MT, Maiti SN, Ghosh AK. Effect of surface treatment of jute fibers on the interfacial adhesion in poly(lactic acid)/jute fiber biocomposites. *Fibers Polym.* 2016;17(2): 266–274.
- 9. Shih YF, Huang CC. Polylactic acid (PLA)/banana fiber (BF) biodegradable green composites. *J. Polym. Res.* 2011;18(6): 2335–2340.
- 10. Hadi A, Radzi M, Akmal N, Saleh M. EP19 Banana Fiber Reinforced Polymer Composites. In: *Empower Sci Technol. Innov. Towar a Better Tomorrow.* 2011. p.192–198.
- 11. Asaithambi B, Ganesan G, Ananda Kumar S. Bio-composites: Development and mechanical characterization of banana/sisal fibre reinforced poly lactic acid (PLA) hybrid composites. *Fibers Polym.* 2014;15(4): 847–854.
- 12. Ranjan R, Bajpai PK, Tyagi RK, Tyagi RK. Mechanical Characterization of Banana/Sisal Fibre Reinforced PLA Hybrid Composites for Structural Application. *Eng. Int.* 2013;1(1): 39.
- 13. Asaithambi B, Ganesan GS, Ananda Kumar S. Banana/sisal fibers reinforced poly(lactic acid) hybrid biocomposites; influence of chemical modification of BSF towards thermal properties. *Polym. Compos.* 2017;38(6): 1053–1062.
- 14. Du Y, Wu T, Yan N, Kortschot MT, Farnood R. Fabrication and characterization of fully biodegradable natural fiber-reinforced poly(lactic acid) composites. *Compos. Part B Eng.* 2014;56: 717–723.
- 15. Kaewpirom S, Worrarat C. Preparation and properties of pineapple leaf fiber reinforced poly(lactic acid) green composites. *Fibers Polym.* 2014;15(7): 1469–1477.
- 16. Chen X, Zhang N, Gu S, Li J, Ren J. Preparation and properties of ramie fabric-reinforced

thermoset poly lactic acid composites. J. Reinf. Plast. Compos. 2014;33(10): 953–963.

- 17. Choi HY, Lee JS. Effects of surface treatment of ramie fibers in a ramie/poly(lactic acid) composite. *Fibers Polym.* 2012;13(2): 217–223.
- 18. Alam AKMM, Mina MF, Beg MDH, Mamun AA, Bledzki AK, Shubhra QTH. Thermomechanical and morphological properties of short natural fiber reinforced poly (lactic acid) biocomposite: Effect of fiber treatment. *Fibers Polym.* 2014;15(6): 1303–1309.
- 19. Luo H, Xiong G, Ma C, Chang P, Yao F, Zhu Y, Zhang C, Wan Y. Mechanical and thermomechanical behaviors of sizing-treated corn fiber/polylactide composites. *Polym. Test.* 2014;39: 45–52.
- 20. Wang L, Tong Z, Ingram LO, Cheng Q, Matthews S. Green Composites of Poly (Lactic Acid) and Sugarcane Bagasse Residues from Bio-refinery Processes. *J. Polym. Environ*. 2013;21(3): 780–788.
- 21. Bajpai PK, Singh I, Madaan J. Comparative studies of mechanical and morphological properties of polylactic acid and polypropylene based natural fiber composites. *J. Reinf. Plast. Compos.* 2012;31(24): 1712–1724.
- 22. Yuan Y, Guo M, Wang Y. Flax Fibers as Reinforcement in Poly (Lactic Acid) Biodegradable Composites. *Commun. Comput. Inf. Sci.* 2011;134(PART 1): 547–553.
- 23. Bax B, Müssig J. Impact and tensile properties of PLA/Cordenka and PLA/flax composites. *Compos. Sci. Technol.* 2008;68(7–8): 1601–1607.
- 24. Huda MS, Drzal LT, Mohanty AK, Misra M. Effect of fiber surface-treatments on the properties of laminated biocomposites from poly(lactic acid) (PLA) and kenaf fibers. *Compos Sci Technol.* 2008;68(2): 424–432.
- 25. Lee SH, Wang S. Biodegradable polymers/bamboo fiber biocomposite with bio-based coupling agent. *Compos Part A Appl Sci Manuf.* 2006;37(1): 80–91.
- 26. Ambone T, Joseph S, Deenadayalan E, Mishra S, Jaisankar S, Saravanan P. Polylactic Acid (PLA) Biocomposites Filled with Waste Leather Buff (WLB). *J. Polym. Environ.* 2017;25(4): 1099–1109.
- 27. Koutsomitopoulou AF, Bénézet JC, Bergeret A, Papanicolaou GC. Preparation and characterization of olive pit powder as a filler to PLA-matrix bio-composites. *Powder Technol*. 2014;255: 10–16.
- 28. Chandradass J, Ramesh Kumar M, Velmurugan R. Effect of clay dispersion on mechanical, thermal and vibration properties of glass fiber-reinforced vinyl ester composites. *J. Reinf. Plast. Compos.* 2008;27(15): 1585–1601.
- 29. Senthil Kumar K, Siva I, Jeyaraj P, Winowlin Jappes JT, Amico SC, Rajini N. Synergy of fiber length and content on free vibration and damping behavior of natural fiber reinforced polyester composite beams. *Mater Des.* 2014;56: 379–386.
- 30. Etaati A, Pather S, Fang Z, Wang H. The study of fibre/matrix bond strength in short hemp polypropylene composites from dynamic mechanical analysis. *Compos. Part B Eng.* 2014;62: 19–28.

THE AUTHORS

Munde Yashwant

ant 🐸

e-mail: yashwant.munde@gmail.com

A.S. Shinde 🗓

e-mail: avinash.shinde@cumminscollege.in

I. Siva 🗓

e-mail: isiva@klu.ac.in

Prashant Anerao (10)

e-mail: prashant.anerao@viit.ac.in

Stiffness characteristics of implanted steel plates after exposure to corrosion

Submitted: September 25, 2023

Approved: October 24, 2023

Accepted: December 4, 2023

R.R. Giniyatullin ^{1 ™}, N.M. Yakupov ¹, V.G. Kuznetsov ^{1 ™}

Abstract. Ensuring the safety of structures from corrosion damage is an important task. One of the promising directions for increasing corrosion resistance is modifying the surface layer of a structural element using the ion implantation method. The standard approach of uniaxial tension for assessing the mechanical properties of thin-walled elements with corrosion defects is also ineffective, and the gravimetric method does not take into account changes in the structure of the material and physical and mechanical characteristics caused by loosening the material to a certain depth. In this work, on the basis of the experimental-theoretical method, the integral mechanical characteristics of the samples after exposure to corrosion were determined. The effectiveness of protecting steel samples from corrosion by pre-treatment of the surface layer with ion implantation has been demonstrated. The results of an experimental study of corrosive wear of a thin-walled sheet steel plate, on the surface layer of which carbon ions were implanted, are presented.

Keywords: ion implantation; surface layer; experimental-theoretical method; corrosion wear; reduced modulus of elasticity; tensile rigidity

Citation: Giniyatullin RR, Yakupov NM, Kuznetsov VG. Stiffness characteristics of implanted steel plates after exposure to corrosion. *Materials Physics and Mechanics*. 2023;51(7): 117-123. DOI: 10.18149/MPM.5172023_10.

Introduction

The structure of the material of structural elements largely determines their properties. In this case, the structure and properties of the surface layer are of particular importance. In metal elements, the morphology, phase composition and dislocation structure of the surface layers determine wear resistance, endurance limit, heat resistance and other characteristics. Of great interest is the method of ion implantation, which makes it possible to introduce a dosed amount of ions of almost any element into a metal without changing the boundaries of its grains.

In the 70s - 80s of the twentieth century, along with traditional methods of volumetric impact on metal materials, such as thermomechanical processing, hardening, shock wave loading and other methods, it became possible to carry out surface treatment with concentrated energy flows (from 10 3 to 10 8 W/cm²) [1–4], using electron and ion beams, laser radiation and plasma flows.

When processing with concentrated energy flows, radiation, thermal and shock-mechanical effects are simultaneously carried out. The processes of structural restructuring that develop during this process make it possible to obtain surface layers with a unique set of physical and mechanical properties.

The use of laser radiation to improve the performance properties of materials is well reflected in monographs and reference books, in particular in works [1,5]. The work [6] presents the structures of various types of steel subjected to laser heating.

Compared with laser radiation, processing with electron and ion beams has a number of advantages: higher efficiency, lower cost per unit of energy, the ability to process large areas, as well as a high degree of absorption of the supplied energy by all materials. When processing solids with electron and ion beams for the purpose of their modification, lowenergy, high-energy and powerful ion beams are used.

Speaking about the advantages of the ion implantation method, we can note the possibility of controlling the number of introduced impurity atoms by simple integration of the ion current, the purity of the technology, and others.

Unfortunately, the ion implantation method also has disadvantages - bombardment with heavy particles leads to the formation of defects on the surface, and the method is also relatively expensive.

Intensive research into ion implantation in metals may have begun with the work of Trillat and Heimann [7] and the experiments of Crowder and Ta in [8]. A natural method of increasing the corrosion resistance of a metal surface is the implantation of ions, which, as alloying additives, can prevent or reduce the development of metal corrosion, for example, nickel or chromium ions in steel.

Many works are devoted to the study of changes in the mechanical properties of metal surfaces. An increase in the microhardness of steel was observed after implantation of nitrogen, argon, boron and carbon ions [9]. When implanting nitrogen ions, the microhardness of steel increases according to Vickers from 300 to 400 kg [10].

The effect of the introduction of titanium-nickel and chromium-nickel ions into the surface layer of structural steel VSt3sp is shown in [11]. After implantation of chromium-nickel atoms, an increase in the wear resistance of steel up to 2.5 times was observed.

Microhardness and corrosion resistance studies have been conducted on the effect of nitrogen ion implantation on 7075 aluminum alloy [12]. Potentiodynamic corrosion tests were carried out in NaCl solution. The results showed that the microhardness increased by 90.81% after implantation. Corrosion testing showed an improvement in corrosion resistance by reducing the corrosion rate by a factor of 3.

A decrease in the corrosion rate by 1.78 times was recorded with two-stage implantation of oxygen ions, as well as combined aluminum and boron ions [13]. Increased corrosion resistance is confirmed by long-term acid corrosion tests at pH 3.5 and accelerated electrochemical testing using a potentiostat.

To increase the corrosion resistance of ferritic-martensitic steel SIMP, the authors of article [14] studied the effect of implantation of silicon ions and preliminary oxidation of the surface. It was found that increasing the Si content on the surface did not improve the corrosion resistance performance. In contrast, the pre-oxidized sample demonstrated high corrosion resistance due to the presence of a thin oxide layer enriched in Cr.

The effect of implantation of calcium ions on the corrosion resistance of titanium is presented in [15]. The results of electrochemical studies show that calcium-ion implantation increases corrosion resistance, but only under stationary conditions; During anodic polarization, samples implanted with calcium ions undergo corrosion.

The authors of the article [16] achieved suppression of local corrosion by using immersion ion implantation of nitrogen plasma on the surface of austenitic, duplex, martensitic and ferritic stainless steels. Nitrided stainless steel has shown high hardness and high corrosion resistance.

The use of the method of surface treatment with cathode spots of a vacuum-arc discharge led to both an increase in resistance to thermal fatigue and an increase in corrosion resistance [17,18].

The purpose of this work is to evaluate, on the basis of the experimental-theoretical method [19,20], the effectiveness of protecting steel samples from corrosion by pre-treating the surface layer with ion implantation.

Methods

Specimens subject to corrosive wear are thin-walled elements with a complex structure. To study the mechanical characteristics, an experimental-theoretical method was used [19]. The method allows, in contrast to the standard uniaxial test and the indenter method, to more accurately determine the integral mechanical properties of thin-walled elements.

In the experimental-theoretical method, at the first stage, round-shaped samples are cut out from the thin-walled element under study. Then, the samples are fixed along the contour on a special installation and loaded with uniform pressure P. In the process of increasing pressure P, the shape of the dome being formed is monitored. In particular, for the top of the dome, data is taken for the graph pressure P - deflection N. At the theoretical stage, experimental data is processed using relationships obtained from the nonlinear theory of shells. In this case, the reduced (integral) characteristics of the samples are determined, for example, the reduced modulus of elasticity. The method captures the influence of surface defects on the integral properties of samples.

For an elastic membrane in the case of average bending, the elastic modulus E and the tensile-compression stiffness *B* are calculated using the formulas:

$$E = \frac{NPa(1-v^2)}{h} \left(\frac{a}{H}\right)^3,$$

$$B = NPa\left(\frac{a}{H}\right)^3, D = B\frac{h^2}{12},$$
(1)

$$B = NPa\left(\frac{a}{H}\right)^3, D = B\frac{h^2}{12},\tag{2}$$

where the values of the coefficients N are shown in Table 1; P is the uniformly distributed pressure; ν is the Poisson's ratio of the material; h is the current membrane thickness; a is the radius of the membrane; H is the current dome lift height (maximum deflection).

Table 1. Values of coefficients *N*

ν	0.25	0.3	0.4	0.5	
N	0.311481993	0.303670085	0.290157232	0.279052533	

Results and Discussion

Corrosive wear tests were carried out on three pairs of metal samples made of sheet steel grade Steel 3 with a thickness of t = 0.5 mm. The surfaces of the samples were subjected to pulsed ion implantation with carbon C atoms. For implantation, a TEMP pulsed ion accelerator was used, with an atomic voltage of 280 keV (the number of pulses was 8). The samples were kept in an aggressive environment (10% hydrochloric acid - HCl): group No. 1 - two days, group No. 2 - three days, group No. 3 - four days. In each group of samples, a control "clean" sample that was not subjected to ion treatment was located next to its pair.

Figures 1-3 show images of the surfaces of samples of groups No. 1-3 after keeping them in an aggressive environment. The images are enlarged 400x, with samples without implantation on the left and samples with implantation on the right. The results of measuring the thickness of samples after exposure to an aggressive environment are presented in Table 2. From Fig. 1-3 it is clear that the surfaces of non-implanted samples have deeper corrosion cavities with larger dimensions in plan. This is obviously due to the fact that when carbon atoms are implanted into the surface layer of steel, the surface layer becomes compacted, the

bonds of the crystal lattice are strengthened, and its chemical composition also changes. All this helps to increase chemical resistance when exposed to aggressive environments.

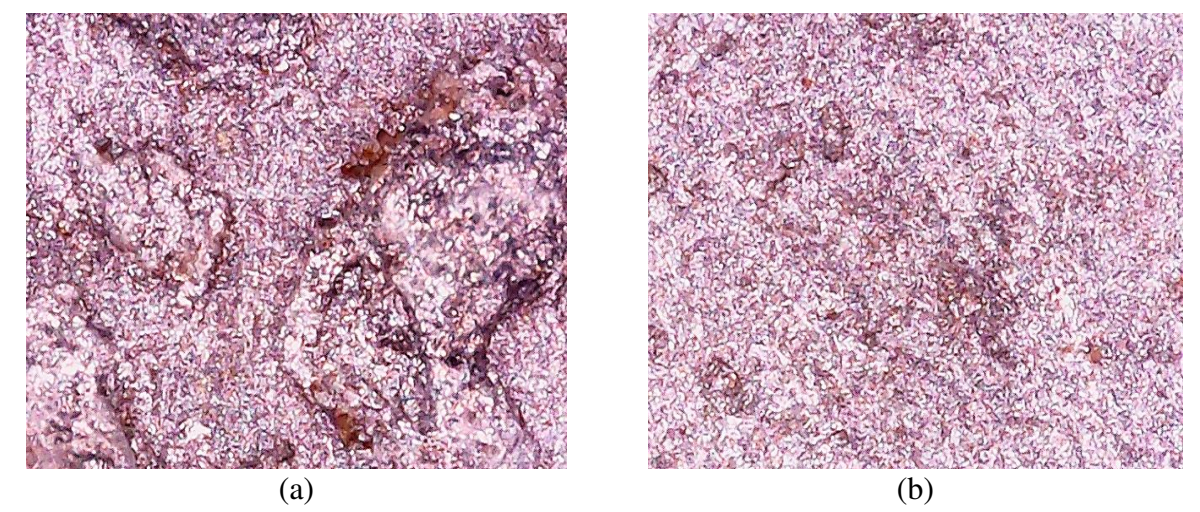


Fig. 1. Samples of the 1st group: (a) not implanted, (b) implanted

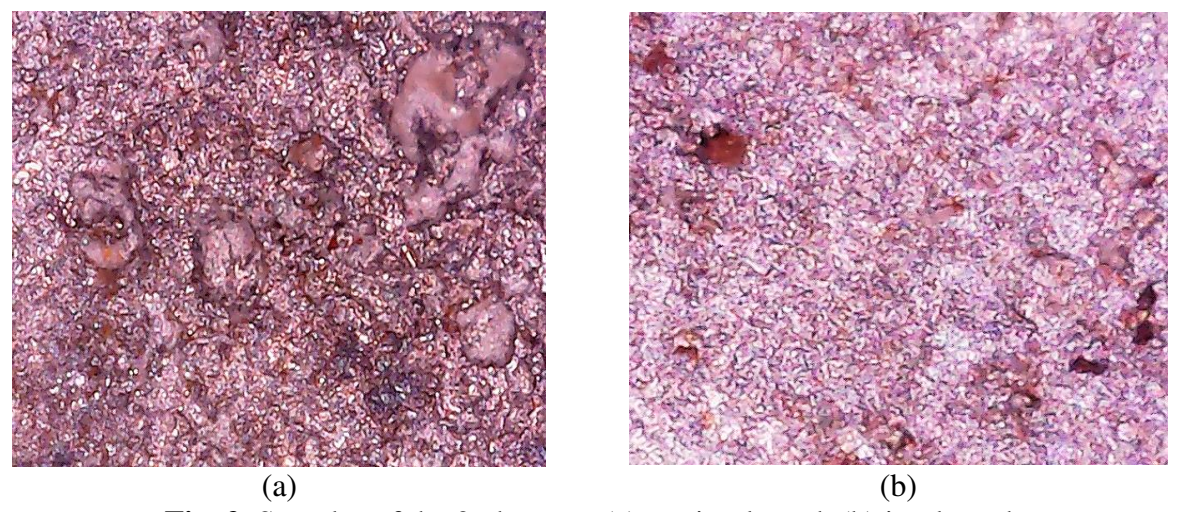


Fig. 2. Samples of the 2nd group: (a) not implanted, (b) implanted

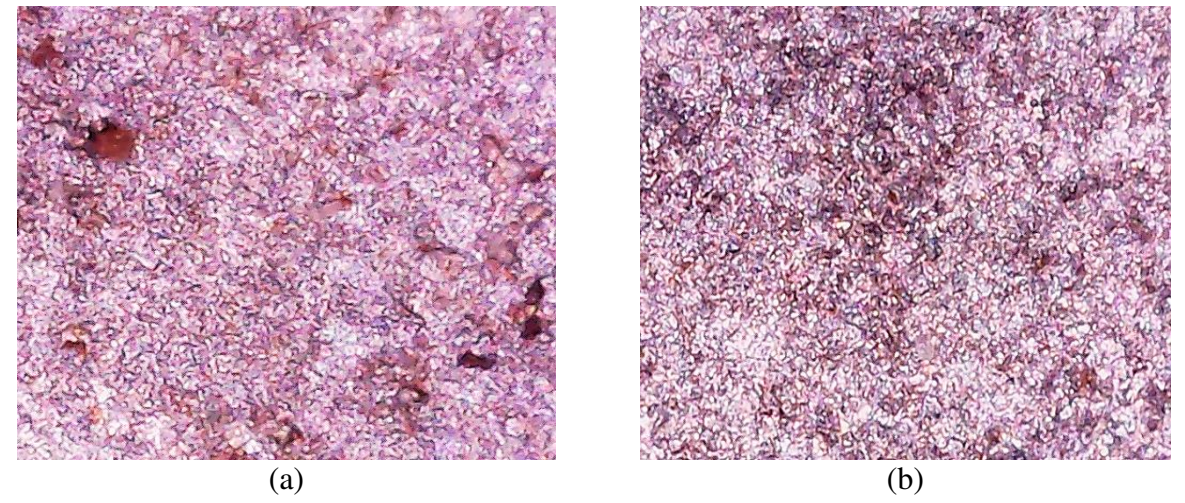


Fig. 3. Samples of the 3rd group: (a) not implanted, (b) implanted

Table 2. Experimental data

Group samples	Group No. 1		Group	No. 2	Group No. 3		
Wear time, days	2		3		4		
Implantation	Yes	No	Yes	No	Yes	No	
Thickness after wear, mm	0.481	0.469	0.478	0.464	0.468	0.452	

Table 2 also shows that the thicknesses of samples subjected to ion implantation for all groups are slightly greater than for non-implanted samples. All this indicates that the implanted samples are more corrosion resistant.

Dependencies pressure P - bending rigidity D for the studied samples are presented in Tables 3 - 5. In the tables, samples previously subjected to ion implantation are designated as D_+ , and those not treated with ion implantation are designated as D -. Stress curves "bending rigidity D - pressure P" are presented in Figs. 4-6. The graphs show two curves: for a sample subject to and not subject to ion implantation. As can be seen from Fig. 4-6, the bending rigidity of the implanted samples are more than those of the samples not subject to ion implantation. This means that the implanted samples are more corrosion-resistant, that is, the effect of implantation is obvious.

Table 3. Dependence "pressure P - bending rigidity D" for sample of group No. 1

P, MPa	0.06	0.08	0.10	0.12	0.16	0.20
D_+ , kg/cm ³	36.15	31.45	29.37	27.02	24.06	21.07
D_{\cdot} , kg/cm ³	18.76	17.57	17.17	17.15	16.34	15.10

Table 4. Dependence "pressure *P* - bending rigidity *D*" for sample group No. 2

R, MPa	0.06	0.08	0.10	0.12	0.16	0.20
D_+ , kg/cm ³	23.0	21.1	19.8	18.7	16.6	14.5
D_{\cdot} , kg/cm ³	17.4	16.7	15.6	14.9	13.8	12.4

Table 5. Dependence "pressure P - bending rigidity D" for sample group No. 3

_	_			_		
P, MPa	0.06	0.08	0.10	0.12	0.16	0.20
D_+ , kg/cm ³	21.3	18.2	15.9	14.7	12.8	11.2
\boldsymbol{D}_{-} , kg/cm ³	13.6	12.5	11.5	10.7	9.4	8.2

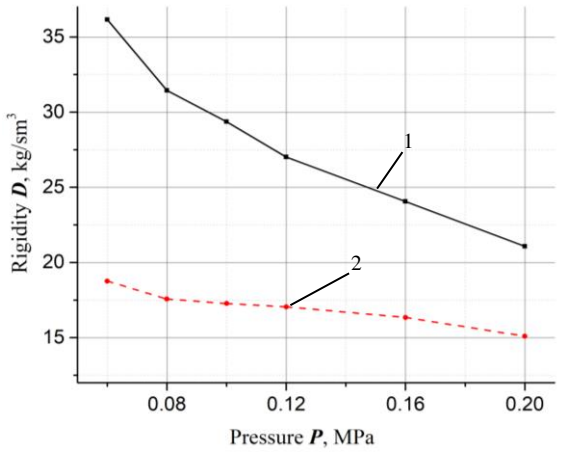


Fig. 4. Dependence "bending rigidity *D* – pressure *P*" for group of samples No. 1: curve 1 – implanted samples; curve 2 – nonimplanted samples

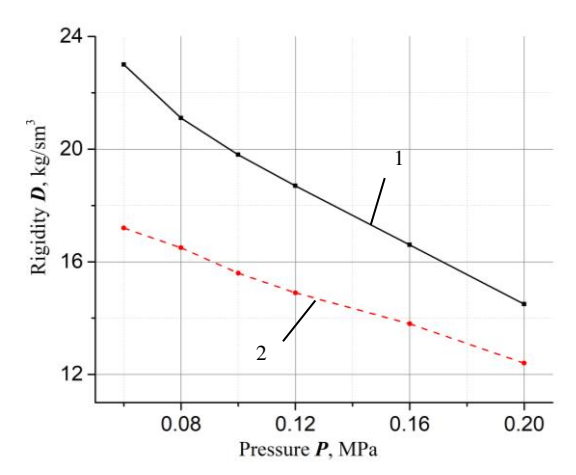
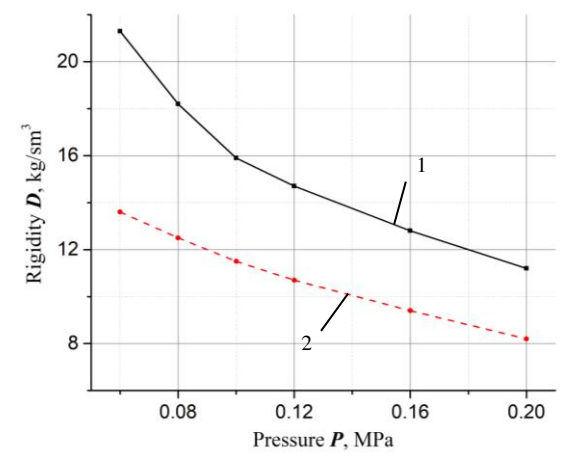


Fig. 5. Dependence "bending rigidity *D* – pressure *P*" for group of samples No. 2: curve 1 – implanted samples; curve 2 – nonimplanted samples



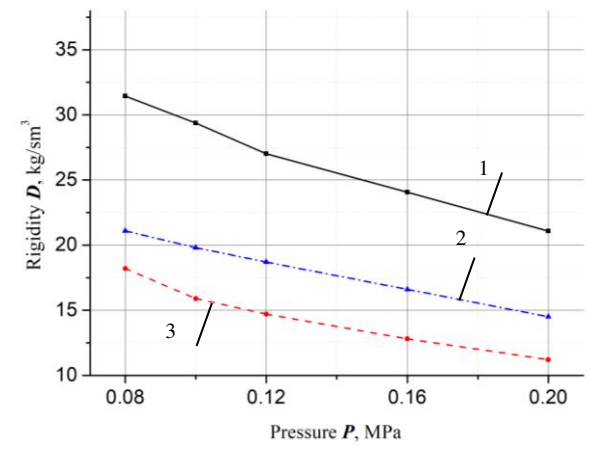


Fig. 6. Dependence "bending rigidity **D** – pressure **P**" for group of samples No. 3: curve 1 – implanted samples; curve 2 – non-implanted samples

Fig. 7. Dependence "bending rigidity *D* – pressure *P*" for implanted samples: curve 1 - 2 days; curve 2 - 3 days; curve 3 - 4 days

Figure 7 shows the "bending rigidity D - pressure P" curves for implanted samples depending on the duration of exposure in an aggressive environment. As can be seen from Fig. 7, with increasing exposure time in an aggressive environment, the degree of corrosive wear increases.

Conclusion

Surface treatment of samples by ion implantation allows maintaining a passivating protective layer and, thereby, helps reduce corrosive wear. Despite the effectiveness of ion implantation treatment, with increasing exposure time in an aggressive environment, the effect of surface protection by ion implantation decreases. This in turn leads to corrosive wear and deterioration of mechanical characteristics. This was investigated using the experimental-theoretical method. Ion implantation is one of the effective ways to protect against corrosive wear.

References

- 1. Misaelides P. *Application of particle and laser beams in materials technology*. Dordrecht: Kluwer Academic Publishes; 1994.
- 2. Uglov AA, Selishchev SV. Boundary large-scale structures under the effect of concentrated energy-flow on metals. *Zhurnal Tekhnicheskoi Fiziki*. 1985;55(4): 649–654. (In-Russian)
- 3. Takagi T, Yamada I, Kimura H. Ion Implantation in Semiconductors. New York; 1970.
- 4. Hartley NE. Application of Ion Beams to Materials. Institute of Physics; 1975.
- 5. Rykalin NN, Uglov AA, Kokora AN. *Laser processing of materials*. Moscow: Mechanical Engineering; 1975. (In-Russian)
- 6. Sadovsky VD, Schastlivtsev VM, Tabatchikova TI, Yakovleva IL. *Laser heating and steel structure: Atlas of microstructures*. Sverdlovsk: Ural Branch of the Academy of Sciences of the USSR; 1989. (In-Russian)
- 7. Trillat JJ, Haymann IN. Le bombardement ionique. Theories et applications. Paris; 1961.
- 8. Crowder BL, Tan SI. IBM Technical Disclosure Bulletin 14. 1971.
- 9. Pavlov AV, Pavlov PV, Zorin EI, Tetel'baum DI. All Soviet Meeting on Ion Beam Physics. Kiev; 1974.
- 10. Gabovich MD, Budernaya LD, Poritskii VY, Protsenko IM. *All Soviet Meeting on Ion Beam Physics*. Kiev; 1974.

- 11. Vasetskaya. Ion implantation as a way to improve the operating durability of fine-size steel tool. *Eastern-European journal of enterprise Technologies*. 2013;6(5): 7–11.
- 12. Hapsari S, Sujitno T, Ahmadi H, Suprapto, Rizky AA. Analysis of nitrogen ion implantation on the corrosion resistance and mechanical properties of aluminum alloy 7075. *J. Phys.: Conf. Ser.* 2020;1436: 012075.
- 13. Dorofeeva TI, Fedorischeva MV, Gubaidulina TA, Sergeev OV, Sungatulin AR, Sergeev VP. Investigation of Corrosion Properties and Composition of the Surface Formed on AISI 321 Stainless Steel by Ion Implantation. *Metals*. 2023;13(8): 1468.
- 14. Xu N, Wang Zh, Shen T, Li B, Li G, Li T, Wei W. The effects of Si-ion implantation and preoxidation on the corrosion behavior of a new steel SIMP in 550°C lead-bismuth eutectic. To be published in *Materials and Corrosion*. [Preprint] 2023. Available from: doi.org/10.1002/maco.202313865
- 15. Krupa D, Baszkiewicz J, Kozubowski JA, Barcz A, Sobczak JW, Bilińiski A, Lewandowska-Szumieł MD, Rajchel B. Effect of calcium-ion implantation on the corrosion resistance and biocompatibility of titanium. *Biomaterials*. 2001;22(15): 2139–2151.
- 16. Luiz LA, Emanuely BC, Kurelo S, Biscaia de Souza G, de Andrade J, Bruno Marino ClEl. Effect of nitrogen plasma immersion ion implantation on the corrosion protection mechanisms of different stainless steels. *Materials Today*. 2021;28: 102655.
- 17. Kuznetsov VG. Vacuum-arc hardening of metals surface. *Journal of Physics: Conference Series*. 2019;1396; 012027.
- 18. Kuznetsov VG. Analysis of stresses and deformations in a hollow cylinder under the influence of internal pressure and of field of temperatures. *Journal of Advanced Research in Technical Science*. 2020;22: 16–21. (In-Russian)
- 19. Yakupov NM, Nurgaliev AR, Giniyatullin RR, Yakupov SN. Operation of Structures with Corrosive Wear. *Russian Engineering Research*. 2013;33(2): 69–73.
- 20. Yakupov NM, Yakupov SN. Diagnostics of thin-walled structures of complex geometry and structure. *Structural Mechanics of Engineering Constructions and Buildings*. 2021;17(6): 576–587.

THE AUTHORS

Giniyatullin R.R.

Yakupov N.M. e-mail: yzsrr@mail.ru

e-mail: true_way@mail.ru

Kuznetsov V.G.

e-mail: kvgipme@gmail.com

Physical and mechanical properties of modified chrome coatings

Submitted: August 7, 2023

Accepted: October 27, 2023

Approved: September 20, 2023

S. Vodopyanova , G. Mingazova, R. Fomina, R. Sayfullin

Kazan National Research Technological University, Kazan, Russia

⊠ vod-sveta@yandex.ru

Abstract. When solving the problems of improving the metal-surface treatment and giving special and anticorrosive properties to such surfaces, electrochemical composite coatings (ECCs) are essential. It is the dispersed phase that, being included in the metal matrix, gives the composite coatings a complex of new properties. This paper discusses how the aluminum/chromium oxide nanoparticles and high-dispersity graphite affect the physical and mechanical properties of coatings with a chrome matrix, i.e., corrosion resistance in 5 % NaCl, hardness, and wear resistance. Using the X-ray diffraction analysis, we have assessed how the particles under study affect the distribution of chromium over the surface of a steel sample. This paper also presents the microhardness test results for the heat treatment modes (temperature and time) of modified chrome coatings.

Keywords: electrochemical composite coatings; chrome matrix; the aluminum/chromium oxide nanoparticles; high-dispersion carbon; corrosion resistance; hardness; wear resistance; heat treatment

Citation: Vodopyanova S, Mingazova G, Fomina R, Sayfullin R. Physical and mechanical properties of modified chrome coatings. *Materials Physics and Mechanics*. 2023;51(7): 124-136. DOI: 10.18149/MPM.5172023_11.

Introduction

Currently, developing electrochemical composite coatings (ECCs) is an up-to-date sector of functional metal plating. Composite coatings are created where it is planned to obtain new properties, improve solidity or corrosion resistant characteristics, and enhance heat/scale resistance [1].

The principle of obtaining ECCs is based on the co-deposition of disperse particles (DPs) of various dispersion grades/nature and metals from the suspension electrolytes. Using various DPs in forming ECCs can help obtain modified strengthening coatings that encompass the properties, such as high corrosion resistance, corrosion protection in atmospheric conditions and in the environments affected by high temperatures and aggressive gases, and high wear resistance in abrasive conditions and in friction units [2].

Currently, some dozens of metals are used for ECCs [3–12]. Review article [13] organizes data on the metal-matrix-based composite coatings obtained over the years 2000-2019, depending on the metal nature and dispersion phase. Analysis of publications included in the VINITI Database RAS showed that producing composite plating coatings is one of the priority areas in the modern plating industry.

Among metal matrices used to obtain ECCs, we should distinguish the chrome one that has some valuable properties:

- 1. Chromium does not oxidize and does not change its color at temperature of up to 500 °C.
- 2. Chromium is resistant against most gases, acids, and alkalis.
- 3. High hardness of metallic chromium puts it on a par with corundum.

- 4. Chromium is of bluish-white color, similar to that of silver or platinum, which allows using it for decorative purposes.
- 5. In contrast to nickel, silver, or other metals, chromium is completely unaffected by the atmosphere and maintains its beautiful appearance.
- 6. Possibility to apply thick coatings firmly adhered to the base.

Of all electrodeposited metals, chromium has the least affinity for second-phase substances. Only in certain conditions, it is possible to obtain Cr-ECCs containing up to 2 % (mass) of dispersion phase [14].

This difficulty is associated with a low current efficiency of chromium (as little as 16-20 %), a significant hydrogen release, and formation of a cathode film preceding the metal release. This applies primarily to coatings obtained from suspension electrolytes containing electrically neutral particles that are highly resistant to electrolyte (Al₂O₃, TiO₂, ZrO₂). There have been a possibility of forming Cr-ECCs with some types of electroconductive particles, as well as the fact that the unsteady electrolysis factors can affect their formation. We also show the beneficial effects provided by organic compounds upon the co-deposition of DPs with chromium.

In [15], two dispersed phases were studied: A non-conductive one, BN (in the wurtzite modification) and an electrically conductive one, WC. We have assessed the physical and mechanical properties of the ECCs obtained, including the particles of wurtzite-BN, and noticed a considerable enhancement in both microhardness (increase of up to 38 %) and wear resistance (3-time decrease in wear-caused weight loss). It is found that the physical and mechanical properties of precipitations modified with WC particles, as well as their quality, are significantly inferior to chrome obtained from a standard chrome-plating electrolyte.

Ultrafine (nanometer-sized) particles are recognized as highly promising DP substances for creating efficient and functional ECCs, which allow improving the quality of the ECC performance characteristics and developing new-purpose materials, even with a lower DP content in the coating and the use of their low concentration in suspension electrolytes [16]. Widely using nano-sized particles is associated with the emergence of new substances, such as graphene, carbon nanotubes, nanodiamonds, silicon carbide, aluminum/silicon oxides, etc.

Authors of articles [17] and [18] have studied the properties of composite chromegraphite coatings, i.e., chrome-containing multiwall carbon nanotubes (MWCNTs) obtained using particles of different dispersion. Graphite grades GC-3 (particles sized $40 \pm 2 \mu m$) and C1 (particles sized $\sim 4 \mu m$) and multiwalled carbon nanotubes were used as the dispersed phase. It is found that adding graphite of various grades to the chrome-plating solution leads to a slight decrease in roughness; that the graphite concentration in chrome-plating solution, while obtaining composite coatings, chrome-graphite does not practically affect the microhardness of the coatings; and that the total wear for the steel-ECC system (Cr–graphite GC-3) changes slightly, a decrease being observed in the graphite concentrations in the solution from 5 to 20 g/l. For the steel-ECC system (Cr-graphite C1), the total wear does not change. However, in both cases, there is a decrease in wear at lapping-in.

DPs affect changes in the parameters of chrome coatings micro- and substructures and, therefore, changes in the physical and mechanical properties of coatings [19].

This study is aimed at investigating of how aluminum/chromium oxide nanoparticles and high-dispersity black carbon affect the Cr-ECC properties.

Materials and Methods

To apply Cr-ECC, a standard chrome-plating electrolyte was used, composed as follows, in g/dm³: CrO 3-250 (2.5 M), H_2SO_4 2.5 (0.025 M). Coatings were applied to steel samples sized 2 × 3 cm. We used the following as the second-phase particles:

1. Al₂O₃ nanopowder: TU 1791-002-36280340-2005: $S_{sp} = 21 \text{ m}^2/\text{g}$; the average particle size is 30 nm;

- 2. Cr_2O_3 nanopowder is a solid green refractory powder with the content of the main substance is 98.4 %, $S_{sp} = 27.4 \text{ m}^2/\text{g}$, $d_{avg} = 42.7 \text{ nm}$;
- 3. high-dispersion graphite, $C_{\text{total}} = 99.9 \%$, $S_{\text{sp}} = 110 \text{ m}^2/\text{g}$, and $\rho = 3.51 \text{ g/cm}^3$.

Electrolysis mode: $t = 50 \pm 5$ and 60 ± 5 °C; cathodic current density = 30 A/dm², and electrolysis time = 1 h. Lead plates were used as anodes, and electrolysis was performed with constant stirring with a magnetic stirrer.

Current efficiency (CE) of metal was computed by Faraday law. Coating thicknesses were found using the gravimetric method in accordance with the Russian standard GOST 9.302-88. Chemical composition of layers in the Fe-Cr system and the coating thicknesses were found using an X-ray fluorescence (XRF) analyzer (X-STRATA 980). Microhardness of coatings was found using the PMT-3M microhardness meter in accordance with GOST 9.450-76. Surface morphology was investigated using microscope ALTAMI MET-15. Structures of control coatings were studied using electronic microscope REM-100U with the energy-dispersive analyzer EDAR.

Corrosion resistance was measured using potentiostat IRC-Pro. We pre-varnished the samples, leaving a 5×5 mm square in the center. After the varnish dries, we degreased, dried, and tested the samples. Then we dipped each sample in a 5% NaCl solution and turned on the machine.

In practice, rate indicators are conventionally used to assess corrosion resistance: corrosion rate $C(g/m^2 \cdot h)$, which characterizes the rate of loss of metal mass during testing and the corrosion penetration rate P(mm/year). For electrochemical corrosion, the current corrosion index (C_i) can be used.

Experiment and Discussion

Coatings modified with Al₂O₃ nanoparticles. Coatings were obtained with a dispersed phase of Al₂O₃ at different temperatures and concentrations. Increasing the electrolysis temperature contributes to increasing the current efficiency of chromium (passivation of anodes decreases), to increasing the electrical conductivity, to decreasing the amounts of chromium-hydrogen penetrating in the electrolytic deposits, and to forming large-crystalline precipitates. The outcomes are presented in Table 1 below.

Table 1. Properties of chrome coatings depending on the concentration of Al₂O₃ nanoparticles in electrolyte and on the temperature

Electrolysis temperature, °C	50			60		
Concentration of particles in electrolyte, g/l	0	5	10	0	10	
Coating thickness, µm	16	18	19.5	16.5	22	
Deposition rate, μm/s	0.23	0.3	0.33	0.28	0.37	
Current efficiency (CE) of metal, %	12	13.6	15	16.4	18	

Introducing the Al_2O_3 nanoparticles into the electrolyte leads to forming more smoothed deposits with a greater thickness. In presence of nanoparticles, deposition rate and coating thickness increase. The greatest thickness and current efficiency of metal are observed in coatings obtained from the deposition electrolyte at the Al_2O_3 concentration of 10 g/l and at a temperature of 60 °C.

Table 2. Corrosion currents of the coatings $(Ki \cdot 10^4, A/m^2)$

A1 O concentration in alastralate of	Temperato	are, °C
Al ₂ O ₃ concentration in electrolyte, g/l	50	60
0	7.9	7.9
5	11.06	12.68
10	_	13.83

(1)

We assessed the corrosion behavior of modified coatings by corroding current. Table 2 shows the results of identifying these indicators.

Corrosion penetration was computed by the following formula: $P = 8.76 \cdot Ki \cdot g$,

where g is the metal density, g/cm^3 (chrome density, $g = 7.1 g/cm^3$).

Computation results are shown in Table 3.

Table 3. Corrosion penetration of chrome coatings, obtained from the suspension electrolyte

Concentration of Al ₂ O ₃ particles in electrolyte, g/l	Corrosion penetration, mm/y	Score	Resistance group.
0(50)	0.001	1	Absolutely resistant
0(60)	0.001	1	Absolutely resistant
5(50)	0.0013	1	Absolutely resistant
10(50)	0.002	2	Very resistant
10(60)	0.002	2	Very resistant

Chromium is considered one of the most corrosion-resistant metals and used in protective coatings. The results obtained confirm that the optimal conditions for obtaining corrosion-resistant coatings are the particle concentration of 10 g/l and the temperature of 60 °C. The coatings have a smoothed surface and are of bluish color.

 Al_2O_3 nanoparticles affect the mechanical properties of deposited coatings, resulting from changes in the electrochemical parameters of the electrode process, including the state of the surface films of hydroxide layers, and not as a result of the particles penetrating in the growing chrome layers [20].

The most important characteristic of coatings that protect metal is their continuity. Defective coatings are less corrosion-resistant. Surfaces of the samples obtained were examined microscopically. Surfaces of control samples are uniform, with small cracks. However, the surfaces of the modified coatings have large and long cracks, which affects their corrosion resistance, reducing it. Since corrosion processes start on open surfaces and the metal destruction is accompanied by the appearance of an electric current flowing between the anode and cathode sections of the metal, the Cr-Al₂O₃ structure will contribute to spreading the corrosion into the depth of the coating due to cracks.

As active cathodic inclusions, the Al₂O₃ particles can cause, reducing the corrosion resistance. Particles are involved in various redox processes occurring on the coating surface.

Coatings modified with Cr_2O_3 nanoparticles. The coatings were obtained from an electrolyte with the DPs of Cr_2O_3 at the concentrations ranging from 10 to 50 g/l. Electrolysis temperature 50 °C. During visual inspection, we found that the samples obtained from the electrolyte with the DP concentration of 10 g/l had a silvery luster, and they were light.

Samples obtained from the deposition electrolyte with the particles concentration of 20 g/l have a noticeably smaller shine than that of the samples obtained from the 10 g/l electrolyte. Samples obtained from electrolyte with the concentrations of 30, 40, or 50 g/l do not shine, they are matte. With an increase of the DP concentrations in electrolyte, the color of samples was slightly darker. Figures 1-3 show the structures of modified coatings.

If follows from Fig. 1 that the galvanic chrome structure has large and deep cracks. Surface is uneven, there are dendrites in the form of well-formed globules with a diameter of $30\text{-}50~\mu m$, consisting of needle-like elements. Oxygen content is 4.67~%, and chrome content is 95.36~%.

Figures 2 shows the structure of a modified coating at the Cr_2O_3 concentration of 10 g/l in the deposition electrolyte. Chromium particles are densely packed and faceted, sized 10-20 μ m, microglobules (20-30 μ m) are with small chromium particles (1-2 μ m). Oxygen content is 4 %, and chrome content is 96 %. No cracks, and there are significantly fewer dendrites, as compared

to the control coating. Globule sizes are also smaller than those of the control coating. Metallic chromium is formed at active sites and at a closer distance from each other than in the control sample. It can be assumed that nanoparticles affect the cathode surface state and thus improve the electrode processes, activating more cathode sites at which chromium is reduced.

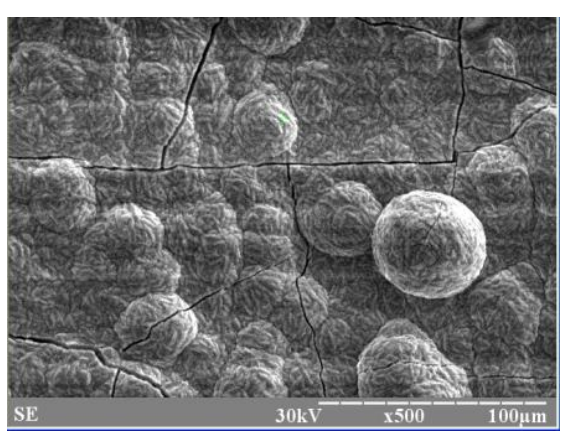


Fig. 1. Structure of control coating

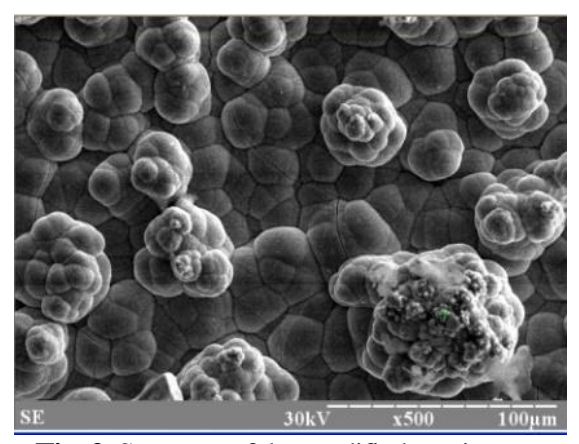


Fig. 2. Structure of the modified coating at a concentration of Cr₂O₃ in the electrolyte of 10 g/l

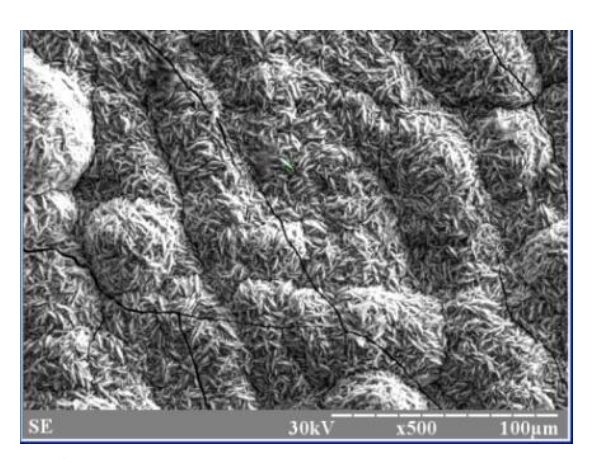


Fig. 3. Structure of the modified coating at a concentration of Cr₂O₃ in the electrolyte of 20 g/l

Figures 3 shows that the structure is represented by chromium microglobules sized $\sim 10~\mu m$. Oxygen content is 5 %, and chrome content is 95 %. Table 4 shows the results of identifying the main indicators of applying the modified coatings.

Table 4. Properties of chrome coatings depending on the concentration of the Cr₂O₃ nanoparticles in electrolyte

Concentration of particles in electrolyte, g/l	0	10	20	30	40	50
Coating thickness, µm	19.6	21.3	22.3	23.0	23.8	24.2
Deposition rate, μm/s	0.33	0.36	0.37	0.38	0.4	0.4
Current efficiency (CE) of metal, %	13.8	15	16.1	18.5	18.8	19.4

Slight increase in the thickness of samples obtained from the pure electrolyte is explained by the treeing taking place at the sample edges during electrolysis. Subsequently, removing them during mechanical treatment affects the weight gains of the coating and, therefore, the thickness computations.

In presence of DPs in electrolyte, treeing is observed to a lesser extent, while the deposition rate and coating thickness increase. At concentrations in the electrolyte of 30, 40, or 50 g/l, no treeing was observed at all.

As can be seen from the table, DPs of Cr_2O_3 provide a good effect on the current efficiency of chrome. CE value increases with the increase in the concentration of particles and reaches its maximum value of 19.4 % in electrolyte with the DP concentration of 50 g/l.

Non-destructive quality control and identifying the elemental composition of the samples were performed using the analyzer X-STRATA 980. To assess the control and composition of modified coatings, we identified the contents of chromium and iron [21].

To assess the uniformity of the chromium distribution over the sample surface, we performed measurements at three different points on the samples (top, middle, and bottom – points 1, 2, and 3, respectively). Our findings are shown in Table 5.

Table 5. Results of finding the percentage of chrome and iron contents, depending on the DPs

concentration in electrolyte

DPs concentration in electrolyte	Points	Chrome content, %	Iron content, %
	1	55.87	21.91
0	2	68.99	8.31
	3	77.52	2.55
	1	86.33	0.38
10	2	88.94	0.43
	3	90.86	0.17
	1	69.3	9.90
20	2	77.55	4.52
	3	83.22	1.96
	1	83.95	1.08
30	2	86.21	0.66
	3	90.16	0.18
	1	72.88	5.55
40	2	83.59	1.72
	3	86.60	0.51
	1	75.12	4.07
50	2	79.45	2.2
	3	80.07	1.77

Based on Table 5, we can conclude that the most "nonuniform" samples were obtained from the control electrolyte. Coatings obtained from the suspension electrolyte are very uniform in terms of chromium content, with a high content and, therefore, high hardness and brittleness of chromium. Table 6 shows the results of identifying the hardness of coatings.

Table 6. Hardness of modified chrome coatings

		0				
DPs concentration in electrolyte	0	10	20	30	40	50
Hardness, GPa	7.75	11.8	11.1	9.2	9.6	9.6

DPs have a positive impact on the hardness of chrome ECCs. The best effect is provided by the DP concentration of 10 g/l: hardness increased to the highest value of 11.8 GPa.

We studied how the thermal treatment of modified chrome coatings affects microhardness.

We annealed the samples obtained from the control electrolyte and from the electrolyte with DPs of Cr₂O₃, 10 mg/l. Annealing was carried out at temperatures of 300, 600, and 900 °C and at the annealing duration of 1 and 2 h. Upon annealing, we identified the values of microhardness. Table 7 shows the results of identifying the hardness of the annealed samples.

Tuble 7. Hardness of the annealed modified coating samples									
Annealing temperature, °C	30	00		600	ç	900			
Annealing duration, h	1	2	1	2	1	2			
Without DPs	9.1	7.3	7.1	12.0	4.8	2.5			
DPs, 10 g/l	9.6	10	10.3	12.4	5.1	3.7			

Table 7. Hardness of the annealed modified coating samples

At 300 °C, the appearance of samples has not changed, and there are no cracks. Metal chrome had a good appearance. At 600 °C, the color of the samples changed from light gray to bright blue, the samples obtained from the electrolyte with the additive having a brighter color and being more uniform. Samples that had been annealed for just 1 h were of pale blue color. Neither pure chromium nor its oxides can be blue. Chromium salts are of sky-blue color. Chromium (III) chloride, CrCl₃, represents purple crystals. It is soluble in water in the presence of reducing agents (Cr²⁺, Fe²⁺). It is used in obtaining chromium by electrolysis and by metallothermic process. At 900 °C, with the annealing lasting for 1 hour, the samples become dark green. Samples obtained from the control electrolyte had large cracks and were destructed at some points. Samples obtained from electrolyte with DPs have no cracks and have not been damaged. If annealing lasted 2 h, the samples were black, crack-free, and strong.

Coatings modified with high-dispersion carbon. To identify the optimal parameters of obtaining composite coatings, we studied how the concentration of high-dispersion particles of black carbon affected the properties of Cr-ECC. Table 8 shows the results of finding the basic parameters of the electrochemical reduction of chrome from the suspension electrolyte.

Table 8. Properties of chrome coatings depending on the concentration of high-dispersion graphite particles in electrolyte

Concentration of particles in electrolyte, g/l	0	5	10	15	20
Deposition rate, μm/h	10.56	11.69	15.27	17.86	20.11
Current efficiency (CE) of metal, %	9.54	10.2	11.01	12.87	14.49
Hardness (H), GPa	7.7	9.23	10.11	9.67	9.11

In all the experiments, coatings were matte and silver-gray. It follows from Table 8 that, with increasing the concentration of graphite particles, the deposition rate of coatings increases. With an increase in DP concentration, the current efficiency of chromium increases from 10 to 15 %. The highest CE value is reached at the concentration of 20 g/l.

Graphite particles contribute to increasing the hardness at smaller concentrations only. If the concentrations in deposition electrolyte is higher, 15 and 20 g/l, then the hardness of samples decreases. The highest hardness value, 10 GPa, can be reached at the concentration of 10 g/l.

It is characteristic of most ECCs that the increase in hardness is determined by changing the matrix structure, grinding the grains, increasing the displacement resistance of individual components of the system with the existing particles, and finally by the presence of the second-phase substances that have a much higher hardness than the matrix.

Decreasing ECC hardness can be found, where materials having lower density are used, such as graphite, disulfide, or molybdenum. This is due to the fact that, when contacting the anode, these particles, in most cases, don't have a sufficient force pulse to ensure a tight contact, and in some cases, they penetrate in the coating as agglomerated groups that give the coating a reduced porosity. With a smaller ECC thickness, the hardness is found for the coating and its sublayer.

To identify the chemical composition of the chrome layers, we used X-ray diffraction analysis. Top, middle, and bottom of the sample were selected as the measurement points of chrome distribution over the metal. The outcomes are presented in Table 9 below. Results shown in Table 9 confirm the outcomes shown in Table 8 above. Since the system under study is a single-layer one, it is natural that the greater the coating thickness, the higher the chromium content.

	Tuble 34 Identifying the chemical composition of chrome lajers, 70							
Co	oncentration, g/l	0	5	10	15	20		
"Top"	Cr	41.53	62.85	65.7	68.75	87		
Тор	Fe	44.77	13.35	21.5	9.95	0.9		
"Middle"	Cr	82.88	83.5	85.05	86.83	96.1		
Middle	Fe	0.76	0.45	0.5	0.52	0.7		
"Bottom"	Cr	92.47	93.45	96.9	99.1	99.8		
DOUGH	Fe	0.34	0.45	0	0.13	0.11		

Table 9. Identifying the chemical composition of chrome layers, %

In control samples, chromium is distributed over the surface of the metallic sample non-uniformly. Chromium is mostly deposited in the middle and bottom of the samples. This can be explained by the poor throwing power of chrome electrolyte. When introducing in the electrolyte the graphite particles at their concentration of 5-15 g/l, chrome content in the coating increases, the influence of particles being observed to a larger extent in the "tops" of the samples. The thickness of the "bottom" changes slightly in all the coatings.

It can be concluded that graphite provides good effects on the throwing power of chrome electrolyte. More uniform, in terms of their compositions, were coatings obtained at the 20 g/l concentration of ultrafine graphite particles. The findings are consistent with the results of computing the CEs (Table 8).

Heat treatment is performed to relieve internal stresses, increase the plasticity of deposits, and homogenize the coating structure. When performing the heat treatment of a dispersed-phase substance can either be partly removed from the superficial layer or be modified and thereby affect the coating structure.

Hydrogen content can be reduced by annealing. Annealing had been performed at a temperature of 300, 600, and 900 °C in an electric furnace until a constant coating mass was established. During annealing, the coating masses decreased by thousandths of a gram. We investigated the influence of graphite particles on the hydrogen content in the chrome matrix. As a criterion for evaluating the hydrogen effect, we took weight before and after annealing and measured the coating hardness.

Hardness was evaluated in control samples after annealing at all the temperatures studied. Hardness of modified coatings was evaluated after annealing them at the temperature of $600\,^{\circ}$ C. The results are shown in Table 10.

Table 10	Hardness	of coatings	depending on the	he annealing	temperature
I abic iv	, i i ai uii coo v	or coaumes	acochaine on a	ne anneanne	Cimborature

Composition of	Temperature, °C				
Concentration of	300.00	600.00	900.00		
particles, g/l	Hardness, H, GPa				
0	7.70	8.00	8.90		
0	Time, h				
	1.00	2.00	1.00		
5	10.74				
3	1.00				
10	11.03				
	2.00				
15	11.64				

Table 10 shows that the hardness of the coatings after annealing increased by an average of 2.7 GPa in coatings at the 5 g/l concentration of particles in electrolyte. Appearance of the coatings: at a temperature of 300 °C, thin films were formed on the samples, which were not at all noticeable to the eye.

At 600 °C, violet-blue films were formed on the smooth surface of metal as a result of forming a thin transparent surficial oxide film and of the light interference in it. Color was

affected by the rate of temperature elevation (from 300 up to 600 °C) and by the holding time (2 hours) of metal samples at such temperature.

These iridescent colors can be observed on the shiny surface of steel objects heated; and they are called "annealing colors". These colors develop due to the fact that, resulting from heating the steel to high temperatures, its surface gets oxidized to form a thin transparent oxide film that reflects light in different ways depending on its thickness, which makes us see one or another annealing color. At the points where the heating temperature was higher, the oxide film thickness is greater, respectively, because at higher temperatures the diffusion rate is higher and the oxygen atoms penetrate deeper; thicker oxide films absorb light waves with a longer wavelength and reflect those with a smaller one.

There is a direct relationship between the film thickness and the wavelength of the light reflected by it: The greater the film thickness is, the shorter-wave reflected light we get. For example, blue is formed when longer waves are "subtracted" from the white, such as red or orange, while yellow is formed when short-wave radiation, such as violet or blue, is "subtracted" from the spectrum. Therefore, blue color is relevant to a higher heating temperature, while yellow color to a lower one.

Many factors influence on the annealing steel color formation: Heating rate, holding time, and steel composition. For example, in alloyed steels (especially with chromium), oxide films are formed slower and at higher temperatures than in common carbon steels.

The oxide film is of such a color due to the fact that hexavalent chromium is oxidized to the trivalent one when heated. As is known from literary references, trivalent chromium salts have a violet and a green modification, the salts of such modifications having different structures.

At 900 °C, well-visible thick marsh-green films were formed; this color is due to forming the trivalent chromium oxide film that a typical green color.

Heating improves the adhesion of chrome coatings to metal, but the heating should not exceed 600 °C, because at the same time, a brittle carbide layer is formed at the boundary between steel and chromium, along which the samples are exfoliated if deformed.

During the thermal oxidation of metallic chromium, chromium (III) oxide can be formed in the coating, as well as chromium hydrides and carbides. Chromium hydride is not formed, since about $80\,\%$ of hydrogen is released at $300\,^\circ\text{C}$ and the remaining $20\,\%$ only at higher temperatures, while chromium recrystallization starts at $900\,^\circ\text{C}$.

Heating improves the adhesion of chrome coatings to metal, but the heating should not exceed 600 °C, because at the same time, a brittle carbide layer is formed at the boundary between steel and chromium, along which the samples are exfoliated if deformed.

Figures 4-10 show the microstructures of coatings, depending on the annealing conditions and the graphite concentrations in the electrolyte.

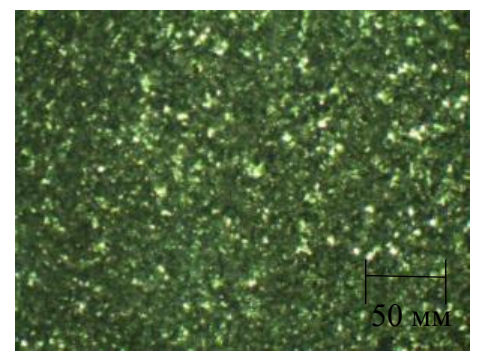


Fig. 4. Control coating microstructure before burning

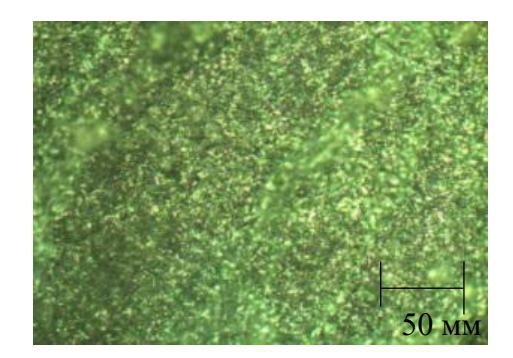


Fig. 5. Control coating microstructure after annealing at 300 °C

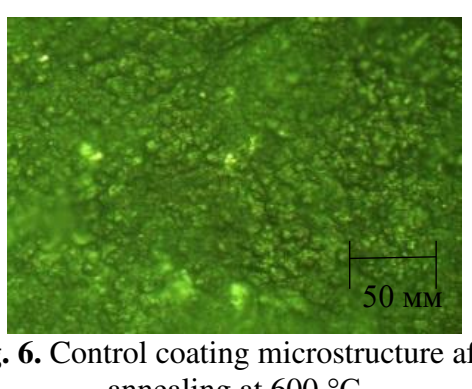


Fig. 6. Control coating microstructure after annealing at 600 °C

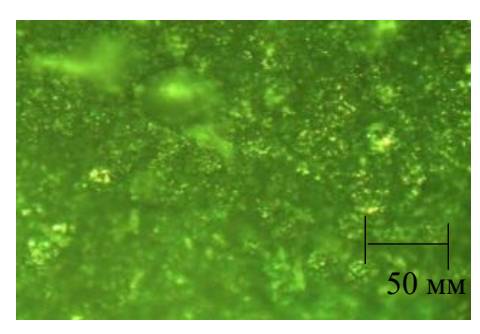
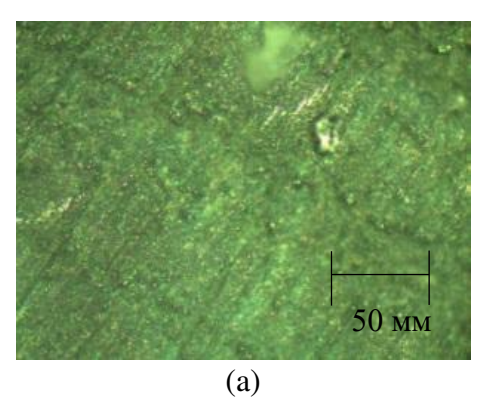


Fig. 7. Control coating microstructure after annealing at 900 °C



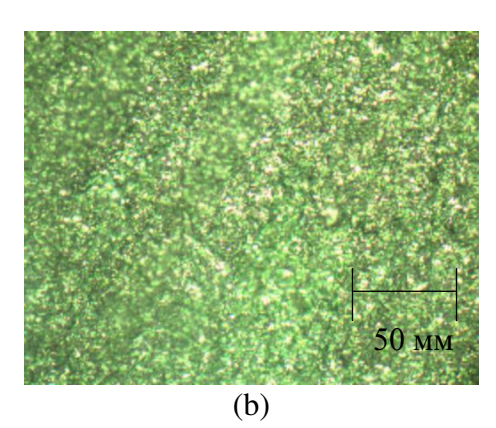
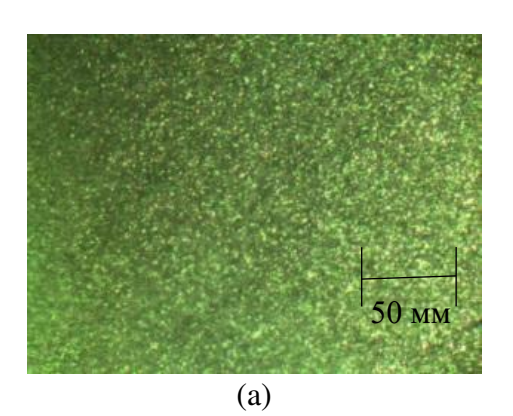


Fig. 8. Chrome coating microstructure at the graphite concentration of 5 g/l in electrolyte (a) before and (a) after annealing at 300 °C



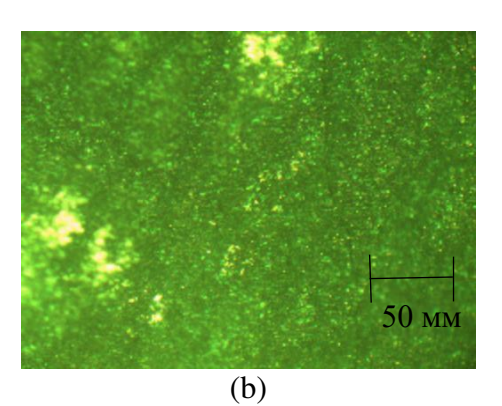
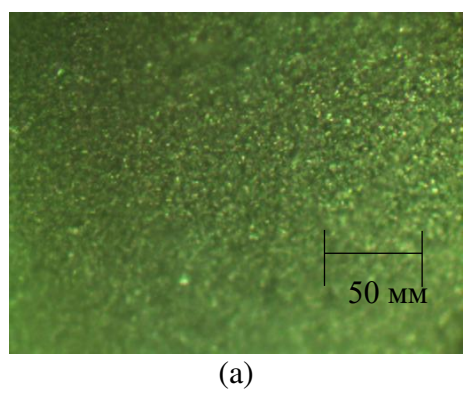


Fig. 9. Chrome coating microstructure at the graphite concentration of 10 g/l in electrolyte (a) before and (b) after annealing at 600 °C



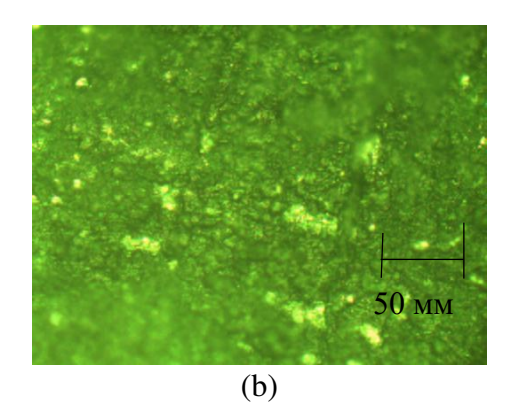


Fig. 10. Chrome coating microstructure at the graphite concentration of 15 g/l in electrolyte (a) before and (b) after annealing at 900 °C

Microphotographs show that chrome coatings have different structures. With the transition of no-DP chrome coating to the ECC, the surface microstructure changes significantly. The surface is better developed and has a noticeable shine; it also has darker areas, corresponding to possible inclusions of graphite particles in the chrome matrix.

Total corrosion rate is evaluated by losing the metal per unit area of corrosion, e.g., in g/m^2 ·h, or by the corrosion penetration rate, i.e., by a single side decrease in the intact metal thickness (P), e.g., mm/year. Tables 11 and 12 present the results of evaluating the corrosion resistance of modified coatings.

Table 11 Influen	as of onne	salina aand	litiana an	the ace	agencian mata
Table 11. Influen	ce or anne	anng conc	muons on	me gas	corrosion rate

Annealing temperature, °C	Concentration of particles, g/l		V gas corrosio	n rate, g/m ² *h	
300	0	1.1·10-4	3.83·10-6	4.8·10-4	3.3·10 ⁻⁶
	5	1 == 106			
600	0	1.77·10 ⁻⁶	$3.33 \cdot 10^{-4}$	3.77·10 ⁻⁵	$2.44 \cdot 10^{-3}$
	10				
900	0	1.15·10 ⁻⁶	1.7·10 ⁻¹²	2.95·10 ⁻⁹	2.25·10 ⁻¹⁰
	15				

Table 12. Corrosion penetration of modified coatings

Temperature, °C	Concentration of particles, g/l	Corrosion penetration, mm/year			
300	0	0.03	0.05	0.07	0.06
300	5				
600	0	0.454	0.21	0.58	0.47
	10				
900	0	0.008	0.002	0.005	0.097
	15				

Gas corrosion rate increases greatly with the temperature exceeding 200-300 °C. The samples of control coatings turned out to be resistant, if they had been annealed at 300 °C and with particles at a concentration of 5 g/l in the deposition electrolyte and at 600 °C with particles of 10 g/l. Samples annealed at 900 °C and the concentration of 15 g/l turned out to be less resistant. Corrosion resistance of coatings is due to forming a protective film, Cr_2O_3 , on the surface. Thickness and composition of this film are evaluated by the coating surface state and by the conditions of evaluating the corrosion resistance. Table 13 shows the results of evaluating the average wear of samples.

Table 13. Average wear of the samples obtained from electrolytes of different compositions.

Electrolyte composition	Average wear, mg		
Control coating	0.0216		
Standard electrolyte with 5 g/l of graphite	0.0289		
Standard electrolyte with 10 g/l of graphite	0.0189		
Standard electrolyte with 15 g/l of graphite	0.0295		

As can be seen from Table 13, the sample obtained from a standard electrolyte with 10 g/l of ultrafine graphite particles demonstrates the least wear, and the dispersed-phase coating resists the wear 1.1 times better than galvanic chromium deposits.

Conclusion

Changes in the physical and mechanical properties of chrome matrix are caused by the effect of dispersed-phase particles, such as aluminum/chromium oxide nanoparticles and high-dispersion carbon, on the state of the deposited chrome layers. When introducing the dispersed phase into the electrolyte, the surface of the electrically deposited chrome gets smoothed, and thicker coatings are obtained. Using the XRF method, we have shown that introducing DPs in the electrolyte contributes to a more uniform chrome distribution over the entire surface of steel samples.

With changes in the concentration of the Cr_2O_3 particles in electrolyte from 10 to 50 g/l, the hardness of deposits increases by 1.2-1.5 times, while when using high-dispersion graphite particles of 5-20 g/l, this indicator changes by 1.2-1.3 times.

In studying corrosion currents, we found that coatings obtained from electrolytes with the Al_2O_3 nanoparticles had corrosion currents greater than those of coatings from a standard chrome-plating electrolyte. Moreover, with an increase in the DP content, the corrosion current increases.

References

- 1. Sayfullin RS. Composite coatings and materials. Moscow: Khimiya; 1977. (In-Russian)
- 2. Yudina EM, Kisel YE, Kadyrov MR, Serguntsov AS. Service properties of composite electrochemical coating. *MATEC Web Conf.* 2021;344: 01022.
- 3. Vodopyanova SV, Fomina RE, Mingazova GG. Properties of Composite Electrochemical Coatings with a Nickel Matrix. *Bulletin of Kazan Techn ol. Un-ty*. 2011;11: 156–160.
- 4. Dolmatov VY, Burkat GK, Safronova IV, Vehanen A, Myllymäki V, Marchukov VA, Almazova NS, Litovka YV, Dyakov IA. The Study of Obtaining Composite Nickel Electroplatings with Detonation Nanodiamonds and Diamond Charge. *Advanced Materials and Technologies*. 2020;20(4): 3–11.
- 5. AlOgab KA, Borisevich IO, Borisevich KO, Zhdanok SA, Krauklis AV, Parshuto AA. Preparation of chromium coatings with additions of carbon nanotubes. *Protection of Metals and Physical Chemistry of Surfaces*. 2018;54(3): 360–364.
- 6. Tseluikin VN. Preparation and properties of graphite nitrate-modified composite electrochemical coatings based on a nickel–chromium alloy. *Inorganic Materials*. 2019;55(7): 656–658.
- 7. Tseluikin VN, Yakovlev AV. Study of electrodeposition and functional properties of nickel—graphite bisulfate composite coatings. *Russian Journal of Applied Chemistry*. 2019;92(5): 614–619.
- 8. Tseluikin VN, Yakovlev AV. On the electrochemical deposition and properties of nickel-based composite coatings. *Protection of Metals and Physical Chemistry of Surfaces*. 2020;56(2): 374–378.
- 9. Bratkov IV, Yudina TF, Melnikov AG Bratkov AV. Production and properties of electrochemical coatings with electrochemically dispersed graphene based on nickel matrix. *ChemChemTech.* 2020;63(8): 90–95. (In-Russian)
- 10. Vinokurov EG, Margolin LN, Farafonov VV. Electrodeposition of composite coatings. *ChemChemTech.* 2020;63(8): 4–38. (In-Russian)
- 11. Tseluikin VN, Dzhumieva AS, Yakovlev AV, Mostovoy AS. Electrochemical deposition and properties of nickel–chromium–grapheme oxide composite coatings. *Protection of Metals and Physical Chemistry of Surfaces*. 2021;57(6): 1231–1234.
- 12. Pyanko AV, Alisienok OA, Kubrak PB, Chernik AA. Formation and physicochemical properties of composite electrochemical coatings of TiN–Nickel alloy with silicon dioxide incapsulated by nanosized titanium dioxide. *Russian Journal of Electrochemistry*. 2022;58(5): 418–424.
- 13. Vinokurov EG, Margolin LN, Farafonov VV. Electrodeposition of Composite Coatings. *News of Higher Educational Institutions. Chemistry and Chemical Engineering*. 2020;63(8): 4–38.

- 14. Belenky MA, Ivanov AF. *Electrodeposition of metal coatings*. Moscow: Metallurgiya; 1985. (In-Russian)
- 15. Zheleznov EV, Kuznetsov VV. Chromium-based Composite Coatings Deposited from Cr (VI) Baths Containing Ultradispersed Particles of BNWuerzie and WC. *Electroplating and processing Surfaces*. 2017;1: 34–40. (In-Russian)
- 16. Sayfullin RS, Khatsrinov AI, Vodopyanova SV, Fomina RE, Mingazova GG. Research in the field of creating composite electrochemical coatings (ECC) with a dispersed phase of microand nanoparticles. *Bulletin of Kazan Technol. Un-ty.* 2009;6: 80–91.
- 17. Makhina VS, Grafushin RV, Vinokurov EG. Wear Resistance of Composite Electrodeposited Coatings Chrome-Graphite. *Advances in Chemistry and Chem. Eng.* 2017;31(5): 54–56.
- 18. Grafushin RV, Vinokurov EG, Makhina VS, Burukhina TF. Electrodeposition and physic-mechanical properties of composite coatings based on chrome with various carbon modifications. *Electroplating and Processing Surfaces*. 2018;26(2): 26–32. (In-Russian)
- 19. Korneychuk NI. Influence of heat treatment conditions on the structure of chrome coatings *Engineering*. *Information Science*. 2015;51(3): 90–96.
- 20 Lubnin EN, Polyakov NA, Polukarov YM. Electrodeposition of Chromium from Sulfate-Oxalate Solutions Containing Aluminum Oxide and Silicon Carbide Nanoparticles. *Metal Protection*. 2007;43(2):199–206.
- 21. Vodopyanova SV, Sayfullin RS, Fomina RE, Mingazova GG. Evaluation of the thickness and chemical composition of chromium coatings with Cr₂O₃ nanoparticles. *Bulletin of Kazan Technol. Un-ty.* 2015;18(4): 125–128.

Increasing of the resistance against contact corrosion of LAIDP with steel tool joints

Submitted: August 7, 2023

Accepted: October 27, 2023

Approved: September 20, 2023

V.N. Malyshev ¹⁰ ^{1 ∞}, M.Ya. Gelfgat ¹, A.I. Shcherbakov ¹, A.A. Alkhimenko ²

¹ National University of Oil and Gas "Gubkin University", Moscow, Russia

² Peter the Great St. Petersburg Polytechnic University, St. Petersburg, Russia

⊠ vmal@inbox.ru

Abstract. This paper discusses the possibility of protection enhancing against contact corrosion of light-alloy drill pipes (LAIDP) by forming a ceramic coating on threaded parts of the aluminum drill pipe using the micro-arc oxidation (MAO) method. When such a coating is formed in the zone of connection of the pipe with steel tool joint and on the threaded part of the pipe, a barrier for contact corrosion between the steel tool joint and the surface of the aluminum pipe is created. Studies of this paper were directed to determine the electrochemical potentials (ECP) on samples in a pair of aluminum alloy 1953T1 and steel 40KhN2MA in a 5 % NaCl solution at 20 °C and their influence on the contact corrosion. The results obtained showed that protective MAO-coating reduce the contact corrosion of the pipe and increase the reliability of connection between the LAIDP pipe body and the steel tool joint.

Keywords: contact corrosion; light-alloy drill pipes; micro-arc oxidation method

Citation: Malyshev VN, Gelfgat MY, Shcherbakov AI, Alkhimenko AA. Increasing of the resistance against contact corrosion of LAIDP with steel tool joints. *Materials Physics and Mechanics*. 2023;51(7): 137-142. DOI: 10.18149/MPM.5172023_12.

Introduction

Nowadays, a significant increase in the share of horizontal wells, wells with complex profiles and multilateral wells is watched when drilling for oil and gas [1,2]. This creates the prerequisites for using LAIDP (light alloy improved dependability drill pipes) which design presents a pressed pipe made of 1953T1 aluminum alloy with upset ends and cut the trapezoidal thread in accordance with ISO 15546-2011 [3] for attaching the tool joint made from the steel 40KhN2MA.

The use of LAIDP allows reducing the torque and drag loads during rotation and movement of the drill string in a borehole during directional wells drilling. Using of LAIDP in the drill string provides the opportunity to make a longer borehole from the same drill rig [4–6]. The connection of an aluminum pipe with a steel tool joint in a corrosive environment, due to the difference in electrochemical potentials of the contacting materials, is often a reason for the contact corrosion which can occur in the section of the aluminum pipe adjacent to the steel tool joint [7–10]. Similar corrosion damages were encountered, for instance, during drilling at the Tarim field located in China [11].

To reduce the contact corrosion in the aluminum-steel connection, it is necessary to create conditions that provide the elimination of direct metal contact between steel tool joints and aluminum pipe. This can be made by applying an insulating coating. The recent research in this field was proposed in [12] when the aluminum oxide obtained by anodization was used as such a coating that showed its effectiveness.

The MAO method [13–15] arose from traditional anodizing, but the processing is carried out at the higher values of potentials and currents that provide the surface of an aluminum alloy treatment not only electrochemical in electrolyte but by the action of micro-arc discharges having temperature up to 6000-8000 °C [16]. Such conditions are highly providential for forming a hard α -aluminum oxide (corundum) with high mechanical properties (microhardness up to 20 GPa). Due to the uncial properties of aluminum oxide, these coatings are very resistant to wear, corrosion, heat, and insulation.

The main feature of this technology is an environmentally friendly process and highly efficient. When such coating is formed in the zone of aluminum pipe connection with steel tool joint including the threaded part of the pipe, a barrier that prevents the contact corrosion between the steel and aluminum surfaces is created. This barrier is reducing the density of corrosive currents and increasing the electrical resistance of the contact on the part of the pipe adjacent to the steel tool joint. The study performed with samples simulating a threaded connection "steel tool joint - aluminum pipe" [17] showed good resistance against contact corrosion in a corrosive environment in these pairs.

This paper is a further investigation in this direction and presents some results of a research program of increasing the corrosion resistance of drilling pipes made of 1953T1 aluminum alloy against contact corrosion by forming MAO-coating in the contact area of the pipe and tool joint.

Materials and Methods

For investigation of electrochemical potentials and corrosion currents on the samples, the same grades of the materials used in the drilling were taken: aluminum alloy -1953T1, and steel -40KhN2MA. This steel is usually used to manufacture tool joints in accordance with International Standard ISO 11961-2020 [18,19] for aluminum pipes connection in the drill string and is chromium-nickel-molybdenum structural alloy steel. 40KhN2MA is smelted in open electric furnaces and by the method of electroslag remelting and characterized by high mechanical properties. The form and dimensions of samples were as follows: square plate from aluminum alloy $-30 \times 30 \times 5$ mm, square plate from steel $-13.4 \times 13.4 \times 5$ mm with 6.5 mm diameter holes in the center.

The MAO-coating was formed on the samples of 1953T1 in the same conditions as during the previous studies [17] – in a weakly alkaline electrolyte for 15 and 30 min and the thickness of the formed coating was 15-20 and 35-40 μ m respectively.

It should be noticed that the coating on samples was formed not on the whole sample surface but only on the part of the surface adjacent to the contact zone. In this connection, the section with MAO-coating on the sample was formed only on one side of the sample and the surface of coating was not more than one-fourth of the whole surface of the sample. To prevent the coating formation on other surfaces of the sample it was isolated by silicone.

The accepted coding of samples was the same as used in ref. [17]. Samples 0 and 1 were without MAO-coating, samples 11-13 were with MAO coating 15-20 μ m thick, samples 21-23 were with MAO-coating 35-40 μ m thick, samples of steel with numbers 1, 12, 13, 22, and 23 were subjected to phosphating at the same conditions as in [17]. Two samples from aluminum alloy with numbers 12 and 22 were treated in addition by fluoroplastic suspension (F-4D).

Before the start of the experiment, measurements of electrochemical potentials and corrosion currents were carried out in an electrochemical cell for each pair of samples in a 5 % NaCl solution at the temperature 20 °C using a two-electrode scheme [20]. For this aim, the potentiostat PARSTAT 4000 and the software VersaStudio were used. After these preliminary measurements, the original samples were assembled into pairs (Fig. 1) and kept for 336 hours in a 5 % NaCl solution at 80 °C in a drying oven (Fig. 2). After exposition in a corrosive environment, the samples were cleaned of corrosion products and visually evaluated.

Then there were carried out the repeated measurement of electrochemical potentials and corrosion currents and the data recorded into the journal.

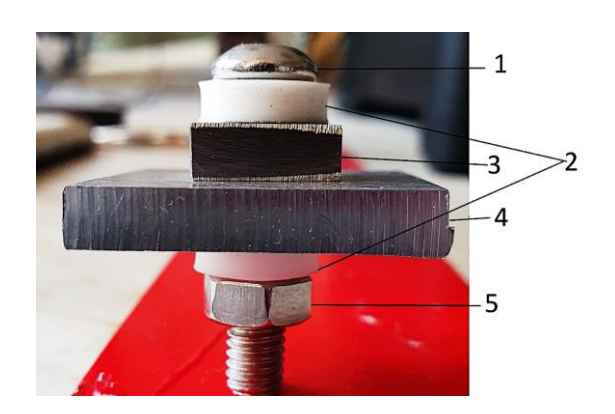


Fig. 1. Assembly of contact pair samples: 1 - bolting; 2 - flouroplastic spacers; 3 - steel sample; 4 - aluminum alloy sample; 5 - nut



Fig. 2. Collected assemblies of pair samples in 5 % NaCl solution at 80 °C

Results and Discussion

The view of samples assembled pairs after exposition in a corrosive environment is represented in Fig. 3.



Fig. 3. Samples after exposition in 5 % NaCl solution at 80 °C during 336 hours

Figure 4 shows the electrochemical potentials versus corrosion currents for samples without MAO-coating (a) - samples 0, and with the coating (b) - samples 23 in two states – before the corrosion test (on the left) and after it (on the right).

All experimental data obtained are represented in Table 1. The results show that the effect of prolonged hydrothermal action on the samples is reduced to the following.

After a corrosive test on the surface of the samples of pair 0, an abundant amount of corrosion product was noticed. After cleaning them, on the surface of the aluminum alloy sample in the contact zone with the steel sample, irregularities in the form of micro-ulcers were observed. Samples of pair 1 did not show outer any signs of corrosion, but after disassembly and cleaning, similar surface damage was revealed as in pair 0 in the form of micro-ulcers, but more pronounced.

For pairs 11 and 12, corrosion of the steel sample in the form of local spots was noted. In pair 13, the same as in pairs 12 and 11, the steel sample corroded, but more actively. The first inspection of pair 21 revealed a large volume of corrosion product deposited on the aluminum sample. But after cleaning them, no any damages of MAO-coating were found. It was concluded that only the steel sample has corroded.

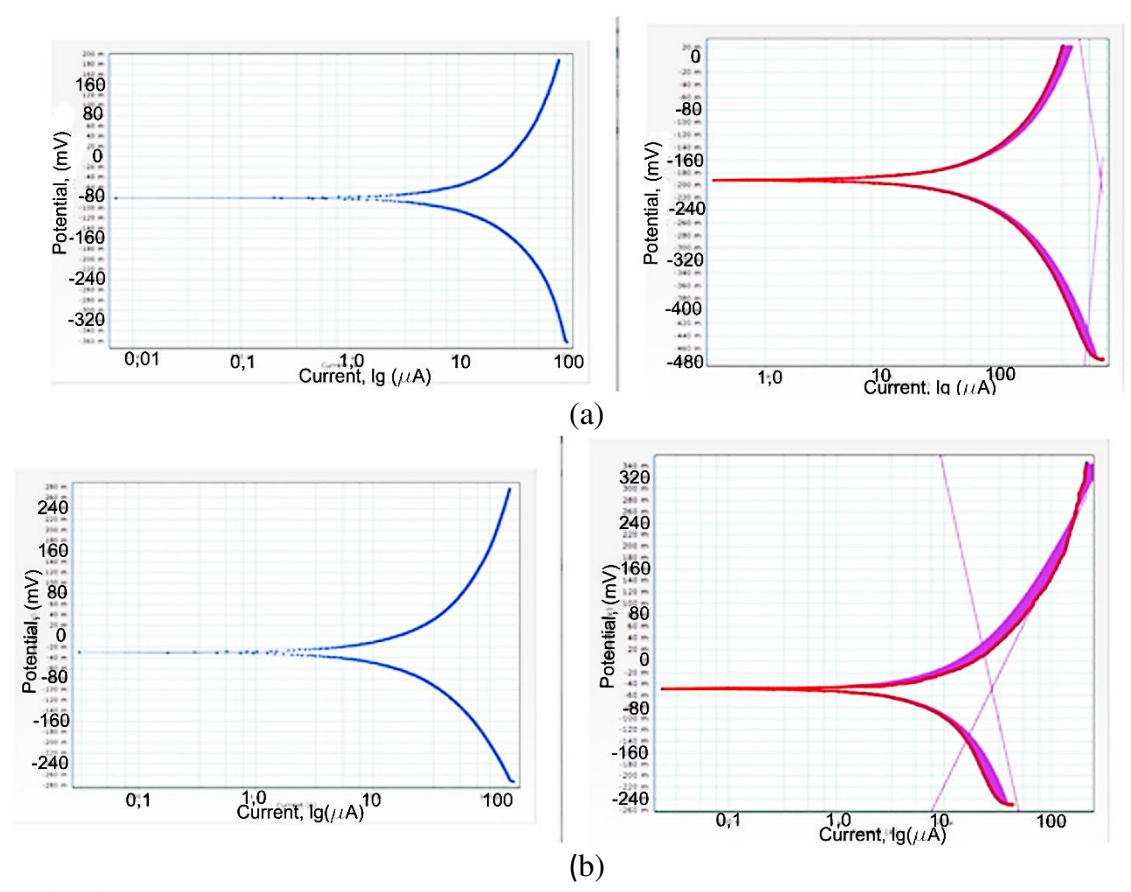


Fig. 4. Tafel polarization curves for samples of some pairs: (a) sample 0; (b) sample 23 (on the left – before corrosion test, on the right – after exposition in corrosion environment)

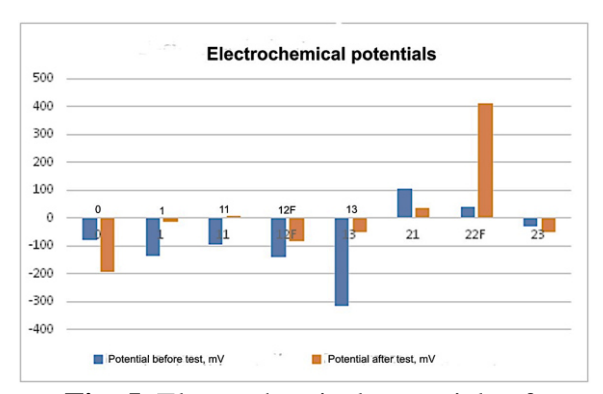
Table 1. Results of measurements and visual estimation

Samples	Thickness of MAO-coating, µm	Potential before test, mV	Corrosion current before test, µA	Potential after test, mV	Corrosion current after test, µA	Corrosion damages	Notes	
0	Without MAO	-80.679	242.291	-191.641	687.463	presence	-	
1	Without MAO	-134.413	13.029	-13.944	465.456	presence	Phosphated steel	
11	15	-96.678	154.236	6.795	365.000	low	Phosphated steel	
12F	23	-138.384	876.718	-82.034	25.890	presence	F-4D added	
13	17	-316.313	2.715	-51.229	22.297	presence	Phosphated steel	
21	28	103.515	94.757	34.403	17.945	presence	Phosphated steel	
22F	36	40.006	79.960	413.415	0.672	no	F-4D added	
23	30	-30.326	149.348	-48.254	27.985	low	Phosphated steel	

Samples of pair 22 did not show any changes on the surfaces in the contact zone, and there were no signs of corrosion. Corrosion products are present around the contact perimeter of pair 23. But signs of MAO-coating violation of the integrity were not noticed.

Repeated measurements of the polarization curves from the samples were also carried out in a 5 % aqueous solution of NaCl at T = 20 °C. During corrosion studies, corrosion potentials, corrosion currents, and Tafel coefficients were determined. All potentials of aluminum samples are represented relative to their corresponding steel samples.

Based on the data in Table 1, for a more visual assessment of the results, diagrams were drawn up (see Figs. 5, and 6).



Corrosion currents

1000
900
800
700
600
500
400
0
0
1
11
12F
13
21
22F
23
Current before test, µA

Fig. 5. Electrochemical potentials of investigated samples

Fig. 6. Calculated corrosion currents

Comparing the results obtained, we can say the following:

- 1. for samples of pair 0, after the test, the corrosion current value was maximum among all presented pairs, and for pair 22, on the contrary, it was minimum. Having linked these values with a visual assessment of samples, it is permissible to assert that the lower the value of the corrosion current, the lower will be the contact corrosion;
- 2. the phosphating of steel samples directly affects the process of contact corrosion, namely, it helps to reduce the corrosion current. This is most likely due to the fact that the phosphating steel layer represents also an insulator at the points of contact;
- 3. samples of pairs 11 and 13 had MAO-coatings 15 and 17 μ m thick, respectively. After exposition in 5% NaCl solution, the coatings were damaged. This means that the thickness of MAO-coating lower than 20 μ m cannot keep the integrity and should be increased over this value;
- 4. additional treatment of samples from aluminum alloy with MAO-coating by fluoroplastic suspension play in whole its positive role but is ambiguous;
- 5. forming the MAO-coating on the contact zone reduces significantly the corrosion current, increasing thereby the corrosion resistance of aluminum alloys.

Conclusions

Thus, the held investigations have shown that in most cases the corroded material was steel. Using the MAO-coating as an insulator to improve the resistance from contact corrosion of aluminum drill pipes is quite appropriate. The recommended thickness of the coating should be about 30-40 μ m because at lower thickness is it possible to develop some damages of coating and breakdown of its completeness.

References

- 1. Gelfgat MY. Razvitie technologiy bureniya skvazhin klyuchevoe napravlenie razvitiya neftegazovoy otrasli. *Vestnik assotsiatsii burovykh podryadchikov*. 2020;1: 19-27. (In-Russian)
- 2. Neskoromnykh VV. *Drilling of inclined, horizontal and multilateral wells: textbook.* Krasnoyarsk: Siberian Federal University; 2016. (In-Russian)
- 3. International Organization for Standardization. ISO 15546:2011. *Petroleum and natural gas industries Aluminum alloy drill pipe*. ISO; 2011.

- 4. Gelfgat MY, Basovich VS, Tikhonov VS. Drillstring with aluminium alloy pipes design and practices. In: 2003 SPE/IADC Conference, Amsterdam, The Netherlands, 19-21 February 2003. p. SPE-79873-MS.
- 5. Chandler RB, Jellison MJ, Payne ML et al. Advanced and emerging drillstring technologies overcome operational challenges. World Oil. 2006;227(10): 23-34.
- 6. Panda K, Williams T, Collins A. Increased Tool Life and Enhanced Reliability for Bottomhole Assemblies in Harsh Environments. In: SPE Middle East Oil and Gas Show and Conference, Manama, Bahrain, 18-21 March 2019. 2019.
- 7. Gelfgat MY, Chizhikov V, Kolesov S, Alkhimenko A, Shaposhnikov V. Application of Aluminum Alloy Tube Semis: Problems and Solutions in the Development of Exploration, Production and Transportation Business of Hydrocarbons in the Arctic. In: 2013 Arctic and Extreme Environments Conference & Exhibition, Moscow, Russia, 15–17 October 2013. p. SPE-166919-MS.
- 8. Kolesov SS, Badrak R, Chizhikov VV. Galvanic effects in drilling equipment challenges and solutions of corrosion resistance. In: Eurocorr 2014, European Corrosion Congress, Pisa, Italy, 8-12 September 2014. 2014.
- 9. Kolesov SS, Kondratev SY, Chizhikov VV, Shvetsov OV. Issledovanie struktury i svoystv burilnykh trub iz splava D16T posle expluatatsii v usloviyakh neftedobychi. Zagotovitelnoe proizvodstvo v mashinistrornii. 2011;4: 39-43. (In-Russian)
- 10. Kang Y, Leng X, Zhao L, Bai B, Wang X, Chen H. Review on the Corrosion Behaviour of Nickel-Based Alloys in Supercritical Carbon Dioxide under High Temperature and Pressure. Crystals. 2023;13(5): 725-746.
- 11. Analysis of damage to LBTPN-147x13 made of alloy D16T, discovered during drilling of the well Xa-15 at the Tarim field in China. Scientific and technical report of the Research and Development Center "Weatherford-Polytechnic" St. Petersburg; 2010. (In-Russian)
- 12. Shvetsov OV. *Improving the operational reliability of drill pipes made of aluminum alloys* D16 and 1953. Ph.D Thesis. St. Petersburg; 2014.
- 13. Logunov AA. (Ed). Microarc oxidation. Science and humanity almanac. Moscow: Znanie; 1981. (In-Russian)
- 14. Nikolaev AV, Markov GA, Peshchevitsky BI. A new phenomenon in electrolysis. Izv. SO AN USSR, Ser. Chem. Sciences. 1977;5: 32-33. (In-Russian)
- 15. Malyshev VN. Effective electrochemical transformation method of valve metals surface layer into high-tensile ceramic coating. In: Duncan JI, Klein AB. (Eds.). Chemical Reactions on Surfaces. Nova Science Publishers; 2008. p.211-262.
- 16. Suminov IV, Belkin PN, Apelfeld AV, Lyudin VB, Crete BL. Plasma-electrolytic modification of the surface of metals and alloys. Moscow: Technosphere; 2011. (In-Russian)
- 17. Malyshev VN, Gelfgat MY, Scherbakov AI, Alkhimenko AA. Protection enhancing of threaded connections of light-alloy drill pipes against contact corrosion. E3S Web of Conferences. 2021;225: 03003.
- 18. International Organization for Standardization. ISO 11961:2020. Petroleum and natural gas industries — Steel drill pipe. ISO; 2020.
- 19. Branch Standard. OST 92014-90. Deformable aluminium alloys. Grades. WILS; 1990. (In-Russian) 20. Cramer SD, Covino BS, Moosbrugger JC. ASM Handbook, Volume 13B: Corrosion Materials. ASM International; 2005.

THE AUTHORS

V.N. Malyshev ⁽¹⁾

e-mail: vmal@inbox.ru

A. I. Shcherbakov

e-mail: ars.scherbakov@yandex.ru

M.Ya. Gelfgat

e-mail: mikhailgelfgat@gmail.com

A.A. Alkhimenko

e-mail: a.alkhimenko@spbstu.ru

Assessment of industrial safety at oil refining facilities based on stochastic modeling

Submitted: August 7, 2023

Accepted: October 27, 2023

Approved: September 20, 2023

G.Kh. Samigullin¹, S.A. Nefedyev¹, L.G. Samigullina ^{2 ⋈}, A.Yu. Bruslinovskiy¹

¹ Saint-Petersburg University of State Fire Service of Emercom of Russia, St. Petersburg, Russia

² Gazprom PJSC, St. Petersburg, Russia

⊠ lil 1992@mail.ru

Abstract. The article deals with the estimation of negative influence (impact), provided by dangerous factors, appearing during fire hazardous situation. It is clear, that both thermal stream and inner overpressure mutually can lead to the machine depressurization and destruction, which can cause cascading troubles, making situation more hurtful, than it was. The application of mathematic model is suggested in order to estimate the probability of equipment backstop integrity, which guarantees the evaluation of prevention possibility of the Domino effect.

Keywords: process equipment; emergency situation; normal distribution; standard deviation; expected value; cascade accident progression

Citation: Samigullin GK, Nefedyev SA, Samigullina LG, Bruslinovskiy AY. Assessment of industrial safety at oil refining facilities based on stochastic modeling. *Materials Physics and Mechanics*. 2023;51(7): 143-147. DOI: 10.18149/MPM.5172023_13.

Introduction

The problem of oil and gas facilities and pipelines ensuring safe operation as a part of technological basements on oil and gas production is claimed to be extremely acute and actual [1,2]. Scientific and technical researches, negotiated nowadays, are directed on quality increasing of production sphere technical regulation in area of resource security and reliability, also they are claimed to guarantee regular requirements of production equipment, infrastructure, personal and population safety [3].

An achievement of required safety level and accident consequences minimization on hydrocarbon feedstock facilities obligates further development and improvement of methodical justification for the activities, referred to trouble-free exploitation of oil and gas equipment and pipelines [4,5].

A significant constructive variety of equipment used at technological installations for oil and gas processing, large-scale industrial technologies, a wide range of fire hazard properties of initial hydrocarbon raw materials, intermediate components and commercial oil products are all the reason of an extremely high level of potential hazard, which is generating during the operation of oil and gas production facilities [6]. A priori there is a constant potential hazard, which is able to cause negative cases, like technical failures, accidents and breakdowns, which are the result of capacitive equipment, unit or process pipelines depressurization. In addition to that, there is a high possibility level for further local accidents to grow up to the catastrophic measures involving fires, explosions, leading to considerable material losses, ecological harm, and injuries among the personal, also leading to the fatal outcome [7,8]. In this chain of negative events, the most unfavorable is a case in which hazardous factors, arising during the accident, will initiate further damage or destruction and

depressurization of process equipment, which undoubtedly leads to an increase in the amount of combustible substances involved in the emergencies formation. Mentioned above way is classified as progressive destruction, appearing as a specific Domino Effect, which means: unfavorable scenarios for the accident to grow up, in which (in case of defense system imperfection and (or) personal incorrect actions) it is possible for the accident harmful factors to overcome emergency unit, equipment item or facility boundaries, and hazardous substance involvement in the nearby none-emergency facilities, growing up to the further accident development stage [9,10].

Foreign specialists found out [11,12], that the biggest number of cascading accidents (55-80 %) occurs while preserving automobile and aviation motor fuels, volatile solvents, mixtures of hydrocarbon gases in various states of aggregation, moreover, increase in storage tonnage and production platform area decrease incredibly enhancing possible negative effects.

Methods

Despite the considerable successes in overall accidents rate reducing at hazardous oil and gas productions facilities [13], the relevance of development of some new methods for oil and gas equipment and pipelines danger estimation still remains. These methods are based on realization possibility of accident cascade development estimation in order to improve the efficiency of technosphere and fire risks management systems, as well as to support management decisions. At the same time, the researchers attempts are focused on the development of universal models for a comprehensive assessment of the level of risks of various natures in the conditions of oil and gas production in the presence of a local source of danger and the resulting hazardous factors [14,15].

Ipso facto, cascade growing of an accident forecasting means to be rather difficult trouble [16,17], as it is being affected by many factors, which cannot be easily formulated, such as technological process consummation degree, engineering quality, amount of technological machinery, qualification level of the personal, weather conditions and so on. Meanwhile, it is the obvious hypothesis, that the main option, which can prevent an accident progressive character, is to secure machinery and pipelines integrity, which can be conditionally defined like:

$$N \le G$$
, (1)

where N – whole amount of negative factors (internal – overpressure and temperature of the facilities process environment, external – appearing as a result of an accident or fire – pressure wave impulse, heat radiation, etc.), G – the material equipment ability to perceive external and internal negative factors (strength, bearing capacity, etc.).

Results and Discussion

In order to preliminary estimate the level of the process environment negative impact and hazardous factors on the equipment technical condition, using as an example a typical thermal cracking separator under the condition of a hypothetical fire, calculations were realized according to the methodology [18]. All calculation results are presented in Table 1.

Table 1. The mechanical stresses when a heat flow is affecting to the walls of the machinery calculating result

Technical condition characteristics	Temperature, °C					
Technical condition characteristics	50	60	70	80	90	
Mechanical tension as a result of internal pressure, MPa	123.7	127.5	131.4	135.2	139.1	
Mechanical tension as a result of heat radiation, MPa		25.2	50.4	75.6	100.8	
Total tension, MPa	123.7	152.7	181.8	210.8	239.9	
Allowed tension, MPa	188.9	186.5	184.1	181.7	179.3	

Initial data: process environment – gasoline fraction, machine diameter -1.5 m, wall thickness -12 mm, operating pressure -1.8 MPa, operating temperature -50 °C, wall material – steel 09G2S, allowed stresses at design temperature 188.9 MPa.

The results, which are given there in the table, indicate that the wall temperature rising above 60 °C leads to efficiency interruption and also leads to the origin of depressurization risk, respectively increases the amount of combustible substance, involved in fires with possible cascade growing of the hazardous situation. The results graphic interpretation of the calculations is shown in the Fig. 1.

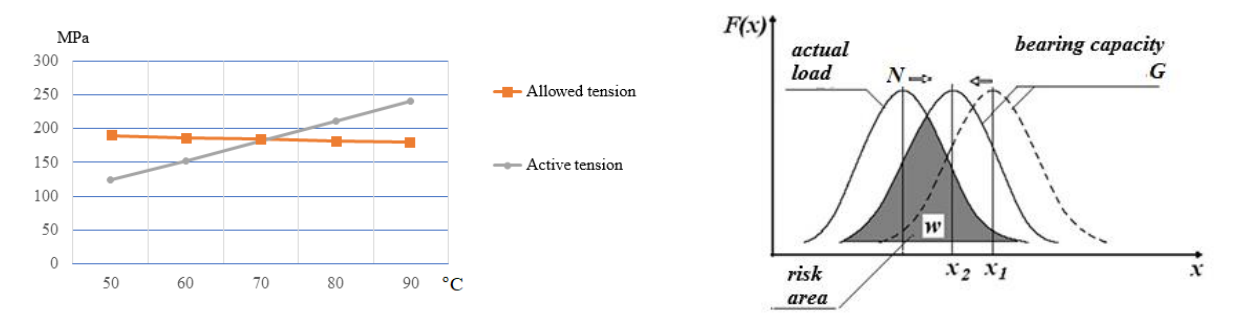


Fig. 1. The comparison of active and allowed tension inside the facilities walls during the fire

Fig. 2. Estimation of impermeability condition of technological condition principle graphic illustration: w – accident risk area, x_I – primary moment of time, x_2 – calculated moment of time

The fire hazardous situation analysis was fulfilled in quasi-stationary conditions, without taking into the consideration the thermal stream dynamic character effect on the facilities, without thermal insulation, without consideration of the thermophysical features of the process environment, without consideration of the wall material. Such deterministic setting makes the final solution for the dangerous situation growth forecasting rather labor-consuming and less perspective [19,20].

In order to estimate the cascade growing of fire-danger realization probability on the oil refining facilities, an algorithm based on stochastic modeling was developed.

Wherein, some simplifications and assumptions were accepted, and one of them is a possibility for these appearances to be described by the random number apparatus. The values, given in the inequality (1), whether the information is lacking, or it is unreliable, can be described due to classical laws of distribution, if we know the expected value and standard deviation.

According to the position, given in the study [21], an application of the function distribution law of random argument, we have:

$$f(N) = \frac{1}{\sqrt{2\pi}S_N} \exp\left[-\frac{(N - M_N)^2}{2S_N^2}\right],\tag{2}$$

$$f(G) = \frac{1}{\sqrt{2\pi}S_G} \exp\left[-\frac{(G - M_G)^2}{2S_G^2}\right],\tag{3}$$

where f(N), f(G) — distribution functions for the cumulatively acting technological effects (burden) and load bearing capacity (mechanical strength) equipment wall material, M_N , M_G — expected values for the cumulatively acting technological effects (burden) and load bearing capacity (mechanical strength) equipment wall material, S_N , S_G — standard deviations for the cumulatively acting technological effects (burden) N and load bearing capacity (mechanical strength) equipment wall material G.

The difference G - N also will be allocated according to the normal law g(G - N) with expected value M_g with dispersion D_g :

$$M_g = M_G - M_N, (4)$$

$$D_g = D_N + D_G, (5)$$

$$S_{g} = \sqrt{D_{g}},\tag{6}$$

where g – sought for random value distribution function (G - N), M_g , D_g , S_g – meanings expected value, dispersion and standard deviation of the difference (G - N), D_N , D_G – dispersions for the cumulatively acting technological effects and load bearing capacity.

The process facilities and pipelines impermeability can be estimated in case we have distribution parameters g(G-N), due to calculated probability value:

$$P(0 < R - Q < \infty) = \int_0^\infty g(R - Q)d(R - Q) = \Phi\left(\frac{M_g}{S_\sigma}\right),\tag{7}$$

where $\Phi\left(\frac{M_g}{S_g}\right)$ – a tabulated normal distribution function.

Impermeability will be provided whether during an accident the probability value, calculated according to the Eq. (7), is close to one.

Respectively, depressurization risks H apparatus can be estimated due to:

$$H = 1 - P, (8)$$

where P – depressurization maintenance probability in case of fire-danger situation.

In the algorithm for the technical state estimation of the equipment mutually competing processes are considered: on the one hand technical loads increasing intensity, on the other hand – damage growing amount and durability decrease with rising temperature from equipment walls and technological environment. These counter-directed processes are graphically given in the Fig. 2.

Apparatus technical condition will be characterized by some value between $(X_1 - X_2)$, which can be matched with operability reserve value, also increasing area where both distribution functions f(N) and f(G) cross, allows us to estimate possible depressurization probability or technological apparatus total distraction in case of $(X_1 - X_2) = 0$, which physically means equality between acting loads and durability of the material.

Conclusion

Thus, basing on the negative impact analysis of the harmful factors, that can lead to the temperature increase up to the 20 °C and higher, the loss of material durability occurs as a result of thermal stream action, which in the fullness of time combined with internal overpressure, supposed to lead to the facilities depressurization or distraction.

It is proposed to estimate the probability of the accident cascade growth for the oil and gas process equipment based on model, which is formulated by the estimation of vessel depressurization probability, which works under the pressure.

References

- 1. Krasnov AV, Sadikova ZKh, Perezhogin DYu, Mukhin IA. Statistics of emergency incidents at the facilities of the oil refining and petrochemical industry for 2007-2016. *Oil and Gas Engineering*. 2017;6: 179-191.
- 2. Kuskildin RA, Abdakhmanov NKh, Zakirova ZA. Modern technologies for production control, increasing the level of industrial safety at oil and gas industrial facilities. *Problems of Collecting, Treating and Transporting Oil and Petroleum Products*. 2017;2: 111-120.
- 3. Bruslinovskiy AYu, Samigullin GKh. Fire hazard assessment at oil refining plants based on stochastic modeling. *Oil and Gas Business.* 2021;6: 23-36.
- 4. Filippova AG, Nuriyeva AZ, Naumkin EA, Kuzeev IR. Assessment of the potential danger of objects of enterprises of the fuel and energy complex. *Reliability and Safety of Energy*. 2018;11: 14-20.
- 5. Samigullin GKh, Schipachev AM, Samigullina LG. Control of physical and mechanical characteristics of steel by Small Punch Test method. *Journal of Physics: Conference Series*. 2018;1118: 012038.

- 6. Samigullin GKh, Zakharov AE. Assessment of fire risk when using polymeric elastic tanks for petroleum and petroleum products storage. *Problems of Risk Management in the Technosphere*. 2021;4(60): 6-13.
- 7. Solodovnikov AV, Shabanova VV, Abrakhmanov NKh. Industrial safety audit of oil and gas complex hazardous production facilities. *Oil and Gas Business*. 2022;1: 1-27.
- 8. Mukhametzyanov NZ, Khafizov FSh. Parameters classification of organizational and technical measures to ensure fire safety of oil industry facilities. *Oil and Gas Business*. 2022;5: 39-54.
- 9. Azarov NI, Koshovetz NV, Lisanov MV. Analysis of the possibility of cascade development of an accident at explosive and fire-hazardous facilities. *Operation Safety in Manufacturing*. 2007;5: 42-47.
- 10. Khakzad N, Reniers G. Low-capacity utilization of process plants: A cost-robust approach to tackle man-made domino effects. *Reliability Engineering & System Safety*. 2019;191: 106114.
- 11. Chen C, Reniers G, Khakzad N. A thorough classification and discussion of approaches for modeling and managing domino effects in the process industries. *Safety Science*. 2020;125: 104618.
- 12. Huang K, Chen G, Yang Y, Chen P. An innovative quantitative analysis methodology for Natech events triggered by earthquakes in chemical tank farms. *Safety Science*. 2020;128: 104744.
- 13. Kovshova YS, Kuzeev IR, Naumkin EA. The assessment of damage and resource of vessel and apparatus elements, taking into account the adaptation of the material to long-term quasistatic loading. *Journal of Physics: Conference Series*. 2020;1515: 052056.
- 14. Abdrakhmanov NKh, Fedosov AV, Shaibakov RA, et al. Organization of safe management of fire operations on gas pipelines. *Bulletin of the National Academy of Sciences of the Republic of Kazakhstan*. 2019;6: 272-279.
- 15. Tagirova KB, Kireev IR, Abdrakhmanova KN. Determination of scenarios of possible accidents at the oil preparation and collection point. *Oil and Gas Engineering*. 2020;1: 89-107.
- 16. Shvyrkov SA, Puzach SV, Goryachev SA, Shvyrkov AS. Research of breakout wave parameters at destruction of tanks with a capacity up to 30 000 m³ in experimental conditions. *Fire and Emergencies: Prevention, Elimination*. 2019;1: 12-18.
- 17. Kozhevin DF, Merkulov AP. On the issue of determining the frequency of fire in buildings of various classes of functional fire hazard. *Problems of Risk Management in the Technosphere*. 2022;2: 34-41.
- 18. Abdrakhmanova KN, Shabanova VV, Abrakhmanov NKh. Application of modeling of the accident development process and risk assessment in order to ensure the safe operation of oil and gas facilities. *Operation Safety in Manufacturing*. 2020;2: 2-13.
- 19. Krasilnikov AV, Vagin AV, Shidlovskiy GL. About some gaps in technical regulation of fire safety. *Bulletin of St. Petersburg University of the State Fire Service of the Ministry of Emergency Situations of Russia.* 2023;2: 10-16.
- 20. Suarez H, Finkelshtein M, Lisanov MV. Foreign experience in risk-informed approach to operation of technical equipment at oil-and-gas facilities. *Operation Safety in Manufacturing*. 2015;8: 24-30.
- 21. Samigullin GKh. Assessment of reliability and residual life of production buildings of oil and gas enterprises based on survivability criteria. *Operation Safety in Manufacturing*. 2016;2: 64-67.

THE AUTHORS

G.Kh. Samigullin (b) e-mail:samigullin.g@igps.ru

L.G. Samigullina b e-mail: lil_1992@mail.ru

S.A. Nefedyev (b) e-mail: doktorsan@mail.ru

A.Yu. Bruslinovskiy 🗓

e-mail: alexander.bruslinovsky@mail.ru

МЕХАНИКА И ФИЗИКА МАТЕРИАЛОВ

51 (7) 2023

Учредители: Санкт-Петербургский политехнический университет Петра Великого, Институт проблем Машиноведения Российской академии наук Издание зарегистрировано федеральной службой по надзору в сфере связи, информационных технологий и массовых коммуникаций (РОСКОМНАДЗОР), свидетельство ПИ №ФС77-69287 от 06.04.2017 г.

Редакция журнала

Профессор, д.т.н., академик РАН, А.И. Рудской – главный редактор
Профессор, д.ф.-м.н., член-корр. РАН, А.К. Беляев – главный научный редактор
Профессор, д.ф.-м.н. И.А. Овидько (1961 - 2017) – основатель и почетный редактор
Профессор, д.ф.-м.н. А.Л. Колесникова – ответственный редактор
Профессор, д.ф.-м.н. А.С. Семенов – ответственный редактор
Л.И. Гузилова – выпускающий редактор, корректор

Телефон редакции +7(812)552 77 78, доб. 224

E-mail: mpmjournal@spbstu.ru Компьютерная верстка Л.И. Гузилова

Подписано в печать 29.12.2023 г. Формат 60x84/8. Печать цифровая Усл. печ. л. $\underline{10,0}$. Тираж 100. Заказ_____.

Отпечатано с готового оригинал-макета, предоставленного автором в Издательско-полиграфическом центре Политехнического университета Петра Великого. 195251, Санкт-Петербург, Политехническая ул., 29. Тел.: +7(812)552 77 78, доб. 224.

N.T. Bagraev, N.A. Dovator, L.E. Klyachkin
Destruction threshold of ZrO ₂ under microsecond magnetic-pulse action S.I. Krivosheev, G.A. Shneerson, S.G. Magazinov, D.V. Zhukov, K.V. Voloshin
Synthesis and characterization of iron-doped TiO ₂ nanotubes for dye-sensitized solar cells 15-21 B. Samran, E. Nyambod Timah, P. Thongpanit, S. Chaiwichian
A kinetic model of the stress-induced void evolution in pentagonal whiskers and rods 22-33 A.S. Khramov, S.A. Krasnitckii, A.M. Smirnov, M.Yu. Gutkin
Toughening of nanocrystalline alloys due to grain boundary segregations: 44-41 Finite element modeling A.G. Sheinerman, R.E. Shevchuk
Elastic properties of additively produced metamaterials based on lattice structures A.I. Borovkov, L.B. Maslov, M.A. Zhmaylo, F.D. Tarasenko, L.S. Nezhinskaya
Modal and harmonic analysis of the rotor system involving four different materials by finite element code: Ansys workbench N. Afane, S. Zahaf, M. Dahmane, A. Belaziz, N. Rachid
Evaluation of mechanical properties of ABS-based fiber composite with infill using 3D printing technology P. Venkataramana, S.P. Jani, U. Sudhakar, M. Adam Khan, K. Sravanthi
Assessment of physical and vibration damping characteristics of sisal/PLA biodegradable composite Y. Munde, A.S. Shinde, I. Siva, P. Anearo
Stiffness characteristics of implanted steel plates after exposure to corrosion R.R. Giniyatullin, N.M. Yakupov, V.G. Kuznetsov
Physical and mechanical properties of modified chrome coatings S. Vodopyanova, G. Mingazova, R. Fomina, R. Sayfullin
Increasing of the resistance against contact corrosion of LAIDP with steel tool joints 137-142 V.N. Malyshev, M.Ya. Gelfgat, A.I. Shcherbakov, A.A. Alkhimenko
Assessment of industrial safety at oil refining facilities based on stochastic modeling 143-147 G.Kh. Samigullin, S.A. Nefedyev, L.G. Samigullina, A.Yu. Bruslinovskiy

